Sara
López de Armentia
Hernández

DEVELOPMENT OF NANOMATERIAL BASED SCAFFOLDS FOR BONE TISSUE REGENERATION

COMILLAS
UNIVERSIDAD PONTIFICIA
ICAI | ICADE | CIHS

Escuela Técnica Superior de Ingeniería (ICAI)
Instituto de Investigación Tecnológica (IIT)

DEVELOPMENT OF NANOMATERIAL BASED SCAFFOLDS FOR BONE TISSUE REGENERATION

Autor: Sara López de Armentia Hernández
Director: Dra. Dña. Eva Paz Jiménez
Dr. D. Nicholas Dunne
Tutor: Dr. D. Juan Carlos del Real Romero

MADRID | Noviembre 2022

En primer lugar, quiero dar las gracias a Eva Paz, Nicholas Dunne y Juan Carlos del Real. Gracias por darme esta oportunidad y por dejarme aprender tantísimo de vosotros. Durante estos años habéis sido un apoyo para mí y he llegado hasta aquí por vosotros. Muchas gracias.

Me gustaría agradecer a las personas que, sin saberlo, sembraron en mí la semilla del interés y la pasión por la ciencia y la investigación: a Paqui Puertas y Mar Alonso, porque con vosotras me di cuenta de que esto era lo que quería hacer en mi vida profesional. Pero mi paso por el iETcc no habría sido igual sin Sara, Roberto, Andrea y Patri. Muchas gracias por hacer esos días de laboratorio tan divertidos.

Pero una semilla no germina si no se riega adecuadamente. Quiero dar las gracias a aquellas personas que la regaron con tanto cariño y paciencia: Juani y Miguel Ángel. Habéis sido como unos padres para mí en la ciencia. De vosotros he aprendido y aún sigo aprendiendo muchísimo.

Quiero también dar las gracias a las personas del grupo de investigación CSM: Mariola, Belén, Susana, Fran, Asun y Manu: muchísimas gracias por todo.

A Berna y Raquel. Muchas gracias por ayudarme tanto en el mundo de los polímeros y la química.

Por supuesto, cuando pienso en la UC3M no puedo dejar de acordarme de los Materialitos. Muchas gracias por tantas horas compartidas en laboratorios, despacho, cafetería y, por supuesto, en nuestro mercado. Un agradecimiento especial merecen mis Charqueras viajeras, mi familia durante esos años en el Charco. Muchas gracias, Gleidys y Nieves.

Finalmente, quiero dar las gracias de nuevo, y a nivel personal, a Eva y Juan Carlos. Vosotros habéis hecho que esta planta crezca y florezca. Eva, muchas gracias por estar siempre ahí, en el día a día, con una sonrisa, dispuesta a ayudarme con cualquier problema, que no han sido pocos. Juan Carlos, gracias por apoyarme siempre y por hacer que siempre haya confiado en que esto iba a llegar a buen puerto.

También me gustaría dar las gracias a Yolanda y Jesús. Yolanda, gracias por estar siempre dispuesta a escuchar todos los problemas que iban surgiendo y buscarles una solución, manchándote en el laboratorio conmigo. Jesús, muchísimas gracias por todo tu apoyo y por esas comidas y cenas Gourmet.

Muchísimas gracias también a Fer y Susana, por vuestra paciencia y por haber hecho que mi trabajo sea mucho más agradable y sencillo en el laboratorio. Sin vosotros, nada de esto funcionaría igual.

A Silvia y Mariano, por haberme iluminado con vuestra experiencia en diseño e impresión 3D. Gracias.

También merecen una mención especial los miembros del DIM y mis compañeros del IIT: Mar, Fran, Marta R, Marta H, Marcos, Katia, Ana, Xavier, Alexis, Pablo, Carlos, Mercedes, Teresa, Miguel y Manuel. Muchas gracias porque, aunque con la pandemia ya no podamos tomar esos cafés, siempre habéis tenido palabras de ánimo para mí.

A los alumnos que han pasado por el laboratorio aportando su granito de arena. Ponram, Matthew, Revant, Juanma, Sergio, Alicia, Sophia, Alessia, Nerea, Manuel: gracias.

De nuevo, gracias a Nicholas por haberme acogido en DCU durante mi estancia, que no habría sido igual sin Antzela, Nikoletta, John, Halima y Ghayadah. Gracias por vuestra ayuda y por hacerme sentir como una más. A Barry O'Connell, por tu ayuda con la nanoindentación.

Muchas gracias a Sophie por haberme acogido en UoB y haber hecho que mi estancia fuera muy productiva y enriquecedora. Gracias especialmente a Víctor, por tu paciencia conmigo. También quiero dar las gracias a Mathieu, Kenny, Emily, Lucy y a todos mis compañeros de laboratorio. Gracias por haberme enseñado tanto.

Gracias también a todos los que, desde fuera del ámbito académico, habéis estado ahí apoyándome. En primer lugar, a mis Turkeys: a Marito, por siempre haberme ayudado con todo, a Sandra, porque juntas hemos crecido y hemos llegado hasta aquí.

A mis Chochis (no estaba segura de usar este nombre, pero lo he visto necesario) porque hacéis que me olvide un poco de mis problemas. Gracias.

También quiero dar las gracias a los de la uni, porque sé que puedo contar con vosotros para todo. Desde que nos conocimos siempre hemos sido una piña. Muchas gracias por haberme ayudado a estar donde estoy ahora.

A los Pomodorini. Pedro, mi hermano en la ciencia, muchas gracias por ayudarme tanto cuando estaba perdida por el laboratorio. Andrea A, siempre sonriente y entusiasmada con cualquier plan. Gracias por contagiarme ese entusiasmo por todo. María, muchas gracias porque siempre he podido hablar contigo de cualquier problema científico y no científico. Morena, mi gran apoyo en la distancia. Muchas gracias por ser mi amiga y diario, siempre dispuesta a escucharme y a ayudarme. Segundo, mi compi de tesis, aunque no compartamos universidad. Gracias por estar ahí.

A María Lucero, por ser siempre esa luz que me ayuda a continuar. Gracias a ti, sé que todo es posible si crees que puedes hacerlo. Muchas gracias por darme fuerza cada vez que quiero rendirme. Fuiste, eres y serás siempre mi ejemplo a seguir.

A mi familia: tías, tíos, primas, primos y cuñado. Muchas gracias porque con una familia así todo es mucho más fácil. Muchas gracias a mis yayos y abuelitos, ojalá pudiera compartir este momento con vosotros, sé lo orgullosos que estaríais. También quiero dar las gracias a los que son mi familia, aunque no lleven mis apellidos: Javi y Luci, muchas gracias por haber sido como mis tíos y haber estado siempre. Miriam, gracias por todo el apoyo que me has dado siempre y por alegrarte tanto cuando las cosas me van bien.

A mis padres, por todo lo que habéis hecho por mi durante estos años. Papá, mamá, gracias a vosotros soy quien soy, no solo a nivel profesional, sino también a nivel personal. Gracias por haberme apoyado siempre en todo, sin dudar de mi criterio en ningún momento. A Meli, mi pilar fundamental. Me cuesta elegir el motivo por el que darte las gracias, porque realmente tengo mil motivos, por ser mi mejor amiga, por escucharme siempre y por tu ilusión por todo, incluso por las scaffolds.

A mi otra familia. Muchas gracias Pino y Carlos por compartir conmigo mis éxitos y fracasos y tratarme siempre como a una hija. Gracias a Piedad, por contagiarme siempre tu alegría.

Por último, quiero dar las gracias a Guille, porque contigo todo es más fácil, haces que sienta que soy capaz de conseguir todo lo que me proponga y que juntos podemos con todo: "Som un equip". Ahora tenemos que continuar nuestro camino como Doctor y Doctora, por fin.

A todos los que en algún momento me habéis ayudado, gracias.

First of all, I want to thank Eva Paz, Nicholas Dunne and Juan Carlos del Real. Thank you for giving me this opportunity and for letting me learn so much from you. During these years you have been a big support for me, and I am here because of you. Many thanks.

I would like to thank to the people who, without knowing it, sowed in me the seed of the interest and the passion for science and research: to Paqui Puertas and Mar Alonso. With you I realized that this was what I wanted to do in my career. But my experience at iETcc had not been the same without Sara, Roberto, Andrea and Patri. Thank you for making my days in the lab so fun.

But a seed does not germinate if it is not watered adequately. I want to thank who watered it with love and a lot of patience: Juani and Miguel Ángel. You have been my parents in science. I have learnt and I am still learning a lot from you.

I would also like to thank in-service materials performance research group: Mariola, Belén, Susana, Fran, Asun y Manu: thank you very much.

To Berna and Raquel. A big thank you for helping me in the world of polymers and chemistry.

Of course, when I think in UC3M I cannot help thinking of Materialitos. Thank you for so many shared hours in labs, office, coffee and, of course, in our market. And a special thank you to my Charqueras viajeras, my family during those years in el Charco. Thank you very much, Gleidys and Nieves.

Finally, I would like to thank again and at a personal level, to Juan Carlos and Eva. You have made this plant to grow and flower. Eva, a big thank you for being always there, in my day-to-day, always with a smile, ready to help me with any problem, which were not few. Juan Carlos, thank you for supporting me and make me always feel that this was going to be a success.

I would also want to thank Yolanda and Jesús. Yolanda, thank you for being always ready to listen and solve all the problems that appeared, getting your hands dirty in the lab with me. Jesús, many thanks for your support and the Gourmet lunches and dinners.

Thank you very much Fer and Susana, for your patience and for making my job very nice and easy in the lab. Without you, this would not work.

To Silvia and Mariano, for enlighten me with your experience in design and 3D printing. Thank you.

DIM and IIT members also deserve a special mention: Mar, Fran, Marta R, Marta H, Marcos, Katia, Ana, Xavier, Alexis, Pablo, Carlos, Mercedes, Teresa, Miguel y Manuel. Thank you because, even if we could not have a coffee together with the pandemic, you always have had supporting words for me.

To the students that have been in the lab playing its part. Ponram, Matthew, Revant, Juanma, Sergio, Alicia, Sophia, Alessia, Nerea, Manuel: thank you.

Again, I want to thank Nicholas for having welcomed me in DCU during my stay, which would not have been the same without Antzela, Nikoletta, John, Halima and Ghayadah. Thank you for your help and for making me feel as if I was there for long time. Thank Barry O'Connel, for your help with nanoindentation.

A big thanks to Sophie for having received me in UoB and having done my stay so fruitful and fulfilling. A special thanks to Victor, for your patience with me. I also want to thank Mathieu, Kenny, Emily, Lucy and all my lab mates. Thank you for having taught me so much.

I want to thank also to everyone who, from outside the academic field have been there supporting me. Firstly, to my Turkeys: Marito. Thank you for always having helped me; Sandra, thank you because we have grown and have arrived here together.

To my Chochis (I was not sure of using this name, but it was necessary) because you make me forget my problems. Thank you.

I also want to thank my university mates because I know I can always count on you. Since we knew each other, we have always been united. Many thanks for having helped me to be where I am now.

To Pomodorini. Pedro, my brother in science, many thanks for helping me when I was lost in the lab. Andrea A, always so happy and enthusiastic with everything. Thank you for letting me share your enthusiasm. María, thank you because I always can talk with you about every scientific and non-scientific issue. Morena, my big distant support. Thank you for being my friend and my diary, always ready to listen and help me. Segundo, my thesis mate, even if we do not share university. Thanks for being there.

To María Lucero, for being always the light that helps me to carry on. Thank to you I know that everything is possible if you believe in you. Thank you so much for giving me strength when I want to give up. You were, are and will always be my example to follow.

To my family: aunts, uncles, cousins and brother-in-law. Thank you very much because with this family everything seems very easy. A special thanks to my yayos and abuelitos, I wish I could share this moment with you, I know how proud you would be. I also want to thank my family, who does not have my last name: Javi and Luci, thank you for being like my aunt and uncle and for being always there. Miriam, thank you for your support and rejoicing over all that I am experiencing.

To my parents, for everything you have done for me in these years. Papá, mama, thank to you I am who I am, not only at a personal level, but also at a personal level. Thank you for having supported me always, without hesitating about my choices. To Meli, my fundamental support. I cannot choose only one reason to thank you, because I have thousands, for being my best friend, for listening always and for your enthusiasm for everything, even for the scaffolds.

To my other family. Thank you, Pino and Carlos, for sharing my successes and my failures with me and treating me always as a daughter. Thank Piedad for make me feel always happy.

Last but not least, I want to thank Guille, because with you everything seems very easy, and you make me feel as I can get everything I pretend and together we can handle it all: "Som un equip". Now we have to continue our path as Doctor and Doctora, finally.

To everyone who has helped me in any moment, thank you.

List of Acronyms

ABS	Acrylonitrile Butadiene Styrene
AM	Additive Manufacturing
ATP	Adenosine Triphosphate
BG	Bioactive Glass
BTE	Bone Tissue Engineering
CBN	Carbon-Based Nanomaterials
CNT	Carbon Nanotubes
Di	Diopside
DIW	Direct Ink Writing
DLP	Digital Light Processing
DMSO	Dimethyl Sulfoxide
DMTA	Dynamic Mechanical Thermal Analysis
DPBS	Dubecco's Phosphate Buffered Saline
DSC	Differential Scanning Calorimetry
FBS	Fetal Bovine Serum
FDM	Fused Deposition Modelling
FTIR	Fourier-Transform Infrared
G	Graphene
GBN	Graphene-Based Nanomaterials
GNP	Graphene Nanoplatelets
GO	Graphene Oxide
GoxNP	Graphite Nanoplatelets
HA	Hydroxiapatite
HPP	Hot Plates Press
IMS	Industrial Methylated Spirit
IPA	Isopropyl Alcohol
LCD	Liquid Crystal Display
MEM	Minimum Essential Medium
MFK	Model Free Kinetic
MMA	Methy Methacrylate
MWCNT	Multi-Walled Carbon Nanotubes
ND	Nanodiamond
NMR	Nuclear Magnetic Resonance

PBS	Phosphate Buffered Saline
PCL	Polycaprolactone
PDMS	Dimethylpolysiloxane
PEEK	Polyether Ether Ketone
PGA	Polyglicolic Acid
PHBV	Poly-(3-Hydroxybutyrate-co-3-Hydroxybutyrate)
PI	Propidium Iodide
PLA	Polylactic Acid
PLGA	Poly(Lactic-co-Glycolic Acid)
PMAA	Poly(Methacrylic Acid)
PMMA	Poly(Methyl Methacrylate)
PU	Polyurethane
PVA	Poly(Vinyl Alcohol)
PVDF	Polyvinylidene Difluoride
R	Acrylic resin
rGO	Reduced Graphene Oxide
ROS	Reactive Oxygen Species
SEM	Scanning Electron Microscopy
SLA	Stereolithography
SLM	Selective Laser Melting
SLS	Selective Laser Sintering
SWCNT	Single-Walled Carbon Nanotubes
TCP	Tricalcium Phosphate
TPU	Thermoplastic Polyurethane
UV	Ultraviolet

Abstract

Nowadays, orthopaedic surgery is one of the areas of greatest interest in medicine, and within it, there are more and more surgical interventions carried out to solve problems related to the repair of large bone defects or damaged cellular tissue. They appear either as a result of disease, some type of trauma or the natural aging process. It is expected that in the near future this type of intervention will be more and more frequent, necessary and serious, due not only to the aging of the population, but also to the appearance of these ailments at younger ages. The decrease of the age when these problems appear is a consequence of a change in lifestyle and an increase in obesity in the population.

Although bone tissue has the ability to self-regenerate, in the case of severe fractures with critical sizes (≥ 7 mm) or in the case of irregular fractures, this natural regeneration process is inhibited, which is a great challenge for orthopedic surgeons. In these cases, when the natural process of healing and bone regeneration is inhibited, the use of support materials, also called scaffolds, has proven to be very effective. These scaffolds act as an extracellular matrix, which provides structural and mechanical support to bone cells for their attachment, viability and growth, thus favouring their regeneration. The main advantage of tissue engineering is the potential elimination of donor scarcity, pathogen transfer, and graft rejection.

To highlight the social impact, it is worth mentioning that in the case of osteoporosis alone, it is known that this disease causes more than 8.9 million fractures per year. One out of three women and one out of five men over the age of 50 will suffer an osteoporotic fracture at some moment in their lives. By 2050, the global incidence of hip fractures is expected to increase by 310% in men and 240% in women, compared to 1990. Consequently, in recent years, an important effort in the development of new repair techniques and in the use of new materials that favour cell regeneration is being done.

Scaffolds have been conventionally manufactured by techniques like solvent casting, freeze-drying and salt leaching. However, these technologies allow to obtain porous structures, but their geometry, porosity and pore size are not controlled. This control can be achieved by Additive Manufacturing (AM) technologies.

Graphene and graphene-based nanomaterials (GBN) are nanomaterials that have generated enormous interest in the scientific community in recent years due to their unique properties (high electrical and thermal conductivity, high mechanical strength, high hardness, flexibility, large surface area, etc). In relation to the field that concerns us, it has been proven that GBN are biocompatible materials with low toxicity, having been discovered that they have very interesting properties from

the biological point of view and especially from the point of view of cell regeneration. It has antimicrobial properties and has been shown to promote cell adhesion and osteoblast growth. Several studies show that the incorporation of GBN in relatively low concentrations to different materials considerably favours the proliferation of bone cells on them. Furthermore, it has been shown that the addition of this material as a reinforcing agent is capable of greatly improving the mechanical properties of many materials.

Therefore, GBN are promising candidates to be used as reinforcement for bone repair and regeneration applications due to the exceptional combination of excellent mechanical, thermal and electrical properties along with their proven antimicrobial and cell regeneration capabilities.

However, to produce scaffolds reinforced with GBN by AM technologies, it is urgent to study the modification of available raw materials to adjust their properties to the needed for this purpose. Besides, in the case of photocurable polymers used in some AM technologies, nanofillers may modify their properties and could also affect other parameters, like printability, polymerization, mechanical and/or biological performance.

Therefore, the main objective of this doctoral thesis is to develop 3D bone scaffolds reinforced with GBN using Vat Photopolymerization techniques, i.e. stereolithography (SLA), that allow to obtain scaffolds with improved mechanical properties and high cell proliferation activity. The addition of GBN affected the resin performance from different points of view. Therefore, to reach the final objective, it is important to understand the effect of GBN on polymerization, mechanical performance, and cell response. To achieve the final objective, some partial objectives are proposed:

1. To define a procedure to prepare photocurable resins reinforced with GBN that allows to obtain structures by vat polymerization technologies.
2. To study GBN effect on the thermal and UV polymerization process of acrylic photopolymer.
3. To optimize the printing and post-printing processes of the GBN-reinforced resins to reach good mechanical properties.
4. To study the efficacy of reinforced photocurable resins in terms of cytotoxicity and cell proliferation.

In this doctoral thesis, a commercial acrylic resin (R) and three different GBN were used, which differ in size, degree of exfoliation and surface functionalization. Firstly, the GBN dispersion was optimized by adding monomer i.e., methyl methacrylate (MMA), to the resin. MMA is a liquid that reduces viscosity, favouring homogeneous dispersion. It was found that MMA does not produce significant changes in the mechanical properties of the resin and catalyzes the polymerization. Therefore, the use of MMA is a very effective technique for obtaining a good dispersion of GBN in acrylic-based resins.

It was found that the effect of GBN on resin properties highly depended on the functionalization and the size of the nanofiller:

- Graphene (G) inhibits UV polymerization due to its high absorbance, which results in a poor printing process, which was improved by increasing the exposure time. Furthermore, this inhibition of polymerization leads to a lack of improvement in mechanical properties when polymerization occurs by UV. However, when the samples were polymerized by heat, this improvement was found. Despite its high absorbency, interlayer adhesion appears to be adequate, but internal stresses occur that can be relieved by annealing after printing.
- Graphene oxide (GO) catalyzes polymerization thanks to the presence of oxygenated groups on its surface. However, it was observed that it gives rise to a less cross-linked polymeric structure than the resin. Despite this, it was observed that GO improves the properties when the samples were post-cured. Therefore, with the adequate post-treatment, the GO shows a reinforcing effect from the mechanical point of view.
- Graphite nanoplatelets (GoxNP) inhibit thermal polymerization but were not found to affect polymerization during printing. However, the mechanical properties of the printed specimens did not achieve the expected improvements. Analyzing the layers by microscopy, it was found that the presence of GoxNP affects the adhesion between layers due to its large size and low degree of exfoliation.

From the biological point of view, the cellular response of MC3T3 preosteoblasts was studied. It was observed that all the nanocomposites made with R and GBN show low cell viability, which can be improved by washing the samples with cell culture medium. Washing improved cell viability because residual photoinitiator and monomer were removed, which were released into the medium, producing a slight decrease in cell viability. However, washing procedure should be optimized in future works to assure the biocompatibility of the nanocomposites.

Based on the results found in this study, future work would involve optimizing the percentage of GBN added to achieve a more pronounced effect on both the mechanical and biological properties. Besides, the study could be extended to the electrical properties of the scaffolds, which are very interesting in biomedical applications. On the other hand, the functionalization of the GBN could also improve the interaction between the resin and the nanofillers, resulting in better final performance of the composite material.

Besides, ideally, the scaffolds should be biodegradable to be reabsorbed once the bone regeneration process is complete. This biodegradation and control over the rate of disappearance of the scaffold can be achieved using a resin synthesized in the laboratory, in which the molecular weight and polymeric structure could be controlled in order to have this control over the rate of degradation. The study carried out in this doctoral thesis opens the door to being able to modify resins synthesized in the laboratory with GBN, understanding the effect that these nanomaterials can have on the process of polymerization, printing and the appearance of internal stresses.

Taking into account all the aspects exposed above, it can be concluded that this thesis has established solid foundations for manufacturing bone scaffolds with GBN by Vat photopolymerization additive manufacturing technologies, i.e. stereolithography (SLA), Digital Light Processing (DLP), Liquid Crystal Display (LCD), taking advantage of the good precision and easy sterilization offered by these technologies.

Resumen

En la actualidad, la cirugía ortopédica es una de las áreas de mayor interés en medicina, y dentro de la misma, cada vez son más las intervenciones quirúrgicas llevadas a cabo para solucionar problemas relacionados con la reparación de grandes defectos óseos o tejido celular dañado, ya sea como consecuencia de una enfermedad, de algún tipo de traumatismo o del proceso de envejecimiento natural. Se prevé que en un futuro próximo este tipo de intervenciones sean cada vez más frecuentes, más necesarias y de mayor gravedad, debido no solo al envejecimiento de la población, sino también a la aparición de estas dolencias a edades más tempranas como consecuencia de un cambio en el estilo de vida y un aumento de la obesidad en la población.

Si bien el tejido óseo tiene la capacidad de auto-regenerarse, en el caso de fracturas graves con tamaños críticos (≥ 7 mm) o en el caso de fracturas irregulares, este proceso natural de regeneración se ve inhibido, lo que supone un gran reto para cirujanos ortopédicos. En estos casos, cuando el proceso natural de curación y regeneración ósea se ve inhibido, la utilización de materiales de soporte, también llamados andamios o "scaffolds", ha demostrado ser muy eficaz. Estos andamios actúan como matriz extracelular, que aporta soporte estructural y mecánico a las células óseas para su adhesión, viabilidad y crecimiento, favoreciendo así su regeneración. La principal ventaja de la ingeniería de tejidos es la potencial eliminación de la escasez de hueso donante, transferencia de patógenos y el rechazo de injertos.

Para comprender el impacto social, cabe comentar que tan solo en el caso de la osteoporosis, se sabe que esta enfermedad causa más de 8.9 millones de fracturas al año. Una de cada tres mujeres y uno de cada cinco hombres mayores de 50 años sufrirán una fractura osteoporótica alguna vez en su vida. Se espera que para 2050, la incidencia mundial de fracturas de cadera aumente en un 310% en los hombres y en un 240% en las mujeres, en comparación con las producidas en 1990. En consecuencia, en los últimos años se está llevando a cabo un esfuerzo importante en el desarrollo de nuevas técnicas de reparación y en el uso de nuevos materiales que favorezcan la regeneración celular.

Convencionalmente, los andamios se han fabricado con técnicas como colada con disolvente, liofilización y lixiviación de sales. Sin embargo, estas tecnologías permiten fabricar estructuras porosas, pero la geometría, porosidad y tamaño de poro no son controlables. Este control se puede lograr con la fabricación aditiva (FA).

El grafeno y los nanomateriales base grafeno (NBG) son nanomateriales que han generado un enorme interés entre la comunidad científica durante los últimos años debido a sus propiedades únicas (elevada conductividad eléctrica y térmica, gran resistencia mecánica, alta dureza, flexibilidad, gran área superficial, etc.). En relación con el campo que nos concierne, se ha comprobado que los NBG son materiales biocompatibles y con una baja toxicidad, habiéndose descubierto que presenta propiedades muy interesantes desde el punto de vista biológico y sobre todo desde el punto de vista de la regeneración celular: posee propiedades antimicrobianas y ha demostrado promover la adhesión celular y crecimiento de osteoblastos. Varios estudios demuestran que la incorporación de NBG en concentraciones relativamente bajas a diferentes materiales, favorece considerablemente la proliferación de células óseas sobre los mismos. Además, se ha demostrado que la adición de este material como agente de refuerzo es capaz de mejorar enormemente las propiedades mecánicas de muchos materiales.

Por tanto, los NBG son candidatos prometedores para ser empleados como refuerzo en aplicaciones de reparación ósea debido a su excepcional combinación de propiedades mecánicas, térmicas y eléctricas, así como su probado efecto antimicrobiano y de regeneración celular.

Sin embargo, para producir andamios reforzados con NBG por tecnologías de FA, es necesario estudiar la modificación de materias primas para ajustar sus propiedades a las necesidades de esta aplicación. Además, en el caso de polímeros fotocurables empleados en algunas tecnologías, las nanocargas pueden modificar sus propiedades y afectar a otros parámetros, como imprimibilidad, polimerización y propiedades mecánicas y/o biológicas.

Con todo ello, el objetivo principal de esta tesis doctoral es desarrollar andamios óseos tridimensionales reforzados con NBG usando tecnologías de fotopolimerización, i.e. estereolitografía (SLA), que permiten obtener andamios con propiedades mecánicas mejoradas y una elevada capacidad de proliferación celular. Los primeros resultados demostraron que la adición de NBG afecta a las propiedades de la resina desde diferentes puntos de vista. Por ello, para alcanzar el objetivo final, es importante entender el efecto de los NBG en la polimerización, propiedades mecánicas y respuesta celular. Por tanto, los objetivos parciales de la tesis son:

- Definir un procedimiento para preparar resinas fotocurables reforzadas con NBG que permitan obtener estructuras por tecnologías de FA basadas en fotopolimerización.
- Estudiar el efecto de los NBG en la polimerización térmica y UV de la resina.

- Optimizar el proceso de impresión y post-impresión de las resinas reforzadas con NBG para obtener unas propiedades mecánicas adecuadas.
- Estudiar la eficiencia de la resina reforzada en términos de citotoxicidad y proliferación celular.

En esta tesis doctoral, se usó una resina acrílica comercial (R) y tres NBG diferentes, los cuales difieren en el tamaño, el grado de exfoliación y la funcionalización de su superficie. En primer lugar, se optimizó la dispersión de los NBG añadiendo monómero i.e., metil metacrilato (MMA), a la resina. El MMA es un líquido que reduce la viscosidad, favoreciendo la dispersión homogénea. Se comprobó que el MMA no produce cambios significativos en las propiedades mecánicas de la resina y cataliza la polimerización. Por tanto, el uso de MMA es una técnica muy eficaz para obtener una buena dispersión de los NBG en resinas base acrílica.

En el caso de los NBG, se observó que su efecto depende de la funcionalización y del tamaño de la nanocarga:

- El grafeno (G) inhibe la polimerización UV por su alta absorbancia, lo que resulta en un deficiente proceso de impresión, el cual se logró mejorar aumentando el tiempo de exposición. Además, esta inhibición de la polimerización conlleva una falta de mejora en las propiedades mecánicas cuando la polimerización ocurre por UV. Sin embargo, esta mejora sí se encontró en las muestras polimerizadas térmicamente. A pesar de su alta absorbancia, la adhesión entre capas parece ser adecuada, pero se producen tensiones internas que se pueden liberar con un proceso de recocido tras la impresión.
- El óxido de grafeno (GO) cataliza la polimerización gracias a la presencia de grupos oxigenados en su superficie. Sin embargo, se observó que da lugar a una estructura polimérica menos entrecruzada que la resina. A pesar de ello, se observó que el GO mejora las propiedades de las muestras impresas postcuradas. Por tanto, con el adecuado post-tratamiento, el GO muestra un efecto de refuerzo desde el punto de vista mecánico.
- Las nanoplaquetas de grafito (GoxNP) inhiben la polimerización térmica, pero no se encontró que afectaran a la polimerización durante la impresión. Sin embargo, las propiedades mecánicas de las probetas impresas no lograban las mejoras esperadas. Analizando las capas por microscopía, se encontró que la presencia de GoxNP afecta a la adhesión entre capas por su gran tamaño y bajo grado de exfoliación.

Desde el punto de vista biológico, se estudió la respuesta celular de preosteoblastos MC3T3. Se observó que todos los materiales compuestos fabricados con R y NBG muestran una baja viabilidad celular, lo que puede ser mejorado lavando las muestras con medio de cultivo celular. El lavado mejoró la viabilidad celular porque se logró eliminar el fotoiniciador y el monómero residuales, los cuales se liberaban al medio produciendo una ligera disminución en la viabilidad celular. Sin embargo, el lavado debe ser optimizado en trabajos futuros para asegurar la biocompatibilidad de todos los materiales estudiados.

A partir de las bases establecidas por este estudio, el trabajo futuro pasaría por optimizar el porcentaje de NBG añadido para lograr obtener un efecto más acusado en las propiedades tanto mecánicas como biológicas, pudiendo ampliar el estudio a las propiedades eléctricas de los andamios, muy interesantes en aplicaciones biomédicas. Por otra parte, la funcionalización de los NBG también podría mejorar la interacción entre la resina y las nanocargas, resultando en unas mejores propiedades finales del material compuesto.

Por otra parte, de forma ideal, los andamios deben ser biodegradables para ser reabsorbidos una vez el proceso de regeneración del hueso ha finalizado. Esta biodegradación y el control en la velocidad de desaparición del andamio se puede lograr empleando una resina sintetizada en el laboratorio, en la cual se podría controlar el peso molecular y la estructura polimérica para poder tener este control en la velocidad de degradación. El estudio llevado a cabo en esta tesis doctoral abre las puertas de poder modificar resinas sintetizadas en el laboratorio con NBG, comprendiendo el efecto que estos nanomateriales pueden tener en el proceso de polimerización, de impresión y de aparición de tensiones internas.

Teniendo en cuenta todo lo anteriormente expuesto, se puede concluir que esta tesis ha establecido unos cimientos sólidos para fabricar andamios óseos con NBG por tecnologías de fabricación aditiva basadas en fotopolimerización, i.e. estereolitografía (SLA), procesamiento de luz digital (DLP), pantalla de cristal líquido (LCD), aprovechando la buena precisión y la fácil esterilización que ofrecen dichas tecnologías.

TABLE OF CONTENT

CHAPTER 1

INTRODUCTION AND OBJECTIVES

Table of Contents

1.1. Introduction and Motivation

1.1.1. Scaffolds for bone tissue engineering

Bone is composed of a mineralised organic matrix and cells. The matrix provides the bone with its mechanical properties and is comprised of organic and inorganic phases. In the organic phase, type I collagen is the major component and it is responsible for the tensile properties of the bone. Conversely, the inorganic phase comprises hydroxyapatite, which is responsible for exhibiting the compressive mechanical properties and for providing the building blocks for new bone formation. Cells are embedded in the matrix, which includes osteoblasts, osteoclasts, osteoprogenitor cells and mature osteocytes [1].

Bone fractures and segmental bone defects are often caused by traumatic injury, cancer or other diseases (e.g., osteoporosis or arthritis) [2]. When a defect appears, the spontaneous fracture healing process begins through two different mechanisms, depending on the mechanical environment. If the strain across the fracture site is less than 2%, primary or direct healing by internal remodeling occurs, whilst secondary or indirect healing by callus formation takes place when strain is between 2 and 10% [3]. The latter type of healing is the process that most fractures follow and it depends on osteogenesis, osteoinductivity and osteoconductivity [4].

However, sometimes bones defect cannot heal spontaneously. This situation occurs especially in large segmental bone defects when the defect reaches a critical size [5]. The precise critical size depends on several factors (i.e., anatomic location, age of the patient, soft tissue environment); in the literature, it is suggested to include defect lengths greater than 1–2 cm and greater than 50% loss of the circumference of the bone [6]. In these cases, additional surgical interventions that help and allow bone healing are required. The available healing processes depending on the size defect are summarized in Figure 1.1.

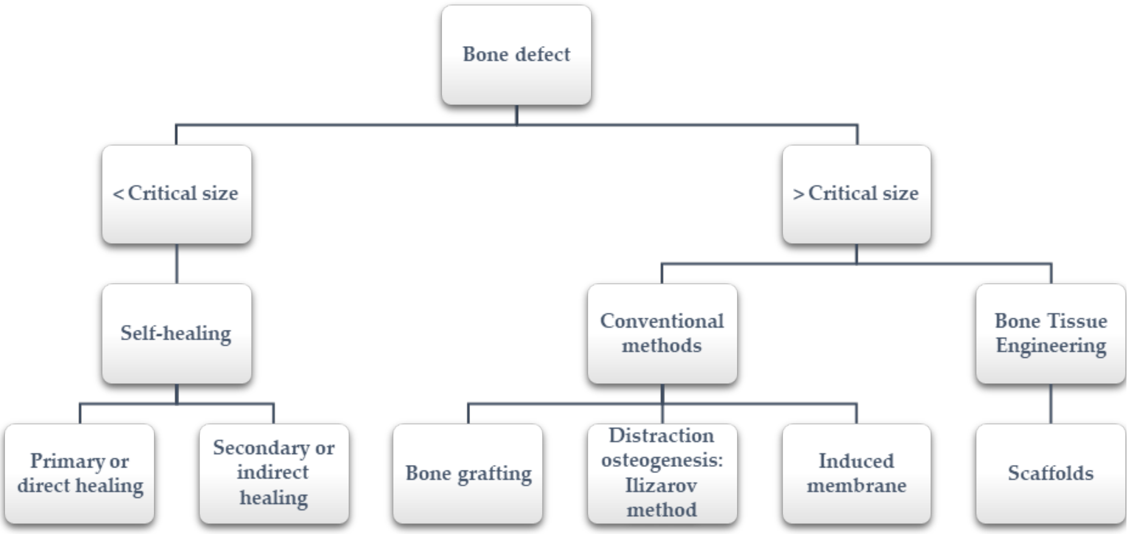

Figure 1.1. *Bone defect healing: from self-healing to bone tissue engineering.*

Among the conventional surgical solutions, it is important to highlight bone grafting, distraction osteogenesis and induced membrane techniques [5]. Autologous [7], allograft [8] and synthetic bone grafting [9] are extensively used for repairing bone defects. More specifically, autograft represents the gold standard for the treatment of critical-sized bone defects since it contains all the characteristics for new bone growth (osteoconductivity, osteogenicity and osteoinductivity). However, significant problems are associated with its use, from donor-site morbidity to a limited amount of donor bone [10–12]. Other associated issues, such as failed anastomosis, microvascular thrombosis and infection or progressive deformities, have also been reported [13,14].

Another technique extensively studied since the 1950s is distraction osteogenesis. Ilizarov successfully treated his first patient in 1954, reducing the healing time of tibial non-union [15]. This method is based on the capacity of regeneration under tension that the bone presents naturally. Despite the good results that the Ilizarov technique present [16,17], it also has some disadvantages, such as prolonged treatment times, pin site infection [18,19], pin breakage and the inconvenience and burden of prolonged external fixation, which includes muscle contractures, joint luxation and axial deviation [20–23].

Finally, the induced membrane technique is a two-stage procedure that combines the use of a temporary poly(methyl methacrylate) (PMMA) cement spacer, followed by bone grafting [24]. In 2000, the first cases using the induced membrane technique were reported [25]. Generally, this technique achieves its purpose; however, some complications have been found. The most common complications include infection, amputation, malunion, fracture and reoperation, and additional bone grafting due to non-union [25–27].

To avoid problems encountered when using conventional methods, the field of bone tissue engineering was developed in the early 1980s [28]. Researchers working in bone tissue engineering have made a significant effort to create 3D porous matrices, known as scaffolds. They are based on guided bone regeneration, the aim of which is bone regeneration and growth along the surface of the scaffold [29].

Scaffolds act as a temporary matrix for the attachment, viability and growth of cells whilst maintaining the structure of the regenerated bone in vivo [30]. The main advantage of bone tissue engineering is the potential elimination of donor scarcity, pathogen transfer and immune rejection [31].

1.1.2. Potential of Additive Manufacturing and Carbon-based nanomaterials in bone tissue engineering

Scaffolds have been conventionally manufactured by techniques like solvent casting, freeze-drying and salt leaching. However, these technologies allow to obtain porous structures, but their geometry, porosity and pore size are not controlled. This control can be achieved by Additive Manufacturing (AM) technologies. AM allows to imitate natural tissue or organs, which could influence in the arrangement among cells, which is crucial for regenerative medicine. One of the main advantages of AM techniques is the possibility to produce customised scaffolds with a reproducible internal morphology and pore architecture control, tailored mechanical and mass transport properties and even produce scaffolds with functionally graded materials [32,33].

Carbon-based nanomaterials are promising candidates to be used as reinforcement for bone repair and regeneration applications due to the exceptional combination of excellent mechanical, thermal and electrical properties along with their proven antimicrobial and cell regeneration capabilities. In general, carbon-based nanomaterials demonstrate antimicrobial activity. The cellular membrane integrity, metabolic processes, and morphology of the microorganisms are affected by direct contact with carbon nanostructures [34].

Besides, nanocomposites with carbon nanomaterials favour cell adhesion and proliferation on their surface and encourage bone growth [35,36]. It is suggested that this bone regeneration capability is due to different effects—e.g., the increase in surface roughness or the improvement of the hydrophilicity because of the presence of carbon-based nanomaterials. It was also reported that carbon-based nanomaterials present an increase in the protein absorption capability due to their large surface area and ability to interact with proteins through van der Wall's interaction, ionic bonding, hydrophobic, and π- π interactions [37]. Furthermore, carbon-based nanomaterials are physically similar to extracellular matrix (ECM) constituents due to their similar dimensions [38], which is vital for scaffolds because cells in native are embedded within a microenvironment where soluble molecules (cytokines and growth factors) and non-soluble components (ECM) can be found. This microenvironment controls cell survival, cell cycle progression, and the expression of different phenotyples while providing structural integrity [39].

The effect of carbon-based nanomaterials when added to a scaffold are summarized in Figure 1.2.

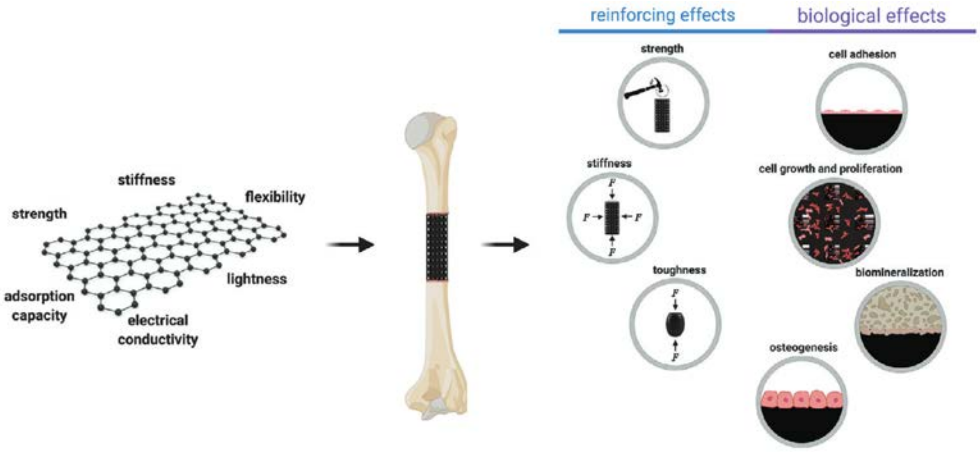

Figure 1.2. *Effects of carbon-based nanomaterials in biomedical engineering field [40]*

However, to fabricate scaffolds reinforced with graphene-based nanomaterials by AM technologies, it is important to study the modification of available raw materials to adjust their properties as and when needed for this purpose. Besides, in the case of photocurable polymers used in some AM technologies, the nanofillers used to modify their properties could also affect other parameters, like printability, polymerization, mechanical and/or biological performance.

1.1.3. Motivation of the thesis

In accordance with the aforementioned aspects, the motivation of this thesis and its contribution is focused on the following concepts:

- In this thesis, the effect of the addition of GBN on the printing process (i.e., stereolithography, SLA) and the final performance of printed samples is studied, with the aim of optimizing the manufacturing of bone scaffolds with improved properties.
- As discussed in Chapter 2, although in the recent years, the use of AM and the addition of GBN have been explored, there are only few studies focused on the use of SLA, and some of them show a detriment on the properties when GBN are introduced in the resin. In this thesis, SLA is used because it presents many advantages in comparison with other AM technologies, i.e. high accuracy, liquid raw material that facilitates the introduction of nanomaterials, high control of porosity and geometry.
- In this thesis, a commercial resin is studied because it is the most widely used with this technology and, very recently, some biocompatible formulations are already available. However, in future research, a resin with controllable biodegradability and adequate properties is required in order to be used as scaffolds. In this sense, this thesis is intended as a proof-of-concept study to elucidate how GBN affect printability and the properties of photocurable resins to provide the basis for further progress in this direction.
- With this study, it is expected to deeply understand how to use GBN in SLA to make the manufacturing of scaffolds by this technology feasible. It will open up new possibilities and research lines focused on aspects like the optimization of the GBN load, the study of the geometry, its effect on mechanical, electrical and biological performance, the compromise between mechanical and biological properties, etc.

1.2. Objectives

The main objective of this doctoral thesis is to develop 3D bone scaffolds reinforced with Graphene-Based Nanomaterials (GBN) using Vat Photopolymerization technology, that will allow to fabricate scaffolds demonstrating adequate mechanical properties and high cell proliferation activity. To achieve it, some objectives are proposed:

1. To define a procedure to prepare photocurable resins reinforced with GBN for the fabrication of scaffolds using Vat Polymerization technologies.
2. To study GBN effect on the thermal and UV polymerization process of acrylic photopolymer.
3. To optimize the printing and post-printing processes of the GBN-reinforced resins to reach good mechanical properties.
4. To study the efficacy of reinforced photocurable resins in terms of cytotoxicity and cell proliferation.

1.3. References

[1] M.S. Jones, B. Waterson, Principles of management of long bone fractures and fracture healing, Surg. 38 (2020) 91–99. https://doi.org/10.1016/j.mpsur.2019.12.010.

[2] E. Jimi, S. Hirata, K. Osawa, M. Terashita, C. Kitamura, H. Fukushima, The current and future therapies of bone regeneration to repair bone defects, Int. J. Dent. 2012 (2012) 148261. https://doi.org/10.1155/2012/148261.

[3] C.E. Baker, S.N. Moore-Lotridge, A.A. Hysong, S.L. Posey, J.P. Robinette, D.M. Blum, M.A. Benvenuti, H.A. Cole, S. Egawa, A. Okawa, M. Saito, J.R. McCarthy, J.S. Nyman, M. Yuasa, J.G. Schoenecker, Bone Fracture Acute Phase Response—A Unifying Theory of Fracture Repair: Clinical and Scientific Implications, Clin. Rev. Bone Miner. Metab. 16 (2018) 142–158. https://doi.org/10.1007/s12018-018-9256-x.

[4] R. Dimitriou, E. Tsiridis, P. V. Giannoudis, Current concepts of molecular aspects of bone healing, Injury. 36 (2005) 1392–1404. https://doi.org/10.1016/j.injury.2005.07.019.

[5] E. Roddy, M.R. DeBaun, A. Daoud-Gray, Y.P. Yang, M.J. Gardner, Treatment of critical-sized bone defects: clinical and tissue engineering perspectives, Eur. J. Orthop. Surg. Traumatol. 28 (2018) 351–362. https://doi.org/10.1007/s00590-017-2063-0.

[6] A. Nauth, E. Schemitsch, B. Norris, Z. Nollin, J.T. Watson, Critical-Size Bone Defects: Is There a Consensus for Diagnosis and Treatment?, J. Orthop. Trauma. 32 (2018) S7–S11. https://doi.org/10.1097/BOT.0000000000001115.

[7] J.M. Sohn, Y. In, S.H. Jeon, J.Y. Nho, M.S. Kim, Autologous Impaction Bone Grafting for Bone Defects of the Medial Tibia Plateau During Primary Total Knee Arthroplasty: Propensity Score Matched Analysis With a Minimum of 7-Year Follow-Up, J. Arthroplasty. 33 (2018) 2465–2470. https://doi.org/10.1016/j.arth.2018.02.082.

[8] N. Shibuya, D.C. Jupiter, Bone Graft Substitute: Allograft and Xenograft, Clin. Podiatr. Med. Surg. 32 (2015) 21–34. https://doi.org/10.1016/j.cpm.2014.09.011.

[9] V. Kumar, M. Ricks, S. Aboul-Enin, D.G. Dunlop, Long term results of impaction Bone grafting using a synthetic graft (Apapore) in revision hip surgery, J. Orthop. 14 (2017) 290–293. https://doi.org/10.1016/j.jor.2017.03.013.

[10] R. Dimitriou, G.I. Mataliotakis, A.G. Angoules, N.K. Kanakaris, P. V. Giannoudis, Complications following autologous bone graft harvesting from the iliac crest and using the RIA: A systematic review, Injury. 42 (2011) S3–S15. https://doi.org/10.1016/j.injury.2011.06.015.

[11] C.J. Damien, J.R. Parsons, Bone graft and bone graft substitutes: a review of current technology and applications., J. Appl. Biomater. 2 (1991) 187–208. https://doi.org/10.1002/jab.770020307.

[12] T.P. Vail, J.R. Urbaniak, Donor-site morbidity with use of vascularized autogenous fibular grafts, J. Bone Jt. Surg. 78 (1996) 204–211. https://doi.org/10.2106/00004623-199602000-00006.

[13] K. Arai, S. Toh, K. Tsubo, S. Nishikawa, S. Narita, H. Miura, Complications of vascularized fibula graft for reconstruction of long bones, Plast. Reconstr. Surg. 109 (2002) 2301–2306. https://doi.org/10.1097/00006534-200206000-00021.

[14] K. Muramatsu, K. Ihara, M. Shigetomi, S. Kawai, Femoral reconstruction by single, folded or double free vascularised fibular grafts, Br. J. Plast. Surg. 57 (2004) 550–555.

https://doi.org/10.1016/j.bjps.2003.08.021.

[15] B. Spiegelberg, T. Parratt, S.K. Dheerendra, W.S. Khan, R. Jennings, D.R. Marsh, Ilizarov principles of deformity correction, Ann. R. Coll. Surg. Engl. 92 (2010) 101–105. https://doi.org/10.1308/003588410X12518836439326.

[16] D.H. Toon, S.A. Khan, K.H.Y. Wong, Lengthening of a below knee amputation stump with Ilizarov technique in a patient with a mangled leg, Chinese J. Traumatol. - English Ed. 22 (2019) 364–367. https://doi.org/10.1016/j.cjtee.2019.07.001.

[17] G. Cai, W. Liu, J. Xiong, L. Liu, D. Wang, J. Yang, Functional Reconstruction of Hindfoot With Total Calcaneus and Talus Loss by Ilizarov Technique: A Case Report, J. Foot Ankle Surg. 59 (2020) 142–148. https://doi.org/10.1053/j.jfas.2019.03.022.

[18] M.D. Stuart A. Green, Skeletal Defects. A Comparison of Bone Grafting and Bone Transport for Segmental Skeletal Defects, Clin. Orthop. Relat. Res. 301 (1994) 111–117.

[19] A.L.L. Blum, J.C. Bongiovanni, S.J. Morgan, M.A. Flierl, F.B. Dos Reis, Complications associated with distraction osteogenesis for infected nonunion of the femoral shaft in the presence of a bone defect: A retrospective series, J. Bone Joint Surg. Br. 92 (2010) 565–570. https://doi.org/10.1302/0301-620X.92B4.23475.

[20] D. Paley, Problems, obstacles, and complications of limb lengthening by Illizarov, Clin. Orthop. Relat. Res. 250 (1990) 81–104.

[21] Y. Palatnik, S.R. Rozbruch, Femoral Reconstruction Using External Fixation, Adv. Orthop. 2011 (2011) 967186. https://doi.org/10.4061/2011/967186.

[22] D. Paley, M. Catagni, F. Argnani, J. Prevot, D. Bell, P. Armstrong, Treatment of Congenital Pseudoarthrosis of the Tibia Using the Ilizarov Technique, Clin. Orthop. Relat. Res. 280 (1992) 81–93.

[23] J. Zhai, X. Weng, B. Zhang, H. Peng, Y. Bian, Management of knee flexion contracture in haemophilia with the Ilizarov technique, Knee. 26 (2019) 201–206. https://doi.org/10.1016/j.knee.2018.08.006.

[24] A.C. Masquelet, T. Begue, The Concept of Induced Membrane for Reconstruction of Long Bone Defects, Orthop. Clin. North Am. 41 (2010) 27–37. https://doi.org/10.1016/j.ocl.2009.07.011.

[25] A.C. Masquelet, F. Fitoussi, T. Begue, G.P. Muller, Reconstruction of the long bones by the induced membrane and spongy autograft, Ann. Chir. Plast. Esthet. 45 (2000) 346–353.

[26] A. Shekaran, J.R. García, A.Y. Clark, T.E. Kavanaugh, A.S. Lin, R.E. Guldberg, A.J. García, Bone regeneration using an alpha 2 beta 1 integrin-specific hydrogel as a BMP-2 delivery vehicle, Biomaterials. 35 (2014) 5453–5461. https://doi.org/10.1016/j.biomaterials.2014.03.055.

[27] C. Seebach, D. Henrich, C. Kähling, K. Wilhelm, A.E. Tami, M. Alini, I. Marzi, Endothelial progenitor cells and mesenchymal stem cells seeded onto β-TCP granules enhance early vascularization and bone healing in a critical-sized bone defect in rats, Tissue Eng. - Part A. 16 (2010) 1961–1970. https://doi.org/10.1089/ten.tea.2009.0715.

[28] A.R. Amini, C.T. Laurencin, S.P. Nukavarapu, Bone tissue engineering: Recent advances and challenges, Crit. Rev. Biomed. Eng. 40 (2012) 363–408. https://doi.org/10.1615/CritRevBiomedEng.v40.i5.10.

[29] M. Kellomäki, H. Niiranen, K. Puumanen, N. Ashammakhi, T. Waris, P. Törmälä, Bioabsorbable scaffolds for guided bone regeneration and generation, Biomaterials. 21 (2000) 2495–2505. https://doi.org/10.1016/S0142-9612(00)00117-4.

[30] M. Meskinfam, 17 - Polymer scaffolds for bone regeneration, in: Charact. Polym. Biomater., Elsevier Ltd., 2017: pp. 441–475. https://doi.org/10.1016/B978-0-08-100737-2.00017-0.

[31] M.S. Chapekar, Tissue engineering: Challenges and opportunities, J. Biomed. Mater. Res. 53 (2000) 617–620. https://doi.org/10.1002/1097-4636(2000)53:6<617::AID-JBM1>3.0.CO;2-C.

[32] Y. Zamani, G. Amoabediny, J. Mohammadi, H. Seddiqi, M.N. Helder, B. Zandieh-Doulabi, J. Klein-Nulend, J.H. Koolstra, 3D-printed poly(Ɛ-caprolactone) scaffold with gradient mechanical properties according to force distribution in the mandible for mandibular bone tissue engineering, J. Mech. Behav. Biomed. Mater. 104 (2020) 103638. https://doi.org/10.1016/j.jmbbm.2020.103638.

[33] D. Ronca, F. Langella, M. Chierchia, U. D'Amora, T. Russo, M. Domingos, A. Gloria, P. Bartolo, L. Ambrosio, Bone Tissue Engineering: 3D PCL-based Nanocomposite Scaffolds with Tailored Properties, Procedia CIRP. 49 (2016) 51–54. https://doi.org/10.1016/j.procir.2015.07.028.

[34] S.M. Dizaj, A. Mennati, S. Jafari, K. Khezri, K. Adibkia, Antimicrobial activity of carbon-based nanoparticles, Adv. Pharm. Bull. 5 (2015) 19–23. https://doi.org/10.5681/apb.2015.003.

[35] L.P. Zanello, B. Zhao, H. Hu, R.C. Haddon, Bone cell proliferation on carbon nanotubes, Nano Lett. 6 (2006) 562–567. https://doi.org/10.1021/nl051861e.

[36] S. Kumar, S. Raj, K. Sarkar, K. Chatterjee, Engineering a multi-biofunctional composite using poly(ethylenimine) decorated graphene oxide for bone tissue regeneration, Nanoscale. 8 (2016) 6820–6836. https://doi.org/10.1039/c5nr06906h.

[37] P.R. Sivashankari, M. Prabaharan, Bioactive nanomaterials/chitosan composites as scaffolds for tissue regeneration, Elsevier Ltd., 2019. https://doi.org/10.1016/B978-0-08-102553-6.00019-2.

[38] M. Rahmati, M. Mozafari, Biological response to carbon-family nanomaterials: Interactions at the nano-bio interface, Front. Bioeng. Biotechnol. 23 (2019) 1–22. https://doi.org/10.3389/fbioe.2019.00004.

[39] H. Shin, Fabrication methods of an engineered microenvironment for analysis of cell-biomaterial interactions, Biomaterials. 28 (2007) 126–133. https://doi.org/10.1016/j.biomaterials.2006.08.007.

[40] L. Daneshmandi, M. Barajaa, A.T. Rad, S.A. Sydlik, C.T. Laurencin, Graphene-Based Biomaterials for Bone Regenerative Engineering : A Comprehensive Review of the Field and Considerations Regarding Biocompatibility and Biodegradation, Adv. Healthc. Mater. 10 (2021) 2001414. https://doi.org/10.1002/adhm.202001414.

CHAPTER 2

STATE OF THE ART

Table of Contents

In this chapter, the main advances up to date in the field of Bone Tissue Engineering (BTE) are going to be summarized. The focus is on biodegradable polymer bone scaffolds reinforced with Carbon-Based Nanomaterials (CBN) and manufactured by 3D printing. The main topics to be covered are:

1. Justification for the use of nanomaterials as reinforcing agents in polymers used for Additive Manufacturing.
2. Use of nanomaterials, especially CBN, as reinforcing agents in BTE. Types, properties, advantages and limitations of these nanomaterials are discussed.
3. Available technologies of Additive Manufacturing to fabricate bone scaffolds are analyzed and compared. Besides, the potential manufacture of nanocomposites with each technology is discussed.
4. Study of the state of the art of fabricating polymer biodegradable bone scaffolds by Additive Manufacturing with the addition of carbon-based nanomaterials. The objective of this topic is to understand the gap to be covered by this thesis.

The content of this chapter was published as a review paper in [1].

2.1. *Scaffolds for Bone Regeneration*

Ideally, to properly promote bone regeneration, scaffolds should meet specific requirements [2–4]:

(1) The material and its degradative by-products should be biocompatible and not evoke inflammation or toxicity when implanted in vivo.

(2) Three-dimensional structures should be manufactured in a reproducible manner.

(3) High surface area is needed for cell–polymer interactions, extracellular matrix regeneration and minimal diffusion constraints, which is important for different processes, e.g., cell migration and nutrients and oxygen availability. It is achieved with a porosity of at least 90% and a pore size of at least 100 μm [2]. Furthermore, it should have an interconnected porous structure, with a pore size suitable to allow cell adhesion, growth, vascularisation of the tissue and transportation of nutrients.

(4) Scaffolds should be capable of being resorbed once their function of providing a template for regenerating bone has been completed. Permanent foreign materials inside the body leads to a permanent risk of inflammation until the foreign body is encapsulated by fibrotic connective tissue. Biodegradability would avoid this non-specific immune response [5].

(5) The degradation or the resorption rate and the rate of bone formation should be similar. For this reason, the degradation rate of the scaffold should have the potential to be adjustable depending on the cell type.

(6) Scaffolds should also demonstrate mechanical properties similar to bone.

It is important to highlight that porosity and mechanical properties have an inverse relation. For this reason, a compromise must be found between these characteristics.

The fabrication of bone tissue-engineered scaffolds is associated with the production of controlled porous and interconnected structures since porosity and interconnectivity are two of the requirements needed for achieving adequate bone repair and regeneration. The porosity is important for cell adhesion, growth, revascularisation and adequate nutrition. Kuboki et al. [6] found that solid particles did not promote the formation of new bone, while for porous particles of the same material, osteogenesis occurred. Regarding interconnectivity, Conrad et al. [7] found that interconnectivity increases permeability and, therefore, improves cell infiltration and bone ingrowth.

The size of pores is critical; if pores are not large enough, cell migration is limited, and they may remain at the edges of the scaffold, thereby forming a cellular capsule. The minimum pore size is approximately 100 µm, due to cell size, migration requirements and transport [8]. Conversely, if the pore size is too large, then the surface area decreases and consequently cell adhesion is limited. The results from the study by Murphy et al. [9] corroborate this fact (Figure 2.1). In extreme cases, for pores that were relatively large or small in size, cell proliferation was not promoted: cell number remained constant or even decreased. However, intermediate pore sizes promoted cell proliferation over time. Besides, the number of cells was not proportional to the pore size.

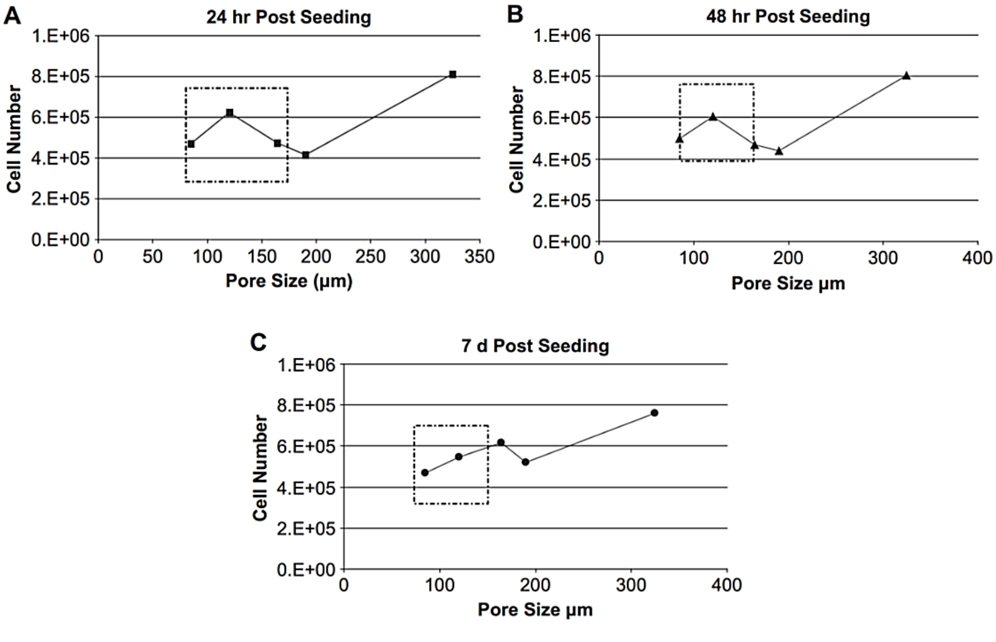

Figure 2.1. *Effect of mean pore size of collagen–glycosaminoglycan scaffolds on MC3T3-E1 cell attachment and proliferation at different time points. The relation between mean pore size and cell response is non-linear (Reprinted from [7], with permission from Elsevier).*

Furthermore, pores within a bone tissue-engineered scaffold must be interconnected since this interconnectivity, as well as the pore structure and overall porosity, is fundamental in determining the osteogenic capability of a bone tissue-engineered scaffold [10,11].

Both pore distribution and geometry of the scaffold are decisive for cell penetration, proliferation, and differentiation, as well as in the rate of scaffold degradation, which must be in accordance with the maturation and regeneration of new tissue.

To have the appropriate pore size distribution and interconnectivity, different approaches for fabricating porous scaffolds have been studied: salt-leaching [12–14], gas foaming [15,16], electrospinning [17–19] and freeze-drying [20,21]. However, with these fabrication methods, it is possible to produce bone tissue-engineered scaffolds without completely controlling pore size distribution and shape, porosity and interconnectivity.

In general, traditional methods present limitations related to the control of overall pore architecture and interconnectivity and bone tissue-engineered scaffolds produced by these techniques present poor reproducibility and accuracy [22,23].

Therefore, despite the great research advancements in the design, manufacture and application of bone tissue-engineered scaffolds for bone repair and replacement, there still are some drawbacks and challenges that need to be addressed. The main drawbacks of synthetic scaffolds are poor biodegradability, potential toxic degradation of by-products, poor osteoconductivity, poor mechanical properties, uncontrolled porosity or complicated reproducibility [24].

To reduce the previous weaknesses, two strategies have been explored:

- Nanomaterials have been proposed as reinforcing agents to improve mechanical and biological properties.

- Additive manufacturing (AM) has emerged as a technology that enables the fabrication of 3D porous scaffolds with a high level of reproducibility and accuracy with minimal human intervention.

2.2. Nanomaterials for Scaffolds

The use of nanocomposite biomaterials in bone tissue engineering has emerged to improve the mechanical properties as well as physicochemical properties of the polymeric matrix, such as mechanical strength and Young's modulus, hydrophilicity or biological response (e.g. cell adhesion, proliferation, and differentiation, biocompatibility and antimicrobial effect). Nanocomposites for biomedical applications normally have two phases: a biocompatible matrix and a nano-sized bioactive/resorbable filler [25–27]. One of the main advantages of nanomaterials is their large surface area, which results in a large volume fraction of interfacial material, even at low loadings.

In general, by controlling the volume fraction, arrangement, and morphology of the filler phase within the matrix, it is possible to tailor the physicochemical and mechanical properties and the response to the host tissue [28]. In this section, some of the most interesting data relating to the application of nanocomposites in bone tissue engineering will be reported, especially the application of carbon-based nanomaterials will be considered.

2.2.1 Ceramic nanomaterials

Ceramic nanomaterials, such as calcium phosphates or calcium silicates, may improve the biological response by releasing calcium and phosphate ions that are essential for bone growth. However, when the amount of inorganic particles is high, a detrimental effect on the mechanical properties has been reported [29].

The most commonly used ceramic-based nanomaterial is nano-hydroxyapatite (nHA). It demonstrates excellent biocompatibility and low toxicity. Several matrices have been filled with nHA (thermoplastic polyurethane/dimethylpolysiloxane (TPU/PDMS), polycaprolactone (PCL), polylactic acid (PLA)…) and, in all cases, it has been observed that comparing the nanocomposite with the pristine matrix, it shows a reduction in hydrophobicity, as well as an increase in cell proliferation, mineralisation, and differentiation [30–33].

Calcium phosphate nanoparticles have proved to improve mechanical resistance and the attachment and proliferation of osteoblasts and can demonstrate an antibacterial effect [34,35].

Other ceramics, like nano-sized aluminium oxide [36], titanium oxide [37] or silicon oxide [38] have been shown to augment different properties that make them very interesting as potential nanomaterials for bone tissue engineering applications.

2.2.2. Metallic nanomaterials

In general, metallic nanomaterials are interesting in bone tissue engineering due to the antimicrobial and bactericidal activity that some of them demonstrate.

Silver nanoparticles are well-known for their antimicrobial activity against a broad spectrum of infectious agents [39]. Specifically, silver ions present a marked antibacterial effect since it causes disruption of bacteria cell membranes, inhibits enzymatic activities and DNA replication [40]. In the same way, copper and bronze also present bactericidal nature [41].

Gold nanoparticles have also been used to create a polymer nanocomposite due to their inherent low toxicity, antiseptic and antibacterial activity, which prevent bacterial growth in the surgical wound [42,43].

Other metal ions, like strontium or copper, have been widely used to dope bioactive glasses, improving their osteogenesis, angiogenesis and antibacterial activity [44,45].

Another interesting metal extensively used in bone tissue engineering is magnesium. It presents adequate mechanical properties, specific strength, and elastic modulus, close to natural bone, biodegradability and biocompatibility. However, its high degradation rate limits its application as a matrix material, but the presence of magnesium as a nanomaterial induces osteogenic differentiation [46,47].

2.2.3. *Polymer nanomaterials*

Polymers are not used as nanomaterials in bone tissue engineering, but as a delivery system for other nanomaterials or to enable modification of the scaffold. For instance, poly(acrylic acid) (PAA) or poly(methacrylic acid) (PMAA) grafted to carbon nanotubes improve the potential for cell differentiation of scaffold [48,49].

In the case of polymers added to the scaffold, there are two different paths: co-polymers, formed by two or more monomeric species; and polymer-polymer blends, which involve a mixture of two polymers [28]. Among the copolymers used in bone tissue engineering, poly(lactic-co-glycolic acid) (PLGA) [50,51] and poly(lactide-co-caprolactone) [52,53] are the most commonly used. Conversely, in the field of polymer blends, many studies are found: gelatin-polyvinyl pyrrolidone [54], gelatin-poly(lactide acid) [55], cellulose acetate-polycaprolactone [56], polyurethane/poly(lactic acid) [57], poly(lactide acid)/polycaprolactone [58,59], etc. Sometimes, they are incorporated into a ceramic scaffold to improve their toughness and processability. Both synthetic [60,61] and natural [62] polymers are used for this purpose.

2.2.4. *Carbon-based nanomaterials*

Carbon-based nanomaterials have shown a high capability for bone tissue engineering since they present excellent mechanical properties and intrinsic antibacterial activity [63]. The majority of carbon-based nanomaterials have also been shown to promote cell regeneration and decrease the hydrophobicity of the composite material. The interaction of carbon-based nanomaterials with biological molecules depends on the chemical composition, shape, size, stability, functionalisation, porosity, agglomeration of the nanomaterial. Therefore, it is important to study each carbon-based nanomaterial individually [64]. All their biological advantages will be discussed in detail in the next section.

Due to their geometry, carbon-based nanomaterials present an interesting toughening effect that can follow four different mechanisms (Figure 2.2): (i) crack bridging - carbon-based nanomaterials delay crack propagation, bridging the two surfaces and providing stress that counteracts the applied stress, (ii) pull-out - carbon-based nanomaterials are pulled out the matrix, slowing down crack propagation by the interfacial friction, (iii) crack deflection - crack cannot continue its path for the presence of carbon-based nanomaterials and it follows a tortuous path with high energy dissipation, (iv) crack tip shielding - the crack has not enough energy for interface debonding and the crack tip is restricted [65].

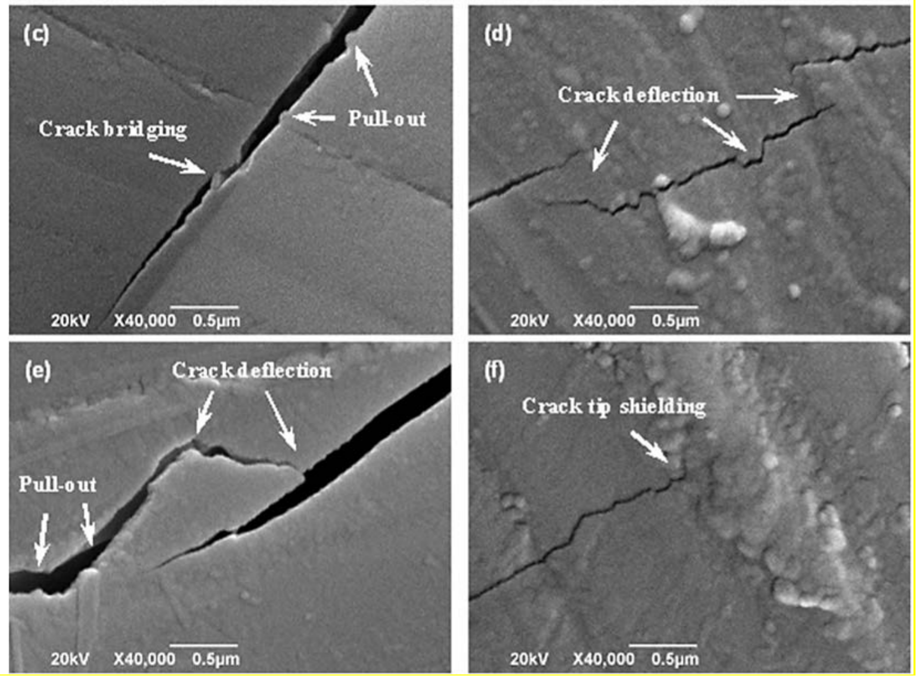

Figure 2.2. *Inhibition of crack propagation by graphene in bioactive glass scaffold by different mechanisms* [65].

Thanks to their biological and mechanical improvements, the addition of carbon-based nanomaterials has the potential to transform relatively inert materials into materials demonstrating appropriate mechanical properties and bioresponsiveness for bone tissue engineering scaffolds.

2.2.4.1. Types of carbon-based nanomaterials

In Figure 2.3, the structure of the different carbon-based nanomaterials is shown.

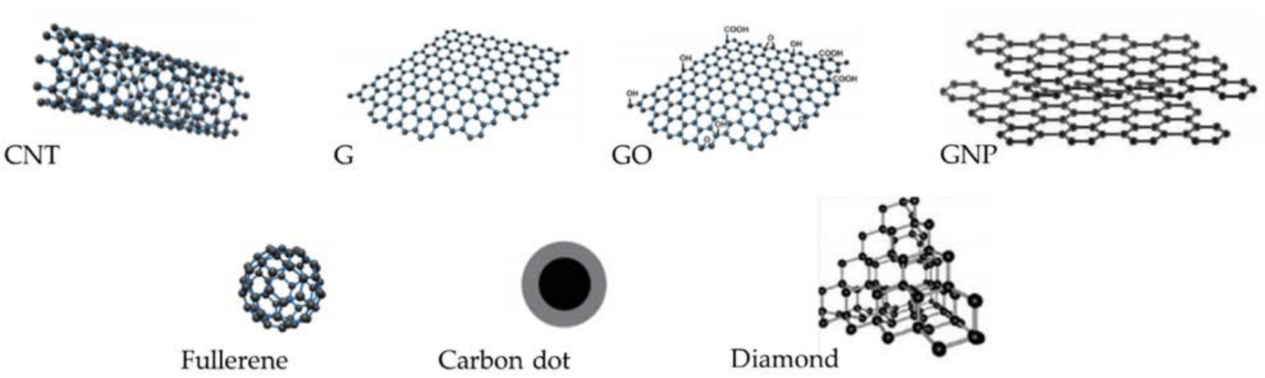

Figure 2.3. *Carbon-Based Nanomaterials (Modified from* [66]*).*

Carbon nanotubes

In 1991, carbon nanotubes (CNT) were first reported by Iijima [67], when he discovered multi-walled carbon nanotubes (MWCNT). Later, in 1993, he discovered single-walled carbon nanotubes (SWCNT) [68].

CNT present a tubular shape; their structure is like rolled-up graphene sheets. SWCNT diameter typically is in the range 1-2 nm, they are generally narrower than MWCNT, and they tend to be curved rather than straight [69]. In the case of MWCNT, the outer diameter depends on the number of layers and ranges from 2 to 30 nm. Typically, the length is in the micrometre range but can differ from 1 μm to a few centimetres, in the case of MWCNT [70].

CNT present unique structural, electrical, mechanical, electromechanical, and chemical properties, and as a consequence, their application in regenerative medicine has been widely investigated [71].

Several studies have demonstrated that MWCNT can promote stem cell differentiation towards bone cells and enhance bone formation. Furthermore, they act as a mode of reinforcement for mechanical strengthening and biocompatibility [48,72–75], improving the performance of different biomaterials. The case of SWCNT is very similar, and it has been proved that SWCNT can be incorporated into some biodegradable polymers that present problems due to their poor mechanical properties to successfully reinforce them [76], without adversely affecting the biocompatibility of the matrix [77].

Graphene derivatives

- *Graphene*

Since its discovery in 2004 [78], the application of graphene (G) has experienced a significant rise. Graphene is a two-dimensional carbon material, one atom thick. Its atomic structure is a honeycomb lattice of carbon atoms and is the basic building block for graphitic materials. It presents a very high surface area (32.216 $m^2 \cdot g^{-1}$), higher than SWCNT, excellent thermal conductivity (3,000-5,000 $W \cdot m^{-1} \cdot K^{-1}$), mechanical properties (130 GPa of intrinsic tensile strength with Young's modulus of 1 TPa) and electrical conductivity ($5.9 \cdot 10^5$ $S \cdot m^{-1}$) [79–82].

Since it presents high electrical conductivity, G is used to manufacture electro-active scaffolds. The addition of G stimulates cell proliferation and decreases the immune response [83]. Graphene has also been shown to improve the mechanical properties of biomaterials without compromising biocompatibility [84].

- *Graphene oxide*

Graphene oxide (GO) is produced by oxidising graphite in an acidic medium, increasing the hydrophilicity of the surface and creating functional groups (i.e. hydroxyl, epoxy, carboxyl, carbonyl, phenol, lactone, and quinone) [85]. It can modulate their characteristics with the degree of oxidation. Graphene oxide is an electrically insulating material because it has disrupted sp^2 bonding networks due to the presence of functional groups. Their mechanical properties are excellent, but they do not reach the values of G (28-47 GPa of intrinsic tensile strength, with Young's modulus of 380-470 GPa) [86,87].

Oxygen functional groups present in GO structure can form strong hydrogen bonding interactions with the polymer matrix, improving the interfacial adhesion between them and, therefore, the mechanical properties of nanocomposites [88].

Recent studies have demonstrated that GO promotes cell regeneration, which makes it an interesting material for its application in regenerative medicine. For example, GO has been used to induce piezoelectric behaviour that promotes cell proliferation by generating electrical stimulation [89].

Many studies have reported the use of reduced graphene oxide (rGO) instead of GO in the preparation of nanocomposites [62,90,91]. The reduction of GO leads to the elimination of most oxygen-containing functional groups, thus the sp^2 structure and, therefore, electrical conductivity are partially restored, consequently, rGO reaches excellent electrical conductivity and high mobility [86,92,93].

- *Graphene nanoplatelets*

Graphene nanoplatelets (GNP) show a structure similar to idealised G, but in comparison, its production is much more cost-effective. They consist of small stacks of G nanosheets, like the structure found on MWCNT, but with a platelet shape. GNP may be functionalised with different chemical entities, like carboxyl graphene nanoplatelets [94] or GO nanoplatelets [95].

In the case of carboxyl GNP, they offer good reinforcement from a mechanical point of view and, due to their large surface area, surface roughness and high protein adsorption, they favour osteoblast cell attachment, proliferation and differentiation [94].

Fullerenes

In 1985, Kroto et al. discovered fullerene [96], the third carbon allotrope, after graphite and diamond. Fullerene presents a structure consisting of sp^2 carbons in a high symmetric cage. Carbon forms pentagons and hexagons packed in a spherical shape [97].

Fullerenes have been used to reinforce polymers with poor mechanical properties. However, ultra-short carbon nanotubes present better results in terms of mechanical reinforcement [98].

Carbon dots

Carbon dots are zero-dimensional nanomaterials that are formed by 2-3- parallel graphene sheets. Carbon dots consist of a carbogenic core with oxygen, hydrogen, and carbon on their surface. They present excellent solubility in water, biocompatibility, optical properties, chemical inertness and neglectable toxicity [99,100].

Some research works suggest that carbon dots do not affect cell viability, proliferation, metabolism and differentiation [101]. They are not extensively used in the fabrication of bone tissue-engineered scaffolds [102]. However, other biomedical applications, like drug/gene delivery, bioimaging or photothermal and photodynamic therapy have been extensively studied [100,103].

Nanodiamond

Carbon atoms in diamond exhibit sp^3 hybridisation. Four bonds are directed towards the corners of a regular tetrahedron. Diamond is extremely hard due to the rigidity of the three-dimensional network [69]. Nanodiamond (ND) was discovered in 1963-1982 [97].

When added to a polymeric matrix, ND act as a cell growth support and improves the chemical stability and the biocompatibility of the nanocomposite [104–106].

2.2.4.2. Carbon-based nanomaterials for bone regeneration

Antimicrobial activity

Contrary to bulk materials, nanomaterials have the capacity of crossing cell membranes easily, leading to a destructive effect on the bacteria cell [107]. There are four main bactericidal mechanisms of antimicrobial nanomaterials, and carbon-based nanomaterials could promote them:

i. Reactive oxygen species (ROS) generation [108]: cell death is produced by the damage of DNA induced by ROS. These ROS include superoxide anions, hydroxyl radicals, and hydrogen peroxide.

ii. Physical damage [109]: some nanostructured materials present sharp edges that can damage the bacterial cell wall membranes.

iii. Binding [110]: loss of cell membrane integrity and efflux of cytoplasmic materials can be caused by binding materials on the bacterial cell wall.

iv. Release of metal ions [111]: inhibition of adenosine triphosphate (ATP) production and DNA replication produced by metal ions released into the media may cause the death of cells.

As a consequence of their different characteristics, each type of carbon-based nanomaterial promotes one or several of these mechanisms, acting in different ways.

The antimicrobial activity of CNT can be related to the formation of cell-CNT aggregates that damage the cell wall of bacteria and release their DNA content [112].

Compared to MWCNT, SWCNT presents more potent antimicrobial activity. Due to their smaller nanotube diameter, they could have tight contact and penetrate easily into the cell wall. Besides, their higher surface area allows SWCNT to interact better with the cell surface [113].

Antimicrobial activity is also affected by the length of the SWCNT. It is reported that the longer the CNT, the higher the antimicrobial activity. It is explained by the interactions between cells and the SWCNT: the shorter SWCNT is more likely self-aggregated without involving lots of bacterial cells [114].

Conversely, the main antimicrobial mechanism of graphene-related nanomaterials is membrane stress provoked by direct contact with sharp nanosheets after cell deposition on graphene-based materials [115]. Furthermore, GO can damage cell membranes via the generation of ROS. Thus, the antibacterial mechanism of GO is affected by both, physical destruction and chemical oxidation, which results in a decrease in bacterial resistance [116].

In the case of fullerenes, their antimicrobial activity could follow three different mechanisms: (i) internalisation of the fullerenes into the bacteria, which inhibits the energy metabolism, (ii) the impairing of the respiratory chain inhibits bacterial growth, and (iii) the induction of cell membrane disruption [113,117]. The hydrophobic surface of fullerenes promotes the interaction with membrane lipids and the intercalation between them [117].

Alternatively, ND presents antibacterial activity since they can form a covalent bond with molecules on cell walls or adhere to intracellular components. This process inhibits vital enzymes and proteins, leading to a rapid collapse of bacterial metabolism and finally cell death [118].

Accordingly, the use of carbon-based materials to improve the antimicrobial capacity of biomaterials is very interesting and, therefore, their use in the manufacturing of scaffolds may bring great improvements.

Osteoconductivity

First of all, it is important to establish the difference between osteoinductivity and osteoconductivity. Osteoinduction is the process by which osteogenesis is induced, i.e. primitive, undifferentiated, and pluripotent cells are stimulated to develop into preosteoblasts. Conversely, osteoconductivity is the capacity of a material to allow bone growth on its surface or down into pores, channels or pipes [119].

CNT demonstrate osteoconductivity and they can provide a favourable extracellular matrix for cell adhesion due to their similar dimensions to natural collagen fibres [120]. Their osteoconductivity may also be explained by electrochemical interactions between CNT and cells and by an increase in hydrophilicity [121,122].

When graphene-related nanomaterials, especially G and GO, are added to a polymer matrix, it is found that they increase cell adhesion and proliferation by increasing hydrophilicity [123–125]. It is reported [126] that this effect is higher in GO, which increases hydrophilicity and it leads to better cell behaviour.

However, to achieve osteoinductivity, it is necessary to add some functionalisation to GO surface, like using poly(ethylamine) [123], poly(lactide-co-glycolide acid) [127], collagen [128], phosphates [129], hydroxyapatite [130] and silanes [131].

In general carbon nanomaterials present osteoconductivity, but they are not osteoinductive. However, a recent study [132] has reported that low oxygen-content graphene nanoparticles may favour the adhesion of cells and they can undergo osteogenesis on the surface of these nanocomposites.

The case of fullerenes is completely different, fullerene-based films present a decrease in the adhesion of cells with less spreading, growth, metabolic activity and viability. This is explained because fullerene presents an electron-deficiency structure, which is responsible for its high chemical reactivity. For presenting osteoconductivity, fullerene films need to be aged for one year. At that moment, due to fragmentation, oxidation and polymerisation, fullerene supports cell colonisation well [133,134].

Finally, ND incorporation leads to an increase in cell growth on the polymer. As in the case of graphene-related nanomaterials, some studies demonstrated that the wettability is increased with the addition of ND due to the oxygen termination of the diamond nanoparticles [135,136].

2.2.4.3. Limitations and toxicity

In general, carbon-based nanomaterials present inconclusive results when studying their cytotoxicity. The reason is that their toxicity depends on many factors, such as the shape, size, purity, post-production processing steps, oxidative state, functional groups, dispersion state, synthesis methods, route and dose of administration, and exposure times [84,137,138]. This makes it very difficult to obtain general conclusions which could be extrapolated to all cases.

Related to the cytotoxicity of CNT, once implanted in the body, MWCNT are thought to be biopersistent [139] and could interfere with different physiological processes. For example, *in vivo* studies reported that the presence of MWCNT agglomerates led to the attachment of multinucleated cells. On its part, SWCNT were transported from the site of implantation to the lymph nodes and potentially block potassium channel activities in mammalian cell systems. It was also found that the needle-like shape of CNT promoted the mobility and penetration of membranes, uptake by cells, and strong interactions with various protein systems. These findings may suggest undesirable effects relating to cytotoxicity [140–142].

Another problem that can be found in the application of CNT is that the metal catalysts used in their fabrication are generally trapped inside the nanotubes, which can lead to an increase in cytotoxicity [143].

However, in contrast to these findings, other studies have reported no cytotoxicity effects when CNT were incorporated into matrix-based materials for bone tissue-engineered scaffolds [144–147].

Concerning graphene-related materials, inconsistencies reported from studies are similar to the studies using CNT. When they are used as substrate or coatings, some research studies [148–150] found that G presented good biocompatibility and the ability to stimulate cell proliferation. Other studies [142,151] reported some cytotoxicity risks since G presented an important tendency of being agglomerate. When G sheets agglomeration occurs on the cell membrane, it can contribute to their toxic properties. Besides, at high concentrations and long exposure times, ROS were generated by G.

In the case of nanocomposites, contradicting evidence has also been reported when G and GO are incorporated into a matrix. Luo et al. [126] found that the addition of G reduced cell adhesion, whilst GO presented a positive effect. Türk et al. [152] also found cytotoxicity when G was introduced into a matrix composed of Bioglass. However, several studies [83,125] reported no cytotoxicity when G was introduced in scaffolds (Figure 2.4 and Figure 2.5).

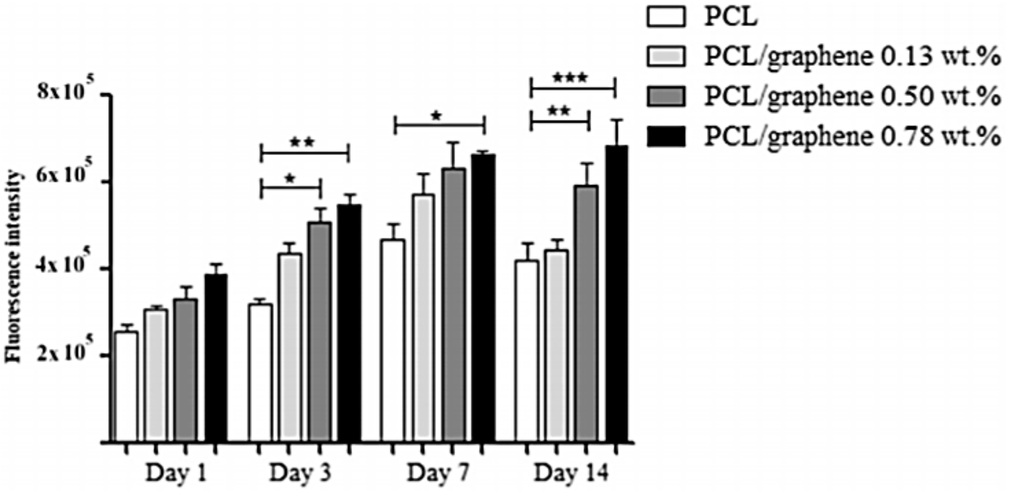

Figure 2.4. *MC3T3 osteoblasts viability and proliferation measured by fluorescence intensity for G-containing PCL scaffolds. The higher the G content, the higher the cell proliferation rate (Reprinted from [93], with permission from Elsevier).*

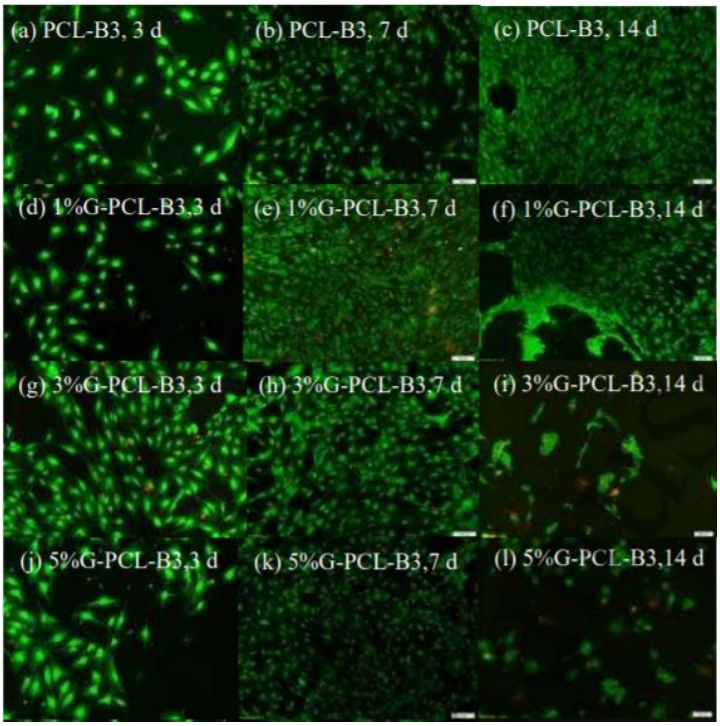

Figure 2.5. *Live (green) and dead (red) MC3T3-E1 cells were seeded on PCL-coated bioactive glass with different percentages of graphene. (a),(b),(c) without graphene, (d),(e),(f) 1 wt.% G, (g),(h),(i) 3 wt.% G, (j),(k),(l) 5 wt.% G. After 7 days the density of cells on G-containing scaffolds was higher than without G. However, after 14 days of incubation, a decrease in cell viability is observed due to the presence of G* [152].

In the case of GO, it was found that its presence may reduce cell proliferation rate due to an increase in the intracellular ROS level [153]. However, other studies [154–158] found that neither GO nor rGO presented cytotoxic effects at low concentrations.

Fullerenes also present contradicting results. On one hand, it was found that fullerene nanoparticles induced DNA breakage [159] and oxidative damage to cellular membranes due to ROS generation [160,161]. However, other studies [162] demonstrated no cytotoxic effect on fullerenes.

In the case of ND, many studies concluded no cytotoxicity had been found [163–165]. In an extensive study, no ROS generation was found. However, it was found that ND could easily access the cell membrane, but they seemed to be nonreactive once inside the cell [166].

All these contradicting results make *in vitro* and *in vivo* studies crucial for the development and the complete understanding of nanocomposites with carbon-based materials. However, despite the contradictions found, in most cases, the biocompatibility of carbon-based nanomaterials was found and cytotoxicity was reduced when carbon-based nanomaterials are used as reinforcement embedded inside a matrix.

The area that needs further investigation relates to biodegradable matrices that release carbon-based nanomaterials during their degradation process. Carbon-based nanomaterials were assumed to be biopersistent, however, oxidative enzymes can catalyse the degradation of some carbon-based nanomaterials (e.g. GO or CNT) [167]. Furthermore, carbon-based nanomaterials may affect the degradation rate of the matrix and the toxicity of the degradation products. To the best of the authors' knowledge, there are not many research studies relating to this approach.

Sánchez-González et al. [168] found that the addition of rGO produced a slight acceleration in the hydrolytic degradation process, reducing its mechanical stability faster when compared to the pristine polymer. However, rGO was not released to the medium, but it remains embedded in the polymer matrix.

Murray et al. [169] found that when G was added at high levels of loading (5 wt.%), the enzymatic degradation rate was lower than the pristine polymer than the polymer with low levels of G (0.1 wt.% and 1 wt.%). They also found that the mechanism by which the G was bonded to the matrix was also affected by the degradation rate. When studying the toxicity of the degradative by-products, it was found that G reduced the toxicity. This decrease in enzymatic and hydrolytic degradation rate when GO was added was also found. [170–173]. In the case of enzymatic degradation, the effect of graphene derivatives was due to the presence of sheets that prevented the diffusion of the enzymes into the scaffold network [174].

Finally, Cabral et al. [62] found that neither G nor rGO had a significant effect on the enzymatic degradation rate.

In the case of MWCNT, Joddar et al. [175] reported a decrease in degradation rate when added to a biodegradable matrix. It may be concluded that the presence of carbon-based nanomaterials incorporated into a matrix reduced the degradation rate and it could be tailored relative to the level of nanomaterial loading.

Table 2.1. Properties of carbon-based nanomaterials for bone tissue engineering applications.

	Bactericidal mechanism	**Osteoconductivity**	**Possible toxicity**	**Refs**
Carbon nanotubes	Binding	Electrochemical interactions with cells Increase wettability	Biopersistent Easy penetration in the cell membrane Metal catalysts trapped	[112,114,139–147]
Graphene	Physical damage	Increase wettability	Agglomeration on cell membranes ROS generation	[83,115,125,126,142,148–152]
Graphene oxide	Physical damage ROS generation	Increase wettability	ROS generation	[115,116,153–158]
Fullerenes	Binding	Only after ageing	Induce DNA breakage ROS generation	[133,134,159–162]
Nanodiamond	Binding	Increase wettability	No cytotoxicity No ROS generation	[135,136,163–166]

2.3. *Additive Manufacturing*

According to ISO/ASTM standard [176], AM technologies can be classified into seven different groups: (i) binder jetting, (ii) direct energy deposition, (iii) material extrusion, (iv) material jetting, (v) powder bed fusion, (vi) sheet lamination, and (vii) vat photopolymerisation.

Outside this classification, other novel techniques are emerging, as is the case of bioprinting, which combines the use of 3D printing technology with materials that incorporate viable living cells. However, this kind of material falls outside the scope of this review.

Among all the AM technologies, the focus of this review is on those used to manufacture biodegradable scaffolds (i.e. polymer-based and ceramic-based), that allow the incorporation of nanomaterials, more specifically carbon-based nanomaterials.

Researchers have developed biodegradable polymer scaffolds loaded with carbon-based materials fabricated using one of three different AM techniques: (i) material extrusion (e.g. Fused Deposition Modelling, FDM and Direct Ink Writing, DIW), (ii) powder bed fusion (e.g. Selective Laser Sintering, SLS and Selective Laser Melting, SLM), and (iii) vat photopolymerisation (e.g. Stereolithography, SLA and Digital Light Processing, DLP).

In the case of biodegradable ceramic scaffolds, since they do not melt easily, these scaffolds are fabricated by AM using mainly powder bed fusion (SLS). However, to counteract the natural fragility of ceramics, they are usually blended with polymers. For this reason, sometimes other 3D printing techniques are used, like DIW [46] or FDM [60].

The advantages and limitations of these technologies are detailed in Table 2.2. Accuracy defines the minimum pore size that can be obtained with each technology. Methods used in each technology for the dispersion of nanoparticles within the matrix are also indicated in the table; this aspect is especially important because the optimal methods to obtain an adequate dispersion are very different depending on the technology.

2.3.1. *Material extrusion*

These technologies are based on the extrusion of the material under pressure. The material is deposited from a nozzle or syringe to fabricate components in a layer-by-layer manner. These technologies require a liquid or a viscous material that is obtained mainly by two methods, melting a thermoplastic material (FDM) or using a viscous ink (DIW) [177].

FDM has shown rapid development in recent years due to its simplicity, speediness and large-scale rate of production. Raw materials in FDM are filaments that are partially melted by a heater and extruded from a nozzle.

In the case of DIW, the material used is colloidal ink which is directly extruded through an orifice or nozzle without heating. These inks can maintain their shapes during solidification or drying.

2.3.2. *Powder bed fusion*

SLS and SLM are categorised as powder bed fusion technologies since it utilises thermal energy to selectively melt powder materials of a powder bed. The raw material is typically in the form of powder-based particles for these AM-based technologies [178]. Complete melting is achieved in SLM, while in SLS heat provokes material fusion at the molecular level, instead of completely melted [179].

Thermal energy may be obtained by different sources such as lasers or electron beams. In the case of scaffolds with carbon-based nanomaterials, technologies that obtain energy from laser sources are used.

2.3.3. *Vat photopolimerization*

SLA technique was developed in the 1980s and was one of the first methods proposed for 3D printing [180]. The SLA and DLP techniques involve solidifying a liquid photocurable polymer by exposure to UV light. The photopolymer is placed in a tank and it is cured layer-by-layer on a support platform with a light source (250 nm-400 nm).

The difference between the two techniques is the light source: in SLA, the polymer is cured using a laser that forms each layer point-by-point; in DLP, all the layers are cured at the same time using a matrix of lasers.

There is a third technology in this group: Liquid Crystal Display (LCD). Its printing process is similar to DLP, but the cross-section is illuminated by using an array of UV-LCDs [181].

In Vat Polymerization technologies, polymerization of the resin occurs directly during the printing process since photocurable resins polymerized by UV exposition. The addition of nanomaterials to the resin to print structures with nanocomposites could affect the polymerization process, resulting in low printability.

Components printed using these AM techniques require a post-curing process (usually, UV exposure + temperature) to achieve their final properties. Considering biomedical applications, this could be used to sterilise the components to be implanted into the body, which could be an additional advantage [182].

Some researchers [183,184] have taken advantage of these AM techniques by modifying a non-photocurable polymer to make it photocurable, allowing the use of biodegradable and biocompatible polymers appropriate for bone tissue-engineered scaffolds.

Table 2.2. *Comparison of AM technologies available for biodegradable materials with nanomaterials.*

	FDM	**DIW**	**SLS**	**SLM**	**SLA/DLP**
Material	Thermoplastic polymer	Polymer or polymer + ceramic	Polymer or ceramic	Thermoplastic polymer	Photocurable polymer
Morphology	Filament	Ink	Powder	Powder	Liquid
Accuracy	Low (250 μm)	Medium-High (50 μm)	Medium-Low (200 μm)	Medium-Low (200 μm)	High (20 μm)
Dispersion	-Solvent dissolution -Melt mixing by extrusion	-Solvent mixing -Centrifuge mixing -Ultrasonication	-Melt mixing by extrusion -Dissolution–precipitation -Physical mixing	-Melt mixing	-Solvent mixing -Ultrasonication
Advantages	-Simplicity, speediness and large-scale production -Low cost -The most common AM technology	-Flexible manufacturing -Low cost -Large parts manufacturing	-High print speed -Good mechanical properties -Printing w/o support structures	-Excellent mechanical properties -Improved density compared to SLS -Printing w/o support structures	-Surface finish -DLP shows higher printing speed -Excellent part quality -Ability to fabricate complex structures -UV sterilisation
Limitations	-Support structures required -Highly anisotropic parts -Clogging -Layer delamination -Materials affected by the sterilisation process -Limited pore size	-Support structures required -Deposited ink should retain its shape	-High temperature -Possible unmelted powders -Extensive cleaning is needed -Powder production with adequate flowability -Expensive	-High temperature -Possible unmelted powders -Extensive cleaning is needed -Powder production with adequate flowability -Limited pore size	-Extensive post-treatments -Uncured resin toxicity -Support structures required -Resin cannot be storage indefinitely - Nanofillers can affect the polymerization process of the resin
Ref	[177,185–188]	[177,189,190]	[177,191–193]	[177,194,195]	[177,196–200]

The addition of nanomaterials to improve the properties of additive manufactured structures has been widely investigated. It is well known that the dispersion of nanomaterials is crucial for the attainment of unique properties for the composite. For example, the presence of agglomerates reduces the mechanical properties of the composite [89,171]. Consequently, the method of incorporating the nanomaterials into the matrix is very important and is decisive to the final composite performance.

In the case of AM technologies, the dispersion of nanomaterials depends on the characteristics of matrix materials. When they are solid (FDM, SLS and SLM), usually a solvent is used to disperse nanomaterials easily by ultrasonication [185,192] or mechanical mixing [186]. In the case of materials that melt easily and their viscosity is low enough, melt mixing can be used as a solvent-free alternative [187,191]. Finally, in the case of powder matrix and powder nanomaterials, they can be mixed using a rotary tumbler [193].

Conversely, DIW, SLA and DLP use liquid raw materials. Ultrasonication is the most common method to achieve optimal dispersion of nanomaterials in liquid-based raw materials [196,198–200], although other mechanical mixing methods have also been used [189]. Sometimes, when the viscosity is high, a solvent is added, which promotes the dispersion of the nanomaterial [197].

2.3.4. Biodegradable materials for 3D printed scaffolds

One of the requirements that the materials must meet for being used as tissue-engineered bone scaffolds is biodegradability. Among biodegradable materials that are used with carbon-based nanomaterials, it is possible to distinguish between polymeric and ceramic materials.

2.3.4.1 Polymer matrices

Polymeric materials have been widely used for bone tissue engineering applications. They are classified by their origin: (i) natural and (ii) synthetic polymers. Natural polymers include silk fibroin, collagen, gelatin fibrin, elastin, cellulose, alginate, dextran, starch, chitin/chitosan, glycosaminoglycans and hyaluronic acid, among others [201]. Bone scaffolds fabricated using natural polymers by conventional methods have been extensively reported [202,203]. However, the preferred polymers for AM are the synthetic biodegradable ones, and can be classified as follows [204–208]:

Aliphatic polyesters: include polylactic acid (PLA), polyglycolic acid (PGA), poly ε-caprolactone (PCL), poly (lactic-co-glycolide) (PLG) and poly-(3-hydroxybutyrate-co-3-hydroxybutyrate) (PHBV). They usually undergo degradation through hydrolysis of the ester group situated along their backbone with degradative by-products that are acidic. The degradation rate of these polymers is easily controlled because they can be produced with a tailored structure. Their main drawback is their reduced bioactivity. PGA presents a rapid degradation (2-4 weeks), while PLA degradation takes months to years since it is more hydrophobic than PGA. To obtain intermediate degradation rates, PLGA with varying lactide/glycolide ratios are synthesised. PCL can be degraded by different agents: microorganisms, hydrolytic, enzymatic, or intracellular. Compared with PLA and PGA, PCL has a slower degradation rate.

Aliphatic polycarbonates: They present low thermal stability and reduced mechanical properties. However, their controlled functional characteristics make them very interesting for bone tissue engineering applications. Among them, poly(trimethylene carbonate) (PTMC) has been used for fabricating bone tissue-engineered scaffolds with carbon-based nanomaterials using AM techniques.

Vinyl polymers: poly(vinyl alcohol) (PVA) is one of the most used vinyl polymers. They are hydrophilic materials. Hydrogels based on PVA show good biomechanical performance, and they retain a large amount of water.

Polyurethanes (PU): are used for the fabrication of medical devices, especially long-term implants and biomedical products (e.g. cardiovascular catheters and diaphragms of blood pumps). The main disadvantage of PU is the toxicity of its degradative by-products, which can be reduced by using specific prepolymers.

Non-biodegradable polymers: despite their inability to degrade when implanted in the body, some different synthetic polymers have also been used in the manufacture of bone tissue-engineered scaffolds: polyether ether ketone (PEEK), polyvinylidene difluoride (PVDF) and acrylonitrile butadiene styrene (ABS).

2.3.4.2. Ceramic matrices

Among ceramic materials, bioceramics exhibit properties like biocompatibility, mechanical compatibility, excellent surface compatibility, anti-thrombus effect, bactericidal effect, and good physical and chemical stability, which make these materials suitable for being used for bone tissue-engineered scaffolds [209]. However, their primary ionic and/or covalent bonds makes them relatively brittle. This inherent brittleness, together with low ductility are major drawbacks for bioceramics and therefore limit their application [210].

Additive Manufacturing has been investigated as a viable approach for the fabrication of ceramic-based bone tissue-engineered scaffolds by Additive Manufacturing, the most common ceramics used include:

Tricalcium phosphate (TCP): has good biocompatibility and does not present any cytotoxic reaction. Bone formation is favoured in contact with TCP due to the release of calcium and phosphate ions. Alpha-TCP (α-TCP) demonstrates a greater degree of solubility and a faster rate of degradation when compared to beta- TCP (β-TCP) [209]. The degradation rate of β-TCP is within the same range as the growth of mature new bone [211].

Hydroxyapatite (HA): its structure and composition are similar to the inorganic component of human bones. HA is highly biocompatible, non-toxic, osteoconductive and it gradually merges with the natural bone [212]. Its main drawbacks are its low mechanical properties and relatively low degradation rate. To improve its mechanical strength, there are two paths: (i) use of reinforcements like other ceramics and (ii) the fabrication of nano-sized ceramics [212].

Ca-Si-based ceramics: they present good compression properties and controllable degradation rate. They improve the rate of new bone formation and bone regeneration through a gradual release of Si and Ca ions. However, like many other bioceramics, their brittle nature and low toughness hinder their development in load-bearing applications [210].

Diopside, MgCaSi2O6 (Di): compared with HA and other bioceramics, offers improved mechanical strength. The Ca, Si and Mg containing ionic products from extracts of Di can stimulate osteoblast proliferation at low concentrations. However, its degradation rate is extremely slow [213].

Bioactive glasses (BG): they can comprise of Na_2O, CaO, SiO_2 and P_2O_5. They are considered to be the most promising biomaterials in bone tissue engineering applications as they exhibit osteoinductive properties. Another attractive aspect of BG-based materials is their degradation rate, which can be regulated by their chemical composition. Their poor mechanical properties (similar to many bioceramics) are the main drawback [210].

2.3.5. 3D printed biodegradable polymer scaffolds with CBN

2.3.5.1. Material extrusion

Due to its simplicity and speediness, FDM is the most used technology when the matrix is a polymer. Many studies incorporating GO into different thermoplastic matrices have been found. Both biological and mechanical properties of the matrix were improved with the addition of GO. Melo et al. [214] and Unagolla et al. [215] reported improvement in the antimicrobial properties and the enhancement of cellular response. Melo et al. found an 80% increase in bacterial death after 24 h in contact with PCL/GO scaffold.

Chen et al. [57] found that an increase of 167% in compressive modulus was achieved when 5 wt.% GO was incorporated into PLA-thermoplastic polyurethane (TPU) matrix and a maximum tensile modulus increase of 75.5% on addition of 0.5 wt.% GO. This wt.% loading was also optimal in terms of cellular growth and proliferation of NIH3T3 mouse embryonic fibroblast cells. Belaid et al. [216] studied both mechanical and biological properties and reported an increase of 30% in Young's modulus when 0.3 wt.% GO was added to PLA. When the proliferation of MC3T3-E1 cells was studied, they concluded that it was not until Day-7 that higher levels of viability were observed for scaffolds containing 0.2-0.3 wt.% GO loading when compared with pristine PLA.

All these studies introduced the nanomaterial using a solvent that was subsequently evaporated to obtain the filament to feed the printer. Figure 2.6 shows SEM images of PCL scaffolds with and without GO and it can be observed how GO addition did not affect the printing process as relatively similar geometries were achieved in all the cases.

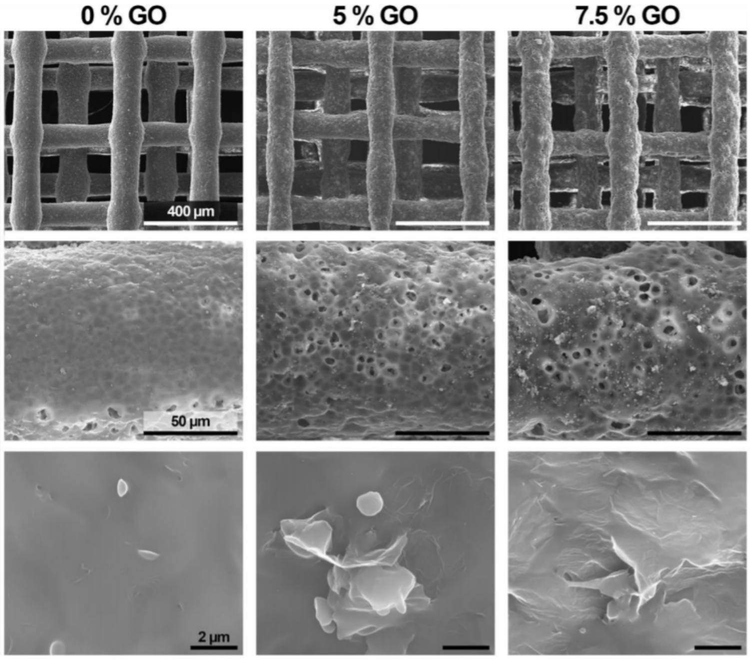

Figure 2.6. SEM images of PCL scaffolds with different percentages of GO, manufactured by FDM. Surface roughness and irregularity increased with the addition of GO. The average diameter of the fibres did not change with GO (Reprinted from [214]*, with permission from Elsevier).*

G has also been used to improve the mechanical and biological properties of tissue-engineered bone scaffolds. Wang et al. [83] conducted in vitro and in vivo studies using G-PCL scaffolds for microcurrent therapy. They had previously found [125] an increase in cell attachment and proliferation due to the high surface area, elastic modulus, and stiffness of the G-PCL scaffold. In this case, it was not until Day-14 when G at a loading level of approx. 0.8 wt.% demonstrated a statistically significant improvement in the proliferation rate. Furthermore, G presented improved mechanical properties (i.e. compressive modulus and compressive strength) and cell affinity when compared to CNT [217].

Sayar et al. [218] also used G powder as the reinforcement phase and FDM as the AM technique and following printing the scaffold was crosslinked using UV exposition. When a loading level of 3 wt.% G was incorporated into PTMC - an increase in tensile strength (100%) and electrical conductivity was demonstrated, which has the potential for electrical stimulation. It was found that cell density, morphology, and viability did not differ when compared to the pristine PTMC.

Mechanical properties of ABS scaffolds reinforced with GNP at a loading level of 4 wt.% was investigated by Dul et al. [219]. They reported an increase in Young's modulus, however, the adhesion between the matrix and reinforcement was relatively poor, which led to a decrease in tensile strength and strain at break.

Alam et al. [220] worked with a commercial filament of PLA loaded with carbon nanofibres and GNP. They found that the presence of nanomaterials produced internal porosity, which resulted in a reduced compressive stiffness of 20%. In contrast, carbon nanomaterials improved hydrophilicity and apatite deposition.

Huang et al. [221] found that an addition of 3 wt.% of MWCNT into PCL increased the compressive modulus, whilst the addition of 0.25-0.75 wt.% of MWCNT did not affect this parameter. Nanoindentation properties improved from the addition of 0.75 and 3 wt.% CNT. These improvements occurred due to an increase in polymer crystallinity due to CNT alignment. It was also found that smaller CNT tended to agglomerate, thereby improving cell attachment and protein absorption. Mimicking the natural bone tissue, Huang et al. [222], incorporated MWCNT and nHA into PCL and found an increase in mechanical properties, cell proliferation, osteogenic differentiation and scaffold mineralisation.

For all studies, the scaffolds fabricated using FDM with carbon-based nanomaterials produced stable porous structures and the addition of nanomaterial did not hinder the printing process.

Another technology derived from material extrusion is Direct Ink Writing. It was more extensively used for polymeric-ceramic matrices than polymeric. Jakus et al. [223] manufactured inks with high levels of G loading in a PLG-based matrix. Tensile modulus increased by 200% with a level of loading of 20 wt.% G. In vitro and in vivo studies demonstrated a good cellular response from approximately 30,000 cells at Day 1 in PLG to more than 50,000 when G was incorporated (Figure 2.7).

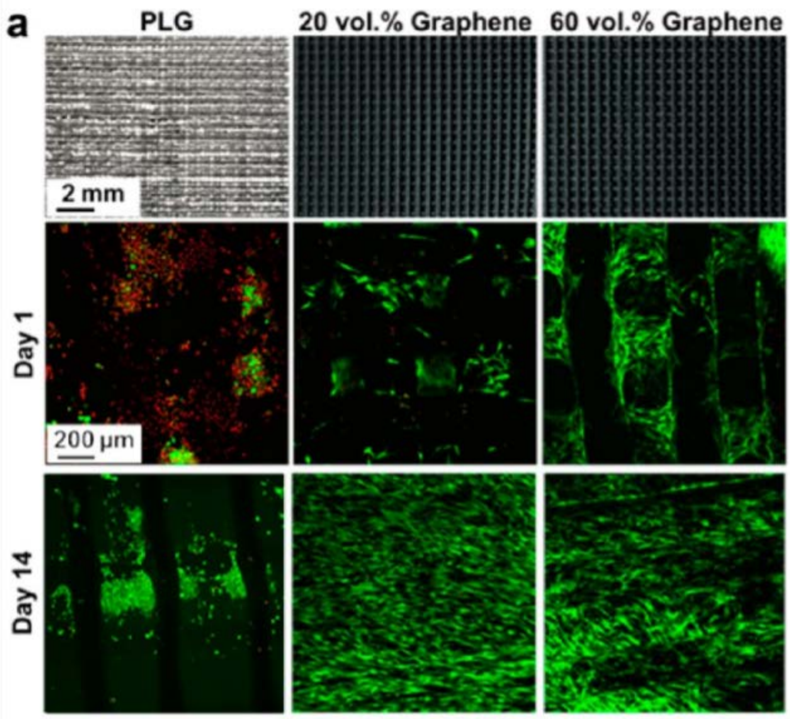

Figure 2.7. *Photographs and cell viability (live cells in green and dead cells in red) of PLG scaffolds loaded with G manufactured by DIW. An increase in cell viability was produced when G was added* [223].

2.3.5.2. Powder bed fusion

Researchers have also shown a high interest in SLS, especially using GO as the nanomaterials. For the application of this technology, different matrices have been investigated. PVA demonstrated very interesting properties for the application of bone tissue-engineered scaffolds. However, its low mechanical properties may be an obstacle in terms of its development. From this point, Shuai et al. [88] achieved an increase in compressive strength, Young's modulus and tensile strength by 60%, 152% and 69% on adding GO into the matrix. This improvement was obtained for relatively low levels of loadings (2.5 wt.%), and increases beyond 2.5 wt.% resulted in the formation of agglomerates and ultimately the reduction of mechanical properties. Furthermore, they found an increase in cell adhesion and attachment of the GO into the PVA matrix.

Feng et al. [224] focused their work on reducing the degradation rate of PVA. They blended PVA with PEEK, a non-biodegradable polymer, which successfully reduced the degradation rate. Additionally, Feng et al. [224] reported that 1 wt.% GO addition improved the interfacial bonding between PEEK and PVA, which resulted in an improvement in mechanical properties (i.e. increases of 97% and 150% in compressive strength and compressive modulus). An increase in MG63 cell adhesion and proliferation was also reported when 1 wt.% GO was added to the PVA-PEEK matrix.

Shuai et al. [225] reported an improvement in the mechanical properties of GO-poly(L-lactic acid) (PLLA) scaffolds when fabricated using SLS, and adding Ag nanoparticles [226], which also enhanced antimicrobial activity due to the combination of the capturing effect of GO and killing effect of Ag.

Shuai et al. [89] also found that GO could be used to reinforce piezoelectric polymers for bone tissue engineering applications. Scaffolds containing 0.3 wt.% GO reported an improvement in compressive strength (100%) and tensile strength (25%) and cell adhesion were also enhanced by electrical charge excitation. However, although the polymer was not biodegradable, it could be applied in the field of bone scaffolds.

Not only have GO nanoparticles been used during SLS technology. Feng et al. [227] achieved improvements for PHBV in terms of tensile strength and compressive strength (i.e. 94% and 52%) when 2 wt.% of ND particles and 1 wt.% of molybdenum disulfide (MoS_2) nanosheets were added. MoS_2 improved the dispersion of ND due to its steric hindrance effect and vice versa and was found to be better dispersed within the matrix when it was added with ND by the sandwiched octahedral ND particles.

All the studies regarding the polymer-based bone scaffolds with carbon-based nanomaterials when fabricated using SLS technology adopted a similar dispersion method of the nanoparticles – good GO dispersion was achieved using ultrasonication in water or a solvent that was evaporated to obtain powder for printing (Figure 2.8).

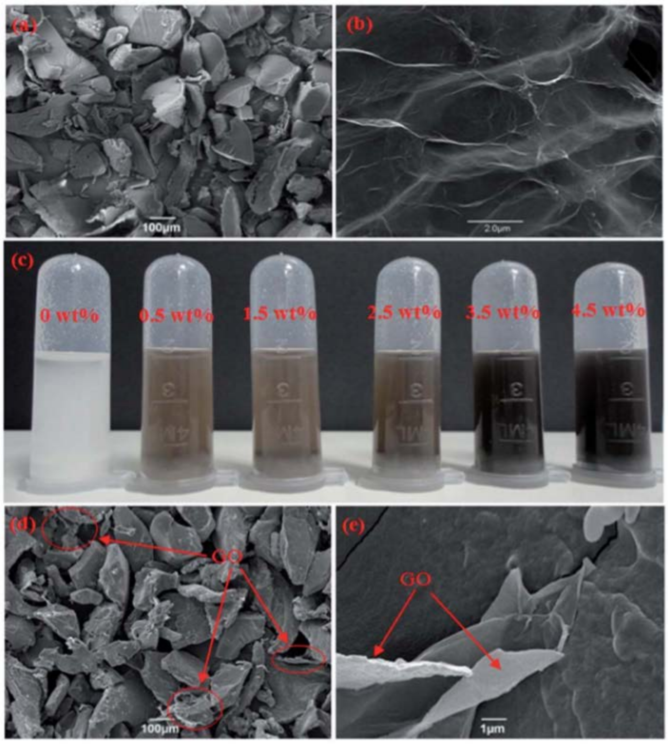

Figure 2.8. *Preparation of PVA-GO powder for SLS printing: (a) SEM image of initial PVA powder; (b) TEM image of initial GO; (c) photographs of GO/PVS suspension in deionized water after ultrasonication; (d),(e) SEM images of the composite powder after evaporation of water* [88].

2.3.5.3. Vat photopolymerisation

Finally, vat photopolymerisation was the least used AM technique for the fabrication of polymer-based bone tissue-engineered scaffolds containing carbon-based nanomaterials.

Feng et al. [198] introduced 0.5 wt.% G into a commercial PU resin for SLA. G increased the tensile and flexural properties of the matrix. Feng et al. [200] also fabricated DLP samples comprised of the same PU resin and 0.5 wt.%. GNP. In this case, the flexural modulus was improved by 14%, while fracture toughness increased by 28%. In both studies, Feng et al. used a solvent-free method to disperse the carbon-based nanomaterials in the matrix using ultrasonication. Consequently, gyroid scaffolds were fabricated by the two-vat polymerization technology (Figure 2.9).

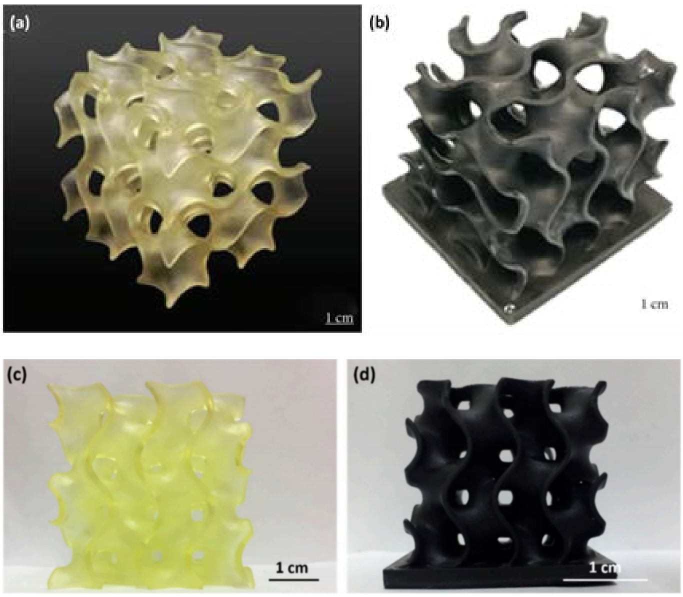

Figure 2.9. *PLA/PUA gyroid scaffolds manufactured by (a),(b) SLA* [198] *and (c),(d) DLP* [200]*. The addition of nanomaterials did not affect the printing process.*

Table 2.3. *Polymer scaffolds obtained by 3D printer with different carbon-based nanomaterials.*

Technology	Nanomaterial	Nanomaterial dispersion	Matrix	Effect of CBN	Ref.
FDM	GO (0.5 wt.%)	Solvent mixing	TPU/PLA	Increase tensile and compression modulus Low amount of GO increases cell proliferation	[57]
	GO (0.3 wt.%)	Solvent mixing	PLA	Increase Young's modulus Increase toughness More efficient promotion of cell adhesion and proliferation	[216]
	GO (7.5 wt.%/ 0.5 wt.%)	Solvent mixing	PCL	Improve antimicrobial properties Enhancement of cellular response	[214,215]
	G (0.78 wt.%)	Melt mixing	PCL	Cell proliferation stimulation Increase hydrophilicity Increase compressive modulus and strength	[83,125,217]

Table 2.3. (Cont) *Polymer scaffolds obtained by 3D printer with different carbon-based nanomaterials.*

Technology	Nanomaterial	Nanomaterial dispersion	Matrix	Effect of CBN	Ref.
FDM	G (3 wt.%)	Solvent mixing	PTMC	Increase electrical conductivity Increase tensile strength, elongation at break and Young's modulus No effect on cell attachment and viability	[218]
	GNP (4 wt.%)	Melt mixing	ABS	Increase tensile modulus Reduction in ultimate tensile stress and strain Reduction in creep compliance	[219]
	Carbon nanofibers/ GNP (18 wt.%)	Commercial filament	PLA	CNF reduces compression stiffness Improve bioactivity	[220]
	MWCNT (3 wt.%)	Melt mixing	PCL	Increase in compressive modulus and strength Improve cell viability and proliferation Increase polymer crystallinity Increase hardness and elastic modulus	[217,221]
	MWCNT/ nHA (0.75 wt.%)	Melt mixing	PCL	Increase compressive strength Improve cell attachment	[222]
DIW	G (20 vol.%)	Solvent mixing	PLG	Increase tensile modulus High loading decreases the tensile strength Increase cell proliferation	[223]

Table 2.3. (Cont) *Polymer scaffolds obtained by 3D printer with different carbon-based nanomaterials.*

Technology	Nanomaterial	Nanomaterial dispersion	Matrix	Effect of CBN	Ref.
SLS	GO (2.5 wt.%)	Ultrasonication of water dispersion	PVA	Increase tensile strength, elongation at break, compressive modulus and strength Good cytocompatibility	[88]
	GO (1 wt.%)	Ultrasonication of water dispersion	PEEK*/ PVA	Increase surface energy Increase compressive modulus and strength Increase cell proliferation	[224]
	GO (1 wt.%)	Ultrasonication of solvent dispersion	PLLA	Increase compressive strength Increase hardness	[225]
	GO/Ag (1 wt.%)	Ultrasonication of solvent dispersion + ball milling	PLLA/ PGA	Increase compressive strength and modulus Increase wettability Antibacterial effect	[226]
	GO (0.3 wt.%)	Ultrasonication of solvent dispersion	PVDF*	Increase compressive strength, tensile strength, and modulus Increase hydrophilicity Improve cellular response	[89]
	ND/MoS_2 (2 wt.%)	Ultrasonication of solvent dispersion	PHBV	Increase tensile strength and modulus Increase compressive strength and modulus Enhanced mineral deposition	[227]
SLA	G (0.5 wt.%)	Ultrasonication	PLA/ PUA	Increase tensile strength Increase flexural strength and modulus	[198]
DLP	GNP (0.5 wt.%)	Ultrasonication	PLA/ PUA	Increase flexural modulus and toughness No effect on printability	[200]

* Non-biodegradable

2.4. Conclusions

Based on the studies, the fabrication of 3D printed biodegradable scaffolds modified with CBN has been demonstrated to be an encouraging solution with interesting benefits: improved mechanical properties, enhanced biological activity, easy control of porosity and design, among others.

However, although considerable progress has been made, thereby providing a promising clinical platform for the repair and regeneration of bone, some aspects need to be examined in greater depth since the technology is still in its infancy. Some of the major research and technical challenges that the scientist community will need to address are:

- Good performance of carbon-based nanomaterials is linked to a good dispersion within the matrix, being one of the crucial and critical aspects to achieve during the manufacturing of carbon-based nanomaterials derived bone tissue-engineered bone scaffolds.
- It is important to study in-depth the influence that the level of nanomaterial loading exhibits on the mechanical and biological properties since there is a balance to be attained to ensure the optimal properties are achieved for both. The optimal level of loading reported depends greatly on the study and the range from 0.2-18 wt.%. In general, using a level of nanomaterial loading less than 1 wt.% offered the best results in terms of mechanical reinforcement.
- AM technologies offer many advantages; however, materials need to have specific characteristics to allow the fabrication method to function both effectively and efficiently. The addition of nanomaterials can affect printability and therefore studying and optimising the addition and dispersion methods are crucial for the development of bone tissue-engineered scaffolds reinforced with carbon-based nanomaterials. Further studies regarding how nanomaterials affect the 3D printing technique and how to mitigate possible adverse effects need investigation.
- The surface of the carbon-based nanomaterials is easily functionalized, and this functionalization could improve the dispersion of the carbon-based nanomaterials and ultimately the mechanical performance. Conversely, carbon-based nanomaterials can be biofunctionalised to be used as biomolecular carriers, thereby increasing their bioactivity. Both approaches are interesting and relevant to the fabrication of bone tissue-engineered scaffolds using AM techniques. However, a better understanding of the regenerative effect and bioresponsiveness of chemically functionalised carbon-based nanomaterials and the mechanical performance of biofunctionalised carbon-based nanomaterials are required.
- Another aspect that has to be highlighted relates to biodegradability. Ideally, bone tissue-engineered scaffolds should be biodegradable; this opens up a new research avenue: to study the behaviour of carbon-based nanomaterials and the associated degradative by-products when implanted into the body. Some studies have appeared related to this issue, but inconclusive and inconsistent results have been found. Further research about cytotoxicity and possible adverse environmental effects is necessary before these scaffolds can be clinically tested.

- Finally, safety and succeed in clinical translation need to be demonstrated by facing the regulatory and economic hurdles. However, the future of this technology is bright, and the commitment of scientists and engineers will lead to a fruitful and impactful future in the coming decades.

2.5. References

[1] S. Lopez de Armentia, J.C. del Real, E. Paz, N. Dunne, Advances in Biodegradable 3D Printed Scaffolds with Carbon-Based Nanomaterials for Bone Regeneration, Materials (Basel). 13 (2020) 5083. https://doi.org/10.3390/ma13225083.

[2] M. Meskinfam, 17 - Polymer scaffolds for bone regeneration, in: Charact. Polym. Biomater., Elsevier Ltd., 2017: pp. 441–475. https://doi.org/10.1016/B978-0-08-100737-2.00017-0.

[3] L.E. Freed, G. Vunjak-Novakoric, R.J. Biron, D.B. Eagles, D.C. Lesnoy, S.K. Barlow, R. Langer, Biodegradable Polymer Scaffolds for Tissue Engineering, Biotechnol. (N Y). 12 (1994) 689–693.

[4] R.G. Ribas, V.M. Schatkoski, T.L. do A. Montanheiro, B.R.C. de Menezes, C. Stegemann, D.M.G. Leite, G.P. Thim, Current advances in bone tissue engineering concerning ceramic and bioglass scaffolds: A review, Ceram. Int. 45 (2019) 21051–21061. https://doi.org/10.1016/j.ceramint.2019.07.096.

[5] L.P. Corrales, M.L. Esteves, J. aime E.. Vick, Scaffold design for bone regeneration, J Nanosci Nanotechnol. 14 (2014) 15–56.

[6] Y. Kuboki, H. Takita, D. Kobayashi, E. Tsuruga, M. Inoue, M. Murata, N. Nagai, Y. Dohi, H. Ohgushi, BMP-induced osteogenesis on the surface of hydroxyapatite with geometrically feasible and nonfeasible structures: Topology of osteogenesis, J. Biomed. Mater. Res. 39 (1998) 190–199. https://doi.org/10.1002/(SICI)1097-4636(199802)39:2<190::AID-JBM4>3.0.CO;2-K.

[7] T.L. Conrad, R.K. Roeder, Effects of porogen morphology on the architecture, permeability, and mechanical properties of hydroxyapatite whisker reinforced polyetheretherketone scaffolds, J. Mech. Behav. Biomed. Mater. 106 (2020) 103730. https://doi.org/10.1016/j.jmbbm.2020.103730.

[8] V. Karageorgiou, D. Kaplan, Porosity of 3D biomaterial scaffolds and osteogenesis, Biomaterials. 26 (2005) 5474–5491. https://doi.org/10.1016/j.biomaterials.2005.02.002.

[9] C.M. Murphy, M.G. Haugh, F.J. O'Brien, The effect of mean pore size on cell attachment, proliferation and migration in collagen-glycosaminoglycan scaffolds for bone tissue engineering, Biomaterials. 31 (2010) 461–466. https://doi.org/10.1016/j.biomaterials.2009.09.063.

[10] N. Abbasi, S. Hamlet, R.M. Love, N.T. Nguyen, Porous scaffolds for bone regeneration, J. Sci. Adv. Mater. Devices. (2020). https://doi.org/10.1016/j.jsamd.2020.01.007.

[11] S.F. Hulbert, F.A. Young, R.S. Mathews, J.J. Klawitter, C.D. Talbert, F.H. Stelling, Potential of ceramic materials as permanently implantable skeletal prostheses, J. Biomed. Mater. Res. 4 (1970) 433–456. https://doi.org/10.1002/jbm.820040309.

[12] G.W. Chang, C.L. Tseng, Y.S. Tzeng, T.M. Chen, H.W. Fang, An in vivo evaluation of a novel malleable composite scaffold (polypropylene carbonate/ poly(D-lactic acid) /tricalcium phosphate elastic composites) for bone defect repair, J. Taiwan Inst. Chem. Eng. 80 (2017) 813–819. https://doi.org/10.1016/j.jtice.2017.06.022.

[13] J. Choi, K. Kim, T. Kim, G. Liu, A. Bar-Shir, T. Hyeon, M.T. McMahon, J.W.M. Bulte, J.P. Fisher, A.A. Gilad, Multimodal imaging of sustained drug release from 3-D poly(propylene fumarate) (PPF) scaffolds, J. Control. Release. 156 (2011) 239–245. https://doi.org/10.1016/j.jconrel.2011.06.035.

[14] M. Świętek, A. Brož, J. Tarasiuk, S. Wroński, W. Tokarz, A. Kozieł, M. Błażewicz, L. Bačáková, Carbon nanotube/iron oxide hybrid particles and their PCL-based 3D composites for potential bone regeneration, Mater. Sci. Eng. C. 104 (2019) 109913. https://doi.org/10.1016/j.msec.2019.109913.

[15] A. Salerno, A.B. Leonardi, P. Pedram, E. Di Maio, M.A. Fanovich, P.A. Netti, Tuning the three-dimensional architecture of supercritical CO2 foamed PCL scaffolds by a novel mould patterning approach, Mater. Sci. Eng. C. 109 (2020) 110518. https://doi.org/10.1016/j.msec.2019.110518.

[16] I. Manavitehrani, T.Y.L. Le, S. Daly, Y. Wang, P.K. Maitz, A. Schindeler, F. Dehghani, Formation of porous biodegradable scaffolds based on poly(propylene carbonate) using gas foaming technology, Mater. Sci. Eng. C. 96 (2019) 824–830. https://doi.org/10.1016/j.msec.2018.11.088.

[17] P. Naderi, M. Zarei, S. Karbasi, H. Salehi, Evaluation of the effects of keratin on physical, mechanical and biological properties of poly (3-hydroxybutyrate) electrospun scaffold: Potential application in bone tissue engineering, Eur. Polym. J. 124 (2020) 109502. https://doi.org/10.1016/j.eurpolymj.2020.109502.

[18] G. Barati, A. Rahmani, S. Nadri, In vitro differentiation of conjunctiva mesenchymal stem cells into insulin producing cells on natural and synthetic electrospun scaffolds, Biologicals. 62 (2019) 33–38. https://doi.org/10.1016/j.biologicals.2019.10.004.

[19] M. Fadaie, E. Mirzaei, B. Geramizadeh, Z. Asvar, Incorporation of nanofibrillated chitosan into electrospun PCL nanofibers makes scaffolds with enhanced mechanical and biological properties, Carbohydr. Polym. 199 (2018) 628–640. https://doi.org/10.1016/j.carbpol.2018.07.061.

[20] Z. Fereshteh, M. Fathi, A. Bagri, A.R. Boccaccini, Preparation and characterization of aligned porous PCL/zein scaffolds as drug delivery systems via improved unidirectional freeze-drying method, Mater. Sci. Eng. C. 68 (2016) 613–622. https://doi.org/10.1016/j.msec.2016.06.009.

[21] Z. Ge, Z. Jin, T. Cao, Manufacture of degradable polymeric scaffolds for bone regeneration, Biomed. Mater. 3 (2008) 022001. https://doi.org/10.1088/1748-6041/3/2/022001.

[22] F. Ghorbani, D. Li, S. Ni, Y. Zhou, B. Yu, 3D printing of acellular scaffolds for bone defect regeneration: A review, Mater. Today Commun. 22 (2020) 100979. https://doi.org/10.1016/j.mtcomm.2020.100979.

[23] X. Du, S. Fu, Y. Zhu, 3D printing of ceramic-based scaffolds for bone tissue engineering: An overview, J. Mater. Chem. B. 6 (2018) 4397–4412. https://doi.org/10.1039/c8tb00677f.

[24] F.N. Alaribe, S.L. Manoto, S.C.K.M. Motaung, Scaffolds from biomaterials: Advantages and

limitations in bone and tissue engineering, Biologia (Bratisl). 71 (2016) 353–366. https://doi.org/10.1515/biolog-2016-0056.

[25] S. Pina, J.M. Oliveira, R.L. Reis, Natural-based nanocomposites for bone tissue engineering and regenerative medicine: A review, Adv. Mater. 27 (2015) 1143–1169. https://doi.org/10.1002/adma.201403354.

[26] W. Bonfield, M.D. Grynpas, A.E. Tully, J. Bowman, J. Abram, Hydroxyapatite reinforced polyethylene - a mechanically compatible implant material for bone replacement, Biomaterials. 2 (1981) 185–186. https://doi.org/10.1016/0142-9612(81)90050-8.

[27] A. Bharadwaz, A.C. Jayasuriya, Recent trends in the application of widely used natural and synthetic polymer nanocomposites in bone tissue regeneration, Mater. Sci. Eng. C. 110 (2020) 110698. https://doi.org/10.1016/j.msec.2020.110698.

[28] A.R. Amini, C.T. Laurencin, S.P. Nukavarapu, Bone tissue engineering: Recent advances and challenges, Crit. Rev. Biomed. Eng. 40 (2012) 363–408. https://doi.org/10.1615/CritRevBiomedEng.v40.i5.10.

[29] M.G. Gandolfi, F. Zamparini, M. Degli Esposti, F. Chiellini, F. Fava, P. Fabbri, P. Taddei, C. Prati, Highly porous polycaprolactone scaffolds doped with calcium silicate and dicalcium phosphate dihydrate designed for bone regeneration, Mater. Sci. Eng. C. 102 (2019) 341–361. https://doi.org/10.1016/j.msec.2019.04.040.

[30] M.P. Drupitha, B. Das, R. Parameswaran, S. Dhara, G.B. Nando, K. Naskar, Hybrid electrospun fibers based on TPU-PDMS and spherical nanohydroxyapatite for bone tissue engineering, Mater. Today Commun. 16 (2018) 264–273. https://doi.org/10.1016/j.mtcomm.2018.06.013.

[31] S. Moeini, M.R. Mohammadi, A. Simchi, In-situ solvothermal processing of polycaprolactone/hydroxyapatite nanocomposites with enhanced mechanical and biological performance for bone tissue engineering, Bioact. Mater. 2 (2017) 146–155. https://doi.org/10.1016/j.bioactmat.2017.04.004.

[32] S. Morelli, S. Salerno, J. Holopainen, M. Ritala, L. De Bartolo, Osteogenic and osteoclastogenic differentiation of co-cultured cells in polylactic acid-nanohydroxyapatite fiber scaffolds, J. Biotechnol. 204 (2015) 53–62. https://doi.org/10.1016/j.jbiotec.2015.03.023.

[33] M.H. Kim, C. Yun, E.P. Chalisserry, Y.W. Lee, H.W. Kang, S.H. Park, W.K. Jung, J. Oh, S.Y. Nam, Quantitative analysis of the role of nanohydroxyapatite (nHA) on 3D-printed PCL/nHA composite scaffolds, Mater. Lett. 220 (2018) 112–115. https://doi.org/10.1016/j.matlet.2018.03.025.

[34] N.T. Ba Linh, K.H. Lee, B.T. Lee, Functional nanofiber mat of polyvinyl alcohol/gelatin containing nanoparticles of biphasic calcium phosphate for bone regeneration in rat calvaria defects, J. Biomed. Mater. Res. - Part A. 101A (2013) 2412–2423. https://doi.org/10.1002/jbm.a.34533.

[35] M. Ezati, H. Safavipour, B. Houshmand, S. Faghihi, Development of a PCL/gelatin/chitosan/β-TCP electrospun composite for guided bone regeneration, Prog. Biomater. 7 (2018) 225–237.

https://doi.org/10.1007/s40204-018-0098-x.

[36] M.J. Chern, L.Y. Yang, Y.K. Shen, J.H. Hung, 3D scaffold with PCL combined biomedical ceramic materials for bone tissue regeneration, Int. J. Precis. Eng. Manuf. 14 (2013) 2201–2207. https://doi.org/10.1007/s12541-013-0298-1.

[37] R. Arumugam, V. Subramanyam, R.K. Chinnadurai, E.S. Srinadhu, B. Subramanian, S. Nallani, Development of novel mechanically stable porous nanocomposite (PVDF-PMMA/HAp/TiO2) film scaffold with nanowhiskers surface morphology for bone repair applications, Mater. Lett. 236 (2019) 694–696. https://doi.org/10.1016/j.matlet.2018.11.023.

[38] W. Guo, L. Xu, P. Feng, Y. Gu, C. Shuai, In-situ growth of silica nano-protrusions on halloysite nanotubes for interfacial reinforcement in polymer/halloysite scaffolds, Appl. Surf. Sci. 513 (2020) 145772. https://doi.org/10.1016/j.apsusc.2020.145772.

[39] A. Hasan, G. Waibhaw, V. Saxena, L.M. Pandey, Nano-biocomposite scaffolds of chitosan, carboxymethyl cellulose and silver nanoparticle modified cellulose nanowhiskers for bone tissue engineering applications, Int. J. Biol. Macromol. 111 (2018) 923–934. https://doi.org/10.1016/j.ijbiomac.2018.01.089.

[40] E. Marsich, F. Bellomo, G. Turco, A. Travan, I. Donati, S. Paoletti, Nano-composite scaffolds for bone tissue engineering containing silver nanoparticles: Preparation, characterization and biological properties, J. Mater. Sci. Mater. Med. 24 (2013) 1799–1807. https://doi.org/10.1007/s10856-013-4923-4.

[41] F. Alam, V.R. Shukla, K.M. Varadarajan, S. Kumar, Microarchitected 3D printed polylactic acid (PLA) nanocomposite scaffolds for biomedical applications, J. Mech. Behav. Biomed. Mater. 103 (2020) 103576. https://doi.org/10.1016/j.jmbbm.2019.103576.

[42] J. Prakash, D. Prema, K.S. Venkataprasanna, K. Balagangadharan, International Journal of Biological Macromolecules Nanocomposite chitosan film containing graphene oxide/hydroxyapatite/gold for bone tissue engineering, Int. J. Biol. Macromol. 154 (2020) 62–71. https://doi.org/10.1016/j.ijbiomac.2020.03.095.

[43] G.N. Abdelrasoul, B. Farkas, I. Romano, A. Diaspro, S. Beke, Nanocomposite scaffold fabrication by incorporating gold nanoparticles into biodegradable polymer matrix: Synthesis, characterization, and photothermal effect, Mater. Sci. Eng. C. 56 (2015) 305–310. https://doi.org/10.1016/j.msec.2015.06.037.

[44] M. Erol, A. Özyuĝuran, Ö. Özarpat, S. Küçükbayrak, 3D Composite scaffolds using strontium containing bioactive glasses, J. Eur. Ceram. Soc. 32 (2012) 2747–2755. https://doi.org/10.1016/j.jeurceramsoc.2012.01.015.

[45] S.Ö. Gönen, M. Erol Taygun, S. Küçükbayrak, Fabrication of bioactive glass containing nanocomposite fiber mats for bone tissue engineering applications, Compos. Struct. 138 (2016) 96–106. https://doi.org/10.1016/j.compstruct.2015.11.033.

[46] H. Golzar, D. Mohammadrezaei, A. Yadegari, M. Rasoulianboroujeni, M. Hashemi, M. Omidi, F. Yazdian, M. Shalbaf, L. Tayebi, Incorporation of functionalized reduced graphene

oxide/magnesium nanohybrid to enhance the osteoinductivity capability of 3D printed calcium phosphate-based scaffolds, Compos. Part B Eng. 185 (2020) 107749. https://doi.org/10.1016/j.compositesb.2020.107749.

[47] J. Shen, W. Wang, X. Zhai, B. Chen, W. Qiao, W. Li, P. Li, Y. Zhao, Y. Meng, S. Qian, X. Liu, P.K. Chu, K.W.K. Yeung, 3D-printed nanocomposite scaffolds with tunable magnesium ionic microenvironment induce in situ bone tissue regeneration, Appl. Mater. Today. 16 (2019) 493–507. https://doi.org/10.1016/j.apmt.2019.07.012.

[48] T.I. Chao, S. Xiang, C.S. Chen, W.C. Chin, A.J. Nelson, C. Wang, J. Lu, Carbon nanotubes promote neuron differentiation from human embryonic stem cells, Biochem. Biophys. Res. Commun. 384 (2009) 426–430. https://doi.org/10.1016/j.bbrc.2009.04.157.

[49] T.I. Chao, S. Xiang, J.F. Lipstate, C. Wang, J. Lu, Poly(methacrylic acid)-grafted carbon nanotube scaffolds enhance differentiation of hESCs into neuronal cells, Adv. Mater. 22 (2010) 3542–3547. https://doi.org/10.1002/adma.201000262.

[50] X. Xie, W. Wang, J. Cheng, H. Liang, Z. Lin, T. Zhang, Y. Lu, Q. Li, Bilayer pifithrin-α loaded extracellular matrix/PLGA scaffolds for enhanced vascularized bone formation, Colloids Surfaces B Biointerfaces. 190 (2020) 110903. https://doi.org/10.1016/j.colsurfb.2020.110903.

[51] M. Rasoulianboroujeni, F. Fahimipour, P. Shah, K. Khoshroo, M. Tahriri, H. Eslami, A. Yadegari, E. Dashtimoghadam, L. Tayebi, Development of 3D-printed PLGA/TiO2 nanocomposite scaffolds for bone tissue engineering applications, Mater. Sci. Eng. C. 96 (2019) 105–113. https://doi.org/10.1016/j.msec.2018.10.077.

[52] M. Honda, N. Morikawa, K. Hata, T. Yada, S. Morita, M. Ueda, K. Kimata, Rat costochondral cell characteristics on poly (L-lactide-co-ε-caprolactone) scaffolds, Biomaterials. 24 (2003) 3511–3519. https://doi.org/10.1016/S0142-9612(03)00210-2.

[53] E. Walejewska, J. Idaszek, M. Heljak, A. Chlanda, E. Choinska, V. Hasirci, W. Swieszkowski, The effect of introduction of filament shift on degradation behaviour of PLGA- and PLCL-based scaffolds fabricated via additive manufacturing, Polym. Degrad. Stab. 171 (2020) 109030. https://doi.org/10.1016/j.polymdegradstab.2019.109030.

[54] R. Mishra, R. Varshney, N. Das, D. Sircar, P. Roy, Synthesis and characterization of gelatin-PVP polymer composite scaffold for potential application in bone tissue engineering, Eur. Polym. J. 119 (2019) 155–168. https://doi.org/10.1016/j.eurpolymj.2019.07.007.

[55] W. Chen, J. Ma, L. Zhu, Y. Morsi, H. EI-Hamshary, S.S. Al-Deyab, X. Mo, Superelastic, superabsorbent and 3D nanofiber-assembled scaffold for tissue engineering, Colloids Surfaces B Biointerfaces. 142 (2016) 165–172. https://doi.org/10.1016/j.colsurfb.2016.02.050.

[56] T. Xu, Z. Liang, B. Ding, Q. Feng, H. Fong, Polymer blend nanofibers containing polycaprolactone as biocompatible and biodegradable binding agent to fabricate electrospun three-dimensional scaffolds/structures, Polymer (Guildf). 151 (2018) 299–306. https://doi.org/10.1016/j.polymer.2018.07.074.

[57] Q. Chen, J.D. Mangadlao, J. Wallat, A. De Leon, J.K. Pokorski, R.C. Advincula, 3D printing

biocompatible polyurethane/poly(lactic acid)/graphene oxide nanocomposites: Anisotropic properties, ACS Appl. Mater. Interfaces. 9 (2017) 4015–4023. https://doi.org/10.1021/acsami.6b11793.

[58] S. Hassanajili, A. Karami-Pour, A. Oryan, T. Talaei-Khozani, Preparation and characterization of PLA/PCL/HA composite scaffolds using indirect 3D printing for bone tissue engineering, Mater. Sci. Eng. C. 104 (2019) 109960. https://doi.org/10.1016/j.msec.2019.109960.

[59] M. Shahrezaee, M. Salehi, S. Keshtkari, A. Oryan, A. Kamali, B. Shekarchi, In vitro and in vivo investigation of PLA/PCL scaffold coated with metformin-loaded gelatin nanocarriers in regeneration of critical-sized bone defects, Nanomedicine Nanotechnology, Biol. Med. 14 (2018) 2061–2073. https://doi.org/10.1016/j.nano.2018.06.007.

[60] Y.H. Lin, T.Y. Chuang, W.H. Chiang, I.W.P. Chen, K. Wang, M.Y. Shie, Y.W. Chen, The synergistic effects of graphene-contained 3D-printed calcium silicate/poly-ε-caprolactone scaffolds promote FGFR-induced osteogenic/angiogenic differentiation of mesenchymal stem cells, Mater. Sci. Eng. C. 104 (2019) 109887. https://doi.org/10.1016/j.msec.2019.109887.

[61] C. Wu, L. Xia, P. Han, M. Xu, B. Fang, J. Wang, J. Chang, Y. Xiao, Graphene-oxide-modified β-tricalcium phosphate bioceramics stimulate in vitro and in vivo osteogenesis, Carbon N. Y. 93 (2015) 116–129. https://doi.org/10.1016/j.carbon.2015.04.048.

[62] C.S.D. Cabral, S.P. Miguel, D. de Melo-Diogo, R.O. Louro, I.J. Correia, Green reduced graphene oxide functionalized 3D printed scaffolds for bone tissue regeneration, Carbon N. Y. 146 (2019) 513–523. https://doi.org/10.1016/j.carbon.2019.01.100.

[63] R. Eivazzadeh-Keihan, A. Maleki, M. de la Guardia, M.S. Bani, K.K. Chenab, P. Pashazadeh-Panahi, B. Baradaran, A. Mokhtarzadeh, M.R. Hamblin, Carbon based nanomaterials for tissue engineering of bone: Building new bone on small black scaffolds: A review, J. Adv. Res. 18 (2019) 185–201. https://doi.org/10.1016/j.jare.2019.03.011.

[64] R. Madannejad, N. Shoaie, F. Jahanpeyma, M.H. Darvishi, M. Azimzadeh, H. Javadi, Toxicity of carbon-based nanomaterials: Reviewing recent reports in medical and biological systems, Chem. Biol. Interact. 307 (2019) 206–222. https://doi.org/10.1016/j.cbi.2019.04.036.

[65] C. Gao, T. Liu, C. Shuai, S. Peng, Enhancement mechanisms of graphene in nano-58S bioactive glass scaffold: Mechanical and biological performance, Sci. Rep. 4 (2014) 4712. https://doi.org/10.1038/srep04712.

[66] X. Han, S. Li, Z. Peng, A.O. Al-Yuobi, A.S.O. Bashammakh, M.S. El-Shahawi, R.M. Leblanc, Interactions between carbon nanomaterials and biomolecules, J. Oleo Sci. 65 (2016) 1–7. https://doi.org/10.5650/jos.ess15248.

[67] S. Iijima, Helical microtubule of graphitic carbon, Nature. 354 (1991) 56–58.

[68] S. Iijima, T. Ichihashi, Single-shell carbon nanotubes of 1-nm diameter, Nature. 363 (1993) 603–605. https://doi.org/10.1038/363603a0.

[69] N. Saifuddin, A.Z. Raziah, A.R. Junizah, Carbon nanotubes: A review on structure and their

interaction with proteins, J. Chem. 2013 (2013) 676815. https://doi.org/10.1155/2013/676815.

[70] A. Eatemadi, H. Daraee, H. Karimkhanloo, M. Kouhi, N. Zarghami, A. Akbarzadeh, M. Abasi, Y. Hanifehpour, S.W. Joo, Carbon nanotubes: Properties, synthesis, purification, and medical applications, Nanoscale Res. Lett. 9 (2014) 393. https://doi.org/10.1186/1556-276X-9-393.

[71] N. Dunne, C. Mitchell, Biomedical/bioengineering applications of carbon nanotube-based nanocomposites, Woodhead Publishing Limited, 2011. https://doi.org/10.1533/9780857091390.3.676.

[72] A. Magiera, J. Markowski, E. Menaszek, J. Pilch, S. Blazewicz, PLA-Based Hybrid and Composite Electrospun Fibrous Scaffolds as Potential Materials for Tissue Engineering, J. Nanomater. 2017 (2017) 924802. https://doi.org/10.1155/2017/9246802.

[73] D. Lahiri, F. Rouzaud, S. Namin, A.K. Keshri, J.J. Valdés, L. Kos, N. Tsoukias, A. Agarwal, Carbon nanotube reinforced polylactide-caprolactone copolymer: Mechanical strengthening and interaction with human osteoblasts in vitro, ACS Appl. Mater. Interfaces. 1 (2009) 2470–2476. https://doi.org/10.1021/am900423q.

[74] A. Abarrategi, M.C. Gutiérrez, C. Moreno-Vicente, M.J. Hortigüela, V. Ramos, J.L. López-Lacomba, M.L. Ferrer, F. del Monte, Multiwall carbon nanotube scaffolds for tissue engineering purposes, Biomaterials. 29 (2008) 94–102. https://doi.org/10.1016/j.biomaterials.2007.09.021.

[75] S.-F. Wang, L. Shen, W.-D. Zhang, Y.-J. Tong, Preparation and Mechanical Properties of Chitosan/Carbon Nanotubes Composites, Biomacromolecules. 6 (2005) 3067–3072.

[76] X. Shi, B. Sitharaman, Q.P. Pham, F. Liang, K. Wu, W. Edward Billups, L.J. Wilson, A.G. Mikos, Fabrication of porous ultra-short single-walled carbon nanotube nanocomposite scaffolds for bone tissue engineering, Biomaterials. 28 (2007) 4078–4090. https://doi.org/10.1016/j.biomaterials.2007.05.033.

[77] B. Sitharaman, X. Shi, X.F. Walboomers, H. Liao, V. Cuijpers, L.J. Wilson, A.G. Mikos, J.A. Jansen, In vivo biocompatibility of ultra-short single-walled carbon nanotube/biodegradable polymer nanocomposites for bone tissue engineering, Bone. 43 (2008) 362–370. https://doi.org/10.1016/j.bone.2008.04.013.

[78] K.S. Novoselov, A.K. Geim, S. V. Morozov, D. Jiang, Y. Zhang, S. V. Dubonos, I. V. Grigorieva, A.A. Firsov, Electric Field Effect in Atomically Thin Carbon Films, Science (80-.). 306 (2004) 666–669.

[79] S.K. Tiwari, V. Kumar, A. Huczko, R. Oraon, A. De Adhikari, G.C. Nayak, Magical Allotropes of Carbon: Prospects and Applications, Crit. Rev. Solid State Mater. Sci. 41 (2016) 257–317. https://doi.org/10.1080/10408436.2015.1127206.

[80] S.K. Tiwari, S. Sahoo, N. Wang, A. Huczko, Graphene research and their outputs: Status and prospect, J. Sci. Adv. Mater. Devices. (2020). https://doi.org/10.1016/j.jsamd.2020.01.006.

[81] T. Ma, Z. Liu, J. Wen, Y. Gao, X. Ren, H. Chen, C. Jin, X.L. Ma, N. Xu, H.M. Cheng, W. Ren,

Tailoring the thermal and electrical transport properties of graphene films by grain size engineering, Nat. Commun. 8 (2017) 14486. https://doi.org/10.1038/ncomms14486.

[82] K. Prusty, S. Barik, S.K. Swain, A Corelation Between the Graphene Surface Area, Functional Groups, Defects, and Porosity on the Performance of the Nanocomposites, Elsevier Inc., 2019. https://doi.org/10.1016/B978-0-12-814548-7.00013-1.

[83] W. Wang, J.R.P. Junior, P.R.L. Nalesso, D. Musson, J. Cornish, F. Mendonça, G.F. Caetano, P. Bártolo, Engineered 3D printed poly(ε-caprolactone)/graphene scaffolds for bone tissue engineering, Mater. Sci. Eng. C. 100 (2019) 759–770. https://doi.org/10.1016/j.msec.2019.03.047.

[84] H. Fan, L. Wang, K. Zhao, N. Li, Z. Shi, Z. Ge, Z. Jin, Fabrication, mechanical properties, and biocompatibility of graphene-reinforced chitosan composites, Biomacromolecules. 11 (2010) 2345–2351. https://doi.org/10.1021/bm100470q.

[85] V.B. Mohan, K. tak Lau, D. Hui, D. Bhattacharyya, Graphene-based materials and their composites: A review on production, applications and product limitations, Compos. Part B Eng. 142 (2018) 200–220. https://doi.org/10.1016/j.compositesb.2018.01.013.

[86] A. Raslan, L. Saenz, J. Ciriza, J.L. Pedraz, Graphene oxide and reduced graphene oxide-based scaffolds in regenerative medicine, Int. J. Pharm. 580 (2020) 119226. https://doi.org/10.1016/j.ijpharm.2020.119226.

[87] L. Liu, J. Zhang, J. Zhao, F. Liu, Mechanical properties of graphene oxides, Nanoscale. 4 (2012) 5910. https://doi.org/10.1039/c2nr31164j.

[88] C. Shuai, P. Feng, C. Gao, X. Shuai, T. Xiao, S. Peng, Graphene oxide reinforced poly(vinyl alcohol): Nanocomposite scaffolds for tissue engineering applications, RSC Adv. 5 (2015) 25416–25423. https://doi.org/10.1039/c4ra16702c.

[89] C. Shuai, Z. Zeng, Y. Yang, F. Qi, S. Peng, W. Yang, C. He, G. Wang, G. Qian, Graphene oxide assists polyvinylidene fluoride scaffold to reconstruct electrical microenvironment of bone tissue, Mater. Des. 190 (2020) 108564. https://doi.org/10.1016/j.matdes.2020.108564.

[90] W. Nie, C. Peng, X. Zhou, L. Chen, W. Wang, Y. Zhang, P.X. Ma, C. He, Three-dimensional porous scaffold by self-assembly of reduced graphene oxide and nano-hydroxyapatite composites for bone tissue engineering, Carbon N. Y. 116 (2017) 325–337. https://doi.org/10.1016/j.carbon.2017.02.013.

[91] E. Correa, M.E. Moncada, O.D. Gutiérrez, C.A. Vargas, V.H. Zapata, Characterization of polycaprolactone/rGO nanocomposite scaffolds obtained by electrospinning, Mater. Sci. Eng. C. 103 (2019) 109773. https://doi.org/10.1016/j.msec.2019.109773.

[92] Q. Zhang, X. Liu, H. Meng, S. Liu, C. Zhang, Reduction pathway-dependent cytotoxicity of reduced graphene oxide, Environ. Sci. Nano. 5 (2018) 1361–1371. https://doi.org/10.1039/c8en00242h.

[93] Y. Wang, Y. Chen, S.D. Lacey, L. Xu, H. Xie, T. Li, V.A. Danner, L. Hu, Reduced graphene oxide film with record-high conductivity and mobility, Mater. Today. 21 (2018) 186–192.

https://doi.org/10.1016/j.mattod.2017.10.008.

[94] T. Kaur, A. Thirugnanam, K. Pramanik, Effect of carboxylated graphene nanoplatelets on mechanical and in-vitro biological properties of polyvinyl alcohol nanocomposite scaffolds for bone tissue engineering, Mater. Today Commun. 12 (2017) 34–42. https://doi.org/10.1016/j.mtcomm.2017.06.004.

[95] Y.W. Cheng, S.H. Wang, C.M. Liu, M.Y. Chien, C.C. Hsu, T.Y. Liu, Amino-modified graphene oxide nanoplatelets for photo-thermal and anti-bacterial capability, Surf. Coatings Technol. 385 (2020) 125441. https://doi.org/10.1016/j.surfcoat.2020.125441.

[96] H.W. Kroto, J.R. Health, S.C. O'Brien, R.F. Curl, R.E. Smalley, C60: Buckminsterfullerene, Nature. 318 (1985) 162–163.

[97] S. Goodarzi, T. Da Ros, J. Conde, F. Sefat, M. Mozafari, Fullerene: biomedical engineers get to revisit an old friend, Mater. Today. 20 (2017) 460–480. https://doi.org/10.1016/j.mattod.2017.03.017.

[98] B. Sitharaman, X. Shi, L.A. Tran, P.P. Spicer, I. Rusakova, L.J. Wilson, A.G. Mikos, Injectable in situ cross-linkable nanocomposites of biodegradable polymers and carbon nanostructures for bone tissue engineering, J. Biomater. Sci. Polym. Ed. 18 (2007) 655–671. https://doi.org/10.1163/156856207781034133.

[99] R. Kumar, V.B. Kumar, A. Gedanken, Sonochemical synthesis of carbon dots, mechanism, effect of parameters, and catalytic, energy, biomedical and tissue engineering applications, Ultrason. - Sonochemistry. 64 (2020) 105009. https://doi.org/10.1016/j.ultsonch.2020.105009.

[100] K. Ghosal, A. Ghosh, Carbon dots: The next generation platform for biomedical applications, Mater. Sci. Eng. C. 96 (2019) 887–903. https://doi.org/10.1016/j.msec.2018.11.060.

[101] W. Shang, X. Zhang, M. Zhang, Z. Fan, Y. Sun, M. Han, L. Fan, The uptake mechanism and biocompatibility of graphene quantum dots with human neural stem cells, Nanoscale. 6 (2014) 5799–5806. https://doi.org/10.1039/c3nr06433f.

[102] S. Gogoi, S. Maji, D. Mishra, K.S.P. Devi, T.K. Maiti, N. Karak, Nano-Bio Engineered Carbon Dot-Peptide Functionalized Water Dispersible Hyperbranched Polyurethane for Bone Tissue Regeneration, Macromol. Biosci. 17 (2016) 1–15. https://doi.org/10.1002/mabi.201600271.

[103] X. Wang, X. Sun, J. Lao, H. He, T. Cheng, M. Wang, S. Wang, F. Huang, Multifunctional graphene quantum dots for simultaneous targeted cellular imaging and drug delivery, Colloids Surfaces B Biointerfaces. 122 (2014) 638–644. https://doi.org/10.1016/j.colsurfb.2014.07.043.

[104] F.A.S. Pereira, G.N. Salles, B.V.M. Rodrigues, F.R. Marciano, C. Pacheco-Soares, A.O. Lobo, Diamond nanoparticles into poly (lactic acid) electrospun fibers: Cytocompatible and bioactive scaffolds with enhanced wettability and cell adhesion, Mater. Lett. 183 (2016) 420–424. https://doi.org/10.1016/j.matlet.2016.07.146.

[105] L. Grausova, A. Kromka, Z. Burdikova, A. Eckhardt, B. Rezek, J. Vacik, K. Haenen, V. Lisa, L.

Bacakova, Enhanced growth and osteogenic differentiation of human osteoblast-like cells on boron-doped nanocrystalline diamond thin films, PLoS One. 6 (2011) e20943. https://doi.org/10.1371/journal.pone.0020943.

[106] M. Parizek, T. El Douglas, K. Novotna, A. Kromka, M.A. Brady, A. Renzing, E. Voss, M. Jarosova, L. Palatinus, P. Tesarek, P. Ryparova, V. Lisa, A.M. dos Santos, L. Bacakova, Nanofibrous poly(lactide-co-glycolide) membranes loaded with diamond nanoparticles as promising substrates for bone tissue engineering, Int. J. Nanomedicine. 7 (2012) 1931–1951. https://doi.org/10.2147/IJN.S26665.

[107] E.O. Ogunsona, R. Muthuraj, E. Ojogbo, O. Valerio, T.H. Mekonnen, Engineered nanomaterials for antimicrobial applications: A review, Appl. Mater. Today. 18 (2020) 100473. https://doi.org/10.1016/j.apmt.2019.100473.

[108] J.P. Ruparelia, A.K. Chatterjee, S.P. Duttagupta, S. Mukherji, Strain specificity in antimicrobial activity of silver and copper nanoparticles, Acta Biomater. 4 (2008) 707–716. https://doi.org/10.1016/j.actbio.2007.11.006.

[109] O. Akhavan, E. Ghaderi, Toxicity of graphene and graphene oxide nanowalls against bacteria, ACS Nano. 4 (2010) 5731–5736. https://doi.org/10.1021/nn101390x.

[110] T. Parandhaman, A. Das, B. Ramalingam, D. Samanta, T.P. Sastry, A.B. Mandal, S.K. Das, Antimicrobial behavior of biosynthesized silica-silver nanocomposite for water disinfection: A mechanistic perspective, J. Hazard. Mater. 290 (2015) 117–126. https://doi.org/10.1016/j.jhazmat.2015.02.061.

[111] C. Gunawan, W.Y. Teoh, C.P. Marquis, R. Amal, Cytotoxic origin of copper(II) oxide nanoparticles: Comparative studies with micron-sized particles, leachate, and metal salts, ACS Nano. 5 (2011) 7214–7225. https://doi.org/10.1021/nn2020248.

[112] L.R. Arias, L. Yang, Inactivation of bacterial pathogens by carbon nanotubes in suspensions, Langmuir. 25 (2009) 3003–3012. https://doi.org/10.1021/la802769m.

[113] S.M. Dizaj, A. Mennati, S. Jafari, K. Khezri, K. Adibkia, Antimicrobial activity of carbon-based nanoparticles, Adv. Pharm. Bull. 5 (2015) 19–23. https://doi.org/10.5681/apb.2015.003.

[114] C. Yang, J. Mamouni, Y. Tang, L. Yang, Antimicrobial activity of single-walled carbon nanotubes: Length effect, Langmuir. 26 (2010) 16013–16019. https://doi.org/10.1021/la103110g.

[115] S. Azimi, J. Behin, R. Abiri, L. Rajabi, A.A. Derakhshan, H. Karimnezhad, Synthesis, characterization and antibacterial activity of chlorophyllin functionalized graphene oxide nanostructures, Sci. Adv. Mater. 6 (2014) 771–781. https://doi.org/10.1166/sam.2014.1767.

[116] M. Yousefi, M. Dadashpour, M. Hejazi, M. Hasanzadeh, B. Behnam, M. de la Guardia, N. Shadjou, A. Mokhtarzadeh, Anti-bacterial activity of graphene oxide as a new weapon nanomaterial to combat multidrug-resistance bacteria, Mater. Sci. Eng. C. 74 (2017) 568–581. https://doi.org/10.1016/j.msec.2016.12.125.

[117] F. Cataldo, T. Da Ros, Medicinal chemistry and pharmacological potential of fullerenes and

carbon nanotubes, Springer, Trieste, 2008.

[118] S. Chauhan, N. Jain, U. Nagaich, Nanodiamonds with powerful ability for drug delivery and biomedical applications: Recent updates on in vivo study and patents, J. Pharm. Anal. 10 (2020) 1–12. https://doi.org/10.1016/j.jpha.2019.09.003.

[119] T. Albrektsson, C. Johansson, Osteoinduction, osteoconduction and osseointegration, Eur. Spine J. 10 (2001) S96–S101. https://doi.org/10.1007/s005860100282.

[120] L.P. Zanello, B. Zhao, H. Hu, R.C. Haddon, Bone cell proliferation on carbon nanotubes, Nano Lett. 6 (2006) 562–567. https://doi.org/10.1021/nl051861e.

[121] C. Zhijiang, Z. Cong, G. Jie, Z. Qing, Z. Kongyin, Electrospun carboxyl multi-walled carbon nanotubes grafted polyhydroxybutyrate composite nanofibers membrane scaffolds: Preparation, characterization and cytocompatibility, Mater. Sci. Eng. C. 82 (2018) 29–40. https://doi.org/10.1016/j.msec.2017.08.005.

[122] Q. Cai, K. Subramani, R.T. Mathew, X. Yang, Chapter 18 - Carbon nanomaterials for implant dentistry and bone tissue engineering, in: Nanobiomaterials Clin. Dent., Second Edi, Elsevier Inc., 2019: pp. 429–468. https://doi.org/10.1016/b978-0-12-815886-9.00018-8.

[123] S. Kumar, S. Raj, K. Sarkar, K. Chatterjee, Engineering a multi-biofunctional composite using poly(ethylenimine) decorated graphene oxide for bone tissue regeneration, Nanoscale. 8 (2016) 6820–6836. https://doi.org/10.1039/c5nr06906h.

[124] H. Zanin, B.V.M. Rodrigues, W.A. Ribeiro Neto, R.E.S. Bretas, N.S. Da-Silva, F.R. Marciano, A. Oliveira Lobo, High loading of graphene oxide/multi-walled carbon nanotubes into PDLLA: A route towards the design of osteoconductive, bactericidal and non-immunogenic 3D porous scaffolds, Mater. Chem. Phys. 177 (2016) 56–66. https://doi.org/10.1016/j.matchemphys.2016.03.040.

[125] W. Wang, G. Caetano, W.S. Ambler, J.J. Blaker, M.A. Frade, P. Mandal, C. Diver, P. Bártolo, Enhancing the hydrophilicity and cell attachment of 3D printed PCL/graphene scaffolds for bone tissue engineering, Materials (Basel). 9 (2016) 992. https://doi.org/10.3390/ma9120992.

[126] H. Luo, H. Ao, M. Peng, F. Yao, Z. Yang, Y. Wan, Effect of highly dispersed graphene and graphene oxide in 3D nanofibrous bacterial cellulose scaffold on cell responses: A comparative study, Mater. Chem. Phys. 235 (2019) 121774. https://doi.org/10.1016/j.matchemphys.2019.121774.

[127] W. Su, Z. Wang, J. Jiang, X. Liu, J. Zhao, Z. Zhang, Promoting tendon to bone integration using graphene oxide-doped electrospun poly(lactic-co-glycolic acid) nanofibrous membrane, Int. J. Nanomedicine. 14 (2019) 1835–1847. https://doi.org/10.2147/IJN.S183842.

[128] H. Fang, C. Luo, S. Liu, M. Zhou, Y. Zeng, J. Hou, L. Chen, S. Mou, J. Sun, Z. Wang, A biocompatible vascularized graphene oxide (GO)-collagen chamber with osteoinductive and anti-fibrosis effects promotes bone regeneration in vivo, Theranostics. 10 (2020) 2759–2772. https://doi.org/10.7150/thno.42006.

[129] A.M. Arnold, B.D. Holt, L. Daneshmandi, C.T. Laurencin, S.A. Sydlik, Phosphate graphene as an intrinsically osteoinductive scaffold for stem cell-driven bone regeneration, Proc. Natl. Acad. Sci. U. S. A. 116 (2019) 4855–4860. https://doi.org/10.1073/pnas.1815434116.

[130] D. Ramani, T.P. Sastry, Bacterial cellulose-reinforced hydroxyapatite functionalized graphene oxide: A potential osteoinductive composite, Cellulose. 21 (2014) 3585–3595. https://doi.org/10.1007/s10570-014-0313-4.

[131] S.S.R. Vuppaladadium, T. Agarwal, S. Kulanthaivel, B. Mohanty, C.S. Barik, T.K. Maiti, S. Pal, K. Pal, I. Banerjee, Silanization improves biocompatibility of graphene oxide, Mater. Sci. Eng. C. 110 (2020) 110647. https://doi.org/10.1016/j.msec.2020.110647.

[132] H. Elkhenany, S. Bourdo, S. Hecht, R. Donnell, D. Gerard, R. Abdelwahed, A. Lafont, K. Alghazali, F. Watanabe, A.S. Biris, D. Anderson, M. Dhar, Graphene nanoparticles as osteoinductive and osteoconductive platform for stem cell and bone regeneration, Nanomedicine Nanotechnology, Biol. Med. 13 (2017) 2117–2126. https://doi.org/10.1016/j.nano.2017.05.009.

[133] L. Bacakova, I. Kopova, L. Stankova, J. Liskova, J. Vacik, V. Lavrentiev, A. Kromka, S. Potocky, D. Stranska, Bone cells in cultures on nanocarbonbased materials for potential bone tissue engineering: A review, Phys. Status Solidi. 211 (2014) 2688–2702. https://doi.org/10.1002/pssa.201431402.

[134] I. Rašović, K. Porfyrakis, 2.06 - Functionalisation of fullerenes for biomedical applications, in: Compr. Nanosci. Nanotechnol., Second Edi, 2019: pp. 109–122. https://doi.org/10.1016/B978-0-12-803581-8.11224-X.

[135] M.A. Brady, A. Renzing, T.E.L. Douglas, Q. Liu, S. Wille, M. Parizek, L. Bacakova, A. Kromka, M. Jarosova, G. Godier, P.H. Warnke, Development of composite poly(lactide-co-glycolide)-nanodiamond scaffolds for bone cell growth, J. Nanosci. Nanotechnol. 15 (2015) 1060–1069. https://doi.org/10.1166/jnn.2015.9745.

[136] L. Stankova, J. Musilkova, A. Broz, S. Potocky, A. Kromka, H. Kozak, T. Izak, A. Artemenko, D. Stranska, L. Bacakova, Alterations to the adhesion, growth and osteogenic differentiation of human osteoblast-like cells on nanofibrous polylactide scaffolds with diamond nanoparticles, Diam. Relat. Mater. 97 (2019) 107421. https://doi.org/10.1016/j.diamond.2019.05.007.

[137] G. Lalwani, M. D'Agati, A.M. Khan, B. Sitharaman, Toxicology of graphene-based nanomaterials, Adv. Drug Deliv. Rev. 105 (2016) 109–144. https://doi.org/10.1016/j.addr.2016.04.028.

[138] X. Guo, N. Mei, Assessment of the toxic potential of graphene family nanomaterials, J. Food Drug Anal. 22 (2014) 105–115. https://doi.org/10.1016/j.jfda.2014.01.009.

[139] J. Muller, F. Huaux, N. Moreau, P. Misson, J.F. Heilier, M. Delos, M. Arras, A. Fonseca, J.B. Nagy, D. Lison, Respiratory toxicity of multi-wall carbon nanotubes, Toxicol. Appl. Pharmacol. 207 (2005) 221–231. https://doi.org/10.1016/j.taap.2005.01.008.

[140] A. Fraczek, E. Menaszek, C. Paluszkiewicz, M. Blazewicz, Comparative in vivo

biocompatibility study of single- and multi-wall carbon nanotubes, Acta Biomater. 4 (2008) 1593–1602. https://doi.org/10.1016/j.actbio.2008.05.018.

[141] K.H. Park, M. Chhowalla, Z. Iqbal, F. Sesti, Single-walled Carbon Nanotubes Are a New Class of Ion Channel Blockers, J. Biol. Chem. 278 (2003) 50212–50216. https://doi.org/10.1074/jbc.M310216200.

[142] Y. Zhang, S.F. Ali, E. Dervishi, Y. Xu, Z. Li, D. Casciano, A.S. Biris, Cytotoxicity effects of graphene and single-wall carbon nanotubes in neural phaeochromocytoma-derived pc12 cells, ACS Nano. 4 (2010) 3181–3186. https://doi.org/10.1021/nn1007176.

[143] T. Kolodiazhnyi, M. Pumera, Towards an ultrasensitive method for the determination of metal impurities in carbon nanotubes, Small. 4 (2008) 1476–1484. https://doi.org/10.1002/smll.200800125.

[144] S. Gholizadeh, F. Moztarzadeh, N. Haghighipour, L. Ghazizadeh, F. Baghbani, M.A. Shokrgozar, Z. Allahyari, Preparation and characterization of novel functionalized multiwalled carbon nanotubes/chitosan/β-Glycerophosphate scaffolds for bone tissue engineering, Int. J. Biol. Macromol. 97 (2017) 365–372. https://doi.org/10.1016/j.ijbiomac.2016.12.086.

[145] S. Türk, I. Altınsoy, G. Çelebi Efe, M. Ipek, M. Özacar, C. Bindal, 3D porous collagen/functionalized multiwalled carbon nanotube/chitosan/hydroxyapatite composite scaffolds for bone tissue engineering, Mater. Sci. Eng. C. 92 (2018) 757–768. https://doi.org/10.1016/j.msec.2018.07.020.

[146] E. Silva, L.M.R. de Vasconcellos, B.V.M. Rodrigues, D.M. dos Santos, S.P. Campana-Filho, F.R. Marciano, T.J. Webster, A.O. Lobo, PDLLA honeycomb-like scaffolds with a high loading of superhydrophilic graphene/multi-walled carbon nanotubes promote osteoblast in vitro functions and guided in vivo bone regeneration, Mater. Sci. Eng. C. 73 (2017) 31–39. https://doi.org/10.1016/j.msec.2016.11.075.

[147] M.H. Mirmusavi, P. Zadehnajar, D. Semnani, S. Karbasi, F. Fekrat, F. Heidari, Evaluation of physical, mechanical and biological properties of poly 3-hydroxybutyrate-chitosan-multiwalled carbon nanotube/silk nano-micro composite scaffold for cartilage tissue engineering applications, Int. J. Biol. Macromol. 132 (2019) 822–835. https://doi.org/10.1016/j.ijbiomac.2019.03.227.

[148] N. Li, X. Zhang, Q. Song, R. Su, Q. Zhang, T. Kong, L. Liu, G. Jin, M. Tang, G. Cheng, The promotion of neurite sprouting and outgrowth of mouse hippocampal cells in culture by graphene substrates, Biomaterials. 32 (2011) 9374–9382. https://doi.org/10.1016/j.biomaterials.2011.08.065.

[149] M. Mallick, N. Arunachalam, Electrophoretic deposited graphene based functional coatings for biocompatibility improvement of Nitinol, Thin Solid Films. 692 (2019) 137616. https://doi.org/10.1016/j.tsf.2019.137616.

[150] I. Lasocka, L. Szulc-Dąbrowska, M. Skibniewski, E. Skibniewska, W. Strupinski, I. Pasternak,

H. Kmieć, P. Kowalczyk, Biocompatibility of pristine graphene monolayer: Scaffold for fibroblasts, Toxicol. Vitr. 48 (2018) 276–285. https://doi.org/10.1016/j.tiv.2018.01.028.

[151] K.H. Liao, Y.S. Lin, C.W. MacOsko, C.L. Haynes, Cytotoxicity of graphene oxide and graphene in human erythrocytes and skin fibroblasts, ACS Appl. Mater. Interfaces. 3 (2011) 2607–2615. https://doi.org/10.1021/am200428v.

[152] M. Türk, A.. Deliormanli, Graphene-containing PCL-coated porous B bioactive glass scaffolds for bone regeneration, Mater. Res. Express. 5 (2018) 0–13.

[153] J. Yuan, H. Gao, J. Sui, H. Duan, W.N. Chen, C.B. Ching, Cytotoxicity evaluation of oxidized single-walled carbon nanotubes and graphene oxide on human hepatoma HepG2 cells: An iTRAQ-coupled 2D LC-MS/MS proteome analysis, Toxicol. Sci. 126 (2012) 149–161. https://doi.org/10.1093/toxsci/kfr332.

[154] A.F. Verre, A. Faroni, M. Iliut, C. Silva, C. Muryn, A.J. Reid, A. Vijayaraghavan, Improving the glial differentiation of human schwann-like adipose-derived stem cells with graphene oxide substrates, Interface Focus. 8 (2018) 20180002. https://doi.org/10.1098/rsfs.2018.0002.

[155] M. Heidari, S.H. Bahrami, M. Ranjbar-Mohammadi, P.B. Milan, Smart electrospun nanofibers containing PCL/gelatin/graphene oxide for application in nerve tissue engineering, Mater. Sci. Eng. C. 103 (2019) 109768. https://doi.org/10.1016/j.msec.2019.109768.

[156] J.C. Boga, S.P. Miguel, D. de Melo-Diogo, A.G. Mendonça, R.O. Louro, I.J. Correia, In vitro characterization of 3D printed scaffolds aimed at bone tissue regeneration, Colloids Surfaces B Biointerfaces. 165 (2018) 207–218. https://doi.org/10.1016/j.colsurfb.2018.02.038.

[157] H. Nalvuran, A.E. Elçin, Y.M. Elçin, Nanofibrous silk fibroin/reduced graphene oxide scaffolds for tissue engineering and cell culture applications, Int. J. Biol. Macromol. 114 (2018) 77–84. https://doi.org/10.1016/j.ijbiomac.2018.03.072.

[158] P.R. Sivashankari, M. Prabaharan, Three-dimensional porous scaffolds based on agarose/chitosan/graphene oxide composite for tissue engineering, Int. J. Biol. Macromol. 146 (2020) 222–231. https://doi.org/10.1016/j.ijbiomac.2019.12.219.

[159] R. Singla, C. Sharma, A.K. Shukla, A. Acharya, Toxicity Concerns of Therapeutic Nanomaterials, J. Nanosci. Nanotechnol. 19 (2019) 1889–1907. https://doi.org/10.1166/jnn.2019.16502.

[160] C.M. Sayes, J.D. Fortner, W. Guo, D. Lyon, A.M. Boyd, K.D. Ausman, Y.J. Tao, B. Sitharaman, L.J. Wilson, J.B. Hughes, J.L. West, V.L. Colvin, The differential cytotoxicity of water-soluble fullerenes, Nano Lett. 4 (2004) 1881–1887. https://doi.org/10.1021/nl0489586.

[161] T.E. Biby, N. Prajitha, J. Ashtami, D. Sakthikumar, T. Maekawa, P. V. Mohanan, Toxicity of dextran stabilized fullerene C60 against C6 Glial cells, Brain Res. Bull. 155 (2020) 191–201. https://doi.org/10.1016/j.brainresbull.2019.11.014.

[162] N. Gharbi, M. Pressac, M. Hadchouel, H. Szwarc, S.R. Wilson, [60] Fullerene is an in vivo Powerful Antioxidant With no Acute or Sub-acute Toxicity, Nano Lett. 5 (2005) 2578–2585.

[163] S. Houshyar, G.S. Kumar, A. Rifai, N. Tran, R. Nayak, R.A. Shanks, R. Padhye, K. Fox, A. Bhattacharyya, Nanodiamond/poly-ε-caprolactone nanofibrous scaffold for wound management, Mater. Sci. Eng. C. 100 (2019) 378–387. https://doi.org/10.1016/j.msec.2019.02.110.

[164] S. Houshyar, A. Sarker, A. Jadhav, G.S. Kumar, A. Bhattacharyya, R. Nayak, R.A. Shanks, T. Saha, A. Rifai, R. Padhye, K. Fox, Polypropylene-nanodiamond composite for hernia mesh, Mater. Sci. Eng. C. 111 (2020) 110780. https://doi.org/10.1016/j.msec.2020.110780.

[165] J. Nunes-Pereira, A.R. Silva, C. Ribeiro, S.A.C. Carabineiro, J.G. Buijnsters, S. Lanceros-Méndez, Nanodiamonds/poly(vinylidene fluoride) composites for tissue engineering applications, Compos. Part B Eng. 111 (2017) 37–44. https://doi.org/10.1016/j.compositesb.2016.12.014.

[166] A.M. Schrand, H. Huang, C. Carlson, J.J. Schlager, E. Osawa, S.M. Hussain, L. Dai, Are diamond nanoparticles cytotoxic?, J. Phys. Chem. B. 111 (2007) 2–7. https://doi.org/10.1021/jp066387v.

[167] C. Martín, K. Kostarelos, M. Prato, A. Bianco, Biocompatibility and biodegradability of 2D materials: Graphene and beyond, Chem. Commun. 55 (2019) 5540–5546. https://doi.org/10.1039/c9cc01205b.

[168] S. Sánchez-González, N. Diban, A. Urtiaga, Hydrolytic degradation and mechanical stability of poly(ε-Caprolactone)/reduced graphene oxide membranes as scaffolds for in vitro neural tissue regeneration, Membranes (Basel). 8 (2018) E12. https://doi.org/10.3390/membranes8010012.

[169] E. Murray, B.C. Thompson, S. Sayyar, G.G. Wallace, Enzymatic degradation of graphene/polycaprolactone materials for tissue engineering, Polym. Degrad. Stab. 111 (2015) 71–77. https://doi.org/10.1016/j.polymdegradstab.2014.10.010.

[170] A. Olad, H. Bakht Khosh Hagh, Graphene oxide and amin-modified graphene oxide incorporated chitosan-gelatin scaffolds as promising materials for tissue engineering, Compos. Part B Eng. 162 (2019) 692–702. https://doi.org/10.1016/j.compositesb.2019.01.040.

[171] P.R. Sivashankari, A. Moorthi, K.M. Abudhahir, M. Prabaharan, Preparation and characterization of three-dimensional scaffolds based on hydroxypropyl chitosan-graft-graphene oxide, Int. J. Biol. Macromol. 110 (2018) 522–530. https://doi.org/10.1016/j.ijbiomac.2017.11.033.

[172] A. Rajan Unnithan, A. Ramachandra Kurup Sasikala, C.H. Park, C.S. Kim, A unique scaffold for bone tissue engineering: An osteogenic combination of graphene oxide–hyaluronic acid–chitosan with simvastatin, J. Ind. Eng. Chem. 46 (2017) 182–191. https://doi.org/10.1016/j.jiec.2016.10.029.

[173] S. Saravanan, A. Chawla, M. Vairamani, T.P. Sastry, K.S. Subramanian, N. Selvamurugan, Scaffolds containing chitosan, gelatin and graphene oxide for bone tissue regeneration in vitro and in vivo, Int. J. Biol. Macromol. 104 (2017) 1975–1985. https://doi.org/10.1016/j.ijbiomac.2017.01.034.

[174] A.M. Pandele, M. Ionita, L. Crica, E. Vasile, H. Iovu, Novel Chitosan-poly(vinyl alcohol)/graphene oxide biocomposites 3D porous scaffolds, Compos. Part B Eng. 126 (2017) 81–87. https://doi.org/10.1016/j.compositesb.2017.06.010.

[175] B. Joddar, E. Garcia, A. Casas, C.M. Stewart, Development of functionalized multi-walled carbon-nanotube-based alginate hydrogels for enabling biomimetic technologies, Sci. Rep. 6 (2016) 32456. https://doi.org/10.1038/srep32456.

[176] ISO / ASTM 52900:2021, Standard Terminology for Additive Manufacturing - General Principles - Terminology, ASTM International, West Conshohocken, PA, 2021.

[177] H. Qu, Additive manufacturing for bone tissue engineering scaffolds, Mater. Today Commun. (2020) 101024. https://doi.org/10.1016/j.mtcomm.2020.101024.

[178] S. Singamneni, R. Velu, M.P. Behera, S. Scott, P. Brorens, D. Harland, J. Gerrard, Selective laser sintering responses of keratin-based bio-polymer composites, Mater. Des. 183 (2019) 108087. https://doi.org/10.1016/j.matdes.2019.108087.

[179] S. Bose, D. Ke, H. Sahasrabudhe, A. Bandyopadhyay, Additive manufacturing of biomaterials, Prog. Mater. Sci. 93 (2018) 45–111. https://doi.org/10.1016/j.pmatsci.2017.08.003.

[180] C.W. Hull, Apparatus for production of three-dimensional objects by stereolithography, 4575330, 1986.

[181] N. Zhu, Y. Hou, W. Yang, G. Wen, C. Zhong, D. Wang, Y. Liu, L. Zhang, Preparation of complex SiOC ceramics by a novel photocurable precursor with liquid crystal display (LCD) 3D printing technology, J. Eur. Ceram. Soc. In Press (2022). https://doi.org/10.1016/j.jeurceramsoc.2022.02.026.

[182] D.J. Riley, V. Bavastrello, U. Covani, A. Barone, C. Nicolini, An in-vitro study of the sterilization of titanium dental implants using low intensity UV-radiation, Dent. Mater. 21 (2005) 756–760. https://doi.org/10.1016/j.dental.2005.01.010.

[183] F.P.W. Melchels, J. Feijen, D.W. Grijpma, A poly(D,L-lactide) resin for the preparation of tissue engineering scaffolds by stereolithography, Biomaterials. 30 (2009) 3801–3809. https://doi.org/10.1016/j.biomaterials.2009.03.055.

[184] M.N. Cooke, J.P. Fisher, D. Dean, C. Rimnac, A.G. Mikos, Use of Stereolithography to Manufacture Critical-Sized 3D Biodegradable Scaffolds for Bone Ingrowth, J. Biomed. Mater. Res. - Part B Appl. Biomater. 64B (2003) 65–69. https://doi.org/10.1002/jbm.b.10485.

[185] K. Gnanasekaran, T. Heijmans, S. van Bennekom, H. Woldhuis, S. Wijnia, G. de With, H. Friedrich, 3D printing of CNT- and graphene-based conductive polymer nanocomposites by fused deposition modeling, Appl. Mater. Today. 9 (2017) 21–28. https://doi.org/10.1016/j.apmt.2017.04.003.

[186] X. Wei, D. Li, W. Jiang, Z. Gu, X. Wang, Z. Zhang, Z. Sun, 3D Printable Graphene Composite, Sci. Rep. 5 (2015) 11181. https://doi.org/10.1038/srep11181.

[187] S. Dul, L. Fambri, A. Pegoretti, Fused deposition modeling with ABS-graphene nanocomposites, Compos. Part A Appl. Sci. Manuf. 85 (2016) 181–191. https://doi.org/10.1016/j.compositesa.2016.03.013.

[188] M. Savaris, V. dos Santos, R.N. Brandalise, Influence of different sterilization processes on the properties of commercial poly(lactic acid), Mater. Sci. Eng. C. 69 (2016) 661–667. https://doi.org/10.1016/j.msec.2016.07.031.

[189] G. Shi, S.E. Lowe, A.J.T. Teo, T.K. Dinh, S.H. Tan, J. Qin, Y. Zhang, Y.L. Zhong, H. Zhao, A versatile PDMS submicrobead/graphene oxide nanocomposite ink for the direct ink writing of wearable micron-scale tactile sensors, Appl. Mater. Today. 16 (2019) 482–492. https://doi.org/10.1016/j.apmt.2019.06.016.

[190] K. Chizari, M.A. Daoud, A.R. Ravindran, D. Therriault, 3D Printing of Highly Conductive Nanocomposites for the Functional Optimization of Liquid Sensors, Small. 12 (2016) 6076–6082. https://doi.org/10.1002/smll.201601695.

[191] Y. Zhang, L. Hao, M.M. Savalani, R.A. Harris, K.E. Tanner, Characterization and dynamic mechanical analysis of selective laser sintered hydroxyapatite-filled polymeric composites, J. Biomed. Mater. Res. - Part B Appl. Biomater. 86A (2008) 607–616. https://doi.org/10.1002/jbm.a.31622.

[192] Y. Chunze, S. Yusheng, Y. Jinsong, L. Jinhui, A nanosilica/nylon-12 composite powder for selective laser sintering, J. Reinf. Plast. Compos. 28 (2009) 2889–2902. https://doi.org/10.1177/0731684408094062.

[193] H. Chung, S. Das, Functionally graded Nylon-11/silica nanocomposites produced by selective laser sintering, Mater. Sci. Eng. A. 487 (2008) 251–257. https://doi.org/10.1016/j.msea.2007.10.082.

[194] A.D. Valino, J.R.C. Dizon, A.H. Espera, Q. Chen, J. Messman, R.C. Advincula, Advances in 3D printing of thermoplastic polymer composites and nanocomposites, Prog. Polym. Sci. 98 (2019) 101162. https://doi.org/10.1016/j.progpolymsci.2019.101162.

[195] D. Drummer, M. Medina-Hernández, M. Drexler, K. Wudy, Polymer powder production for laser melting through immiscible blends, Procedia Eng. 102 (2015) 1918–1925. https://doi.org/10.1016/j.proeng.2015.01.332.

[196] S.-J. Lee, W. Zhu, M. Nowicki, G. Lee, D.N. Heo, J. Kim, Y.Y. Zuo, L.G. Zhang, 3D printing nano conductive multi-walled carbon nanotube scaffolds for nerve regeneration, J. Neural Eng. 15 (2018) 016018.

[197] C. Sciancalepore, F. Moroni, M. Messori, F. Bondioli, Acrylate-based silver nanocomposite by simultaneous polymerization–reduction approach via 3D stereolithography, Compos. Commun. 6 (2017) 11–16. https://doi.org/10.1016/j.coco.2017.07.006.

[198] Z. Feng, Y. Li, L. Hao, Y. Yang, T. Tang, D. Tang, W. Xiong, Graphene-Reinforced Biodegradable Resin Composites for Stereolithographic 3D Printing of Bone Structure Scaffolds, J. Nanomater. (2019) 1–13. https://doi.org/10.1155/2019/9710264.

[199] J.R.C. Dizon, Q. Chen, A.D. Valino, R.C. Advincula, Thermo-mechanical and swelling properties of three-dimensional-printed poly (ethylene glycol) diacrylate/silica nanocomposites, MRS Commun. 9 (2018) 209–217. https://doi.org/10.1557/mrc.2018.188.

[200] Z. Feng, Y. Li, C. Xin, D. Tang, W. Xiong, H. Zhang, Fabrication of Graphene-Reinforced Nanocomposites with Improved Fracture Toughness in Net Shape for Complex 3D Structures via Digital Light Processing, J. Carbon Res. 5 (2019) c5020025.

[201] S. Bose, C. Koski, A.A. Vu, Additive manufacturing of natural biopolymers and composites for bone tissue engineering, Mater. Horizons. 7 (2020) 2011–2027. https://doi.org/10.1039/d0mh00277a.

[202] H.S. Sofi, R. Ashraf, M.A. Beigh, F.A. Sheikh, Scaffolds Fabricated from Natural Polymers/Composites by Electrospinning for Bone Tissue Regeneration, Adv. Exp. Med. Biol. 1078 (2018) 49–78. https://doi.org/10.1007/978-981-13-0950-2_4.

[203] I. Subuki, N. Adnan, R.W. Sharudin, Biodegradable scaffold of natural polymer and hydroxyapatite for bone tissue engineering: A short review, AIP Conf. Proc. 2031 (2018) 020019. https://doi.org/10.1063/1.5066975.

[204] P. Chocholata, V. Kulda, V. Babuska, Fabrication of scaffolds for bone-tissue regeneration, Materials (Basel). 12 (2019) 568. https://doi.org/10.3390/ma12040568.

[205] B. Guo, P.X. Ma, Synthetic biodegradable functional polymers for tissue engineering: A brief review, Sci. China Chem. 57 (2014) 490–500. https://doi.org/10.1007/s11426-014-5086-y.

[206] C. Migliaresi, A. Motta, L. Rojo, B. Vázquez, J. Román, Biomaterials for Scaffolds: Synthetic Polymers, in: Scaffolds Tissue Eng., 2014: pp. 263–300. https://doi.org/10.1201/b15649-9.

[207] N.A. Chartrain, C.B. Williams, A.R. Whittington, A review on fabricating tissue scaffolds using vat photopolymerization, Acta Biomater. 74 (2018) 90–111. https://doi.org/10.1016/j.actbio.2018.05.010.

[208] A. George, M.R. Sanjay, R. Srisuk, J. Parameswaranpillai, S. Siengchin, A comprehensive review on chemical properties and applications of biopolymers and their composites, Int. J. Biol. Macromol. 154 (2020) 329–338. https://doi.org/10.1016/j.ijbiomac.2020.03.120.

[209] Y. Wen, S. Xun, M. Haoye, S. Baichuan, C. Peng, L. Xuejian, Z. Kaihong, Y. Xuan, P. Jiang, L. Shibi, 3D printed porous ceramic scaffolds for bone tissue engineering: A review, Biomater. Sci. 5 (2017) 1690–1698. https://doi.org/10.1039/c7bm00315c.

[210] H. Jodati, B. Yılmaz, Z. Evis, A review of bioceramic porous scaffolds for hard tissue applications: Effects of structural features, Ceram. Int. Im press (2020). https://doi.org/10.1016/j.ceramint.2020.03.192.

[211] T. Tanaka, H. Komaki, M. Chazono, S. Kitasato, A. Kakuta, S. Akiyama, K. Marumo, Basic research and clinical application of Beta-tricalcium phosphate (β-TCP), Morphologie. 101 (2017) 164–172. https://doi.org/10.1016/j.morpho.2017.03.002.

[212] K. Lin, J. Chang, Structure and properties of hydroxyapatite for biomedical applications, Woodhead Publishing Series in Biomaterials, 2015. https://doi.org/10.1016/b978-1-78242-033-0.00001-8.

[213] C. Wu, J. Chang, Degradation, Bioactivity, and Cytocompatibility of Diopside, Akermanite, and Bredigite Ceramics, J. Biomed. Mater. Res. Part B Appl. Biomater. 83 (2007) 153–160. https://doi.org/10.1002/jbmb.

[214] S.F. Melo, S.C. Neves, A.T. Pereira, I. Borges, P.L. Granja, F.D. Magalhães, I.C. Gonçalves, Incorporation of graphene oxide into poly(ε-caprolactone) 3D printed fibrous scaffolds improves their antimicrobial properties, Mater. Sci. Eng. C. 109 (2020) 110537. https://doi.org/10.1016/j.msec.2019.110537.

[215] J.M. Unagolla, A.C. Jayasuriya, Enhanced cell functions on graphene oxide incorporated 3D printed polycaprolactone scaffolds, Mater. Sci. Eng. C. 102 (2019) 1–11. https://doi.org/10.1016/j.msec.2019.04.026.

[216] H. Belaid, S. Nagarajan, C. Teyssier, C. Barou, J. Barés, S. Balme, M. Bechelany, Development of new biocompatible 3D printed graphene oxide-based scaffolds, Mater. Sci. Eng. C. 110 (2020) 110595. https://doi.org/10.1016/j.snb.2019.127177.

[217] W. Wang, B. Huang, J.J. Byun, P. Bártolo, Assessment of PCL/carbon material scaffolds for bone regeneration, J. Mech. Behav. Biomed. Mater. 93 (2019) 52–60. https://doi.org/10.1016/j.jmbbm.2019.01.020.

[218] S. Sayyar, M. Bjorninen, S. Haimi, S. Miettinen, K. Gilmore, D. Grijpma, G. Wallace, UV cross-linkable graphene/poly(trimethylene carbonate) composites for 3D printing of electrically conductive scaffolds, ACS Appl. Mater. Interfaces. 8 (2016) 31916–31925. https://doi.org/10.1021/acsami.6b09962.

[219] S. Dul, L. Fambri, A. Pegoretti, Fused deposition modelling with ABS-graphene nanocomposites, Compos. Part A Appl. Sci. Manuf. 85 (2016) 181–191. https://doi.org/10.1016/j.compositesa.2016.03.013.

[220] F. Alam, K.M. Varadarajan, S. Kumar, 3D printed polylactic acid nanocomposite scaffolds for tissue engineering applications, Polym. Test. 81 (2020) 106203. https://doi.org/10.1016/j.polymertesting.2019.106203.

[221] B. Huang, C. Vyas, I. Roberts, Q.A. Poutrel, W.H. Chiang, J.J. Blaker, Z. Huang, P. Bártolo, Fabrication and characterisation of 3D printed MWCNT composite porous scaffolds for bone regeneration, Mater. Sci. Eng. C. 98 (2019) 266–278. https://doi.org/10.1016/j.msec.2018.12.100.

[222] B. Huang, C. Vyas, J.J. Byun, M. El-Newehy, Z. Huang, P. Bártolo, Aligned multi-walled carbon nanotubes with nanohydroxyapatite in a 3D printed polycaprolactone scaffold stimulates osteogenic differentiation, Mater. Sci. Eng. C. 108 (2020) 110374. https://doi.org/10.1016/j.msec.2019.110374.

[223] A.E. Jakus, E.B. Secor, A.L. Rutz, S.W. Jordan, M.C. Hersam, R.N. Shah, Three-dimensional printing of high-content graphene scaffolds for electronic and biomedical applications, ACS

Nano. 9 (2015) 4636–4648. https://doi.org/10.1021/acsnano.5b01179.

[224] P. Feng, J. Jia, S. Peng, W. Yang, S. Bin, C. Shuai, Graphene oxide-driven interfacial coupling in laser 3D printed PEEK/PVA scaffolds for bone regeneration, Virtual Phys. Prototyp. (2020). https://doi.org/10.1080/17452759.2020.1719457.

[225] C. Shuai, Y. Yang, P. Feng, S. Peng, W. Guo, A. Min, C. Gao, A multi-scale porous scaffold fabricated by a combined additive manufacturing and chemical etching process for bone tissue engineering, Int. J. Bioprinting. 4 (2018) 1–12. https://doi.org/10.18063/IJB.v4i2.133.

[226] C. Shuai, W. Guo, P. Wu, W. Yang, S. Hu, Y. Xia, P. Feng, A graphene oxide-Ag co-dispersing nanosystem: Dual synergistic effects on antibacterial activities and mechanical properties of polymer scaffolds, Chem. Eng. J. 347 (2018) 322–333. https://doi.org/10.1016/j.cej.2018.04.092.

[227] P. Feng, Y. Kong, L. Yu, Y. Li, C. Gao, S. Peng, H. Pan, Z. Zhao, C. Shuai, Molybdenum disulfide nanosheets embedded with nanodiamond particles: co-dispersion nanostructures as reinforcements for polymer scaffolds, Appl. Mater. Today. 17 (2019) 216–226. https://doi.org/10.1016/j.apmt.2019.08.005.

CHAPTER 3

MATERIALS AND TECHNIQUES

Table of Contents

During the doctoral thesis, a commercial acrylic resin was used to optimize the dispersion, SLA printing and post-printing processes with GBN. It was a commercial resin that was not certified as biocompatible. This resin was selected because when this thesis started, there were not resins certified as biocompatible commercially available. Acrylic resin was modified with three different graphene-based nanomaterials, which differed in the exfoliation degree (size) and the surface functionalization.

In this chapter, the used materials and their composition are described in detail. In the second section of this chapter, the focus is on the techniques used during the development of the experimental research. The first two subsections explain the preparation of the mixtures and the obtention of the solid samples that were subjected to the tests explained in the following subsections. These tests were divided into five categories: thermal, physico-chemical, micro- and nanoscopic analysis, mechanical and biological.

3.1. Materials

3.1.1. Acrylic resin

The resin used for SLA was a commercial photocurable acrylic-based resin Formlabs Clear FLGPCL4 (Formlabs, Somerville, MA, USA), whose composition is shown in Table 3.1. From now on, this resin will be called R.

Table 3.1. *Acrylic resin composition according to manufacturer data sheet.*

Component	*Weight %*
Urethane dimethacrylate (CAS No: 72869-86-4)	55-75
Methacrylate Monomer(s) (CAS No: Trade secret)	15-25
TPO* Photoinitiator (CAS No: 75980-60-8)	<0.9

* Diphenyl(2,4,6-trimethylbenzoyl)phosphine oxide

In Figure 3.1, the chemical structure of the main resin component is shown.

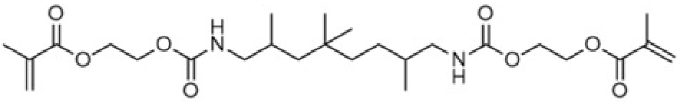

Figure 3.1. *Chemical structure of urethane dimethacrylate.*

3.1.2. Graphene-Based Nanomaterials

Three different Graphene-Based Nanomaterials (GBN) were used in this thesis: Graphene, Graphene Oxide, and Graphite Nanoplatelets. Its main characteristics are shown in Table 3.2.

Table 3.2. *Different GBN used and their characteristics according to manufacturer data sheet.*

GBN	***Average lateral size (µm)***	***Thickness***	***Supplier***
Graphene (G)	2-4	1-2 sheets	Avanzare Nanotechnology (La Rioja, Spain)
Graphene Oxide (GO)	4-8	0.7-1.2 nm	NanoInnova Technologies (Toledo, Spain)
Slightly* Oxidized Graphite Nanoplatelets (GoxNP)	2-3	< 5 sheets	NanoInnova Technologies (Toledo, Spain)

*The oxygen content of GoxNP is < 2 wt.%.

SEM images of the different GBN are shown in Figure 3.2. The lateral size of the different GBN given by the manufacturer in the datasheet corresponded to the size measured by SEM.

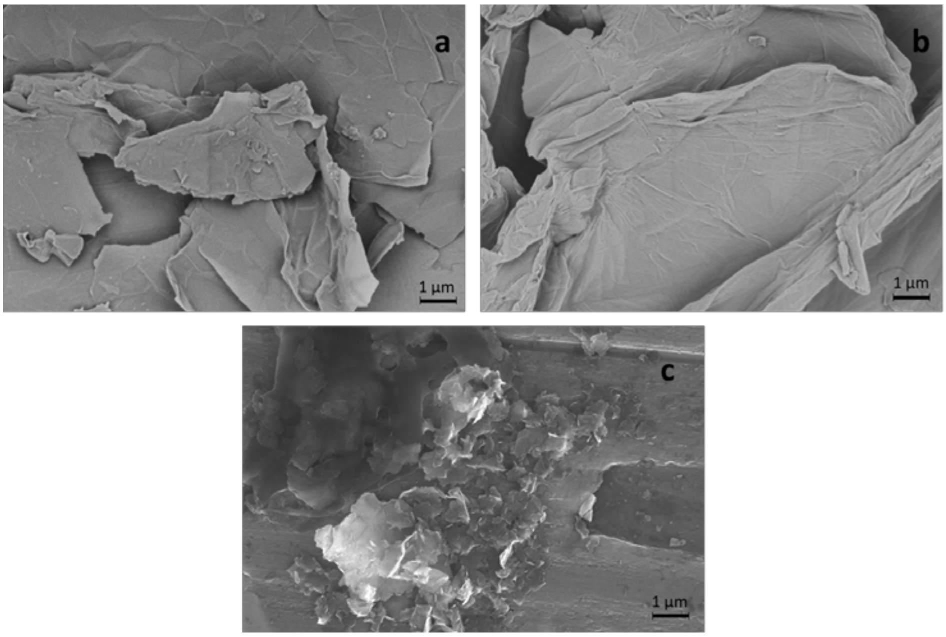

Figure 3.2. *SEM images of the different GBN: G (a), GO (b) and GoxNP (c).*

3.1.3. Reagents

In addition to resins and GBN, some chemical reagents were used to prepare the samples and to carry out some tests:

- Isopropyl alcohol (IPA) supplied by PanReac AppliChem (Castellar del Valles, Spain) was used to clean samples after printing.

- Phosphate buffered saline (PBS) tablets supplied by Sigma Aldrich (UK) was used to carry out biodegradability tests.
- Methyl methacrylate (MMA) supplied by Sigma Aldrich (UK) was used to reduce acrylic resin viscosity and to improve the dispersion of GBN.
- Industrial methylated spirit (IMS) supplied by Fisher Scientific (UK) and diluted to 70% was used to clean and sterilized samples in cell culture lab.
- Minimum essential medium eagle (MEM) alpha modification, with sodium bicarbonate, without L-glutamine, ribonucleosides and desoxyribonucleosis supplied by Sigma Aldrich (UK) was used to prepare cell media.
- Fetal bovine serum (FBS) supplied by Biosera (Nuaille, France) was added to MEM to prepare cell media.
- L-glutamine supplied by Sigma Aldrich (UK) was the carbon source in the cell media.
- Penicillin/streptomycin supplied by Sigma Aldrich (UK) was the last component of cell media. It was a solution with 10,000 units penicillin and 10 mg streptomycin/mL.
- Trypsin-EDTA solution (0.25%) supplied by Sigma Aldrich (UK) was used to collect cells from the flask. Its function is to detach cells from the surface by attacking proteins.
- Dimethyl sulfoxide (DMSO) supplied by Sigma Aldrich (UK) was used to avoid ice crystals formation during the freezing of cells.
- Dubecco's phosphate buffered saline (DPBS) supplied by Sigma Aldrich (UK) was used to completely remove media from cell culture flasks.
- Resazurin sodium salt (Alamar blue) supplied by BioLegend (San Diego, USA) was used to evaluate cell viability on the samples surface.
- Calcein-AM supplied by Fisher Scientific (UK) was used for the cell viability tests.
- Propidium iodide (PI) supplied by Sigma Aldrich (UK) was used for cell viability tests. Images were taken after staining of samples with Calcein-AM and PI.

3.2. Experimental Techniques

3.2.1. Dispersion of nanomaterials

To prepare the nanocomposites, different techniques to disperse and mix them with the resin were used. Here, equipment is presented, but the experimental procedure and the load used will be explained in the corresponding chapter (Chapter 4).

3.2.1.1. Ultrasonication

One of the methods employed to disperse nanofillers was ultrasonication by probe. In this thesis, Branson 450 (Branson Ultrasonics Corp., CT., USA) was used. The frequency range applied was 1,985-2,050 kHz at a 50% amplitude.

Ultrasounds were applied in 10 ± 0.5 min intervals - pulses of 10 ± 0.5 s on and 30 ± 0.5 s off. Besides, the solution was placed in an ice bath (6 ± 2 °C) to avoid the overheating. On-Off cycles were previously optimized by Paz et al [1] to assure that overheating did not occur.

3.2.1.2. Degassing equipment

After mixing and dispersion, degassing process was carried out in order to avoid the presence of air in the mixture that could affect to the printing process and the final properties obtained. This process consisted of two steps:

1) Ultrasounds bath: mixture was placed in an ultrasonic bath (Elmasonic p60h, Elma Schmidbauer GmbH, Germany) for 15 ± 0.5 min.
2) Vacuum application: after US bath, vacuum was applied in a vacuum drying oven (Vaciotem-T, Selecta, Spain) for 15 ± 0.5 min.

3.2.2. Preparation of samples

Samples were prepared by two different methods: compression molding using a hot plates press and 3D printing.

3.2.2.1. UV lamp

Prior to some tests, samples were subjected to UV exposure. To do that, an UV LED lamp of 358 mW/cm^2 of light power and 405 nm of wavelength, supplied by Sovol (Shenzhen, Guangdong, China) was used.

3.2.2.2. Hot Plates Press

To obtain samples by compression molding, Fontijne LabEcon 300 (Fontijne Grotnes B.V., Vlaardingen, The Netherlands) was used. Liquid resin was poured into a silicone mold with dog bone shape and it was placed between two aluminum plates to assure the same pressure on the mold surface. Pressure was set at 1.8 MPa to avoid the break of the mold and temperature was set at 160°C to the acrylic resin.

3.2.2.3. SLA Printer

Acrylic resin samples were printed with SLA printer Form 2 (Formlabs, Somerville, MA, USA). The layer thickness was set at 100, 50 or 25 μm, depending on the experiment, and the exposure time was adjusted depending on the sample. G do not allow to obtain printed structures using the same exposure time than R. For that reason, for samples R+G, exposure time was increased by 8.9 %, which is the exposure time for standard black resin.

3.2.2.4. Postprocessing of printed samples

Cleaning

After printing, samples needed to be cleaned with Isopropyl Alcohol (IPA) in FormWash (Formlabs, Somerville, MA, USA) equipment. It consists of a tank full of IPA where ultrasounds are applied to improve the cleaning of the samples. The time inside FormWash was optimized.

Post-curing

After cleaning, SLA printed samples were subjected to a postcuring process in FormCure chamber (Formlabs, Somerville, MA, USA). In this chamber, heat and UV is applied to finish the polymerization process that has been started in the printer. Manufacturers of Acrylic resin recommended to carry out this post-treatment.

Annealing

Annealing of printed samples was explored to release internal stresses and improve mechanical properties. Annealing was carried out in the drying oven (Vaciotem-T, Selecta, Spain) at atmospheric pressure and 100°C for 12 hours, as recommended by Manapat et al [2].

3.2.3. Jacobs' working curve

Jacobs' working curve was used to analyze the behavior of light when it penetrated inside the resin. It gave information about the penetration of light and the energy needed to polymerize the liquid resin. The power of light decreased when depth increased, following a Beer-Lambert relationship (Eq. 3.1):

$$P_z = P_0 \cdot e^{-z/D_p} \tag{3.1}$$

Where P_0 and P_z is the power of light (mW/cm^2) at the surface and at some depth z, respectively, and D_p is the depth where the penetrating light intensity falls 1/e of P_0. Writing Eq. 3.1 in terms of energy instead of power, Jacobs' working curve equation (Eq. 3.2) is obtained [3].

$$C_d = D_p \cdot ln\left[\frac{E_0}{E_c}\right] \tag{3.2}$$

Being C_d the cured depth, E_0 the energy of the light at the surface and E_c the "critical" energy needed to start the polymerization.

Liquid mixtures were placed in small trays and the UV lamp was placed at 45 mm from the resin surface. Cured surfaces were cleaned with IPA in the FormWash for 3 minutes and, once cleaned, the thickness was measured with a caliper with a precision of 0.01 mm. Exposure time was 3, 5, 10 and 15 s. At least, six measurements were done for each sample and they were averaged. In all cases, the coefficients of determination (R^2) of the regression line were higher than 0.99.

The power (P_0) of the UV lamp used was 358 mW/cm^2. From this known information, it was possible to calculate the energy for different exposure times (Eq. 3.3).

$$E_0 = P_0 \cdot t \tag{3.3}$$

From Jacobs' working curve equation (Eq. 3.2), if C_d vs $\ln(E_0)$ was plotted, it was possible to obtain D_P and E_c. D_P corresponded with the slope of the line, whilst E_c was calculated from the intersection with x-axis, knowing that it was plotted as the natural logarithm.

Another useful parameter was the volume efficiency, γ_V. It was used to evaluate the effectiveness of the polymerization, and it could be calculated from the parameters previously introduced following Eq. 3.4 [4]:

$$\gamma_V = \frac{D_p}{E_c} \tag{3.4}$$

3.2.4. *Thermal characterization*

To carry out the thermal studies, i.e. polymerization degree, glass transition temperatures, polymerization kinetics and thermal conductivity, DSC 882e Mettler Toledo (Greifensee, Switzerland) and STARe software (Mettler Toledo, Greifensee, Switzerland) were used. Samples were placed into aluminum crucibles with a capacity of 40 μL and 50 μm hole in the lid. In all tests, nitrogen was used as the purge gas and was delivered at a rate of 80 mL/min.

3.2.4.1. Thermal and UV polymerization

Thermal polymerization of pristine (R) and reinforced (R+G, R+GO and R+GoxNP) resin was studied with a heating ramp from 20°C to 250°C at 10°C/min. Three tests of each sample were performed and the DSC thermogram of heat flow vs. polymerisation time was obtained.

To study the UV polymerization process and the effect that nanofillers could have on the UV polymerization degree, three samples of the pristine and the reinforced resin were cured inside the Form Cure chamber for different exposure times. The wavelength used for the UV cure was 405 nm, the same value than during the printing of the samples. After UV exposition, DSC analysis was carried out to the samples with a heating ramp from 20°C to 250°C at 10°C/min to complete the cure of the samples.

3.2.4.2. Polymerization kinetics

A drop of 15-20 mg was placed in the DSC crucible and scans from 20 to 250 °C at three different rates (5, 10 and 20 °C/min) were carried out. Activation energy (E_a) of the polymerization process was evaluated by model free kinetic (MFK) method, applied with STARe Software. Firstly, conversion degrees (α) were calculated from the curves obtained at the three different rates. From these values, E_a was calculated as a function of α.

It is important to highlight that activation energy calculated by MFK method changes with the extent of the polymerization. Therefore, it is possible to distinguish between the different stages of the polymerization reaction. Finally, MFK allows to simulate isothermal conditions to obtain the needed time to cure the sample at different temperatures.

3.2.4.3. Glass transition temperature

A scan from 20 to 200 °C was carried out at 20 °C/min. T_g was read in the second scan to have the thermal history erased. It was calculated as the midpoint of the step of the base line through endothermal direction.

3.2.4.4. Thermal conductivity

Thermal conductivity (λ) was measured by means of DSC following the procedure proposed by Hakvoort et al. [5]. As pure metal, gallium was used and silicone oil was applied to improve the contact with the sample, which was cut into cylinders with a height between 1 and 2 mm, and a diameter of 6 mm.

The DSC scan was from 28 to 38 C at 0.5 °C/min, followed by cooling to -5 °C at 10 °C/min to ensure the solidification of the gallium after each measurement. It was calculated according to Eq. 3.5:

$$\lambda = \frac{1}{\left(\frac{1}{S_G} - \frac{1}{S_S}\right)} \frac{h}{A} \tag{3.5}$$

where S_G and S_S are the slopes of the linear side of the melting peak obtained from the heat flow vs. temperature curves for gallium and the sample, respectively; h is the height of the sample, and A, its area.

3.2.5. Physico-Chemical Analysis

To analyze the chemical structure and the interaction with light of resins and their nanocomposites, some techniques were used.

3.2.5.1. Fourier-Transform Infrared Spectroscopy

Infrared spectra were obtained with a Tensor27 Fourier-Transform Infrared (FTIR) spectrometer from Bruker (Bruker Optik GmbH, Madrid, Spain), with attenuated total reflectance (ATR) technique. DuraSample Diamond accessory formed by a 0.5 mm diameter diamond embedded in a ZnSe crystal was used. The ratio signal-to-noise is better than 8000:1 (5.4×10^{-5} noise absorbance). Spectra were recorded with a resolution of 4 cm^{-1} from 4000 to 400 cm^{-1} by taking 32 scans.

Polymerization degree (X) was calculated analyzing the peaks at 1733 and 810 cm^{-1}, corresponding to C=O and C=C, respectively, and using Eq 3.6. I_{liquid} is the intensity of the peak in the corresponding liquid resin.

$$X = \left[1 - \frac{I_{C=C}}{I_{liquid\ C=C}} \cdot \frac{I_{liquid\ C=O}}{I_{C=O}}\right] \cdot 100 \tag{3.6}$$

3.2.5.2. UV-vis Spectrophotometry

Absorbance of the different samples at wavelength of 405 nm was measured by UV-Vis spectroscopy using a Cary 4000 UV-Vis spectrophotometer (Agilent Technologies, Santa Clara, CA, USA). Resin sample was used as reference to study the absorbance of the nanofillers.

3.2.5.3. Nuclear Magnetic Resonance (NMR)

The samples were all ran in deuterated water (D2O) on a Bruker Avance-NEO-400 spectrometer in D2O at 298 K. Samples were left in D2O for at least 24 hours before testing.

3.2.5.4. Viscosity

Viscosity was measured using a rotational viscometer Fungilab Smart Serie (Fungilab, Barcelona, Spain). The measurements were made using a R3 stainless steel spindle at a rotation speed of 100 rpm.

3.2.5.5. Wettability

To determine water contact angle, Dataphysics OCA15 plus goniometer and SCA20 software (DataPhysics Instruments GmbH, Filderstandt, Germany) were used. Drops of 3 µL of deionized water were used to determine contact angle.

3.2.5.6. Density

Density was obtained applying Archimedes' Principle with the Density Kit (Mettler Toledo, Greifensee, Switzerland). The solid was weighed in air (A) and then again (B) in the auxiliary liquid with a known density (distilled water). The density of the solid (d) can be calculated with the Eq. 3.7:

$$d = \frac{A}{A - B}(d_0 - d_L) + d_L \tag{3.7}$$

Where d_0 is the density of the auxiliary liquid, 0.99777 g/cm^3 at 22°C, and d_L is the density of air, 0.0012 g/cm^3.

3.2.6. Micro- and nanoscopic surface analysis

3.2.6.1. Dimensional stability

The effect of the nanofillers on printability and dimensional stability was studied by 3D printing cube samples containing holes of different geometric shapes (i.e., circular and square holes) on their faces in order to determine if the addition of nanoparticles influenced the quality and accuracy of the 3D printed samples. The measurement of the images obtained with the optical microscope was completed with GIMP 2.10.12 software. The background of the image was removed and it was transformed into a binary image. The difference image with the reference (CAD file) was obtained and black and white pixels were counted. Accuracy was obtained using Eq. 3.8 [6]:

$$\% \, Accuracy = \frac{Black\ pixels}{Black\ pixels\ +\ White\ pixels} \cdot 100 \tag{3.8}$$

3.2.6.2. Optical microscopy

To obtain micrographs, Olympus DSX1000 digital microscope (Olympus, Shinjuku, Tokyo, Japan) was used. To observe GBN in the resin matrix, in some cases, polarized light was used.

Besides, this microscope allows to measure roughness of the surfaces with a cut-off of 600 µm. To carry out the measurements, 10x zoom and bright field were used. At least 6 measurements at random directions were done in each sample.

3.2.6.3. Scanning Electron Microscopy

Images of the different GBN and the surfaces were taken by TENEO-LoVac (Eindhoven, Nederland) Field-Emission Scanning Electron Microscope (FE-SEM).

3.2.6.4. Nanoindentation

Nanoindentation measurements were done with Hysitron TI Premier Nanoindenter (Bruker, Dublin, Ireland). A Berkovich tip with a 50 nm of radius was used to carry out these tests. The loading function of nanoindentation is shown in Figure 3.3. It is a trapezoidal loading function with loading and unloading times fixed at 5 s and a holding time at peak load (2400 µN) for 2 s.

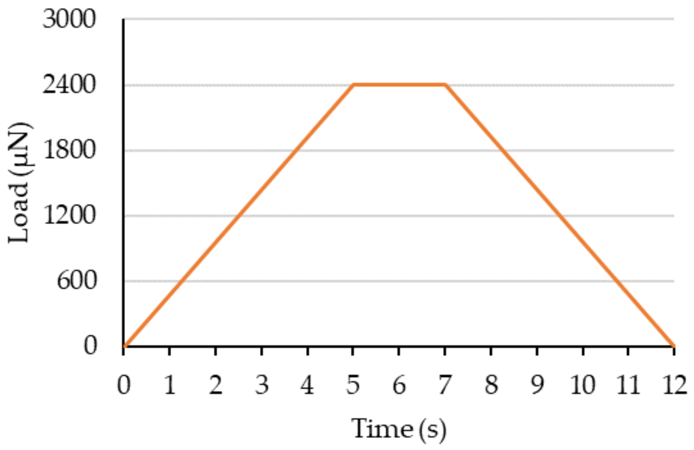

Figure 3.3. *Cycle of nanoindentation.*

Samples used to carry out these tests were parallelepiped of 20x20x5 mm printed with different layer thickness: 100, 50 and 25 µm.

From these measurements, stiffness, hardness and Young's modulus of the samples were obtained and related with polymerization degree.

Stiffness (S) is the derivative of the load (P) with respect to indentation depth (h) in the initial unloading curve. From this value, reduced Young's modulus (E_r) is calculated following Eq. 3.9.

$$E_r = \frac{\sqrt{\pi}}{2\beta\sqrt{A_c}} S \tag{3.9}$$

Where A_c is the contact area, and β is a constant that depends on probe tip geometry.

Besides, hardness (H) was calculated from maximum load (P_{max}) and the contact area (Eq. 3.10).

$$H = \frac{P_{max}}{A_c} \tag{3.10}$$

Prior to indentation, a delay of 1000 s was introduced to avoid artefacts related to inertia of tip motion.

3.2.7. Mechanical Analysis

To evaluate the mechanical performance of the obtained samples, different tests were carried out: hardness, tensile and dynamic mechanical thermal analysis.

3.2.7.1. Hardness

Shore D hardness tester (Bareiss GmbH, Berlin, Germany) was used for hardness measurements, applying 50 N, following the standard UNE-EN ISO 868:2003 [7]. At least, four measurements were taken for each sample.

3.2.7.2. Tensile properties

Standard dog bone samples 1BA from ISO 527-2:2012 [8] were printed and obtained by molding. Tests were conducted using a Universal Testing Machine IBTH/500 (Ibertest, Madrid, Spain) with a load cell of 5 kN, operating at a crosshead speed of 3 mm/min.

3.2.7.3. Dynamic Mechanical Thermal Analysis (DMTA)

Dynamic mechanical thermal characterization (DMTA, TA instrument Q800) was performed with printed rectangular specimens (15.3 x 5.0 x 1.4 mm) in tension mode in a temperature range of 30-225 °C, at a single frequency of 1 Hz and a heating rate of 2 °C/min.

With the data obtained from DMTA, it was possible to calculate the molecular weight between crosslinks in a thermosetting resin. Firstly, storage modulus had to be measured within the rubbery plateau region ($E'_{rubbery}$) and, from that value and applying Eq. 3.11, molecular weight between crosslinks (M_c) could be calculated:

$$M_c = \frac{R \cdot T \cdot d}{E'_{rubbery}} \tag{3.11}$$

Where R is the universal gas constant, T is the absolute temperature at which the modulus was calculated (448 K) and d is the density of the polymer.

3.2.8. Biological Analysis

3.2.8.1. Basal culture media

Basal media without further enrichment was used as the selected medium for cell culture comprised of MEM with 10% of FBS and supplemented with 1% penicillin/streptomycin, and 0.5 g/L L-glutamine was used as the medium for cell culture.

3.2.8.2. Sterilization of samples

To carry out cellular studies, it was necessary to sterilize all the samples. The sterilization process was carried out in two steps:

1) Cleaning with Industrial Methylated Spirit (IMS) 70% for 10 minutes in an ultrasonic bath.
2) UV exposure for 20 minutes inside the fume hood.

As control samples, polyester plastic coverslips (ThermoFisher, D13 mm) were used in all the tests.

3.2.8.3. Cell culture preparation

Mouse osteoblastic precursor cell line (MC3T3-E1, P26) was used to evaluate cell response. First, the retrieval of cells from -80°C was carried our in a water bath at 37°C. Cells were stored with DMSO, which had to be removed by centrifugation (1500 rpm for 5 min). Media was added and cells were transferred to a 175 cm^2 cell culture flask and incubated at 37°C and 5% CO_2. Cells were regularly checked under inverted microscope for growth rate, signs of infection or differentiation.

Every 2 days, media was changed until confluence was around 80%. When it happened, cells were expanded into more flasks until the amount needed was achieved. To expand cells, trypsin was used to detach cells from the flask surface and they were split in different flasks after trypsin removal by centrifugation (1500 rpm for 5 min). Cell counting was done in a haemotocytometer (Marienfeld Superior, Germany) to know the cell concentration and carry out the adequate dilution.

3.2.8.4. Cell viability

Samples used for these tests were disks of 10 mm of diameter and 4 mm thickness. In the case of acrylic resin samples, they were printed, cleaned in IPA for 3 min and postcured with UV at 80°C for 90 min and, in the case of PLA and its nanocomposites, they were cleaned in IPA for 5 min.

After sterilization, samples were placed in 24 well-plates (suspension plates) and they were inoculated with 20,000 osteoblastic cells and incubated for 30 min to allow initial cell adhesion to the surface. Subsequently, 1 mL of culture media was added and cells were cultured for different times (1, 3 and 7 days) at 37°C and 5% CO_2. Two different tests were carried out with these samples:

1) Live/dead staining: two samples for condition was washed with DPBS and stained with 100 µL of calcein-AM and PI solution (1.5 µL of calcein-AM and 10 µL of PI in 1 mL of DPBS). They were incubated for 30 minutes and images were taken with a microscope imaging system (EVOS M5000, Thermo Scientific). Live cells were stained in green and dead cells in red.
2) Alamar Blue: this test detects cellular metabolic activity and is based on the incorporation of an oxidoreduction (REDOX) indicator that shows color change in response to aerobic respiration, which lead to a chemical reduction of the culture medium. The equivalent to 10% of the medium volume of Alamar Blue solution was added together with the culture medium. After 4 hours of incubation, 100 µL were transferred to a 96-well plate. A TECAN Spark plate reader (Tecan Trading AG, Switzerland) at a wavelength of 560 nm excitation and 590 nm emission was used to determine fluorescence and absorbance at 570 nm was measured with the same equipment. Three measurements were done for each of the three samples for each condition.

3.2.8.5. Elusion tests

The objective of these tests was to analyze the cytotoxicity of possible leaching components (residual monomer, photoinitiator, additives, etc). To carry out the tests, the procedure is the following:

1) Sterilize the samples.
2) In a 24 well-plate, add 1mL of fresh media in contact with 4 samples for each condition.
3) Two different ways to obtain the media were explored:
    a. Use 3 different samples, one for each time slot (24, 48 and 72 hours).
    b. Use the same sample, changing the media each day until 3 days:
        i. 24-1: collect eluate after 24h of incubation
        ii. 24-2: removed old media, add fresh media and collect it after 24 h
        iii. 24-3: 24h after 2 washes.

    From these tests, it is possible to know if the component that is released from the sample can be removed.
4) Freeze the collected media.
5) Seed cells in a 96 well-plate (culture plates) with a population of 5,000 cells/well, with fresh media.
6) Incubate for 24 hours at 37°C and 5% CO_2.

7) Change the media for the eluates previously collected.
8) Incubate for 24 hours at 37°C and 5% CO_2.
9) Carry out Live/Dead tests.

3.2.9. Statistical Analysis

The results were also evaluated for statistical significance using a one-way analysis of variance (ANOVA) test with a post-hoc Scheffe´s test (SPSS 20.0 for Windows; IBM SPSS, USA). A p-value lower than 0.05 was indicative of statistical significance.

3.3. References

[1] E. Paz, Y. Ballesteros, F. Forriol, N.J. Dunne, J.C. del Real, Graphene and graphene oxide functionalisation with silanes for advanced dispersion and reinforcement of PMMA-based bone cements, Mater. Sci. Eng. C. 104 (2019) 109946. https://doi.org/10.1016/j.msec.2019.109946.

[2] J.Z. Manapat, J.D. Mangadlao, B.D.B. Tiu, G.C. Tritchler, R.C. Advincula, High-Strength Stereolithographic 3D Printed Nanocomposites: Graphene Oxide Metastability, ACS Appl. Mater. Interfaces. 9 (2017) 10085–10093. https://doi.org/10.1021/acsami.6b16174.

[3] P.F. Jacobs, Fundamentals of stereolithography, Proc. Solid Free Form Symp. (1992) 196–211. https://doi.org/10.1016/0278-6125(93)90311-g.

[4] T. Schlotthauer, D. Nolan, P. Middendorf, Influence of short carbon and glass fibers on the curing behavior and accuracy of photopolymers used in stereolithography, Addit. Manuf. 42 (2021) 102005. https://doi.org/10.1016/j.addma.2021.102005.

[5] G. Hakvoort, L.. van Reijen, Measurement of the thermal conductivity of solid substances by DSC, Thermochim. Acta. 93 (1985) 317–320.

[6] Z.X. Zhou, F. Buchanan, A. Lennon, N. Dunne, Investigating Approaches for Three-Dimensional Printing of Hydroxyapatite Scaffolds for Bone Regeneration, Key Eng. Mater. 631 (2014) 306–311. https://doi.org/10.4028/www.scientific.net/kem.631.306.

[7] UNE-EN ISO 868:2003 Plastics and ebonite - Determination of indentation hardness by means of a durometer (Shore hardness), (2003).

[8] UNE-EN ISO 527-2:2012 Plastics - Determination of tensile properties - Part 2: Test conditions for moulding and extrusion plastics, (2012).

CHAPTER 4

DISPERSION OF GBN: EFFECT ON POLYMERIZATION, PRINTABILITY AND MECHANICAL PROPERTIES

Table of Contents

The objective of this chapter was to explain the importance of the research presented in this thesis. For this, the effect of the GBN on the different properties of the selected photocurable resin were thoroughly studied.

Firstly, to succeed on the manufacturing of samples by SLA, the study of the effect of GBN on printability was necessary, since the presence of GBN change the properties of the resin and may affect its polymerization reaction and, therefore, its printability. Once a good printability was obtained with all the nanofillers, mechanical properties of printed structures were studied. From the obtained results, we realized that a deeper study regarding the polymerization process was necessary and, therefore, polymerization kinetics were carried out (Chapter 5).

This chapter is divided into four sections. The first one is a brief introduction. In the second section, the polymerization reaction of the GBN-reinforced resin was analyzed, then printability was studied. These studies (polymerization and printability) were done with GBN dispersed directly in the resin. However, in view of the results, dispersibility was improved with MMA and finally, mechanical properties of tensile samples with MMA were explored.

Most of the content of this chapter was published in [1].

4.1. Introduction

As explained in Chapter 2, Graphene (G) presents properties that makes its use of very interest in many fields. These properties include high surface area, superior mechanical properties, thermal and electrical conductivity, excellent intrinsic carrier mobility and barrier properties [2,3], to mention some of them. The main limitation of G is its difficulty to be manufactured at scale and its tendency to form agglomerates when being dispersed within a solution [4]. Generally, other G-based nanomaterials, such as graphene oxide (GO) or graphite nanoplatelets (GoxNP), present lower properties than G (in terms of mechanical or electrical properties), but they demonstrate the ability to be manufactured at scale and also can be dispersed more easily in a solution.

To achieve the advantages that nanomaterials offer, it is important to obtain a good dispersion within the matrix materials. Many methods have been investigated to improve the GBN dispersion within the matrix materials and reduce the incidence of agglomerate formation. In order to achieve a good dispersion, it is important to pay particular attention to the methods used for mixing and dispersion, and also chemical functionalization of the GBN.

In terms of mixing and dispersion, techniques like sonication using a soniprobe [5,6] or bath [7], high-shear mixing [8], high-speed disk [9] and calendering processes [10,11] have been commonly applied. When the resin viscosity is too high then ultrasonic or mechanical mixing cannot be applied successfully, therefore it is necessary to reduce the resin viscosity. For this purpose, different solvents have been used, e.g. THF [6], acetone [5,12], isopropanol [7] and water [13]. To improve GBN dispersion, chemical functionalization like polymer grafting [6], self-assembly functionalization [12] and the use of dispersants [13,14] have also successfully applied.

In Vat Photopolymerization technologies, the polymerization of the resin occurs directly during the printing process. Therefore, when a solvent is added to improve dispersion of GBN, it has to be properly removed. If there are traces of solvent in the mixture, it can lead to a reduction in mechanical properties since it can affect polymerization process impeding the crosslinking [15,16]. An alternative for the use of solvents is the dispersion of GBN into the liquid with low-viscosity monomers before curing [17,18].

Currently, GBN have been introduced to AM technology with respect to the fabrication of SLA printed constructs. In terms of Biomedical Engineering applications, GBN have been reported to offer enhanced mechanical properties [15,19–21], promoted cell differentiation [22], and increased hydrophilicity and subsequently improved cell adhesion [23].

However, with respect to SLA and LCD techniques, there is currently a lack of knowledge about the influence of GBNs on the polymerization reaction, but some issues relating to delamination [24] and a reduction in maximum curable thickness per scan [25] have been reported when GBNs have been incorporated into photocurable resins. With the addition of nanomaterials into the resin, a competition takes place in terms of light absorption between the photoinitiator and the nanomaterial. Usually, this competition leads to a less effective UV polymerization process.

Nanomaterials may influence the UV polymerization reaction due to changes in optical properties, which results in variations in absorbance or transmittance of the resin [26,27]. They also can act as light scattering and shielding centers [28]. Besides, the polymerization reaction may be affected by the nanomaterial [29,30] if they act as chain transfer agents, thereby inhibiting polymer chain growth [21], or as free radical scavengers that reduce the extent of polymerization reaction [31,32].

These possible effects on polymerization reaction make a study investigating the influence of nanomaterials on the polymerization reaction of photocurable resins of great importance, especially in the context of efficacious 3D printing, as these modifications can affect printability and the practicality of a particular 3D printing technique. These effect depends on many factors, e.g. type and specific surface area of the nanomaterial – the latter factor affects the extents of shielding, which can affect the degree of polymerization [33].

4.2. Effect of GBN on polymerization of acrylic resin

4.2.1. Experimental Methodology

Chapter 3 provides all the details regarding the methodology used in all the experimentation stages. In this section, particularities of experimental methodology that only applies to this chapter are exposed.

Polymer resin blends containing 0.1 wt.% of each GBN were prepared and homogenously mixed to ensure the full dispersion of the nanomaterial. The wt.%. of nanomaterial used was based on a previous study [18], which reported that 0.1 wt.% of G and GO demonstrated significant improvement in mechanical performance when incorporated into an acrylic-based resin for orthopaedic applications.

Base resin (R) and resin with the different nanofillers (R+G, R+GO and R+GoxNP) were studied in this chapter. The method used to disperse the nanofillers in the resin was via sonication for 30 ± 0.5 min. Degassing process was carried out after the sonication, as described in Section 3.2.1.2.

The extent of the polymerization reaction of the resin and the effect of nanofiller incorporation was determined using Differential Scanning Calorimetry (DSC), testing at least three samples per condition. The acrylic resin can cure via two different mechanisms (or a combination of both): (1) thermal polymerization – by the application of temperature, (2) Ultraviolet (UV) polymerization – by the application of UV light at 405 nm wavelength.

To determine the effect of nanofiller incorporation on these mechanisms, two different DSC tests, already explained in Section 3.2.4.1., were performed: (1) Thermal polymerization: from these tests, the effect of nanofillers on Thermal Polymerization Energy (E_{total}) and Polymerization Temperature was studied. The E_{total} expressed in J/g was determined as the area under the heat flow versus polymerisation time curve. (2) UV polymerization: the degree of UV polymerization was studied by subjecting the sample to different exposure times and completing the cure by thermal energy. In this scan a first peak appeared due to the crystallization or crosslinking of the UV-cured resin. The area of this peak will be referred to as E_{UV}. By knowing the total energy for thermal polymerization (E_{total}) and the energy needed to complete polymerization after UV (E_{tc}), polymerization degree due to UV radiation may be calculated (Eq. 4.1).

$$Polymerization\ degree\ (\%) = \frac{E_{total} - E_{tc}}{E_{total}} \cdot 100 \tag{4.1}$$

FTIR spectra at different UV polymerization times, prepared as previously explained, were normalised from the peak of $–CH_3$ symmetric stretching (1,375 cm^{-1}), and the polymerization process was followed by observing the reduction of the C=C peak (1,636 cm^{-1}) [34]. These peaks were selected because $–CH_3$ did not change during the polymerization process, and C=C was the bond that changes during this process. Furthermore, Shore D hardness was measured for samples as a function of different UV exposure times.

4.2.2. Results

In this section, results are exposed, but they will be discussed in depth in the following section.

4.2.2.1. Thermal polymerization

It can be noted that the required energy (E_{total}), calculated by measuring the area under the polymerization peak (Figure 4.1), is similar for all material formulations investigated, being all the values in the range from 21.2 to 22.0 J/g. Peak temperatures (polymerization temperatures) are between 179-185 °C, being the values also similar for all resins (Table 4.1). A small shoulder appeared around 120°C, which could correspond to a glass transition. A possible explanation could be that a small part of the resin was polymerized during the sonication process, but it was negligible. The most marked glass transition was found for R+GO sample, probably because of the catalysis effect that was found in Chapter 5.

Table 4.1. *Polymerization energy (mean value ± SD) and Polymerization temperature (mean value ± SD) of R, R+G, R+GO, R+GoxNP.*

Material Type	*Polymerization energy ($J \cdot g^{-1}$)*	*Polymerization temperature (°C)*
R	22.0 ± 2.3	179 ± 3
R+G	21.6 ± 1.8	183 ± 2
R+GO	21.2 ± 1.6	185 ± 4
R+GoxNP	21.6 ± 2.2	179 ± 3

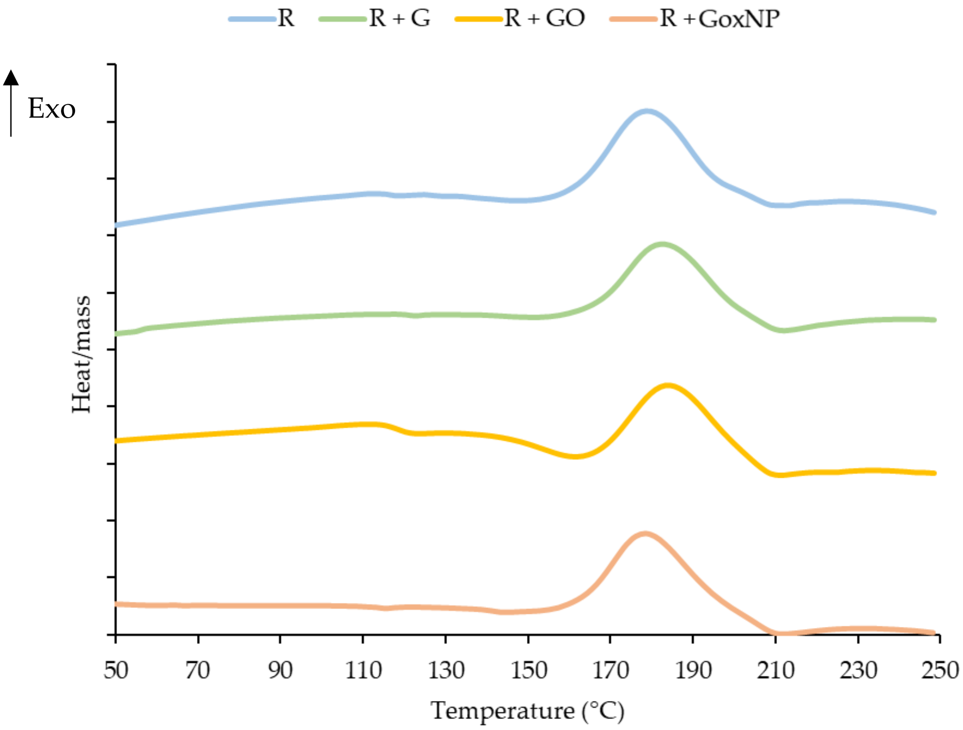

Figure 4.1. *DSC thermograms of R, R+G, R+GO, R+GoxNP.*

4.2.2.2. UV polymerization

DSC and FTIR analysis

To compare the effect of applying different UV-light times during resin polymerization and as example, base resin DSC curves are shown in Figure 4.2. It can be observed that, when samples are irradiated with UV light, DSC curves show two exothermic peaks, the first one was between 70-84 °C, and the second one between 146-166 °C, depending on the UV exposure time. To the best of our knowledge, there were no similar studies using photocurable polymers, however, Vicard et al. [35] reported DSC curves of polymerization-crystallization process of polyamides. They reported a first exothermic peak of polymerization, followed by another exothermic peak that corresponds to the crystallization of the polymer formed in the previous peak. In the case of the resin used in this study, it was a thermosetting polymer, which could not crystallize. The process that the cured resin could carry out was crosslinking.

In this study, there was some cured polymer from the beginning of the DSC test due to the previous UV exposition (DSC curves were obtained after the UV radiation; then, samples were already pre-polymerized when DSC experiments began). Therefore, the first peak could be assigned to the crosslinking of the UV cured polymer (UV-peak), whilst the second peak could be due to the thermal polymerization of the non-UV polymerized resin (thermal-peak).

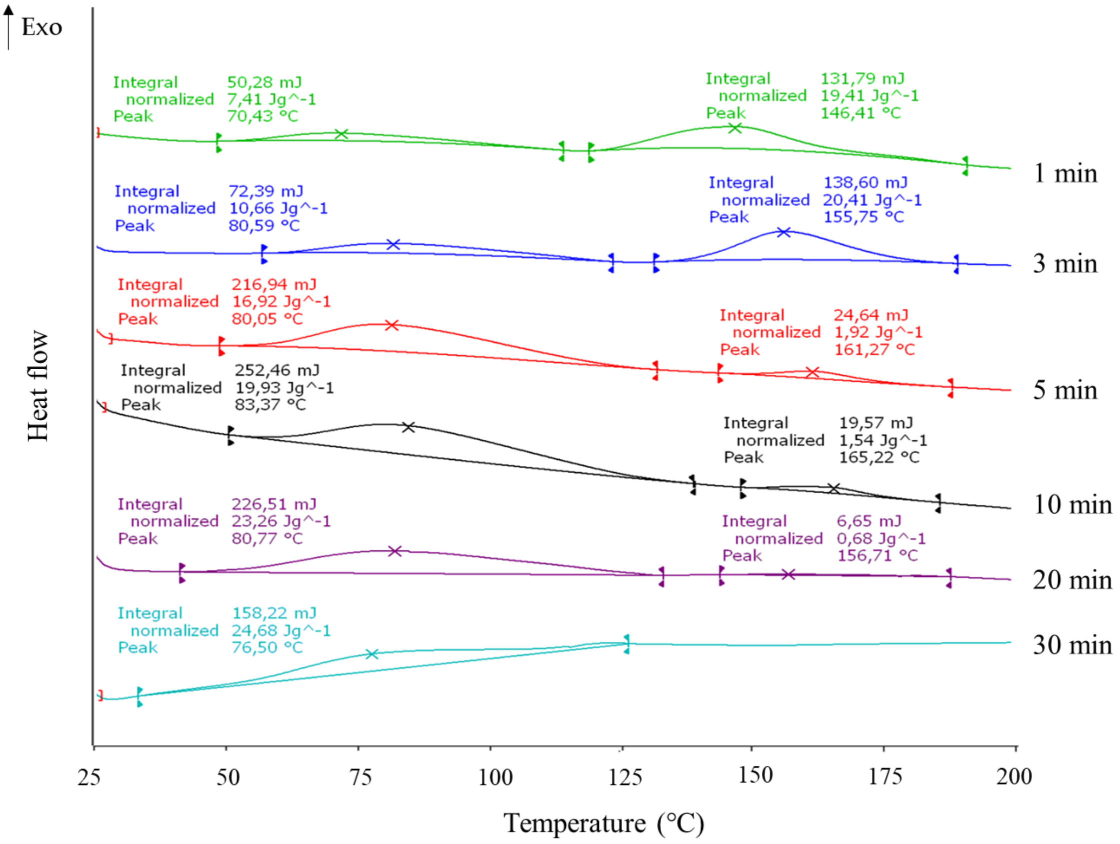

Figure 4.2. *DSC thermograms of R as a function of different times of UV polymerization.*

For all material types investigated, the same trend was observed in relation with these two exothermic peaks and the increase in the UV exposure time. The first peak increases with UV time due to the increment of cured polymer by photopolymerization – the greater the UV-cured polymer, the greater the necessary energy to crosslink it when temperature was applied. In contrast, as expected, the peak of the thermal polymerization decreased as a function of UV time – the greater the UV-cured polymer, the lower the remaining uncured polymer. When it is exposed to ultraviolet radiation for 30 min, UV-polymerization of the resin is completed and, therefore, the peak of thermal polymerization disappears.

Table 4.2 summarises DSC energies obtained from DSC thermograms for each measured time and each nanofiller. It can be observed that at 0 min, all the samples showed similar behavior – non UV-peak and a similar thermal peak with an energy about 21-22 J/g. However, for low UV exposure times (1 min), when the nanocomposites are compared to R, it was observed that all nanofillers reduced the extent of UV polymerization, with E_{UV} lower than 3 J/g whilst R reached 11.3 J/g. From 5 min, this reduction was only found on the addition of G and GoxNP, being the energies of R+GO similar than R. Finally, for longer times (20 min) R+G was the only material type that showed differences compared to R. The sum of E_{UV} + E_{tc} was constant, with some differences inside the deviation of the energy measurements.

Table 4.2. *Mean DSC energies ($J \cdot g^{-1}$) of R, R+G, R+GO, R+GoxNP.*

	R		**R + G**		**R + GO**		**R + GoxNP**	
min	E_{UV}	E_{tc}	E_{UV}	E_{tc}	E_{UV}	E_{tc}	E_{UV}	E_{tc}
0	0.0	22.0	0.0	21.6	0.0	21.2	0.0	21.6
1	11.3	15.9	1.3	23.4	2.8	22.2	2.2	24.3
5	18.1	1.5	13.2	9.7	17.5	2.3	11.9	9.6
10	18.3	1.5	15.8	4.8	18.0	2.1	18.6	4.0
20	22.9	0.7	17.9	2.8	19.7	0.0	21.0	1.1

FTIR spectrum of uncured resin is shown in Figure 4.3. Peaks corresponding to an acrylic resin are observed in the spectra. Alkyl groups are found as two peaks in the range of 2870-2950 cm^{-1} [36], whilst the bonds C=O, C-O and -C-C(=O)-O- of ester group appear at 1707, 1636 and 1165 cm^{-1}, respectively [37].

Using FTIR analysis, the polymerization process can be followed as the polymerization occurs by the opening of C=C bond at 1637 cm^{-1} [34]. The detail of the decreasing of this peak with the UV exposure time for R is shown in Figure 4.4. It can be seen how it decreases as the UV polymerization time increases, until its disappearance at 30 min, when the polymer is completely cured. This complete polymerization time is in accordance with the DSC results previously discussed.

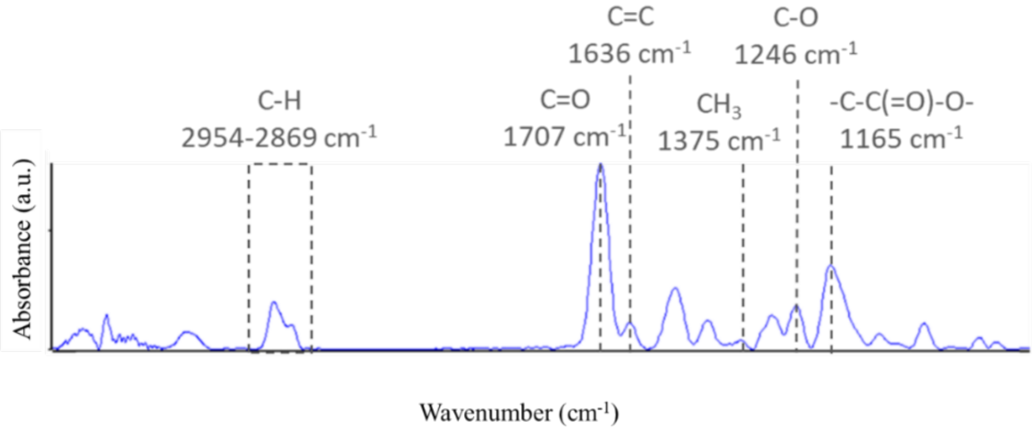

Figure 4.3. *FTIR spectra of uncured R.*

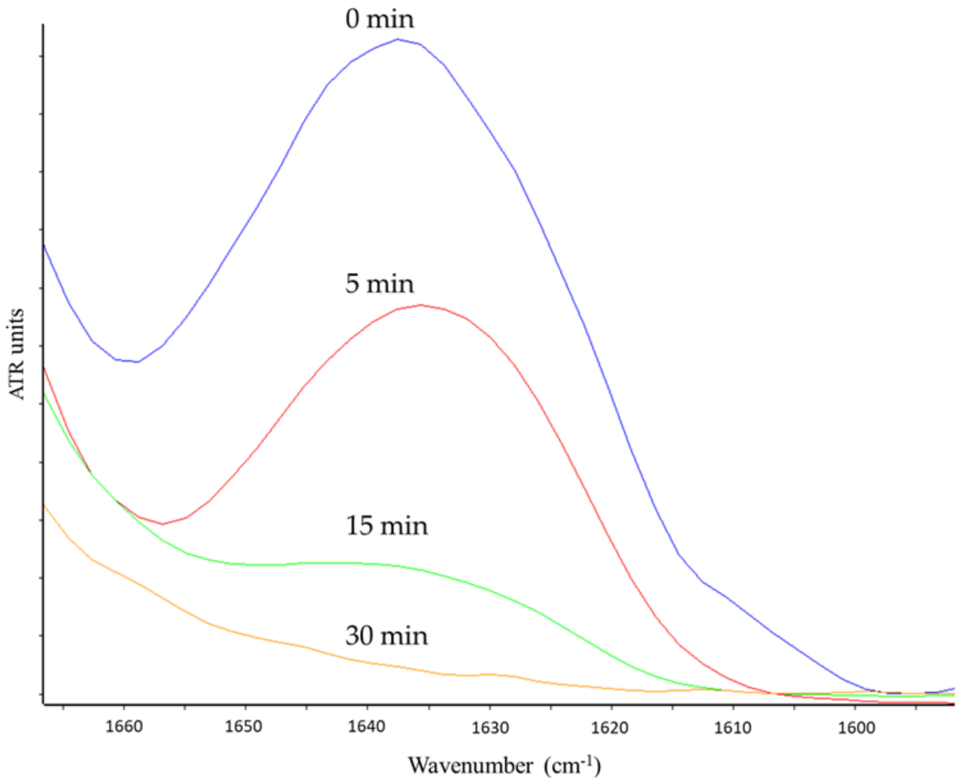

Figure 4.4. *FTIR spectra of C=C peak (1637 cm^{-1}) of R with different times of UV exposure.*

To determine the effect that the nanofillers addition has over the UV polymerization process, DSC and FTIR results were compared for all samples at the same UV exposure time. Figure 4.5 shows the effect of the different nanofillers for 5 min of polymerization on the DSC thermograms. The first peak, located between 70 and 80°C, as commented above, was due to the crystallization of the polymer cured by UV. The higher the UV polymerization degree, the greater was this crystallization peak. It can be seen how G and GoxNP presence reduced the area of this peak, which suggests that for the same UV exposure time, the UV polymerization degree was lower in the case of these nanofillers.

The second peak (150 – 160°C) corresponded to the thermal polymerization process of the uncured polymer. Obviously, when the first peak increased, this second peak decreased because the remaining unpolymerized resin decreased. In this case, G and GoxNP showed higher peaks than R and R+GO, confirming the lower UV polymerization degree.

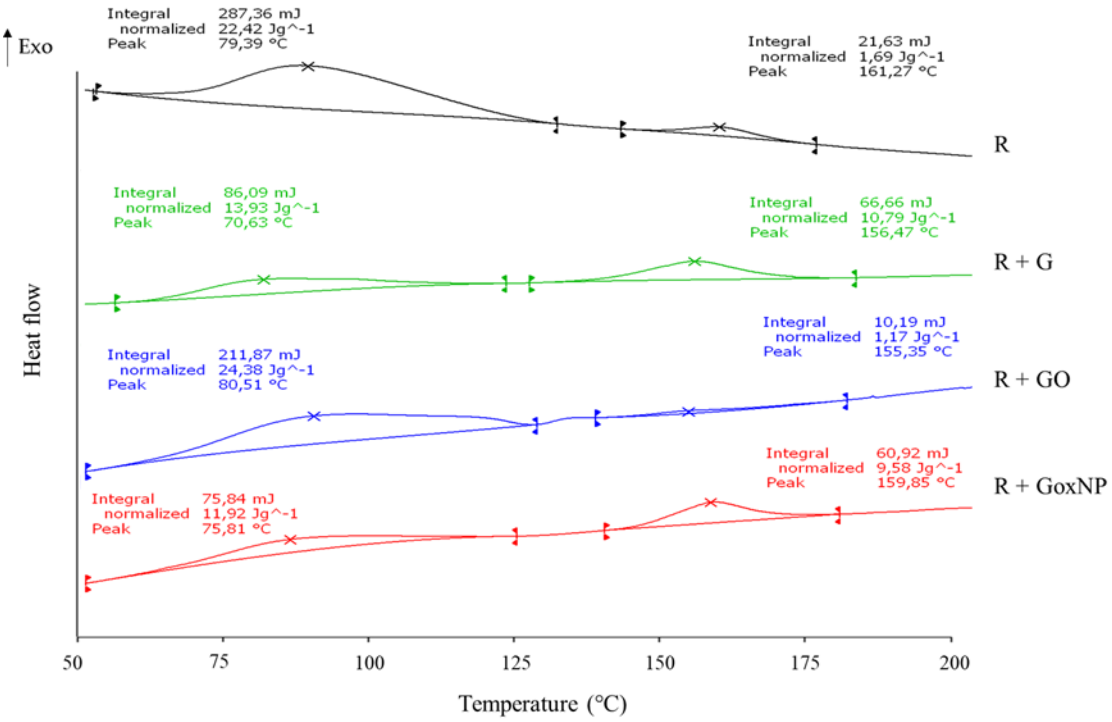

Figure 4.5. *DSC thermograms of R, R+G, R+GO, R+GoxNP after 5 min of UV cure.*

When FTIR spectra were compared, the same tendency was observed. By studying the C=C peak at 1637 cm^{-1} (Figure 4.6), it is possible to compare the polymerization degree, which is more advanced when the peak is less intense.

The FTIR results showed that R+G and R+GoxNP followed the same trend when compared to the observed DSC data, after 5 minutes of UV exposure, their polymerization degree was lower than in the case of the base resin and R+GO.

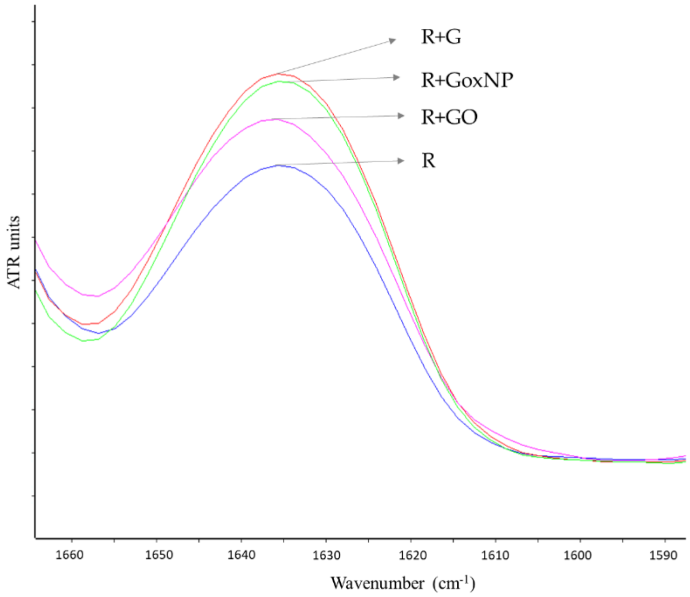

Figure 4.6. *FTIR spectra of C=C peak (1637 cm-1) of R, R+G, R+GO, R+GoxNP after 5 minutes of UV cure.*

Figure 4.7 showed the polymerization degree due to the UV exposure (Eq. 4.1) and data presented in Table 4.2, at different exposure times. It can be seen how GO retarded the polymerization process for short UV times; however, from 5 min of UV exposure the polymerization degree was similar to R.

On the other hand, R+G and R+GoxNP showed similar tendencies regarding the evolution of polymerization degree with time. The presence of these nanofillers showed a higher impact on the degree of polymerization when compared to GO, especially for relatively medium and long periods. They affect the process, achieving lower polymerization degrees than the initial resin, this effect was especially notable in the case of G.

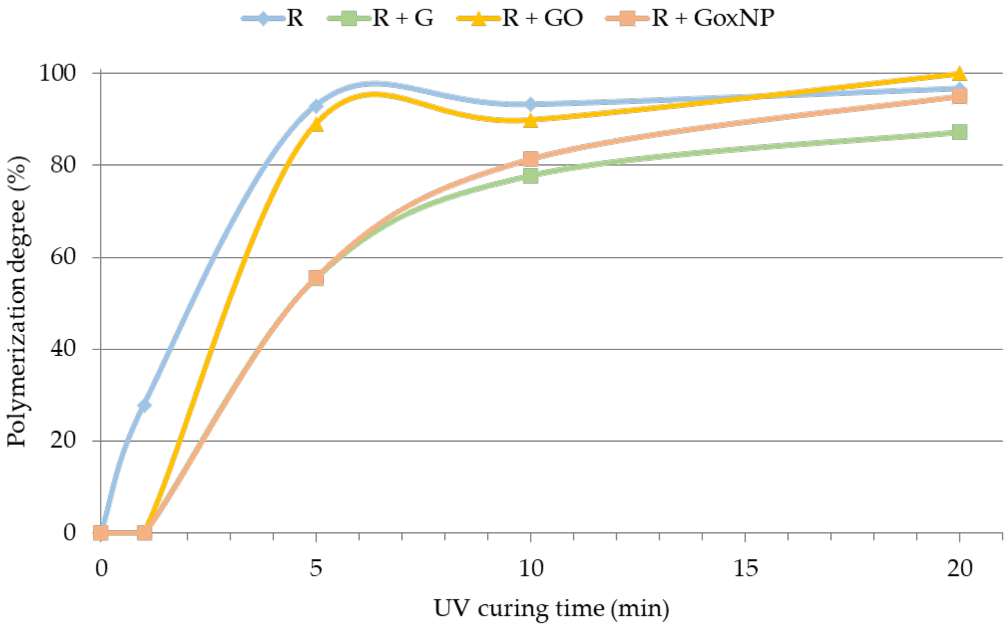

Figure 4.7. *Polymerization degree vs UV polymerization time of R, R+G, R+GO, R+GoxNP.*

<u>Hardness tests</u>

Table 4.3 shows changes in hardness as a function of UV polymerization time for the different nanocomposites. In all cases, hardness increased with time, showing the polymerization process advance. The trend observed in the hardness was similar to the obtained data from the DSC and FTIR analysis, the addition of G and GoxNP influenced the polymerization process of the resin; they did not allow the resin to cure completely. Therefore, Shore D hardness was lower for these GBN. Whilst hardness value of R was 82 after 60 min of exposure time, R+G and R+GoxNP were 67 and 71, respectively. However, GO did not change the polymerization degree of resin – with a Shore D hardness of 81 after 60 min.

Table 4.3. *Shore D Hardness of R, R+G, R+GO, R+GoxNP with different UV polymerization time.*

	R	***R+G***	***R+GO***	***R+GoxNP***
5 min	71 ± 1[a]	43 ± 2[b]	76 ± 2[a]	53 ± 4[c]
10 min	79 ± 1[a]	54 ± 3[b]	79 ± 2[a]	65 ± 2[c]
20 min	81 ± 1[a]	63 ± 3[b]	79 ± 2[a]	69 ± 2[c]
60 min	82 ± 2[a]	67 ± 1[b]	81 ± 1[a]	71 ± 2[b]

[a,b,c] Values with different letters are significantly different ($p < 0.05$). ANOVA analysis was made for each time but different times are not compared between them.

4.3. Effect of GBN on printability of acrylic resin

4.3.1. Experimental Methodology

One of the most important parameters that need to be controlled to assure good printability is viscosity. The viscosity was measured at 31°C, the printing temperature. At least three measurements were conducted for each sample. Viscosity has a relation with dispersion and free volume of the polymers. These two parameters also present a high effect on T_g and thermal conductivity. Therefore, with T_g and thermal conductivity measurements it was possible to understand the changes in viscosity and the dispersion of the nanocomposites.

Even with the adequate viscosity, in the printing process the light absorbance of the resin is of vital importance because light has to reach the photoinitiator to trigger the polymerization reaction. Besides, the characteristics of the resin (i.e. viscosity, absorbance, homogeneity of the dispersion) can affect printing quality, which can be determined by dimensional stability. It will be analysed as exposed in Chapter 3.

Dispersibility of the GBN was observed by optical microscopy on printed samples surface. Polarized light was used to observe GBN agglomerates.

Wettability measurements can give information about layers adhesion since polymerized layer has to be wetted by liquid resin to obtain adequate adhesion between the polymerized layer and the new one. Hydrophilicity was studied by measuring the contact angle of water on the sample surface at room temperature (20°C). At least ten contact angles were measured for each sample. Finally, surface roughness of each 3D printed sample was measured following the procedure of Chapter 3.

4.3.2. Results

4.3.2.1. Characterization before printing

After the study of the effect of GBN before printing, it is important to analyse the characteristics of liquid resin: viscosity and light absorbance. They can give information about possible problems that could occur during the printing process.

It is observed that, in comparison with R, the incorporation of G produced a marked decrease of the viscosity (59.1 %); on the contrary, the incorporation of GO and GoxNP showed a slight increase by 18.2 and 25 %, respectively (Table 4.4). These differences are not statistically significant; however, significant differences ($p\text{-value} < 0.05$) were found between R+G viscosity and R+GO/R+GoxNP viscosity.

The reduction of viscosity could be due to an increase in free volume generated around the nanoparticles [38]. To corroborate this hypothesis, T_g measurements were completed. It was observed that the addition of G significantly reduced the T_g value, from 106 °C to 73 °C, which suggested an increase in free volume. However, GO and GoxNP showed similar T_g than R (Table 4.4).

Table 4.4. *Viscosity (mean ± SD) and T_g (mean ± SD) of R, R+G, R+GO, R+GoxNP.*

Material Type	*Viscosity at 31 °C (Pa·s)*	*Tg (°C)*
R	$0.44 \pm 0.02^{a,b}$	106 ± 3
R+G	0.18 ± 0.09^{a}	73 ± 4
R+GO	0.52 ± 0.07^{b}	105 ± 2
R+GoxNP	0.55 ± 0.06^{b}	108 ± 3

^{a,b} Values with different letters are significantly different ($p < 0.05$)

To determine if the presence of the nanofillers affects to the UV absorption, the absorbance of the different uncured samples was measured by means of UV-Vis spectroscopy taking R as a reference. Wavelength was set at 405 nm, the same that the printer used. Results are shown in Table 4.5.

Table 4.5. *Absorbance at wavelength of 405 nm measured by UV-Vis spectroscopy.*

	Absorbance at 405 nm (a.u.)
R+G	1.43
R+GO	0.32
R+GoxNP	1.10

Measurements were taken using as reference the base R, then absorbance values showed the difference between the light absorption of R and the resin with the different nanofillers. In general, it was observed that, in all cases, samples with nanofillers had higher absorbance than R, being especially noticeable in the case of R+G. These results suggest that G and GoxNP nanoparticles could be absorbing a significant part of the UV-light that reaches the sample.

4.3.2.2. Printability

Cube samples were printed with the different resins prepared as explained in Chapter 3, an example of the resultant samples is shown in Figure 4.8.

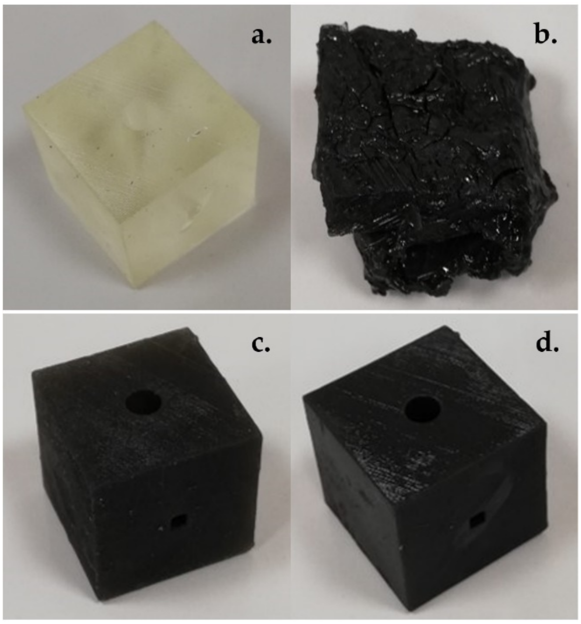

Figure 4.8. *Printed cubes with (a) R, (b) R+G, (c) R+GO and (d) R+GoxNP.*

It can be observed that R+GO and R+GoxNP samples showed good printability, whilst R+G presented important problems during printing process.

R+GO showed similar polymerization degree that R, therefore, a good printability was expected. In the case of R+GoxNP, it seems that the slight decrease in polymerization degree showed did not impede structure formation by 3D printing. However, the effect of G on the UV polymerization of the resin prevented the structure to be properly formed. This could be due to a decrease in curing depth, leading to a lack of adhesion between layers when G is present. It could be related with the retardation in the UV polymerization previously discussed.

To avoid the problem of printability of R+G samples, exposure time was increased by 8.9%. With this increment in exposure time, printability was not a problem when G is added to the resin. Dimensional stability of R+G printed samples was carried out with this increase in exposure time.

4.3.2.3. Dimensional stability

Table 4.6 and Table 4.7 show dimensional stability of the different samples. As explained before, R+G samples were printed with higher exposure time. Difference images – designed geometry versus printed geometry - were obtained by subtracting the reference image (CAD file) to the binary image, and these images were used to determine the percentage printing accuracy.

Table 4.6. *Accuracy of printed samples with circular holes.*

Sample	*Original image*	*Binary image*	*Difference image*	*% Accuracy*
R	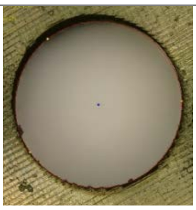	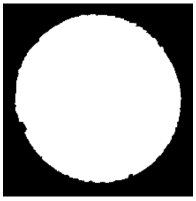	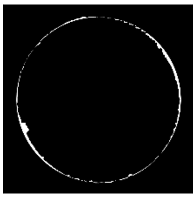	98.61 ± 1.12
R+G			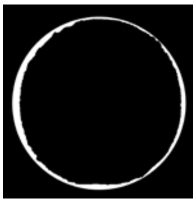	97.32 ± 1.56
R+GO	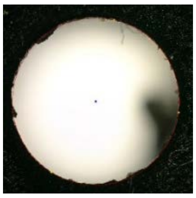		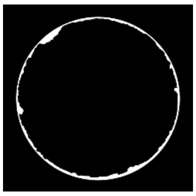	96.92 ± 2.53
R+GoxNP	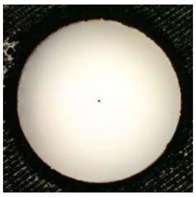	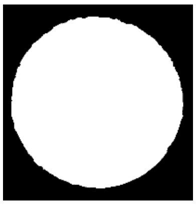	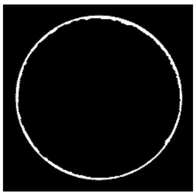	98.64 ± 0.14

Table 4.7. *Accuracy of printed samples with square holes.*

Sample	*Original image*	*Binary image*	*Difference image*	*% Accuracy*
R	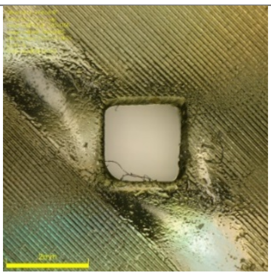		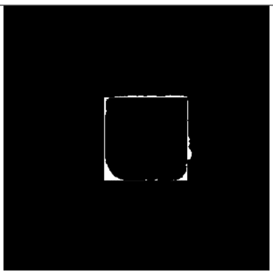	99.09 ± 0.31
R+G	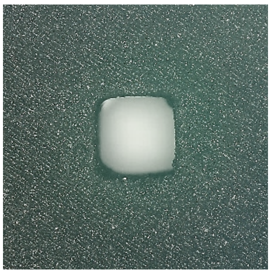		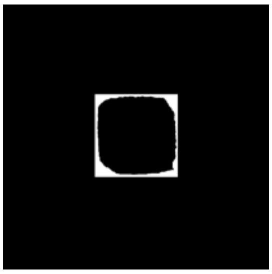	97.13 ± 1.02
R+GO	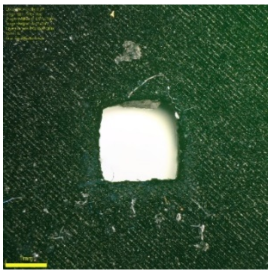		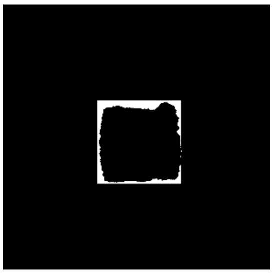	97.92 ± 0.50
R+ GoxNP		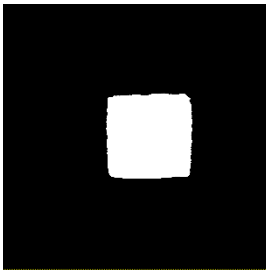	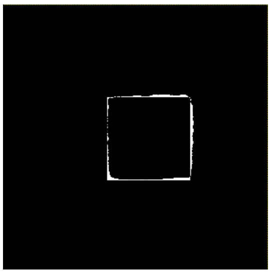	99.11 ± 0.31

Comparing both geometries, it was found that, in all cases except for R+G, the accuracy for square-shaped geometry was higher than the circular-shaped geometry. Besides, it was noticed that in comparison with base resin, G and GO reduced slightly printing accuracy, whilst this parameter was not affected by GoxNP.

4.3.2.4. Dispersibility

Images taken to the different surfaces are shown in Figure 4.9. It can be observed that the best dispersion is obtained for the sample R+GoxNP. In the case of R+GO some agglomerates can be observed, being agglomerates more and higher for R+G sample.

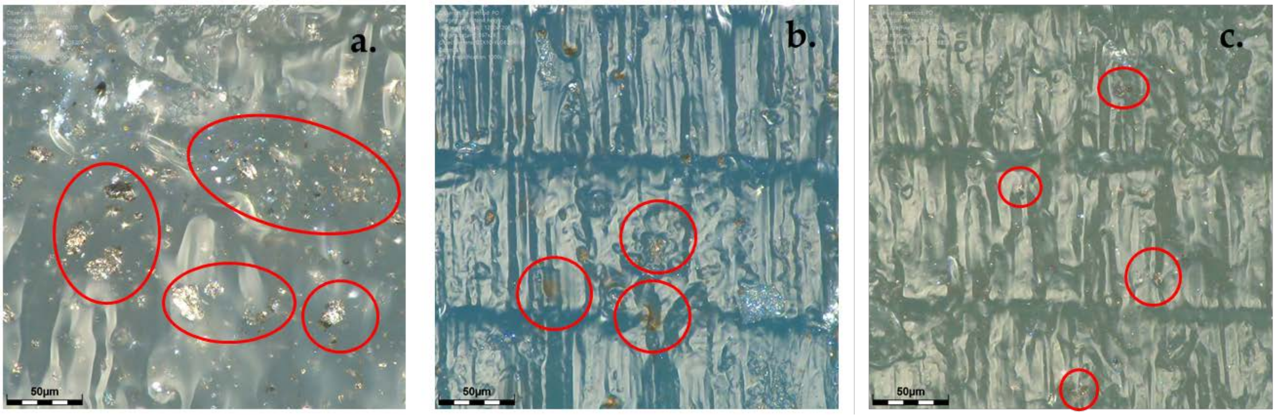

Figure 4.9. *GBN dispersion of (a) R+G, (b) R+GO and (c) R+GoxNP. Red circles show GBN agglomerates of different size.*

4.3.2.5. Thermal conductivity

Thermal conductivity measurements were completed to evaluate, together with viscosity, the nanofiller dispersion. Amongst other parameters (i.e. GBN type, amount), thermal conductivity decreases with free volume; therefore, it is possible to have information about it through thermal conductivity measurements.

Figure 4.10 shows the results obtained for the different nanofillers. The addition of GoxNP slightly increased thermal conductivity, whilst G reduced this parameter. In the case of GO, thermal conductivity was not affected by this nanoparticle. However, differences found between the nanocomposites and R were not significant (p-value > 0.05).

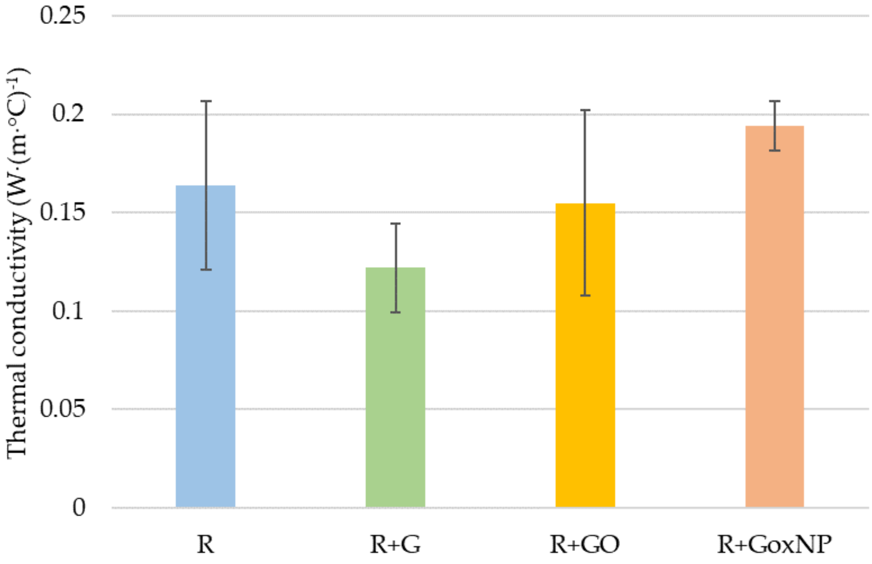

Figure 4.10. *Thermal conductivity of R, R+G, R+GO, R+GoxNP.*

4.3.2.6. Wettability

Water contact angle on the different investigated surfaces are presented in Table 4.8. These measurements could give information about wettability and surface energy, which could affect the adhesion between layers adhesion and, therefore, printability.

R+GO and R+GoxNP slightly increased hydrophilicity of the resin. There were minor decreases in contact angle: 4% for R+GO and 6.2% for R+GoxNP. However, R+G showed a subtle increase in contact angle which means that its hydrophilicity was lower. However, with the deviations that these values presented, differences were not significant.

Table 4.8. *Contact angle (°) of water on sample surface.*

R	*R+G*	*R+GO*	*R+GoxNP*
72.9 ± 1.6	74.0 ± 3.7	70.0 ± 2.7	68.4 ± 3.6

4.3.2.7. Roughness

The R_a parameters of roughness of the different samples are shown in Table 4.9.

Table 4.9. *Roughness (R_a) of printed samples (μm).*

R	*R+G*	*R+GO*	*R+GoxNP*
1.90 ± 0.24	2.56 ± 1.20	2.23 ± 0.53	1.87 ± 0.48

The obtained results showed that the addition of nanofillers may affect the roughness of 3D printed samples. These differences of surface roughness are due to the surface finish; the higher the roughness, the worse the surface finish. Therefore, these measurements were used as an indicator of the printing quality. Although there were not major differences, it could be observed how the addition of GoxNP did not affect roughness compared to R, GO addition slightly increased it (17%) and G showed the highest increase (34%).

4.4. Effect of GBN on tensile properties of acrylic resin

4.4.1. Experimental methodology

Dispersion of GBN in this case was done in a different way since in the previous section, it was found that there were many agglomerates. It was thought that the problem could be the high viscosity of the resin. Therefore, two options were considered to reduce the viscosity and improve the dispersion:

(i) Addition of acetone to reduce the viscosity and improve the dispersion of GBN in the liquid. Acetone needs to be properly evaporated after the dispersion because its presence may affect mechanical properties, even if resin contains only small residues or traces [15,16].

(ii) Addition of methyl methacrylate (MMA) which is also a liquid with low viscosity. MMA does not need to be removed because in the composition of the resin (Chapter 3) there are already methacrylate monomers.

To facilitate the dispersion of GBN in the resin, the amount was reduced to 0.05 %wt. The following procedure was followed:

(i) GBN were dispersed in the solvent via probe ultrasonication for 10 ± 0.5 min.

(ii) Resin was added gradually. The volume was doubled in each stage until the whole volume of resin (300 mL) was added. After each addition of resin, the same sonication cycle was applied.

(iii) Finally, degasification was undertaken.

(iv) In the case of acetone, evaporation was carried out overnight with magnetic stirring at 35°C.

Prior to add GBN, it is necessary to know if these solvents had effect on the mechanical properties of the resin. Samples of resin with acetone/MMA were prepared following the same procedure expect step i. The ratio solvent:resin was 30:100 v/v.

Dog bone samples were printed by SLA with resin and resin with solvents to see the effect of the solvents on the mechanical properties of the resin. With the best solvent, dog bone samples were prepared and printed with the different GBN. As seen previously, the mixture R+G needs higher exposure time.

Dispersibility was studied as previously explained in section 4.3.1.5. Besides, absorbance of the liquid nanocomposite gives information about the dispersion of the nanomaterials and is related with printability. Therefore, dispersibility was evaluated by means of optical microscopy and UV absorbance.

4.4.2. Results

4.4.2.1. Effect of solvent addition

Firstly, the effect of the solvents in the resin mechanical properties was studied. In Figure 4.11, the normalized values of tensile strength and Young's modulus are shown. The values of R were taken as a reference: 34.5 MPa and 1.3 GPa, respectively.

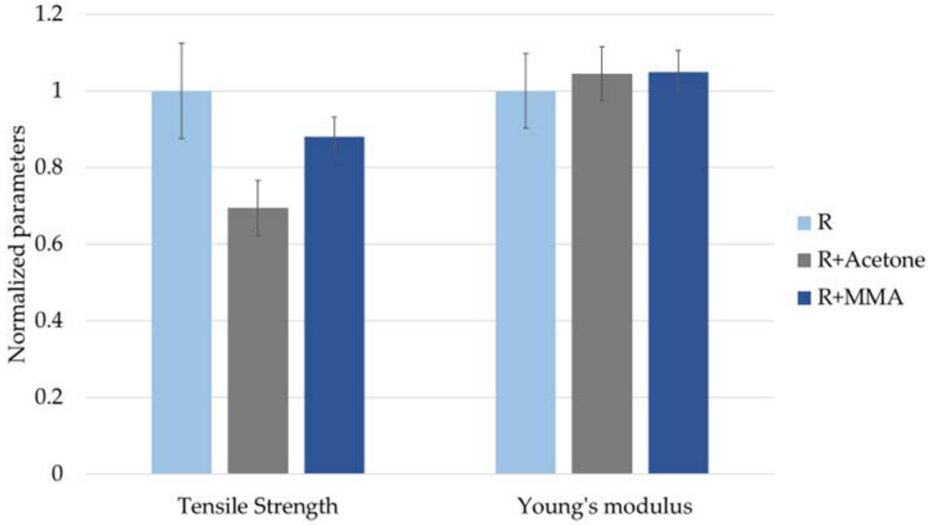

Figure 4.11. *Effect of acetone and MMA on tensile properties of the resin.*

The addition of acetone and MMA had no significant effect on Young's modulus of the acrylic-based resin, with p-values of 0.910 and 0.726, respectively. However, analyzing tensile strength it was observed that the addition of MMA produced a non-significant (p-value = 0.131) decrease in tensile strength of 12%. Meanwhile, the tensile strength of the R+Acetone was approx. 70% of the tensile strength of the resin (p-value = 0.001). This could be due to the presence of small traces of acetone due to the evaporation process being incomplete or because the acetone degraded or changed the reactant structure responsible for the polymerization. Considering these results, acetone was discarded as a solvent to reduce the resin viscosity and only MMA was used to add the GBN. From now on, R+MMA will be referred to as R'.

4.4.2.2. Effect of GBN addition

After the printing of the dog bone samples, they were tested and the results can be found in Figure 4.12. The normalized values respect to R has been represented to facilitate the comparison between the nanocomposites and the resin.

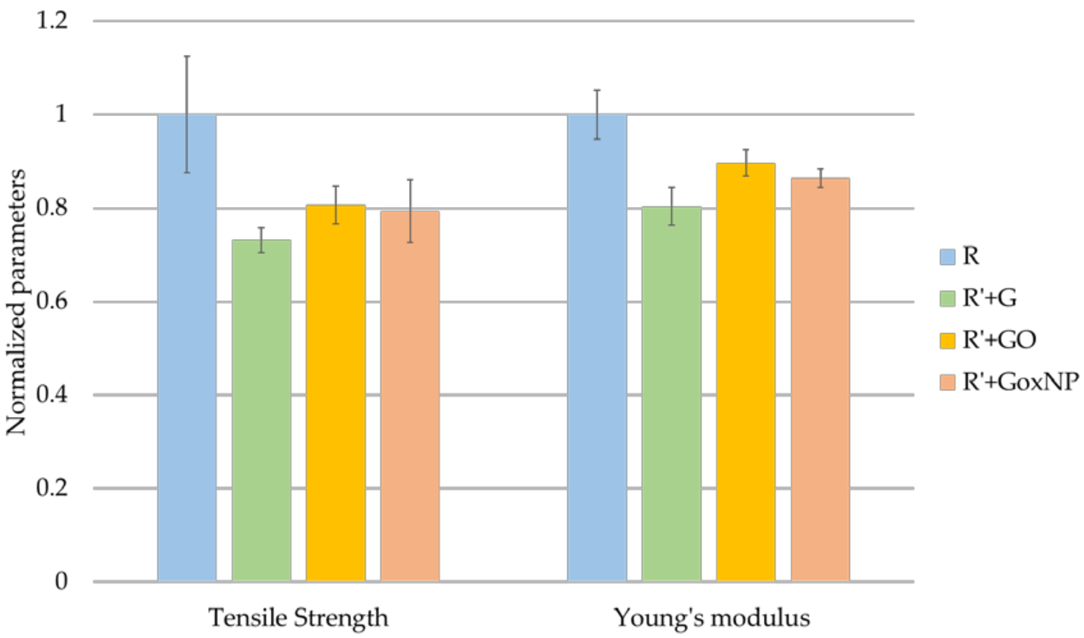

Figure 4.12. *Effect of GBN on tensile properties of the resin.*

Unexpectedly, all the GBN produced a reduction on mechanical properties of the resin of around 20%. The highest decrease was found for R+G sample, probably due to the worse dispersion of this nanofillers in the absence of oxygenated groups than improves dispersibility [4]. However, even in the case of the nanofilles with these groups (GO and GoxNP), improvements were not found.

4.4.2.3. Dispersibility

In Figure 4.13, images taken with the microscope are shown to have an approximation of the improvement in dispersion when MMA is added.

Figure 4.13. *GBN dispersion of (a) R+G, (b) R+GO and (c) R+GoxNP with the addition of MMA.*

When images of Figure 4.9 and Figure 4.13 are compared, an improvement in dispersion can clearly be seen. Thanks to the reduction of the amount of GBN and the addition of MMA to reduce the viscosity, the GBN are better dispersed inside the matrix. However, this improvement in dispersibility is not associated with an improvement in mechanical properties.

Table 4.10 shows the absorbance of the different mixtures, including the resin with MMA (R').

Table 4.10. Absorbance of the different samples taking R as a reference.

	Absorbance at 405 nm (a.u.)
R'	0.02
R'+G	1.62
R'+GO	1.00
R'+GoxNP	1.82

The addition of MMA to the resin did not produce a variation on the absorbance of the sample. However, the addition of GBN produced important changes in this parameter. The addition of GoxNP showed a more notable increase of the absorbance than G, and the lowest effect was found for GO.

4.5. Discussion of the results

In this chapter, the effect of different GBN on the polymerization reaction and the printability of an acrylic photocurable resin has been demonstrated. It was found that G affected polymerization degree due to its high light absorption and, therefore, it also affected printability, being needed a higher exposure time to manufacture printed structures. Conversely, GoxNP did affect polymerization degree slightly, but it did not difficult the printing process. Finally, GO did not affect polymerization reaction nor printability of the resin. Although the differences on UV polymerization and wettability between G and GoxNP are subtle, their impact on the printing performance are highly notable, due to the differences in light absorbance. R+G showed the highest light absorbance (Table 4.5). Therefore, G absorbs more amount of light (1.43 a.u) than GoxNP (1.10 a.u) and curing depth could be reduced, which leads to lower interlayer adhesion and worse printability.

Polymerization reaction was studied using DSC, FTIR and Shore D hardness measurements. First, thermal polymerization was studied to know the effect of GBN on the polymerisation separately from the effect on UV absorption. Hence, it was demonstrated if nanofillers influence the polymerization reaction by avoiding the polymer chain growth or terminating the polymerization process. The obtained results suggested that the incorporation of nanofillers did not influence the thermal polymerization process. Some studies [31,32] explored the capability of G to act as free radical scavengers, which, in this study, could result in the capture of free radicals formed during polymerization leading to a slowdown of this process. However, in this study, GBN did not seem to impede polymerization reaction acting as free radical scavengers.

In terms of UV polymerization, the results of this study have demonstrated that the incorporation of GBN has a significant impact on UV polymerization since the presence of these nanoparticles could affect the UV-Vis light absorption. This effect could decrease the energy caught by the photoinitiator resulting in a lower polymerization degree. It was more noticeable with the addition of G than GO and GoxNP, which could be attributed to the darker color of G nanoparticles [39]. The higher the light absorption, the lower the polymerization degree because the light that actually reaches the photoinitiator is reduced. G, GO and GoxNP showed different colour and, therefore they hamper the light absorption of the photoinitiator in different extent. G was the darkest, followed by GoxNP and, finally GO, with a brownish colour. All of them presented a decrease in polymerization degree at low exposure times; however, for high exposures times (>5 min) G only achieved 87.3 % compared to 96.7 % of base resin. Conversely, GoxNP achieved a 95% and GO was similar to base resin. It was found that GBN do not change polymerization energy when this process is done by heat. For this reason, it seems that when light is not involved in the process, GBN do not affect it. Therefore, the effect that was found in polymerization degree is not due to GBN inhibiting polymerization, but avoiding light to reach the photoinitiator.

The extent of the polymerization reaction determined the printability of the samples. If polymerization degree is not adequate, curing depth decreases, leading to lack of interlayer adhesion. GO and GoxNP allowed the printing process with the same parameters than base resin, whilst G did not allow to obtain satisfactory printed structures. This negative effect on the printability suggests that the G resin did not present enough polymerization degree to achieve the minimum interlayer adhesion to obtain a printed structure. This minimum polymerization degree was obtained by increasing exposure time.

In terms of printing accuracy, GoxNP showed higher accuracy than GO and G, and similar to R. Besides, the study of surface roughness revealed that the smoothest surface was obtained with R+GoxNP and it was similar to R. These differences in accuracy could be explained by GBN dispersion, viscosity results suggested that the dispersibility of GoxNP was slightly better that GO and significantly higher than G. Perhaps the presence of agglomerates could diffract the light affecting to the accuracy of the printed cross-section. To the best of our knowledge, this effect has not been previously reported, however, some studies [40] using other 3D printing technologies found that functionalized G nanoplatelets did not affected printing accuracy, except when the layer thickness was high. Besides, this study shows the good accuracy of SLA compared to other 3D printing techniques. For example, Zhou et al. [41] found a maximum accuracy of 85.68% using powder-based ink-jet 3D printing.

Results suggest that there was a relation between printability, dimensional stability and roughness. It was observed that the higher the effect of GBN on printability and dimensional stability, the higher the surface roughness. In this sense, R+G showed the highest values of roughness and also the higher dispersion in this value; R+GoxNP had similar roughness than R, and R+GO showed an intermediate value.

In relation to nanoparticle dispersion, the differences observed between G, GO and GoxNP could be better understood from a chemical point of view. Both, GO and GoxNP, had oxygenated groups in their composition. These groups were the responsible for the better interaction between the nanomaterial and the matrix thanks to the polarity of the nanomaterial, which increases the stability of the dispersion [42]. It was seen in viscosity, glass transition temperature, and thermal conductivity measurements.

It has been reported that an increase in viscosity is expected when nanofillers are well-dispersed since more surface area is available for interaction with the matrix [43]. Therefore, GO and GoxNP viscosity increase could suggest a homogenous dispersion of the nanofiller, probably improved due to the presence of the oxygenated groups on their surface. Conversely, the addition of G decreased the viscosity, suggesting a poor dispersion of these nanoparticles within the polymer matrix. Similar findings were reported in other studies [38,44,45].

This decrease in the viscosity caused by the nanoparticles addition was attributed to some physicochemical phenomena. Jain et al. [44] postulated that the decrease in viscosity could be due to a selective physisorption of the highest molecular weight polymer chains on the nanoparticle surface, leaving the low molar mass in the surrounding molten matrix. Conversely, Merkel el at. [38] explained the decrease in viscosity by the excluded free volume induced around the nanoparticles, which was accompanied by a reduction in the Tg.

Therefore, since a decrease in Tg of G samples was found, it could be concluded that probably the addition of G led to a decrease in viscosity due to the excluded free volume induced around the nanoparticles. In the case of GO and GoxNP, viscosity was higher than R because the dispersion of them was homogeneous and no changes were found in Tg.

In any case, despite the increase in viscosity observed when some nanofillers were added, the viscosity is adequate for 3D printing since the values measured are ≤ 5 Pa·s, which is the highest viscosity recommended [21].

In terms of thermal conductivity, it was highly affected by the type of GBN and, for this reason, the direct comparison could not be done. However, G should present higher thermal conductivity than the oxidized forms (GO and GoxNP) [46]. Therefore, the study of thermal conductivity led to a similar conclusion: the slight decrease in thermal conductivity of R+G samples could be due to the excluded free volume induced due to the presence of agglomerates.

In general, the larger particle size of the nanofillers, the better the exfoliation degree, better dispersion of nanoparticles and better interfacial connections with the matrix, which leads to an enhancing in thermal conductivity [47]. Furthermore, it is known that thermal conductivity increases when the average size increases and the number of layers decreases due to the smaller total thermal boundary resistances from the interface area [48]. The higher thermal conductivity of R+GoxNP could be explained by its size and dispersion. According to data sheet, GoxNP average size (200-300 nm) is x100 times the average size of GO (1.8-2.7 nm). Besides, viscosity measurements show better dispersion of GOxNP than G and GO.

In the case of G, a reduction of thermal conductivity was observed. It could be due to the poor dispersion of G within the matrix and the increase in excluded free volume, which could corroborate the viscosity results and its effect on printability. The lack of chemical functionalization of G explained the worst dispersibility of this GBN.

Previous studies [49] found that adding 0.5 wt.% of GO to an epoxy resin leads to an increase in thermal conductivity of more than 200%. However, another study [50] found that GO presents no effect on thermal conductivity of epoxy resin until a load of 2 wt.% Conversely, Wang et al. [51] studied the effect of graphene nanoplatelets (GNP) on thermal conductivity by adding 25 vol.%.

Therefore, the effect of nanofillers on thermal conductivity depends on many factors, such as the degree of dispersion. In this case, no significant effect was found and it could be due to the low amount added. If a higher amount of well-dispersed GBN were added, free volume would be reduced and thermal conductivity would increase [52].

Finally, wettability was studied. Previous studies have investigated the effect of GBN addition on the hydrophilicity of polymers. It was found that the addition of GO coating to PCL scaffolds increased hydrophilicity [23]. Different oxidation degrees was also studied and it was concluded that the higher the O/C ratio of G, the higher the hydrophilicity [53,54].

In this study, it is noted that both GO and GoxNP increased slightly the wettability of the resin, which could be due to their hydrophilic oxygenated groups (carboxyl, hydroxyl and epoxide functional groups) [55]. In contrast, the contact angle of R+G is subtly higher than R, which could be due to the lack of oxygenated groups present on the G surface. However, there are no significant differences between R and R+G; hence, printability issues do not seem to be caused by wetting problems between liquid and cured resin.

In general, wettability is defined by surface energy, however, roughness can affect it. In this study, results showed no tendency that could show a relation between roughness and wettability. Therefore, it could be concluded that, in this case, wettability was affected mainly by chemical functional groups and it was not related with roughness.

Results show a first approach to understand the effect of GBN on resin polymerization. The current study tried to simulate the printing process by exposing the resin to UV light followed by DSC analysis. However, the designed methodology differs from polymerization of the resin during printing process because of the light source – 3D printed use a punctual laser light and Form Cure use a UV lamp. Therefore, the effect of other parameters should be studied, as the UV source power or intensity. Besides, different techniques to improve dispersion (e.g. combination of mechanical stirring and sonication) could be tested.

It has been proved the viability of GBN to be used as fillers of photocurable resins; for potential applications it would be necessary to continue studying these nanocomposites. For example, it would be interesting to test them mechanically to assure their suitability to build 3D-printed structures with improved properties and cell studies should be carried out to assure the effect of GBN in cell adhesion, proliferation and differentiation.

Dispersion has been improved by the addition of MMA to reduce the viscosity of the resin. However, an improvement in mechanical properties was not found when GBN were added.

Some studies show how the printed samples with GBN have a reduction in mechanical properties [21,56]. Manapat et al [21] made four hypothesis: (i) the increasing concentration of GO could produce an excessive inter-platelet interaction instead of GO-resin hydrogen bonding; (ii) GO could act as barrier or hindrance to incoming laser light, reducing the efficiency of photopolymerization; (iii) GO could inhibit the polymerization acting as a chain transfer agent; and (iv) the presence of wrinkles in the graphene sheets could affect the stress distribution, hindering good adhesion between GO and the resin. The effect of GBN in polymerization could be better understood by studying the polymerization kinetics of the resin in the presence of GBN.

Therefore, a deeper study regarding the effect of GBN on polymerization reaction and mechanical properties of acrylic resin needs to be done. And from this point, the research approach of this thesis was done, being the focus of the work on understanding the effect of GBN and their dispersion on the polymerization process and on the mechanical properties of the printed structures.

4.6. Conclusions of this chapter

Before using a nanocomposite to print structures, it is important to know the effect that nanofillers will have on the whole printing process, since it has been observed that the dispersion of nanofillers on SLA resin can compromise many parameters, ranging from viscosity of the blended resin to printability properties.

- In terms of polymerization degree, it was found that G and GoxNP have a significant negative effect when they are added to the resin. In the case of GO, its incorporation does not affect polymerization degree.
- Despite the negative effect that GoxNP showed on polymerization degree, it has been proved that the incorporation of 0.1 wt.% of GO and GoxNP to the photocured resin did not significantly affect printing quality, allowing their use in the preparation of new nanofilled photocurable resins for SLA printing. However, it has been observed that the addition of 0.1 wt.% G demonstrated a notable negative effect on the printability. This could be explained by the differences on type, functionalization and structure of GBN, that change dispersibility and light absorbance. However, negative effect of G does not mean that it is not possible to print with R+G mixture, but to compensate the negative effect of G on polymerization, exposure time must be increase.
- To improve the dispersion, solvents are usually added and, in this case, the addition of MMA as solvent seems to present an improvement in dispersibility of GBN. However, in terms of mechanical properties, the addition of well-dispersed GBN did not lead to an increase in tensile strength and Young's modulus. Consequently, it could be concluded that GBN were affecting polymerization or printing processes of the resin.

Therefore, understanding how GBN affect polymerization and the properties of the resin is crucial to adapt printing parameters (e.g., light intensity, exposure time, layer thickness, etc.) and resin formulation (e.g., maximum permissible nanoparticles amount, photoinitiator amount, etc.) in order to obtain a success 3D printing and take advantage of SLA accuracy.

4.7. References

[1] S. Lopez de Armentia, S. Fernández-Villamarín, Y. Ballesteros, J.C. del Real, N. Dunne, E. Paz, 3D Printing of a Graphene-Modified Photopolymer Using Stereolithography for Biomedical Applications : A Study of the Polymerization Reaction, Int. J. Bioprinting. 8 (2022) 1–16.

[2] A.A. Iqbal, N. Sakib, A.K.M.P. Iqbal, D.M. Nuruzzaman, Graphene-based nanocomposites and their fabrication, mechanical properties and applications, Materialia. 12 (2020) 100815. https://doi.org/10.1016/j.mtla.2020.100815.

[3] M. Azizi-Lalabadi, S.M. Jafari, Bio-nanocomposites of graphene with biopolymers; fabrication, properties, and applications, Adv. Colloid Interface Sci. 292 (2021) 102416. https://doi.org/10.1016/j.cis.2021.102416.

[4] Y. Li, Z. Feng, L. Huang, K. Essa, E. Bilotti, H. Zhang, T. Peijs, L. Hao, Additive manufacturing high performance graphene-based composites: A review, Compos. Part A Appl. Sci. Manuf. 124 (2019) 105483. https://doi.org/10.1016/j.compositesa.2019.105483.

[5] S. Guo, Y. Lu, X. Wan, F. Wu, T. Zhao, C. Shen, Preparation, characterization of highly dispersed reduced graphene oxide/epoxy resin and its application in alkali-activated slag composites, Cem. Concr. Compos. 105 (2020) 103424. https://doi.org/10.1016/j.cemconcomp.2019.103424.

[6] Z. Sekhavat Pour, M. Ghaemy, Polymer grafted graphene oxide: For improved dispersion in epoxy resin and enhancement of mechanical properties of nanocomposite, Compos. Sci. Technol. 136 (2016) 145–157. https://doi.org/10.1016/j.compscitech.2016.10.014.

[7] A.S. Al-Asadi, Q.M.A. Hassan, A.F. Abdulkader, M.H. Mohammed, H. Bakr, C.A. Emshary, Formation of graphene nanosheets/epoxy resin composite and study its structural, morphological and nonlinear optical properties, Opt. Mater. (Amst). 89 (2019) 460–467. https://doi.org/10.1016/j.optmat.2019.01.078.

[8] U. Kilic, M.M. Sherif, O.E. Ozbulut, Tensile properties of graphene nanoplatelets/epoxy composites fabricated by various dispersion techniques, Polym. Test. 76 (2019) 181–191. https://doi.org/10.1016/j.polymertesting.2019.03.028.

[9] X. Wang, F. Tang, X. Qi, Z. Lin, Mechanical, electrochemical, and durability behavior of graphene nano-platelet loaded epoxy-resin composite coatings, Compos. Part B Eng. 176 (2019) 107103. https://doi.org/10.1016/j.compositesb.2019.107103.

[10] R. Sánchez-Hidalgo, V. Yuste-Sanchez, R. Verdejo, C. Blanco, M.A. Lopez-Manchado, R. Menéndez, Main structural features of graphene materials controlling the transport properties of epoxy resin-based composites, Eur. Polym. J. 101 (2018) 56–65. https://doi.org/10.1016/j.eurpolymj.2018.02.018.

[11] R. Moriche, S.G. Prolongo, M. Sánchez, A. Jiménez-Suárez, M.J. Sayagués, A. Ureña, Morphological changes on graphene nanoplatelets induced during dispersion into an epoxy resin by different methods, Compos. Part B Eng. 72 (2015) 199–205. https://doi.org/10.1016/j.compositesb.2014.12.012.

[12] F. Fang, S. Ran, Z. Fang, P. Song, H. Wang, Improved flame resistance and thermo-mechanical properties of epoxy resin nanocomposites from functionalized graphene oxide via self-assembly in water, Compos. Part B Eng. 165 (2019) 406–416.

https://doi.org/10.1016/j.compositesb.2019.01.086.

[13] S. Kugler, K. Kowalczyk, T. Spychaj, Hybrid carbon nanotubes/graphene modified acrylic coats, Prog. Org. Coatings. 85 (2015) 1–7. https://doi.org/10.1016/j.porgcoat.2015.02.019.

[14] Z. Baig, O. Mamat, M. Mustapha, A. Mumtaz, K.S. Munir, M. Sarfraz, Investigation of tip sonication effects on structural quality of graphene nanoplatelets (GNPs) for superior solvent dispersion, Ultrason. Sonochem. 45 (2018) 133–149. https://doi.org/10.1016/j.ultsonch.2018.03.007.

[15] K. Markandan, C.Q. Lai, Enhanced mechanical properties of 3D printed graphene-polymer composite lattices at very low graphene concentrations, Compos. Part A Appl. Sci. Manuf. 129 (2020) 105726. https://doi.org/10.1016/j.compositesa.2019.105726.

[16] M.R. Loos, L.A.F. Coelho, S.H. Pezzin, S.C. Amico, The effect of acetone addition on the properties of epoxy, Polimeros. 18 (2008) 76–80. https://doi.org/10.1590/S0104-14282008000100015.

[17] M. Sangermano, S. Marchi, L. Valentini, S.B. Bon, P. Fabbri, Transparent and conductive graphene oxide/poly(ethylene glycol) diacrylate coatings obtained by photopolymerization, Macromol. Mater. Eng. 296 (2011) 401–407. https://doi.org/10.1002/mame.201000372.

[18] E. Paz, F. Forriol, J.C. del Real, N. Dunne, Graphene oxide versus graphene for optimisation of PMMA bone cement for orthopaedic applications, Mater. Sci. Eng. C. 77 (2017) 1003–1011. https://doi.org/10.1016/j.msec.2017.03.269.

[19] D. Lin, S. Jin, F. Zhang, C. Wang, Y. Wang, C. Zhou, G.J. Cheng, 3D stereolithography printing of graphene oxide reinforced complex architectures, Nanotechnology. 26 (2015) 434003. https://doi.org/10.1088/0957-4484/26/43/434003.

[20] Z. Feng, Y. Li, L. Hao, Y. Yang, T. Tang, D. Tang, W. Xiong, Graphene-Reinforced Biodegradable Resin Composites for Stereolithographic 3D Printing of Bone Structure Scaffolds, J. Nanomater. (2019) 1–13. https://doi.org/10.1155/2019/9710264.

[21] J.Z. Manapat, J.D. Mangadlao, B.D.B. Tiu, G.C. Tritchler, R.C. Advincula, High-Strength Stereolithographic 3D Printed Nanocomposites: Graphene Oxide Metastability, ACS Appl. Mater. Interfaces. 9 (2017) 10085–10093. https://doi.org/10.1021/acsami.6b16174.

[22] X. Zhou, M. Nowicki, H. Cui, W. Zhu, X. Fang, S. Miao, S.J. Lee, M. Keidar, L.G. Zhang, 3D bioprinted graphene oxide-incorporated matrix for promoting chondrogenic differentiation of human bone marrow mesenchymal stem cells, Carbon N. Y. 116 (2017) 615–624. https://doi.org/10.1016/j.carbon.2017.02.049.

[23] A. Lipovka, R. Rodriguez, E. Bolbasov, P. Maryin, S. Tverdokhlebov, E. Sheremet, Time-stable wetting effect of plasma-treated biodegradable scaffolds functionalized with graphene oxide, Surf. Coatings Technol. 388 (2020) 125560. https://doi.org/10.1016/j.surfcoat.2020.125560.

[24] S.M. Lim, B.S. Shin, K. Kim, Characterization of products using additive manufacturing with graphene/photopolymer - Resin nano-fluid, J. Nanosci. Nanotechnol. 17 (2017) 5492–5495. https://doi.org/10.1166/jnn.2017.14159.

[25] R. Moriche, J. Artigas, L. Reigosa, M. Sánchez, S.G. Prolongo, A. Ureña, Modifications induced in photocuring of Bis- GMA/TEGDMA by the addition of graphene nanoplatelets for 3D printable electrically conductive nanocomposites, Compos. Sci. Technol. 184 (2019) 107876.

https://doi.org/10.1016/j.compscitech.2019.107876.

[26] M.N. dos Santos, C. V. Opelt, F.H. Lafratta, C.M. Lepienski, S.H. Pezzin, L.A.F. Coelho, Thermal and mechanical properties of a nanocomposite of a photocurable epoxy-acrylate resin and multiwalled carbon nanotubes, Mater. Sci. Eng. A. 528 (2011) 4318–4324. https://doi.org/10.1016/j.msea.2011.02.036.

[27] Q. Mu, L. Wang, C.K. Dunn, X. Kuang, F. Duan, Z. Zhang, H.J. Qi, T. Wang, Digital light processing 3D printing of conductive complex structures, Addit. Manuf. 18 (2017) 74–83. https://doi.org/10.1016/j.addma.2017.08.011.

[28] Z. Weng, Y. Zhou, W. Lin, T. Senthil, L. Wu, Structure-property relationship of nano enhanced stereolithography resin for desktop SLA 3D printer, Compos. Part A Appl. Sci. Manuf. 88 (2016) 234–242. https://doi.org/10.1016/j.compositesa.2016.05.035.

[29] E. Paz, Y. Ballesteros, J. Abenojar, J.C. del Real, N.J. Dunne, Graphene oxide and graphene reinforced PMMA bone cements: Evaluation of thermal properties and biocompatibility, Materials (Basel). 12 (2019) 3146. https://doi.org/10.3390/ma12193146.

[30] J. Abenojar, J.C. Del Real, Y. Ballesteros, M.A. Martinez, Kinetics of curing process in carbon/epoxy nano-composites, IOP Conf. Ser. Mater. Sci. Eng. 369 (2018) 012011. https://doi.org/10.1088/1757-899X/369/1/012011.

[31] H. Liang, Y. Bu, Y. Zhang, J. Zhang, Graphene oxide as efficient high-concentration formaldehyde scavenger and reutilization in supercapacitor, J. Colloid Interface Sci. 444 (2015) 109–114. https://doi.org/10.1016/j.jcis.2014.12.063.

[32] W. Xia, H. Xue, J. Wang, T. Wang, L. Song, H. Guo, X. Fan, H. Gong, J. He, Functionlized graphene serving as free radical scavenger and corrosion protection in gamma-irradiated epoxy composites, Carbon N. Y. 101 (2016) 315–323. https://doi.org/10.1016/j.carbon.2016.02.004.

[33] M. Martin-Gallego, M. Hernández, V. Lorenzo, R. Verdejo, M.A. Lopez-Manchado, M. Sangermano, Cationic photocured epoxy nanocomposites filled with different carbon fillers, Polymer (Guildf). 53 (2012) 1831–1838. https://doi.org/10.1016/j.polymer.2012.02.054.

[34] F. Courtecuisse, F. Karasu, X. Allonas, C. Croutxé-Barghorn, L. Van Der Ven, Confocal Raman microscopy study of several factors known to influence the oxygen inhibition of acrylate photopolymerization under LED, Prog. Org. Coatings. 92 (2016) 1–7. https://doi.org/10.1016/j.porgcoat.2015.11.020.

[35] C. Vicard, O. De Almeida, A. Cantarel, G. Bernhart, Experimental study of polymerization and crystallization kinetics of polyamide 6 obtained by anionic ring opening polymerization of ε-caprolactam, Polymer (Guildf). 132 (2017) 88–97. https://doi.org/10.1016/j.polymer.2017.10.039.

[36] N. Tudorachi, I. Bunia, Synthesis and thermal investigation by TG-FTIR-MS analysis of some functionalized acrylic copolymers and magnetic composites with Fe3O4, J. Anal. Appl. Pyrolysis. 116 (2015) 190–201. https://doi.org/10.1016/j.jaap.2015.09.010.

[37] L. Ortiz-Herrero, I. Cardaba, S. Setien, L. Bartolomé, M.L. Alonso, M.I. Maguregui, OPLS multivariate regression of FTIR-ATR spectra of acrylic paints for age estimation in contemporary artworks, Talanta. 205 (2019) 120114. https://doi.org/10.1016/j.talanta.2019.120114.

[38] T.C. Merkel, B.D. Freeman, R.J. Spontak, Z. He, I. Pinnau, P. Meakin, A.J. Hill, Ultrapermeable, reverse-selective nanocomposite membranes, Science (80-.). 296 (2002) 519–522. https://doi.org/10.1126/science.1069580.

[39] A. Chiappone, I. Roppolo, E. Naretto, E. Fantino, F. Calignano, M. Sangermano, F. Pirri, Study of graphene oxide-based 3D printable composites: Effect of the in situ reduction, Compos. Part B Eng. 124 (2017) 9–15. https://doi.org/10.1016/j.compositesb.2017.05.049.

[40] E. García, P.J. Núñez, J.M. Chacón, M.A. Caminero, S. Kamarthi, Comparative study of geometric properties of unreinforced PLA and PLA-Graphene composite materials applied to additive manufacturing using FFF technology, Polym. Test. 91 (2020) 106860. https://doi.org/10.1016/j.polymertesting.2020.106860.

[41] Z.X. Zhou, F. Buchanan, A. Lennon, N. Dunne, Investigating Approaches for Three-Dimensional Printing of Hydroxyapatite Scaffolds for Bone Regeneration, Key Eng. Mater. 631 (2014) 306–311. https://doi.org/10.4028/www.scientific.net/kem.631.306.

[42] A. Chouhan, H.P. Mungse, O.P. Khatri, Surface chemistry of graphene and graphene oxide: A versatile route for their dispersion and tribological applications, Adv. Colloid Interface Sci. 283 (2020) 102215. https://doi.org/10.1016/j.cis.2020.102215.

[43] S.G. Miller, J.L. Bauer, M.J. Maryanski, P.J. Heimann, J.P. Barlow, J.M. Gosau, R.E. Allred, Characterization of epoxy functionalized graphite nanoparticles and the physical properties of epoxy matrix nanocomposites, Compos. Sci. Technol. 70 (2010) 1120–1125. https://doi.org/10.1016/j.compscitech.2010.02.023.

[44] S. Jain, J.G.P. Goossens, G.W.M. Peters, M. Van Duin, P.J. Lemstra, Strong decrease in viscosity of nanoparticle-filled polymer melts through selective adsorption, Soft Matter. 4 (2008) 1848–1854. https://doi.org/10.1039/b802905a.

[45] M.. Mackay, T.. Dao, A. Tuteja, D.. Ho, B. van Horn, H.-C. Kin, C.. Hawker, Nanoscale effects leading to non-Einstein-like decrease in viscosity, Nat. Mater. 2 (2003) 762–766.

[46] N.K. Mahanta, A.R. Abramson, Thermal conductivity of graphene and graphene oxide nanoplatelets, Intersoc. Conf. Therm. Thermomechanical Phenom. Electron. Syst. ITHERM. (2012) 1–6. https://doi.org/10.1109/ITHERM.2012.6231405.

[47] M. Rafiee, F. Nitzsche, J. Laliberte, S. Hind, F. Robitaille, M.R. Labrosse, Thermal properties of doubly reinforced fiberglass/epoxy composites with graphene nanoplatelets, graphene oxide and reduced-graphene oxide, Compos. Part B Eng. 164 (2019) 1–9. https://doi.org/10.1016/j.compositesb.2018.11.051.

[48] Y. Sun, B. Tang, W. Huang, S. Wang, Z. Wang, X. Wang, Y. Zhu, C. Tao, Preparation of graphene modified epoxy resin with high thermal conductivity by optimizing the morphology of filler, Appl. Therm. Eng. 103 (2016) 892–900. https://doi.org/10.1016/j.applthermaleng.2016.05.005.

[49] R. Aradhana, S. Mohanty, S.K. Nayak, Comparison of mechanical, electrical and thermal properties in graphene oxide and reduced graphene oxide filled epoxy nanocomposite adhesives, Polymer (Guildf). 141 (2018) 109–123. https://doi.org/10.1016/j.polymer.2018.03.005.

[50] T. Huang, X. Zeng, Y. Yao, R. Sun, F. Meng, J. Xu, C. Wong, Boron nitride@graphene oxide hybrids for epoxy composites with enhanced thermal conductivity, RSC Adv. 6 (2016) 35847–35854. https://doi.org/10.1039/c5ra27315c.

[51] J. Wang, J.J. Li, G.J. Weng, Y. Su, The effects of temperature and alignment state of nanofillers on the thermal conductivity of both metal and nonmetal based graphene nanocomposites, Acta Mater. 185 (2020) 461–473. https://doi.org/10.1016/j.actamat.2019.12.032.

[52] G. Xue, J. Zhong, S. Gao, B. Wang, Correlation between the free volume and thermal conductivity of porous poly(vinyl alcohol)/reduced graphene oxide composites studied by positron spectroscopy, Carbon N. Y. 96 (2016) 871–878. https://doi.org/10.1016/j.carbon.2015.10.041.

[53] J. Li, Y. Yu, D. Chen, G. Liu, D. Li, H.S. Lee, Y. Feng, Hydrophilic graphene aerogel anodes enhance the performance of microbial electrochemical systems, Bioresour. Technol. 304 (2020) 122907. https://doi.org/10.1016/j.biortech.2020.122907.

[54] Y. Hou, W. Wang, P. Bártolo, Investigating the effect of carbon nanomaterials reinforcing poly(ε-Caprolactone) printed scaffolds for bone repair applications, Int. J. Bioprinting. 6 (2020) 1–9. https://doi.org/10.18063/ijb.v6i2.266.

[55] S. Yang, S. Sha, H. Lu, J. Wu, J. Ma, D. Wang, C. Hou, Z. Sheng, Graphene oxide and reduced graphene oxide coated cotton fabrics with opposite wettability for continuous oil/water separation, Sep. Purif. Technol. 259 (2021) 118095. https://doi.org/10.1016/j.seppur.2020.118095.

[56] C.H.A. Tsang, A. Zhakeyev, D.Y.C. Leung, J. Xuan, GO-modified flexible polymer nanocomposites fabricated via 3D stereolithography, Front. Chem. Sci. Eng. 13 (2019) 736–743. https://doi.org/10.1007/s11705-019-1836-x.

CHAPTER 5

EFFECT OF GBN ON POLYMERIZATION KINETICS

Table of Contents

In this chapter, polymerization reaction of acrylic resin is studied in depth by means of polymerization kinetics and curing depth. Besides, the optimization of post-printing parameters is carried out. In SLA printer, it is only possible to choose between two exposure times: the preset for Clear Resin and the one for Black Resin, which is 8.9%. higher. Resin manufacturer recommends to postcure the resin after printing, and three different parameters can be optimized: cleaning time in isopropanol (FormWash) and time and temperature in curing chamber (FormCure).

5.1. Introduction

Chapter 4 showed that many parameters could affect mechanical performance of the resin when GBN were added, even when dispersion seemed to be adequate. From that point, we considered that a complete understanding of the polymerization process could provide a relevant knowledge and tools to achieve the objective of the thesis. In general, photocurable resins may present three different photocuring mechanisms: cationic, radical or hybrid photopolymerization. The mechanism is chosen depending on the wavelength of the lamp and the printing technology. With a wavelength of the laser beam of 355 nm, both radical and cationic polymerization could be proceeded. However, cationic photopolymerization could hardly work under 405 nm irradiation [1]. The printer used in this work uses 405 nm wavelength, therefore, the polymerization of the acrylic resin is expected to be radical polymerization.

In literature, the effect of different GBN on the thermal curing of different polymeric resins has been widely studied, and two different tendencies were found: (i) the presence of nanofillers accelerated the polymerization process by increasing thermal conductivity [2] or catalyzing the reactions due to the presence of oxygenated groups [3,4]; (ii) nanofillers reduced the polymerization reaction rate due to the steric hindrance that impeded the mobility of the reactants [2], or the increase in viscosity, which hindered the mobility of the reactive species [5]. To the best of our knowledge, few studies have been reported relating to acrylic-based photocurable resins. However, in the case of epoxy-based photocurable resins, nanofillers may reduce the polymerization reaction rate acting as radical scavengers, i.e. deactivating the photoinitiator, or due to its opaqueness against UV wavelength, which led to a reduction of the quantum efficiency. Besides, the surface functional groups may also deteriorate the photo-generated species [6].

Photopolymerization process is mainly governed by two parameters: the penetration depth of the curing light and the critical energy. The penetration depth is specific for each resin, and it is related to the absorbance, which depends on the composition. On the other hand, the critical energy is the energy needed to polymerize [7]. Jacob's working curve is widely used in literature as a basic procedure for testing and characterizing photocurable resins, both theoretically and empirically [8–12]. It establishes a relationship between the absorbed UV light energy and the cured thickness of the photocurable polymer during UV light exposure.

To ensure sufficient interlaminar bonding, the actual curing depth has to be larger than the layer thickness. If curing depth is not large enough, delamination may occur and, therefore, printed structures present inferior properties [9]. To avoid delamination, exposure time could be increased to increase curing depth [8]. However, over-curing could occur, leading to a detriment in printing accuracy.

The photopolymerization of acrylics present three different stages [13]: (i) Initialization: when the photoinitiator, in this case, TPO (diphenyl(2,4,6-trimethylbenzoyl)phosphine oxide) absorbs UV light, free radicals are produced, as shown in Figure 5.1a. These free radicals trigger the polymerization by promoting the homolytic cleavage of carbon bonds (Figure 5.1b).

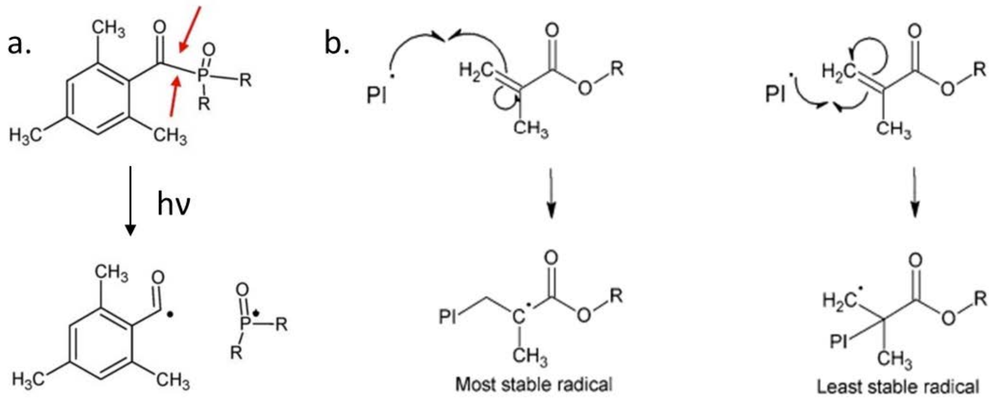

Figure 5.1. *Initialization stage. (a) Free radical production of TPO and (b) Cleavage of carbon double bonds.*

(ii) Propagation: the radical monomer reacts with more acrylate or methacrylate monomers and forms a radical oligomer. This stage can be seen in Figure 5.2.

(iii) Termination: it can occur via combination or disproportion. In the case of methacrylate monomers the most probable pathway is disproportion [14].

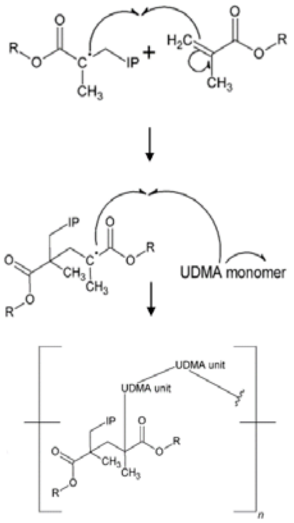

Figure 5.2. *Propagation stage of photopolymerization of acrylic resin.*

However, even without thermal initiator, acrylate and methacrylate monomers have the ability of initiate polymerization if heat is applied [15]. The resin used in this study is made of urethane dimethacrylate and methacrylate monomers; therefore, the reaction that could occur is the methacrylate monomers spontaneous self-initiated polymerization.

When a solvent is added to reduce the viscosity of the resin and improve the dispersibility of the nanofillers, its addition could affect polymerization kinetics of the resin for different reasons: (i) decrease in viscosity, (ii) change in components proportion, (iii) change in polymerization mechanism, because the excess of monomer could disrupt the crosslinked polymer structure [16].

5.2. Penetration of UV light: curing depth and nanoindentation

5.2.1. Experimental methodology

In this chapter, GBN were dispersed in the acrylic resin by using MMA, as explained in Section 4.4.1. To determine the behavior of light inside the resin, penetration depth was studied with Jacobs' working curve, obtaining D_P, E_c and γ_V. Besides, to understand the relation between the layer thickness and the curing depth, nanoindentation tests were carried out.

Nanoindentation measurements were done with the following procedure. In each sample, a matrix of 3x9 measurements with a separation between each measured point of 12, 25 and 50 µm for 25, 50 and 100 µm of layer thickness, respectively were developed and these data were averaged (Figure 5.3).

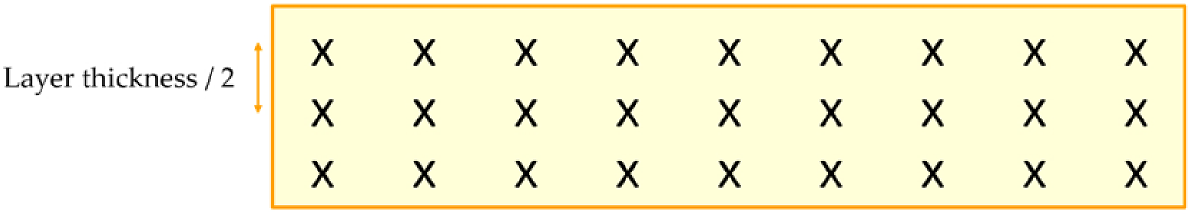

Figure 5.3. *Matrix of nanoindentation measurements.*

Moreover, in samples with 100 µm of layer thickness, three different zones were distinguished to study the penetration of light inside a single layer (Figure 5.4). Zone 1 (top) is the zone of the layer that is the nearest to the UV laser; zone 2 (center) is further that top and, finally, zone 3 (bottom) is the furthest zone. In each part, a matrix of 1x9 measurements were done in three different layers for each sample.

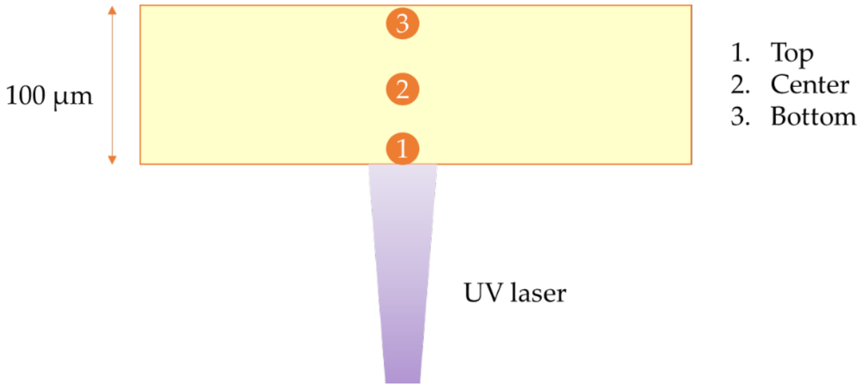

Figure 5.4. *Separated zones measured for samples with 100 µm of layer thickness.*

5.2.2. Results

5.2.2.1. Jacobs' working curve

Figure 5.5 shows the Jacobs' working curves of the different mixtures and the regression lines. C_d was calculated as the average of the measurements carried out at different zones of the cured sample, whilst E_0 was calculated for the different exposure times.

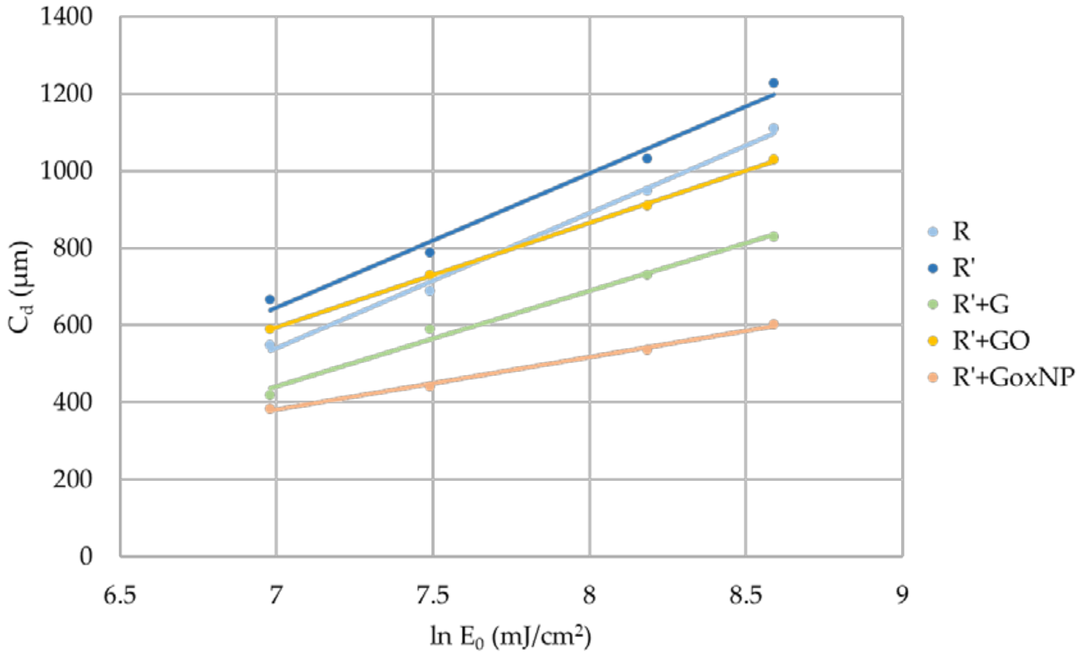

Figure 5.5. *Working curves of acrylic resin and its nanocomposites with different exposure times.*

R' showed the highest values of curing depth, whilst R'+GoxNP showed the lowest. In the case of R'+GO, the curing depth was similar to R. From Jacobs' working curves, the critical energy (E_c), depth of penetration (D_p) and volume efficiency (γ_V) were extracted from the slope and the intersection with x-axis of the regression lines (Table 5.1). These parameters directly affected the C_d. The higher the E_c and/or the lower the D_p, the lower the C_d.

The obtained results are summarized in Table 5.1 where the absorbance values obtained in Chapter 4 (Table 4.10) were also shown because a relationship between absorbance and the parameters obtained from Jacobs' working cure was found.

Table 5.1. Summarized data of Jacobs' working curve.

	E_c (mJ/cm^2)	D_p (µm)	γ_V (mm^3/J)	Abs (a.u.)
R	235.10	351.22	149.4	0
R'	170.18	347.39	204.1	0.02
R'+G	183.09	247.24	135.0	1.62
R'+GO	121.51	271.10	223.1	1.00
R'+GoxNP	65.41	135.46	207.1	1.82

The addition of MMA did not affect D_P for the acrylic-based resin. However, E_c was reduced, which means that less energy was needed to trigger the polymerization. When GBN were added, both parameters change. Comparing to R, D_P was reduced, as well as E_c. However, when R' was taken as reference, the effect of GBN was different - G produced an increase in E_c and a decrease in D_P, whilst GO and GoxNP reduced both parameters. The reduction of E_c observed when GO and GoxNP were added could suggest a catalytic effect of these GBN on the polymerization reaction. The decrease of D_P observed for every GBN could be due to the absorbance of these GBN that led to a reduction of the efficiency of light exposure in terms of free radical generation. This decrease was more pronounced in the case of GoxNP, being consistent with the results observed in the absorbance measurements.

5.2.2.2. Nanoindentation

To study the differences of mechanical properties throughout the layer thickness, normalized values were calculated, taking as a reference the values measured in zone 1. Figure 5.6 shows the results of each nanocomposite.

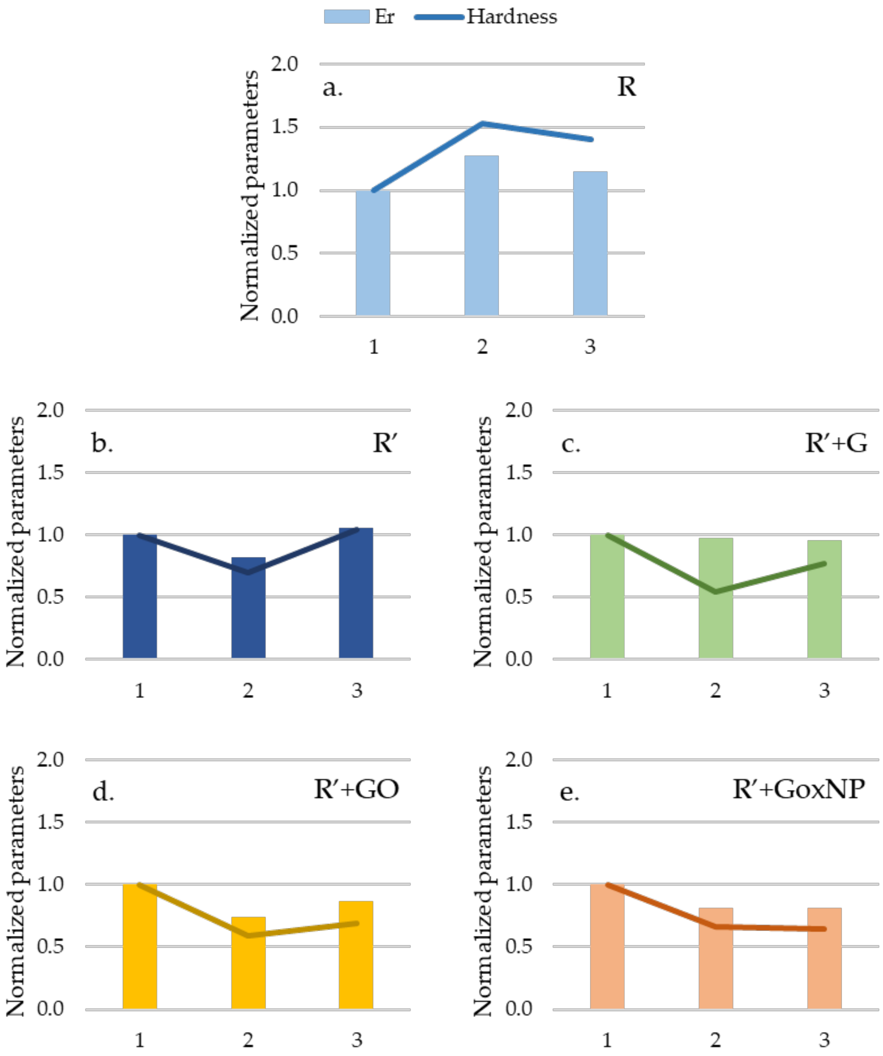

Figure 5.6. *Normalized reduced Young's modulus and hardness measured at different zones of the layer of (a) R, (b) R′, (c) R′+G, (d) R′+GO and (e) R′+GoxNP printed with 100 µm of layer thickness.*

Theoretically, mechanical properties of the top zone should be higher than for the center and bottom because it was directly exposed to the UV light, regardless penetration depth. However, this trend was not found in any case, being the differences negligible considering the high deviations ($p > 0.05$). This, together with the D_P values found in working curves, suggested that the laser was reaching all the points inside the layer and, therefore, in the whole layer polymerization was triggered by UV in the printer and finished by heat and UV.

The effect of MMA and GBN on mechanical properties at nanoscale may be different depending on the layer thickness. Therefore, the comparison of the different mixtures was done for each studied layer thickness (25, 50 and 100 µm). Table 5.2 shows the values of reduced Young's modulus and hardness for the resin.

Table 5.2. *Reduced Young's modulus and hardness of R printed with different layer thickness.*

	Reduced Young's modulus (GPa)			***Hardness (GPa)***		
Layer thickness (μm)	*25*	*50*	*100*	*25*	*50*	*100*
R	2.09 ± 0.32	1.98 ± 0.55	2.83 ± 1.38	0.04 ± 0.01	0.04 ± 0.02	0.07 ± 0.04

To facilitate the comparison and the drawing of conclusion, normalized values were calculated and represented in Figure 5.7. As reference, the values of Table 5.2 were taken for each layer thickness.

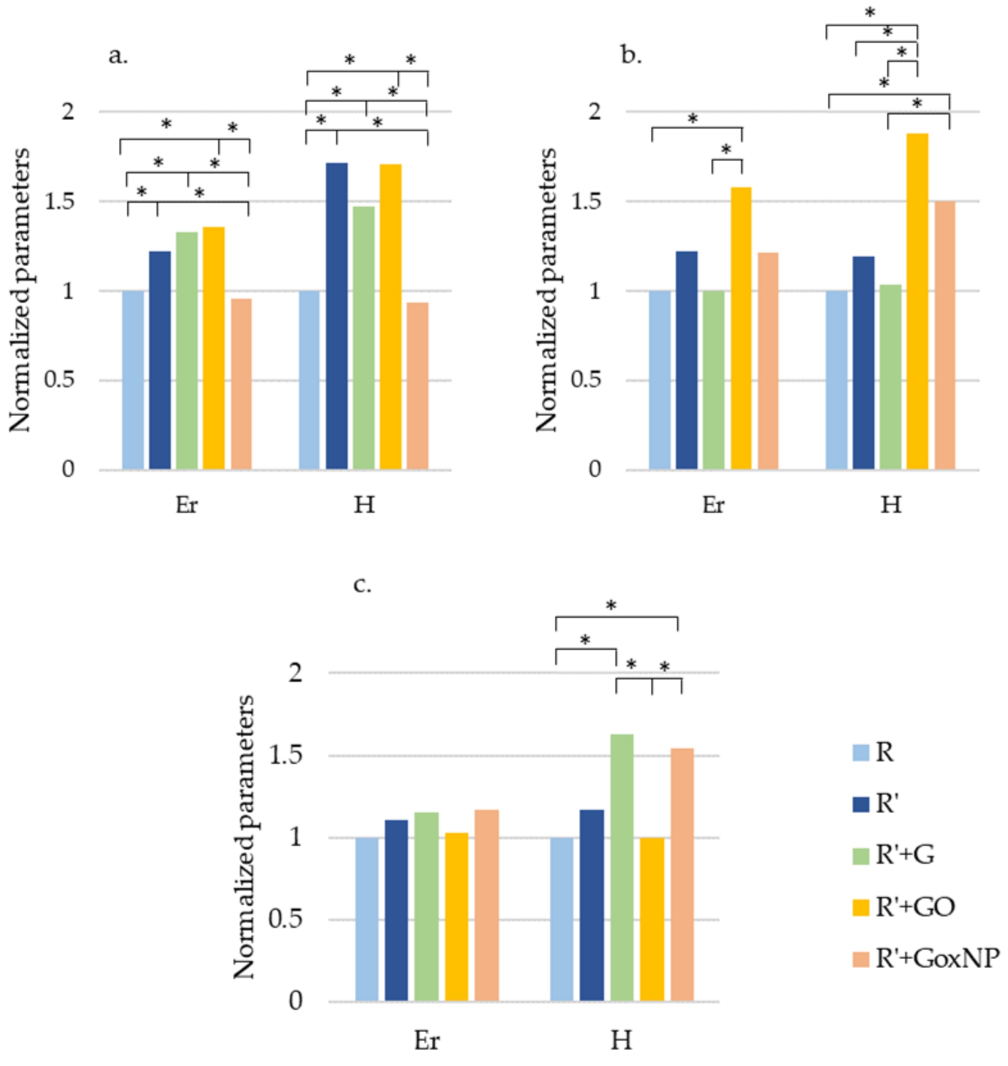

Figure 5.7. *Normalized E_r and H of samples with (a) 25 μm, (b) 50 μm and (c) 100 μm of layer thickness. * means differences with p-value < 0.05*

In general, there are more differences between the samples in terms of hardness than reduced Young's modulus. A significant effect of the addition of MMA was only found for the layer thickness of 25 μm in both, reduced Young's modulus and hardness. It could be because in this case, when the layer thickness is low, the light penetrated well in all the layer and then the polymerization occurs homogenously via UV exposition. As the GBN mainly affect to UV polymerization, as seen in Jacobs' working curves, in this layer that was mainly cured via UV exposure, the effect of GBN was more pronounced that in those cured by two mechanisms (thermal and UV).

When G was added to R', no significant differences were found, however, for the layer thickness of 100 µm, hardness showed an increase with its addition, and for 25 and 50 µm of layer thickness, a slight decrease is found.

In the case of R'+GO, it presented significantly higher ($p\text{-value} < 0.05$) hardness and modulus than R for 25 and 50 µm of layer thickness. However, they are similar for the thickest layer. Compared to R', only the intermediate layer thickness showed higher values.

Finally, when R'+GoxNP samples were analyzed, it was found that their mechanical properties were lower than the other mixtures for the smallest layer thickness, but this decrease in mechanical properties was not found for 50 and 100 µm of layer thickness, being the hardness similar than R'+G for 100 µm.

Therefore, a clear trend was not found for any mixture and the conclusion that may be extracted from the results was that depending on the kind of GBN and the layer thickness the response was different but, in general, GBN did not produce a decrease in mechanical properties at nanoscale. It was also seen that the higher the layer thickness, the lower the differences between the different samples and the original resin.

5.2. Polymerization kinetics

5.2.1. Experimental methodology

Liquid samples of R, R′, R′+G, R′+GO and R′+GoxNP were prepared following the procedure of Section 4.4.1. Polymerization kinetics were carried out as explained in Section 3.2.4.1. MFK model calculated activation energy (E_a) of the polymerization process from, at least, three thermograms obtained at different rates. In this model, E_a was not considered as a constant during the whole process, and it was calculated as a function of the conversion degree of curing. Two different polymerization processes were studied: thermally-triggered and UV-triggered. The first process was carried out with the liquid sample, whilst samples for UV-triggered polymerization were exposed to 2 s of UV light using the UV lamp before the DSC scan. FTIR spectra were recorded after 2s of UV exposition to calculate the degree of polymerization following Eq 3.6.

Finally, samples subjected and non-subjected to UV exposition were polymerized in the DSC chamber and, from the second DSC scan, glass transition temperature was also analyzed. It gives information regarding the crosslinking degree achieved after the thermally- and UV-triggered polymerization of the different nanocomposites.

5.2.2. Results

5.2.2.1. Thermally-triggered polymerization

All the thermograms obtained showed one exothermic peak, which corresponds to the radical polymerization of the resin. In this part of the study, TPO (the photoinitiator) did not produce free radicals because the UV did not trigger its decomposition. Therefore, R polymerization occurred via spontaneous self-initiated thermal polymerization of methacrylate monomers, which was triggered at high temperatures (100-130°C). In general, it was found that this reaction resulted in a low conversion of monomers to polymers and high conversion to oligomers (dimers or trimers) [15].

(1) Effect of MMA addition

The polymerization enthalpy and temperature were calculated from the first heating scan in DSC (Table 5.3). Enthalpy corresponds to the area of the exothermal peak and temperature was determined at the most exothermal point of the curve.

Table 5.3. *Polymerization enthalpy and curing peak temperature of R and R′.*

	$\Delta H_{polymerization}$ (J/g)	**T_p (°C) at different rates (°C/min)**		
		5	**10**	**20**
R	122 ± 3	151 ± 2	162 ± 2	176 ± 3
R′	56 ± 5	152 ± 1	160 ± 2	174 ± 1

The addition of MMA to the resin produced a reduction of 54% in the energy released during polymerization. A ΔH decrease means that MMA promoted and facilitated the polymerization reaction [17]. In terms of peak temperature, it showed similar values for both samples at every rate.

The effect of MMA on conversion curves can be seen in Figure 5.8, where both, conversion curve of R and R’ are shown.

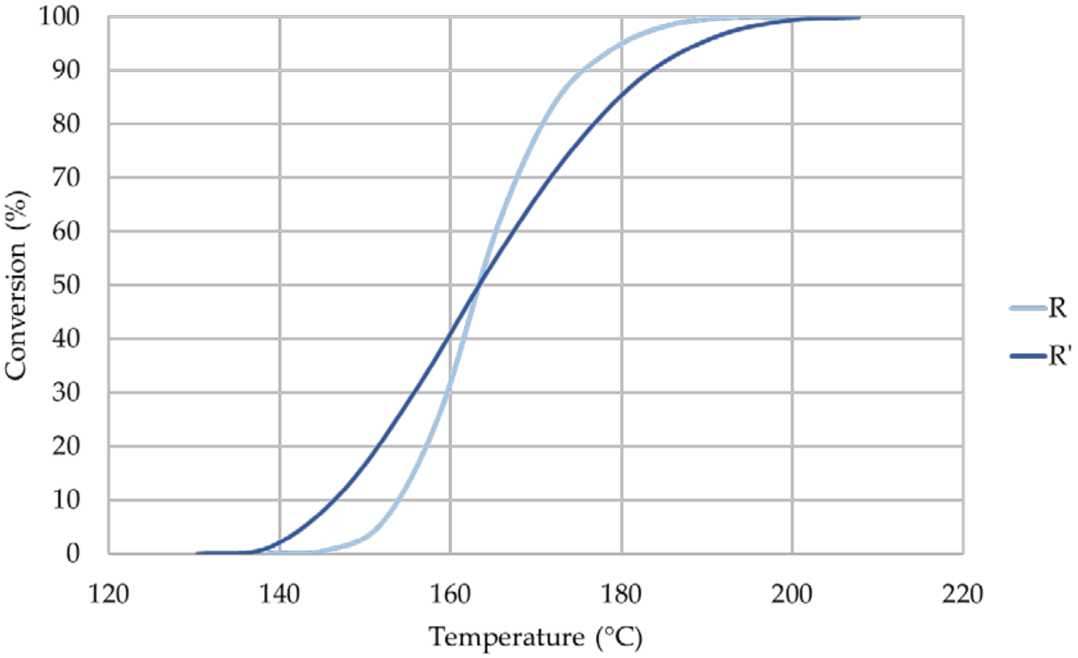

Figure 5.8. *Conversion curves at 10°C/min of thermally-triggered polymerization of R and R’.*

The polymerization reaction of R’ started at lower temperature than R. However, once 50% of conversion was reached, R’ required higher temperatures to continue its polymerization. Besides, the slope of the conversion curve changed slightly on MMA addition, which could be attributed to a change in polymerization rate. The addition of monomer led to a formation of more radicals, which resulted in an increase in the initial polymerization rate (Figure 5.1b).

From conversion curves, activation energy as a function of polymerization degree was calculated and plot in Figure 5.9.

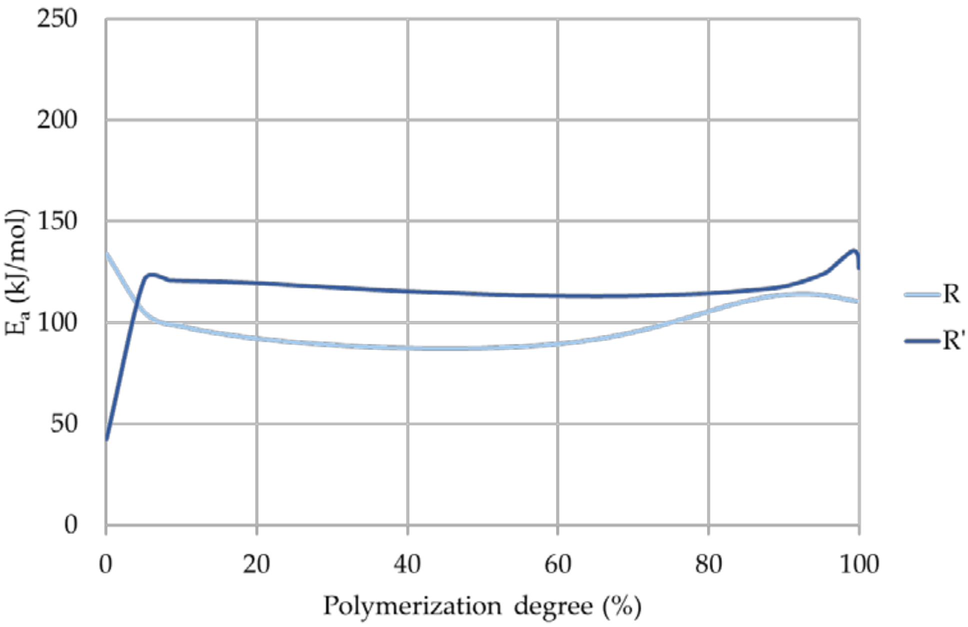

Figure 5.9. *Activation energy of thermally-triggered polymerization of R and R′.*

On the contrary to R, analyzing the activation energy of R′ reaction, it was observed that during the initialization stage the values or E_a are notably lower than propagation and termination stages, which means that MMA favored the reaction. This was probably due to the decrease in viscosity, which resulted in a higher mobility of chains. Besides, with the addition of MMA there was a higher probability of occurrence of spontaneous self-initiated thermal polymerization of MMA compared to larger acrylate monomers (e.g., UDMA).

Once a 5-10% of conversion was achieved, the E_a of R′ was higher due to the increase in viscosity due to the formation of a three-dimensional crosslinked network. Finally, in the termination stage, from around 85% of conversion, E_a in both cases increased because this stage of the reaction was diffusion-controlled because of the high polymerization degree and the restriction of chains mobility [18].

(2) Effect of GBN addition

When GBN were added to the resin, they produced a change in both, polymerization enthalpy and temperature. The parameters for the nanocomposites were shown in Table 5.4. As a reference, results of R′ were also shown.

Table 5.4. *Polymerization enthalpy and curing peak of R′ and R′+GBN.*

	$\Delta H_{polymerization}$ (J/g)	**T_p (°C) at different rates (°C/min)**		
		5	**10**	**20**
R′	56 ± 2	152 ± 3	160 ± 3	174 ± 1
R′+G	29 ± 3	169 ± 1	178 ± 3	181 ± 3
R′+GO	38 ± 2	159 ± 2	168 ± 2	181 ± 2
R′+GoxNP	42 ± 4	164 ± 2	171 ± 2	178 ± 3

GBN showed a decrease in the polymerization enthalpy. This effect was more pronounced for graphene. In all cases, peak temperature was higher than control sample (R′). This increase in the peak temperature showed a retardation effect of GBN in the polymerization reaction [19]. R′+G showed the most pronounce increase in temperature and the lower ΔH; therefore, it is possible that R′+G reached a lower crosslinking or polymerization degree.

Conversion as a function of the temperature was plotted for every nanocomposite and they are shown in Figure 5.10.

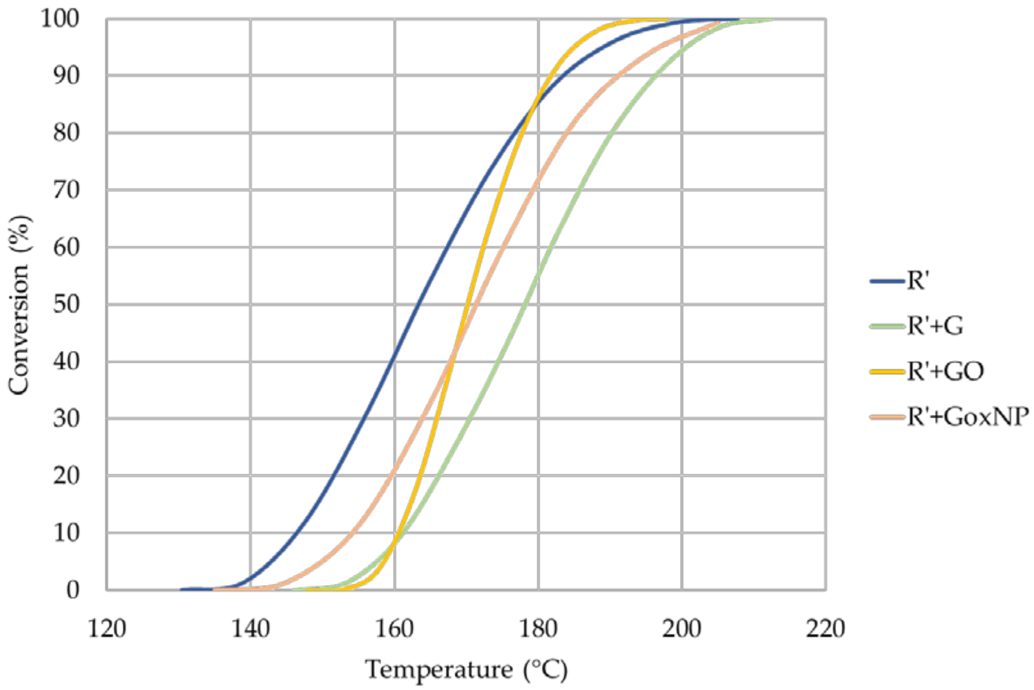

Figure 5.10. *Conversion curves at 10°C/min of thermally-triggered polymerization of R′ and GBN-reinforced R′.*

In the conversion curves, a shift to higher temperatures of the curve produced by GBN was clearly shown. Besides, a change of the slope of the R′+GO curve could indicate a change in polymerization rate towards a faster mechanism, where GO acts as reaction catalyzer.

These effects were better analyzed from the activation energy curves shown in Figure 5.11.

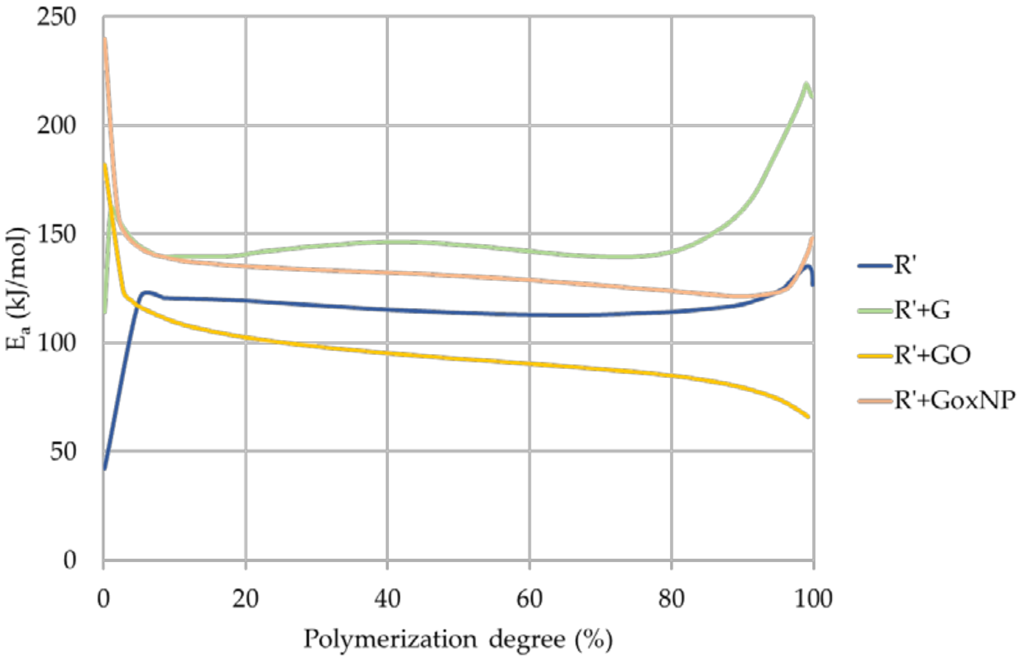

Figure 5.11. *Activation energy of thermally-triggered polymerization of R′ and GBN-reinforced R′.*

It can be observed that GBN had a different effect on E_a during the polymerization. The addition of G resulted in higher activation energy in all the conversion range and it could be attributed to the increase in viscosity and the hindering of chains mobility produced by the presence of graphene [19]. However, although the addition of GO also produced this increase in viscosity, in propagation and termination stages the activation energy needed to complete the reaction was lower than R′. This could be explained by a catalytic effect of the GO. Conversely, despite this catalytic effect during last stages, it is observed that at initialization stage, GO inhibited the self-initiated polymerization. This effect will be discussed later and is attributed to the oxygenated presents on the GO surface. In the case of GoxNP, in the initialization stage, its effect was similar to GO, but in propagation and termination stages it still showed an inhibition effect, probably because of the lower level of oxygenated groups.

5.2.2.2. UV-triggered polymerization

The residual reactivity was also measured. Initially, the acrylic-based resin was already polymerized to a certain degree, but this study was focused on how the reaction proceeded when it is triggered by UV. FTIR was used to calculate the degree of polymerization after 2s of UV exposure. Results obtained from FTIR spectra are shown in Table 5.5.

Table 5.5. *Degree of polymerization of samples subjected to UV for 2s.*

	Polymerization degree (%)
R	8.42
R′	41.03
R′+G	2.87
R′+GO	6.96
R′+GoxNP	4.18

It can be observed that the addition of MMA greatly increased polymerization degree whilst when GBN were added to R′, the polymerization degree decreased, especially in the case of G. This lower polymerization degree agreed with the lower γ_V.

(1) Effect of MMA addition

Table 5.6 shows the analysis of the polymerization peak obtained for the thermal polymerization of samples previously exposed to UV for 2s. In this case, as explained in Chapter 4, two exothermic peaks appeared, but only the second peak corresponded to the polymerization reaction, and it was the peak of interest in this study.

Table 5.6. *Residual enthalpy and curing peak of R and R′ after UV exposure.*

	$\Delta H_{residual}$ (J/g)	***T_p (°C) at different rates (°C/min)***		
		5	**10**	**20**
R	60 ± 3	157± 1	160 ± 2	169 ± 1
R′	108 ± 4	140 ± 3	153 ± 3	160 ± 3

In comparison with thermal polymerization, when polymerization was triggered by UV, the effect of the addition of MMA drastically changed. In this case, the area under the polymerization peak suffered an increase of 74% and the temperature decreased. This reduction in temperature suggests that this composite with MMA polymerized by heat more readily following UV when compared to R, and the increase in enthalpy suggests that the crosslinking degree is higher than R. From the DSC spectra, conversion curves of these samples were obtained (Figure 5.12).

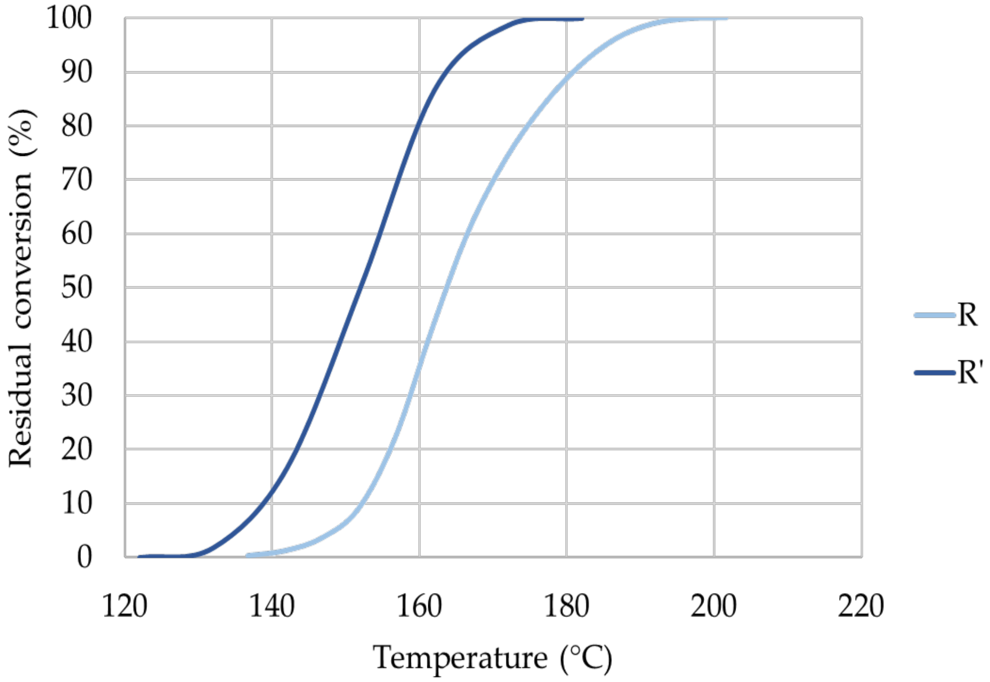

Figure 5.12. *Conversion curves at 10 °C/min of UV-triggered polymerization of R and R′.*

The addition of MMA produced a shift in the curve towards a lower temperature. However, the slope of the curve was the same, meaning that the polymerization rate did not changed. In this case, the photoinitiator was the source of free radicals in both cases and therefore, the presence of MMA did not change the polymerization rate or mechanism. From conversion curves, activation energy was calculated for each residual polymerization degree. The resultant curves are shown in Figure 5.13.

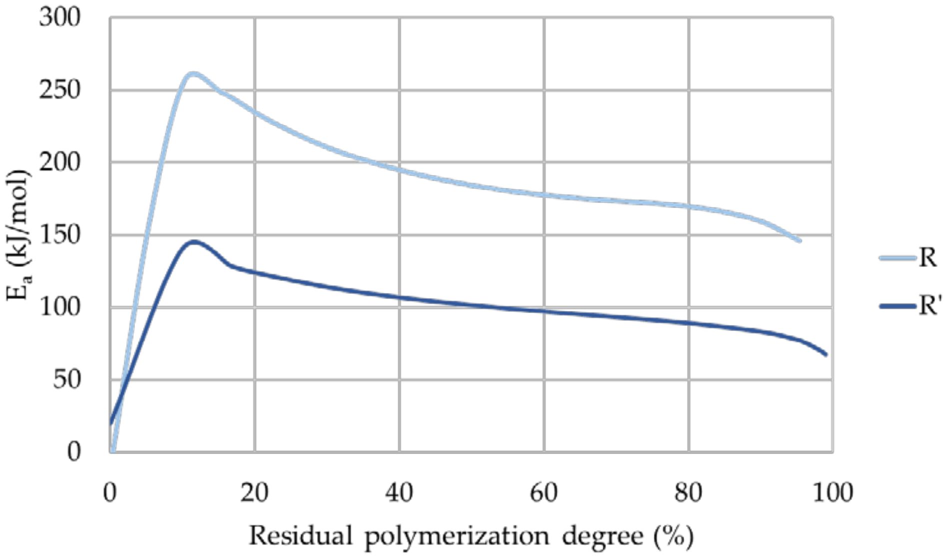

Figure 5.13. *Activation energy of UV-triggered polymerization of R and R′.*

At the beginning, both curves showed low activation energy because the reaction was initiated by UV and therefore, there were free radicals available to polymerize. However, it could be seen how the activation energy of R was higher than R′ for every conversion degree, which was consistent with the catalytic effect previously commented. This could be explained by the higher viscosity of R compared to R′ and the subsequent restriction in chains mobility. Besides, R′ had a higher concentration of monomers available, which could result in a lower E_a.

(2) Effect of GBN addition

Table 5.7 shows the residual enthalpy and the temperature of the polymerization peak of the nanocomposites after UV exposition.

Table 5.7. *Residual enthalpy and curing peak of R′ and R′+GBN after UV exposure.*

	$\Delta H_{residual}$ (J/g)	T_p (°C) at different rates (°C/min)		
		5	**10**	**20**
R′	113 ± 2	140 ± 3	153 ± 3	160 ± 1
R′+G	56 ± 3	155 ± 2	164 ± 3	176 ± 3
R′+GO	81 ± 3	154 ± 4	161 ± 2	176 ± 4
R′+GoxNP	80 ± 2	153 ± 2	163 ± 3	179 ± 2

As reported previously in thermally-triggered polymerization, GBN reduced the energy and increased the temperature. The increase in temperature explains that GBN retarded polymerization and, together with the decrease in enthalpy, suggest a decrease in crosslinking degree.

The representation of the residual conversion after the UV initialization is showed in Figure 5. 14.

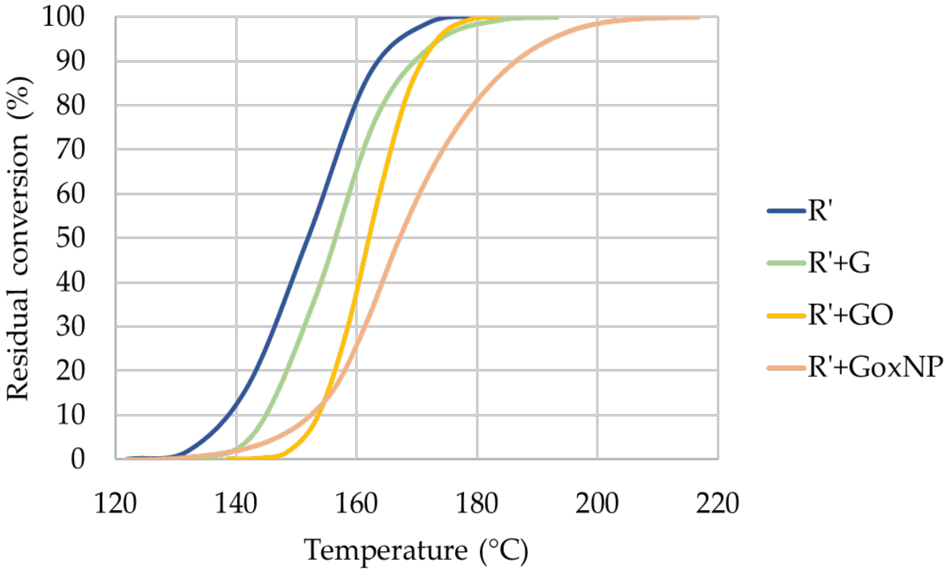

***Figure* 5. 14.** *Conversion curves of UV-triggered polymerization of R′ and GBN-reinforced R′.*

The addition of G did not change the slope of conversion curves. However, the addition of GO slightly increased the slope. This means that the addition of GO modified polymerization rate, probably due to its catalytic effect, which was also observed in Figure 5.10. GoxNP produced a decrease in the conversion curve slope, which could be interpreted as an inhibition in the polymerization process, which was previously observed in thermally-triggered polymerization (Figure 5.10).

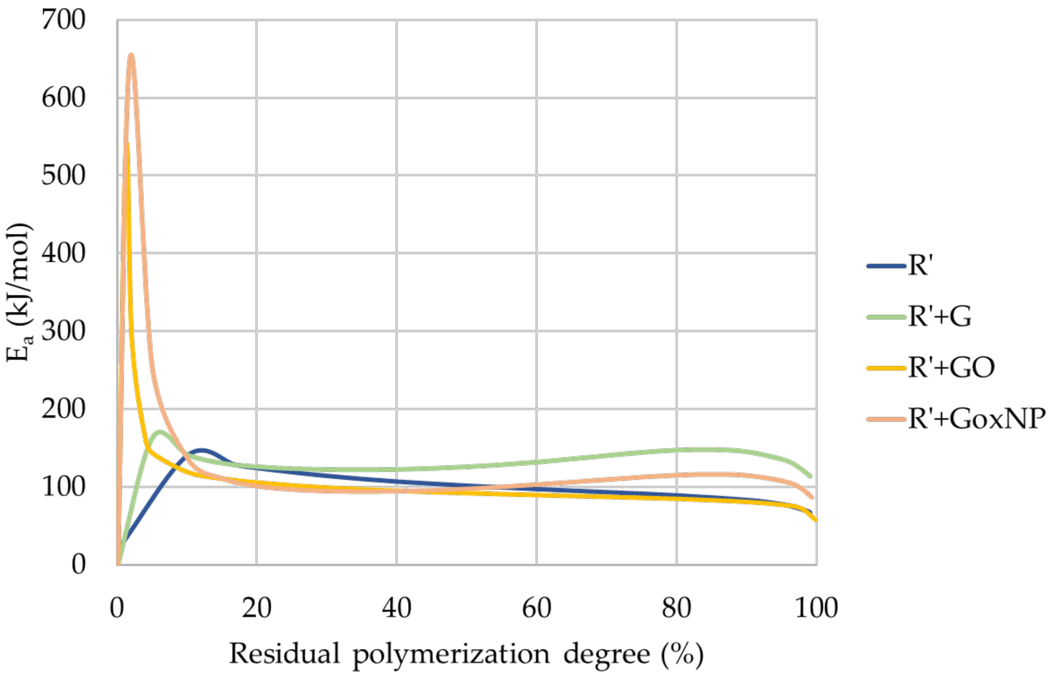

***Figure* 5.15.** *Activation energy of UV-triggered polymerization of R′ and GBN-reinforced R′.*

In relation with the activation energy, Figure 5.15 reported a similar trend to the thermally-initiated polymerization. In the case of GO and GoxNP, at the initial stage, they inhibited the polymerization. Once a certain conversion level was reached, this effect slightly changed and GO catalyzed the reaction, whilst GoxNP still inhibited polymerization. This effect of GoxNP can be seen in the conversion curve (Figure 5. 14) as a decrease in the curve slope. In the case of R'+G mixture, the exposure to UV produced less free radicals, as graphene had a very high absorbance and did not allow the whole light to reach the photoinitiator. For this reason, its polymerization enthalpy was lower and its activation energy was higher.

The trend found for thermally- and UV-triggered polymerization was different and they were compared in the discussion section.

5.2.2.3. Glass transition temperature

Table 5.8 reported the glass transition temperatures of the different samples. The polymerization was triggered by heat and by UV.

Table 5.8. *Glass transition temperature of samples with thermally- and UV- triggered polymerization.*

		T_g (°C)
R	Thermal	209 ± 2
	UV	208 ± 4
R'	Thermal	206 ± 3
	UV	202 ± 3
R'+G	Thermal	208 ± 2
	UV	210 ± 3
R'+GO	Thermal	207 ± 2
	UV	210 ± 4
R'+GoxNP	Thermal	205 ± 4
	UV	211 ± 2

Differences found were within the error of DSC measurements. Therefore, the differences in polymerization did not result in changes in the T_g.

5.3. Discussion of the results

MMA effect (decrease in E_c maintaining D_p) has previously been reported by Hofstetter et al [9] when increasing the photoinitiator content. Therefore, the effect of MMA could be similar to the effect of an increase in photoinitiator amount and promoted the UV polymerization, as can be seen in the increase in γ_V. It could be due to the decrease in viscosity, which increased chains mobility and facilitated the light to reach the photoinitiator, increasing the UV polymerization efficiency.

When GBN were added, absorbance of the resin greatly increased. This increase in absorbance had an effect in the penetration depth of light. It was found that the presence of G, GO and GoxNP produced a reduction in D_p (i.e., 29.6%, 22.8% and 61.4%, respectively), which is consistent with the results observed in the absorbance measurements. The planar shape of GBN may block light scattering throughout the resin [20], resulting in lower penetration depth.

In the case of critical energy, it was found that the addition of MMA produced a reduction of 27.6% of this parameter. Compared to R', GO and GoxNP produced a reduction of E_c and G did not change it. The reduction of E_c observed when GO and GoxNP were added could suggest a catalytic effect of these GBN on the polymerization reaction due to their oxygenated groups. It was previously found [4] that G and GO produced a catalytic effect on the polymerization of acrylics, being the effect of GO more marked that G due to its higher levels of functionalisation.

The parameter of volume efficiency contains the combination of the effect of GBN on D_p and E_c. Compared to R', G reduced the efficiency (-34%) because it blocked the light and did not have a catalytic effect, whilst GO (+9%) increased efficiency by catalyzing polymerization reaction. In the case of GoxNP, it did not produce an important effect on this parameter (+1%). Its catalytic effect was hindered by its low D_p.

Nanoindentation study showed that in every case, UV light cured the whole layer and, therefore, no differences were found between the zones close to the light compared to the most distant areas. These results agree with the D_p found which, in all the cases, was higher than 100 µm. Besides, samples with layer thickness of 100 µm showed more subtle differences than the smaller layers, except for R'+G and R'+GoxNP, which showed higher hardness for thicker layers because they mainly affected UV polymerization and thicker layers had more thermally polymerized resin than thinner layers. Therefore, for G and GoxNP it could be concluded that they needed UV exposition in the printer to build the structure, but higher hardness was obtained when the degree of thermally polymerized resin was higher. However, for R'+GO samples, improvements were found when the layer thickness is low because GO catalyzes UV polymerization.

Polymerization degree measured using FTIR spectroscopy reinforced the conclusions extracted from Jacobs' working curves. The higher polymerization degree was found for R', which showed the lower E_c with the same D_p than R. In the case of R'+GBN, their E_c are also lower than R, but the decrease in D_p resulted in lower polymerization degree because light effect was hampered by the presence of GBN. A relation between polymerization degree and γ_V was found.

However, Jacobs' working curves give little information about polymerization kinetics [9]. For this reason, it is necessary to broaden the study to completely characterize the polymerization process of nanocomposites.

To analyze polymerization kinetics, it is important to highlight some aspects:

- It can be appreciated that all curves showed a sigmoidal form, which indicated that the polymerization reaction was autocatalytic, as corresponds to free-radical polymerization of acrylics [5].
- In general, a change in the heat released during polymerization may be due to two causes [4]: (i) the degree of polymerization has changed and (ii) the polymerization mechanism or rate has been modified. It is possible to know if the reaction mechanism and the polymerization parameters are the same by observing the conversion vs temperature curve. Its shape and slope is related with the polymerization mechanism and rate; therefore, a change in its shape and/or its slope indicates a change in the mechanism and the parameters [21,22].
- In the case of resin with GBN, the decrease of enthalpy showed could be due to two reasons [20]: (i) heat generated during the polymerization could be transferred to GBN, which would result in a decrease of enthalpy; (ii) the planar shape of GBN could block light scattering throughout the resin, impeding, totally or partially, the polymerization.

During thermally-initiated polymerization, when MMA is added, ΔH decreased and the slope of conversion vs temperature curve changed. Therefore, a change in polymerization rate occurred due to the addition of a new monomer: polymerization reaction of R' was faster than R. It could be explained by three events: (i) the concentration of monomer was higher, (ii) the viscosity was lower, and (iii) MMA is the smallest methacrylate monomer with the higher mobility. The combination of these facts made the concentration and the mobility of reactants to increase [23].

To facilitate the comparison and the discussion of the polymerization kinetics, the activation energy required for each stage of the polymerization is summarized in Table 5.9.

Table 5.9. *Activation energy (kJ/mol) of thermally- and UV-triggered resins.*

		Initialization (α=2%)	***Propagation (α=50%)***	***Termination (α=90%)***
R	Thermal	100	88	113
	UV	79	184	159
R′	Thermal	82	114	118
	UV	92	101	83
R′+G	Thermal	156	145	162
	UV	78	126	145
R′+GO	Thermal	124	93	79
	UV	535	92	81
R′+GoxNP	Thermal	158	131	121
	UV	652	97	115

The effect of MMA was also found in activation energy (Table 5.9), especially in the initialization stage. Besides, R′ presents a broader range of temperature to complete its polymerization (Figure 5.8). This could indicate that a less homogeneous network is formed during the reaction [24] because UDMA and MMA could generate different networks.

The addition of GBN also produced changes in polymerization kinetics, but its effect was different depending on the nature of the GBN. The addition of graphene did not change polymerization mechanism nor rate. Therefore, the decrease in enthalpy observed in Table 5.4 could be due to a decrease in crosslinking or polymerization degree. Besides, there was an increase in temperature, which showed a retardation in the polymerization [19]. The extent of the reaction was lower because graphene could cause steric hindrance and did not allow the polymerization to occur properly. This effect was also found in the increase of activation energy compared to R′ in all the stages (Figure 5.11).

In the case of GO, its effect was different. In Figure 5.10, it can be seen a modification on the polymerization rate. It could be due to the catalytic effect of the high concentration of oxygenated groups that GO presented, which was also found in the decrease of enthalpy [17]. However, this effect was not shown at the beginning of the reaction, where GO inhibited polymerization acting as radical scavenger probably due to its oxygenated groups [6]. These groups are electrophiles and they can react with nucleophiles carbons of methacrylate monomers, inhibiting this first stage of the reaction.

Finally, GoxNP effect was midway between G and GO. It decreased the enthalpy because the crosslinking or polymerization degree achieved was lower than R′. As GO, it inhibited polymerization reaction via radical scavenging, increasing activation energy (Figure 5.11). However, due to the lower amount of oxygenated groups, this trend was found in every stage, especially the initialization.

When polymerization was initiated by UV exposure, the reaction completion by heat was studied by DSC. It is important to highlight that in this case the initial conversion was not 0, since some polymerization occurred during the UV exposure. This previous polymerization was not monitored, but, as explained above, polymerization degree was obtained by FTIR spectroscopy (Table 5.5). It can be seen that conversion vs temperature curves of R and R’ presented a similar slope (Figure 5.12). Therefore, a change in polymerization rate did not occurred. R’ demonstrated higher initial polymerization degree than R and, for this reason, the polymerization released more energy.

In the case of R’+G, it was previously found, by absorbance measurements and Jacobs’ working curve, that light could not reach photoinitiator because of the presence of G. For this reason, there was less free radicals present in the mixture and the polymerization progress was retarded. It was shown in a lower enthalpy, higher polymerization temperature and higher activation energy. When GO and GoxNP were added, in the first stage, it seemed that they acted as radical scavenger due to its phenolic hydroxyl or carboxyl groups on its surface. These groups may react with the initiator primary radicals by hydrogen abstraction. This resulted in a reduction in the initiator efficiency and, therefore, a retardation of the initialization stage of the reaction and an increase in activation energy [25] (Table 5.9). When the reaction progressed, the functional groups on the surface were not free and the scavenger effect disappeared.

If the released enthalpy of thermally-triggered polymerization is compared to UV-triggered polymerization, different trends were found. At this point, it is important to highlight again that UV-triggered initialization stage is not the real initialization because the formation of free radicals was done prior to these tests and it was not monitored. In all cases, it was found that the enthalpy for UV-triggered polymerization was higher than for the reaction triggered by heat. It could be explained by the initial polymerization degree than involved an increase in viscosity and, therefore, an increase in activation energy. This trend was not found for R since it did not have MMA in its composition and, therefore, the spontaneous self-initiated polymerization probably did not occur in the same extent.

Finally, no significant changes were observed in T_g values, which suggests that, despite the changes produced by MMA and GBN on the polymerization process, the resulting polymer was not affected in terms of glass transition.

5.4. Conclusions of this chapter

This chapter focused on the effect of MMA and GBN on the polymerization reaction of an acrylic-based photopolymer when this reaction has been triggered by heat or UV. The addition of MMA produced improvements in dispersibility and its presence favors the interaction of light with the resin by increasing chains mobility. It resulted in an enhancement of both, thermal and UV polymerization. The effect of GBN depended on the kind of nanofiller:

- In the case of G, it inhibited thermal and UV polymerization, as was observed in the increase in activation energy and in Jacobs' working curve. When it was added to the resin, it hindered the penetration of UV light, resulting in lower volume efficiency.
- GO showed a double effect. On one hand, it chemically inhibited the polymerization reaction during the initialization stage but, conversely, during the propagation stage the R'+GO showed a higher polymerization rate than R'. Therefore, it showed a catalytic effect during this stage. In the case of UV polymerization, GO produced a decrease in D_P, but it was counterbalanced by the catalytic effect, resulting in higher volume efficiency.
- A similar trend than GO was found by GoxNP, but the reduction of E_c was lower than GO and the volume efficiency was not affected by its presence. GoxNP chemically inhibited polymerization when it was triggered by heat. In the case of UV-triggered polymerization, GoxNP acted as radical scavenger, increasing the activation energy of the whole polymerization process, especially initialization when a higher amount of oxygenated groups are available to react with free radicals.

Therefore, this research study demonstrated that G negatively affected the polymerization process and printing parameters must be optimized, while GO favored the polymerization, without presenting any negative effect. GoxNP affected polymerization, but printability was found to be adequate (Chapter 4). Besides, MMA can be used to get nanocomposites with homogenously dispersed nanofillers, which will allow to take advantage of the improvements of nanofillers together with the good performance of Additive Manufacturing.

5.5. References

[1] H. Quan, T. Zhang, H. Xu, S. Luo, J. Nie, X. Zhu, Photo-curing 3D printing technique and its challenges, Bioact. Mater. 5 (2020) 110–115. https://doi.org/10.1016/j.bioactmat.2019.12.003.

[2] S. Rehman, S. Akram, A. Kanellopoulos, A. Elmarakbi, P.G. Karagiannidis, Development of new graphene/epoxy nanocomposites and study of cure kinetics, thermal and mechanical properties, Thermochim. Acta. 694 (2020) 178785. https://doi.org/10.1016/j.tca.2020.178785.

[3] X. Chen, W. Jiang, B. Hu, Z. Liang, Y. Zhang, J. Kang, Y. Cao, M. Xiang, Effects of graphene oxide size on curing kinetics of epoxy resin, RSC Adv. 11 (2021) 29215–29226. https://doi.org/10.1039/d1ra05234a.

[4] E. Paz, Y. Ballesteros, J. Abenojar, J.C. del Real, N.J. Dunne, Graphene oxide and graphene reinforced PMMA bone cements: Evaluation of thermal properties and biocompatibility, Materials (Basel). 12 (2019) 3146. https://doi.org/10.3390/ma12193146.

[5] V. García-Martínez, M. R.Gude, S. Calvo, M.R. Martínez-Miranda, A. Ureña, Influence of graphene nanoplatelets on curing kinetics and rheological properties of a benzoxazine resin, Mater. Today Commun. 24 (2020) 100990. https://doi.org/10.1016/j.mtcomm.2020.100990.

[6] M. Sharif, B. Pourabbas, M. Sangermano, F. Sadeghi Moghadam, M. Mohammadi, I. Roppolo, A. Fazli, The effect of graphene oxide on UV curing kinetics and properties of SU8 nanocomposites, Polym. Int. 66 (2017) 405–417. https://doi.org/10.1002/pi.5271.

[7] J. Bennett, Measuring UV curing parameters of commercial photopolymers used in additive manufacturing, Addit. Manuf. 18 (2017) 203–212. https://doi.org/10.1016/j.addma.2017.10.009.

[8] J.H. Lee, R.K. Prud’homme, I.A. Aksay, Cure depth in photopolymerization: Experiments and theory, J. Mater. Res. 16 (2001) 3536–3544. https://doi.org/10.1557/JMR.2001.0485.

[9] C. Hofstetter, S. Orman, S. Baudis, J. Stampfl, Combining cure depth and cure degree, a new way to fully characterize novel photopolymers, Addit. Manuf. 24 (2018) 166–172. https://doi.org/10.1016/j.addma.2018.09.025.

[10] K. Kowsari, B. Zhang, S. Panjwani, Z. Chen, H. Hingorani, S. Akbari, N.X. Fang, Q. Ge, Photopolymer formulation to minimize feature size, surface roughness, and stair-stepping in digital light processing-based three-dimensional printing, Addit. Manuf. 24 (2018) 627–638. https://doi.org/10.1016/j.addma.2018.10.037.

[11] D.C. Aduba, E.D. Margaretta, A.E.C. Marnot, K. V. Heifferon, W.R. Surbey, N.A. Chartrain, A.R. Whittington, T.E. Long, C.B. Williams, Vat photopolymerization 3D printing of acid-cleavable PEG-methacrylate networks for biomaterial applications, Mater. Today Commun. 19 (2019) 204–211. https://doi.org/10.1016/j.mtcomm.2019.01.003.

[12] Y. Li, Q. Mao, J. Yin, Y. Wang, J. Fu, Y. Huang, Theoretical prediction and experimental validation of the digital light processing (DLP) working curve for photocurable materials, Addit. Manuf. 37 (2021) 101716. https://doi.org/10.1016/j.addma.2020.101716.

[13] T. Pirman, M. Ocepek, B. Likozar, Radical Polymerization of Acrylates, Methacrylates, and Styrene: Biobased Approaches, Mechanism, Kinetics, Secondary Reactions, and Modeling, Ind. Eng. Chem. Res. 60 (2021) 9347–9367. https://doi.org/10.1021/acs.iecr.1c01649.

[14] Y. Nakamura, S. Yamago, Termination Mechanism in the Radical Polymerization of Methyl Methacrylate and Styrene Determined by the Reaction of Structurally Well-Defined Polymer End Radicals, Macromolecules. 48 (2015) 6450–6456. https://doi.org/10.1021/acs.macromol.5b01532.

[15] S. Srinivasan, A.M. Rappe, M. Soroush, Theoretical Insights Into Thermal Self-Initiation Reactions of Acrylates, in: Comput. Quantum Chem., Elsevier Inc., 2019: pp. 99–134. https://doi.org/10.1016/b978-0-12-815983-5.00004-0.

[16] E.A. Ayaz, R. Durkan, Influence of acrylamide monomer addition to the acrylic denture-base resins on mechanical and physical properties, Int. J. Oral Sci. 5 (2013) 229–235. https://doi.org/10.1038/ijos.2013.69.

[17] Q. Bi, L. Hao, Q. Zhang, P. Wang, P. Xu, Y. Ding, Study on the effect of amino-functionalized alumina on the curing kinetics of epoxy composites, Thermochim. Acta. 678 (2019) 178302. https://doi.org/10.1016/j.tca.2019.178302.

[18] W. Bessa, D. Trache, M. Derradji, A.F. Tarchoun, Non-Isothermal Curing Kinetics of Alkali-Treated Alfa Fibers/Polybenzoxazine Composites Using Differential Scanning Calorimetry, ChemistrySelect. 5 (2020) 5374–5386. https://doi.org/10.1002/slct.202000596.

[19] S.H. Ryu, J.H. Sin, A.M. Shanmugharaj, Study on the effect of hexamethylene diamine functionalized graphene oxide on the curing kinetics of epoxy nanocomposites, Eur. Polym. J. 52 (2014) 88–97. https://doi.org/10.1016/j.eurpolymj.2013.12.014.

[20] D. Park, Y. Kim, S. Lee, J. Kim, Selectively distributed graphene in 1,6-hexanediol diacrylate/epoxy composites via digital light processing 3D printing for enhanced thermal conductivity, Synth. Met. 276 (2021) 116763. https://doi.org/10.1016/j.synthmet.2021.116763.

[21] S.L. Qiu, C.S. Wang, Y.T. Wang, C.G. Liu, X.Y. Chen, H.F. Xie, Y.A. Huang, R.S. Cheng, Effects of graphene oxides on the cure behaviors of a tetrafunctional epoxy resin, Express Polym. Lett. 5 (2011) 809–818. https://doi.org/10.3144/expresspolymlett.2011.79.

[22] L. Li, X. Liao, X. Sheng, P. Liu, Z. Hao, L. He, G. Qin, Influence of surface modified graphene oxide on the mechanical performance and curing kinetics of epoxy resin, Polym. Adv. Technol. 31 (2020) 1865–1874. https://doi.org/10.1002/pat.4913.

[23] M.J. Minkler, X. Hou, N. Alizadeh, M.L. Auad, A.K. Schindler, L.E. Beckingham, B.S. Beckingham, Curing kinetics of tetrathiol-crosslinked diglycidyl ether of bisphenol A and poly(ethylene oxide)diglycidylether, Mater. Lett. 310 (2022) 131491. https://doi.org/10.1016/j.matlet.2021.131491.

[24] C. Monteserín, M. Blanco, E. Aranzabe, A. Aranzabe, J.L. Vilas, Effects of graphene oxide and chemically reduced graphene oxide on the curing kinetics of epoxy amine composites, J. Appl. Polym. Sci. 134 (2017) 44803. https://doi.org/10.1002/app.44803.

[25] I.S. Tsagkalias, D.S. Achilias, Role of Functional Groups in the Monomer Molecule on the Radical Polymerization in the Presence of Graphene Oxide. Polymerization of Hydroxyethyl Acrylate under Isothermal and Non-Isothermal Conditions, Molecules. 27 (2022) 345. https://doi.org/10.3390/molecules27020345.

CHAPTER 6

MECHANICAL PROPERTIES OF THE NANOCOMPOSITES

Table of Contents

In this chapter, mechanical properties of the nanocomposites are investigated. In Chapter 4, it had been found that the expected reinforcing effect of GBN did not appear for printed samples. Therefore, samples obtained by compression molding and UV molding were analyzed to study the behaviour of the material in mass and suppress the effect of the printing process. Besides, different post-treatments for the printed acrylic resin were explored in terms of tensile, dynamo-mechanical and thermal response.

6.1. Introduction

VAT polymerization technologies have demonstrated some limitations with the addition of GBN in terms of the modification of mechanical properties, regardless of the degree of dispersion achieved. Hanon et al [1] found a reduction in ultimate tensile strength (UTS) of Digital Light Processing (DLP) printed resin when graphene nanoplatelets (GNP) were added for every layer thickness (35, 50 and 100 μm), being the UTS for the thinner layer the highest. The decrease in the mechanical performance was attributed to the generation of a more porous structures due to the presence of GNP and the scattering of UV light, which generated unpolymerized regions around the nanoparticles. It was also found that during the SLA printing process, less cohesion occurs between the layers due to the presence of nanofillers [2]. Conversely, Feng et al. [3] compared conventional manufacturing (direct casting) with the SLA of graphene-reinforced resin and found an increase in mechanical properties when SLA was used as manufacturing technology. It could be due to the defects and bubbles that inevitably appeared during casting, being the printed samples almost defect-free. Therefore, the decrease in mechanical properties found by some researchers could be due to different effects of the nanofillers on the printing process: decrease in cure depth and penetration depth, reduction of polymerization degree, the absorbance of UV light, etc.

Besides, VAT polymerization technologies are based on the polymerization of photopolymers by UV exposition. However, regardless of the addition of GBN, this polymerization is not complete during the manufacturing process in the printer due to different reasons [4]: (i) low reaction temperature, which results in trapped free radicals; (ii) radicals' poor efficiency; (iii) fast curing monomers and short UV exposure times, and (iv) high viscosity of the resin, which hinders the dispersion and reaction of radicals.

Therefore, printed samples must be subjected to post-treatments to achieve complete polymerization. Mendes-Felipe et al. [5] found that postcuring processes at room temperature with and without UV highly affected mechanical properties, crosslink density and T_g of samples obtained by SLA. Cingesar et al. [6] explored different post-treatments with and without UV exposition and found that mechanical, thermal and physico-chemical properties were affected by the treatment. Besides, Manapat et al. [7] reported a decrease in the mechanical properties of printed parts compared to casted parts when Grey Forms resin with GO was used. To obtain similar properties, a mild annealing (50 or 100 °C for 12 hours) was needed. The best results were found for 100 °C for 12 hours. They hypothesized that the improvement was due to the removal of GO wrinkles.

Both, post-treatments with and without UV light were explored in the literature. However, Bauer et al. [8] stated that UV post-treatment can only marginally increase crosslinking unless an additional photoinitiator was added to the material. Therefore, thermal post-treatment of acrylate based-resins is achieved via thermal self-initiation reactions, which do not depend on photoinitiator availability.

It is important to keep in mind some limitations of VAT photopolymerization technologies. One of the main shortcomings of these technologies is the distortion caused by shrinkage during polymerization and layer-by-layer manufacturing processes. Residual stresses generated during this process can cause cracks and delamination, which leads to a decrease in mechanical properties [9]. Even using commercial resins, shrinkage appears; therefore, when printing nanocomposites it is an important aspect to study.

Shrinkage involves two different components: chemical or polymerization and thermal shrinkage. The first kind of shrinkage occurs during crosslinking of the photopolymer and depends on the chemical composition and polymerization reaction. Green samples (printed samples without any post-treatment) present different curing percentages in their bulk due to different exposure to the laser during the printing process. For this reason, during the post-curing process samples shrink disproportionately causing distortion [10].

Chemical shrinkage can also be affected by the source that initiates polymerization since it can be triggered by heat or by UV. Fuh et al. [10] found that different amount of energy is released when heat or UV polymerization occurs, being the energy of heat polymerization lower than UV polymerization.

Mechanical properties of printed samples depend on many factors [11]: adhesion between layers, possible internal stresses due to shrinkage, polymerization degree, post-curing process, etc. All these factors can hinder the reinforcing effect of GBN – starting from the premise that they are properly dispersed. In this chapter, samples were manufactured with a hot plate press to reduce the effect of the manufacturing process since parts were not manufactured layer-by-layer and, therefore, adhesion between the layers did not affect final properties and they are less affected by shrinkage and subsequent internal stresses. The objective of this part of the thesis is to understand which factors affect the mechanical performance of printed samples and how these properties are affected by each factor. Factors were classified into three groups:

- Polymerization: together with the conclusions obtained in Chapter 5, samples prepared by molding were studied to remove the effect of the layer-by-layer manufacturing and elucidate the effect of the polymerization source and trigger: by heat or UV-light.
- Adhesion between layers: printed and molded samples were compared and by micrographs the interlayer zone was analyzed.
- Internal stresses: it was already explained how shrinkage produced during polymerization could result in internal stresses, which could affect mechanical performance. To study the possibility of reducing these internal stresses, different post-treatments were explored.

This methodology is summarized in Figure 6.1.

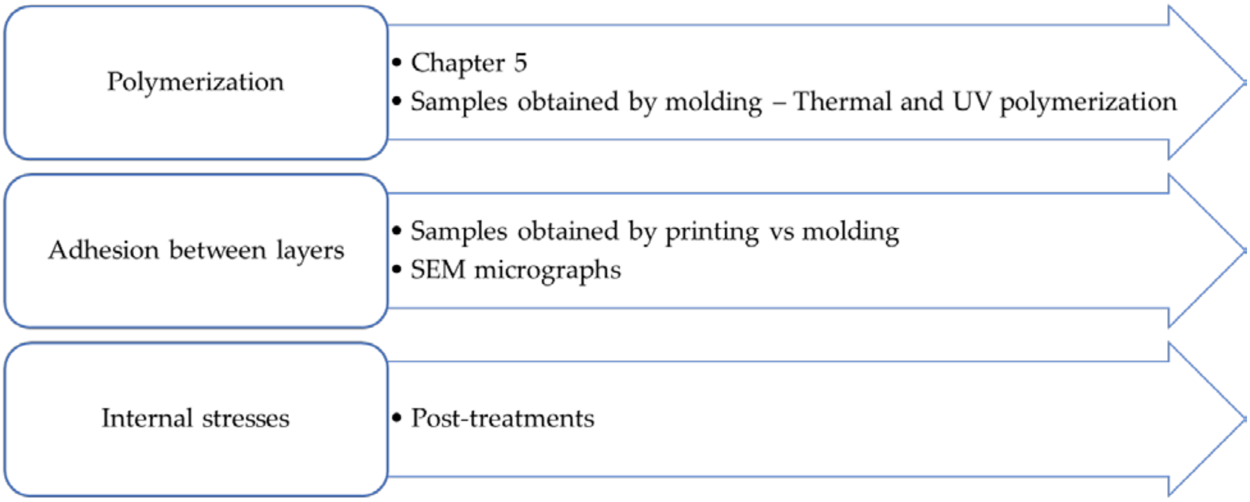

Figure 6.1. *Factors affecting mechanical performance of nanocomposites and methodology used to analyze them.*

6.2. Mechanical properties of thermal and UV-polymerized nanocomposites

To obtain samples polymerized by heat and/or UV, different tests were carried out. Samples were divided into three main groups, depending on the way they were manufactured: (i) samples obtained by compression molding (thermally polymerized), where the main part of the polymerization occurred in the hot plates press (HPP), (ii) samples obtained by UV molding (UV polymerized), where the polymerization occurred in the FormCure chamber, and (iii) samples obtained by additive manufacturing (SLA).

6.2.1. Experimental methodology

6.2.1.1. Experimental design

Standard dog bone samples were obtained with a silicone mold. The cycle in HPP was the same for all the samples: 11 minutes at 160°C and cooling down with water.

Samples with UV exposition before HPP ("UV + HPP"), were subjected to UV for 2 seconds at room temperature using the UV LED lamp. Conversely, samples with UV exposition after HPP ("HPP + Post") were subjected to the post-printing process.

At least three batches of five samples were prepared for each condition. The different studied combinations of heat and UV exposure are shown in Table 6.1.

Table 6.1. *Conditions and nomenclature of samples prepared by compression molding.*

	Temperature (°C)	*Pressure (MPa)*	*Time (min)*	*UV application*
HPP 11′	160	0.8	11	No
HPP 11′ + Post				After HPP
UV + HPP 11′				Before HPP
UV + HPP 11′ + Post				Before and after HPP

To prepare samples by UV molding (Table 6.2), a FormCure chamber was used for both, "UV 11′" and "Post" processes. "UV 11′" process was carried out at room temperature (20 ± 2°C) with UV exposition, whilst "Post" process was carried out as explained above.

Table 6.2. *Conditions and nomenclature of samples prepared by UV molding.*

	UV Exposure time (min)	*Postcuring*
UV 11′	11	No
UV 11′ + Post		UV + 80°C for 90 minutes

Besides, they were compared with samples obtained by SLA: "UV (printer)" and "UV (printer)+Post". Therefore, samples were prepared with different sources of initialization and propagation of the polymerization. They are summarized in Figure 6.2.

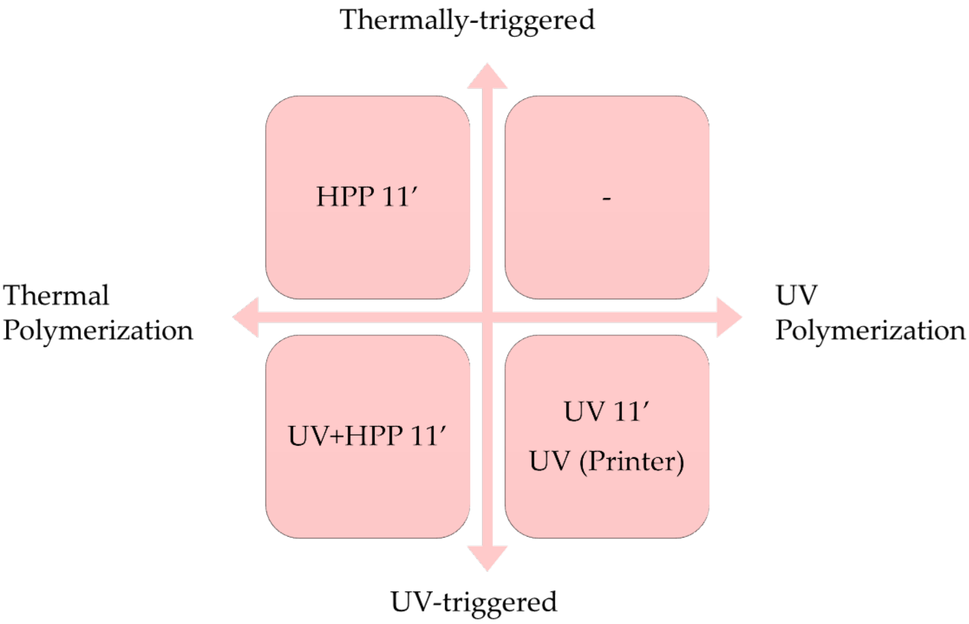

Figure 6.2. *Matrix of studied samples classified by the trigger and the propagation of the polymerization sources.*

6.2.1.2. Post-curing treatment optimization

Besides, postcuring process needed to be optimized. To do that, dog bone standard samples were prepared with the SLA printer with a layer thickness of 100 μm. They were tested following the procedure explained in Section 3.2.7.2.

Post-curing consists of two steps: firstly, samples were immersed in IPA in the FormWash and then, samples were placed inside the FormCure chamber. This process determines the final mechanical properties of the samples, and it needs to be optimized. The manufacturer suggested 10 min of IPA cleaning followed by 15 min at 60 °C in the FormCure. However, the manufacturer suggested that 30 min at 60 °C resulted in a higher Young's modulus. For that reason, this was the time that was tested.

To optimize the postcuring process, one-factor-at-time (OFAT) was used to reduce the number of tests needed. Three factors were studied: time in the FormCure (t), the temperature in the FormCure (T) and time in FormWash (C). Two levels were set for each parameter (Table 6.3).

Table 6.3. *Parameters and their levels for OFAT method.*

Parameter	*Level -*	*Level +*
T	60 ºC	80 ºC
t	30 minutes	90 minutes
C	5 minutes	10 minutes

Eight configurations were tested and at least four samples were manufactured for each one. They are shown in Table 6.4.

Table 6.4. *Experiments were carried out to optimize post-curing process.*

Configuration	*T*	*t*	*C*
1	-	-	-
T	+	-	-
t	-	+	-
C	-	-	+
tC	-	+	+
TC	+	-	+
Tt	+	+	-
TtC	+	+	+

Tensile strength was used as a response to obtain the factor effects by applying Yates algorithm [21].

6.2.2. Results

6.2.2.1. Effect of GBN on samples obtained by different trigger sources

To compare both thermally and UV-triggered polymerized samples, dog bone samples were manufactured by compression molding. Thermally-triggered polymerized samples correspond to

HPP 11′ samples, whilst UV-triggered polymerized samples are referred to as UV+HPP 11′. The tensile strength of both is compared in Figure 6.3.

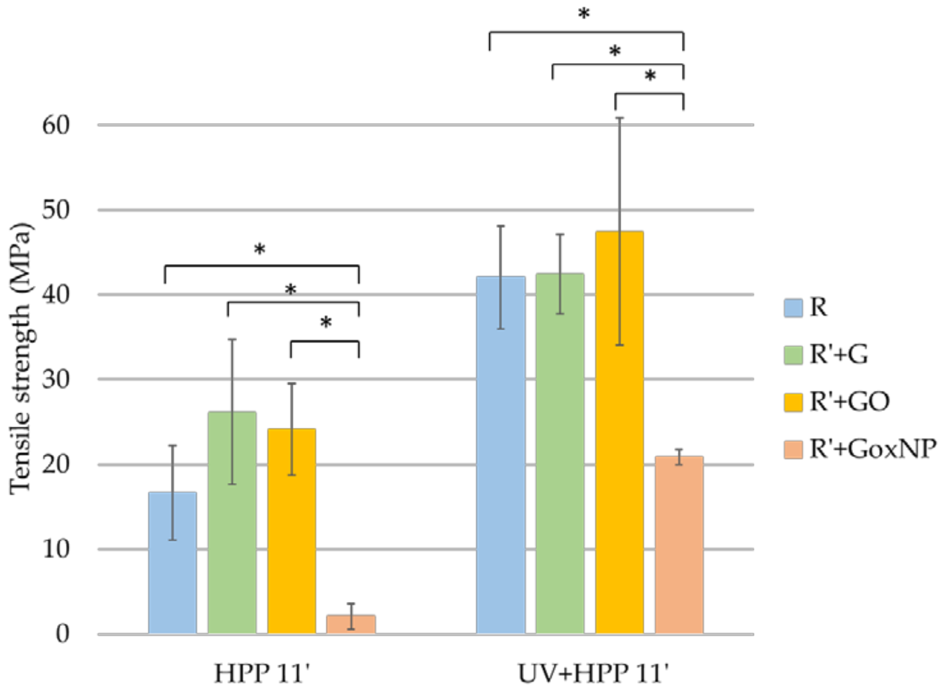

Figure 6.3. *Thermally and UV-triggered polymerized samples obtained by compression molding. * means differences with p-value < 0.05*

These samples showed the difference between the source that initiated the polymerization. In both cases, propagation and termination were carried out by temperature and pressure. It was found that for all the samples, UV-triggered polymerization resulted in higher mechanical properties. The addition of G in HPP11′ samples led to a slight increase in tensile strength, which was not found for UV-triggered polymerized samples. GO produced a small increase in tensile strength for both trigger sources. In the case of GoxNP, its addition resulted in a decrease in mechanical properties in both cases probably due to the higher activation energy required to polymerized, regardless of the source that initiated the process, found in Chapter 5.

To check if differences found in terms of mechanical performance were due to differences in the polymerization degree, it was calculated, and the results are shown in Table 6.5.

Table 6.5. *Polymerization degree of thermally- and UV-triggered samples obtained by compression molding.*

	R	*R′+G*	*R′+GO*	*R′+GoxNP*
HPP 11′	29.2	34.5	28.7	16.4
UV + HPP 11′	50.5	56.6	62.7	19.4

Analyzing the achieved polymerization degrees, the most important differences compared to R were found for R’+GO (in the case of UV+HPP 11’) and R’+GoxNP samples (in both cases). When polymerization occurred by heat, regardless of the trigger source, i.e. thermal or UV, is was found that mechanical performance was directly related with the polymerization degree. Besides, the reduction on mechanical properties of R’+GoxNP were due to the inhibition of the polymerization process, as was found in Chapter 5.

6.2.2.2. Effect of GBN on samples obtained by different polymerization sources

Samples obtained by a different kind of polymerization (i.e. thermal and UV) were compared. In this case, the whole polymerization process occurred by heat (HPP 11’) or by UV (UV 11’). Results are shown in Figure 6.4.

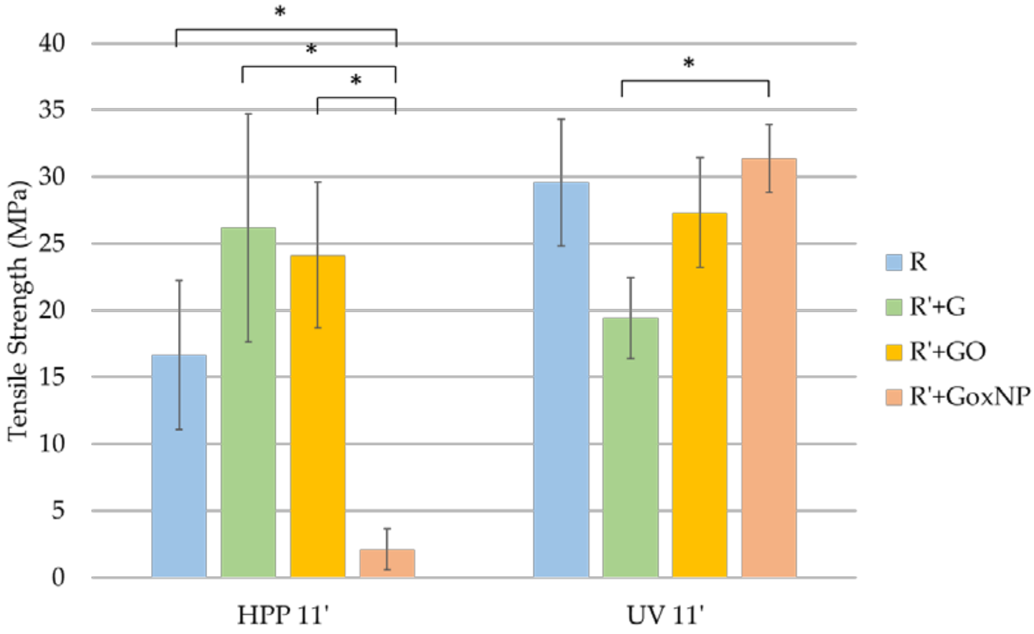

Figure 6.4. *Tensile strength of samples obtained by compression and UV molding. * means differences with p-value < 0.05*

All samples except R’+G presented higher tensile strength when the polymerization occurred by UV than thermal, +78% for R, +13% for R+GO and +140% for R+GoxNP. In the case of R’+G, samples obtained by UV polymerization show slightly lower strength (-26%). It is important to highlight that G and GO produced improvements in the resin when they were thermally polymerized, however, these improvements were not produced by UV polymerization.

To make a deeper analysis of these results, the polymerization degree was determined by FTIR. It is shown in Table 6.6.

Table 6.6. *Polymerization degree of samples obtained by thermal and UV polymerization.*

	R	*R'+G*	*R'+GO*	*R'+GoxNP*
HPP 11'	29.2	34.5	28.7	16.4
UV 11'	24.3	19.5	10.2	16.7

These results were related to the conclusions extracted from Chapter 5. It was found that R'+G required lower activation energy at the first stage of thermally-triggered process, leading to a higher polymerization degree as well as mechanical properties. However, when polymerization was triggered by UV, R'+G samples were found to produce fewer radicals when subjected to UV, which agreed with the lower mechanical properties. This relation between mechanical properties and polymerization degree was not observed in the case of GO and GoxNP. It is interesting to remark that the case of GoxNP, presented a similar polymerization degree for both, however, it showed considerable differences in tensile strength. This suggested that the lack of mechanical properties could be due to other phenomena such as changes in polymer structure or shrinkage.

6.2.2.3. Effect of GBN on samples obtained by different manufacturing technologies

The printing process is different from the molding process and more factors appear due to the layer-by-layer manufacturing, e.g. adhesion between layers. In Figure 6.5 tensile strength of samples obtained via UV polymerization by molding and SLA are shown.

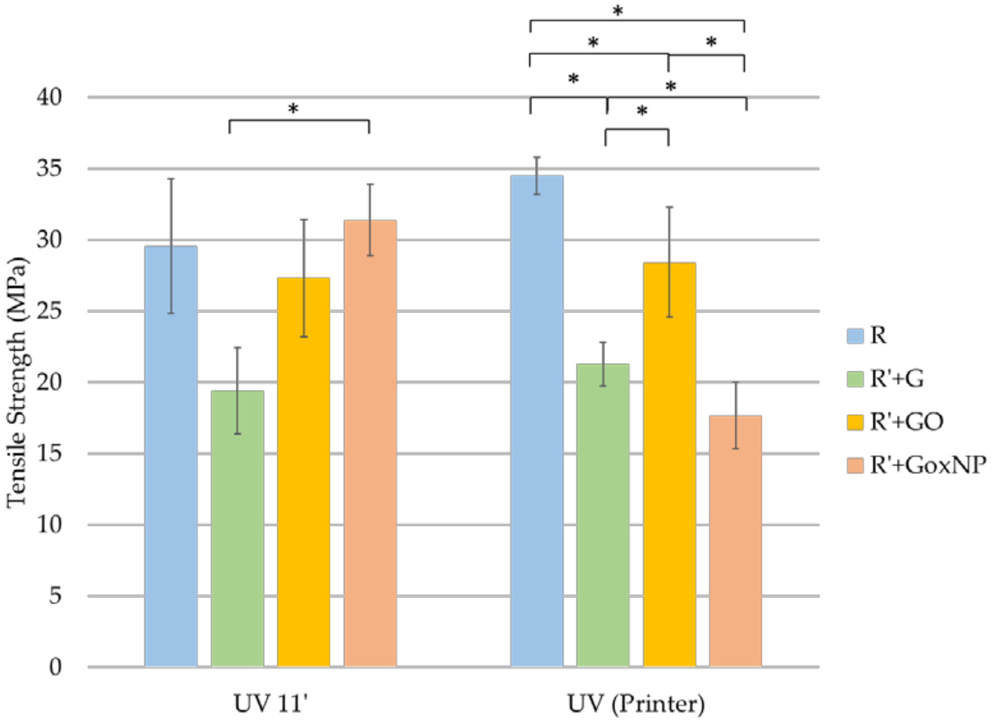

Figure 6.5. *Tensile strength of samples prepared by SLA and molding.*
** means differences with p-value < 0.05*

Samples obtained by SLA showed higher tensile strength than those obtained by molding, except for the sample R′+GoxNP. This decrease when GoxNP was added could be due to a reduction in polymerization degree or an issue related to the layer formation that could affect the adhesion between layers. To corroborate these hypotheses, polymerization degree was determined (Table 6.7) and layers were observed by microscopy (Figure 6.6).

Table 6.7. *Polymerization degree of samples obtained by UV molding and printing.*

	R	*R′+G*	*R′+GO*	*R′+GoxNP*
UV 11′	24.3	19.5	10.2	16.7
UV (printer)	48.6	46.0	46.3	42.1

Samples obtained by printing showed a higher polymerization degree than those obtained by UV molding. However, tensile strength was not proportional to the polymerization degree; therefore, the GBN effect was not only due to their effect on the polymerization reaction. The most remarkable case was GoxNP, which showed a higher polymerization degree and lower tensile strength for printed samples. Layers of UV (printer) samples were analyzed by optical microscopy to determine the influence of GBN on layer formation. The detail of the interface between the layers can be seen in Figure 6.6.

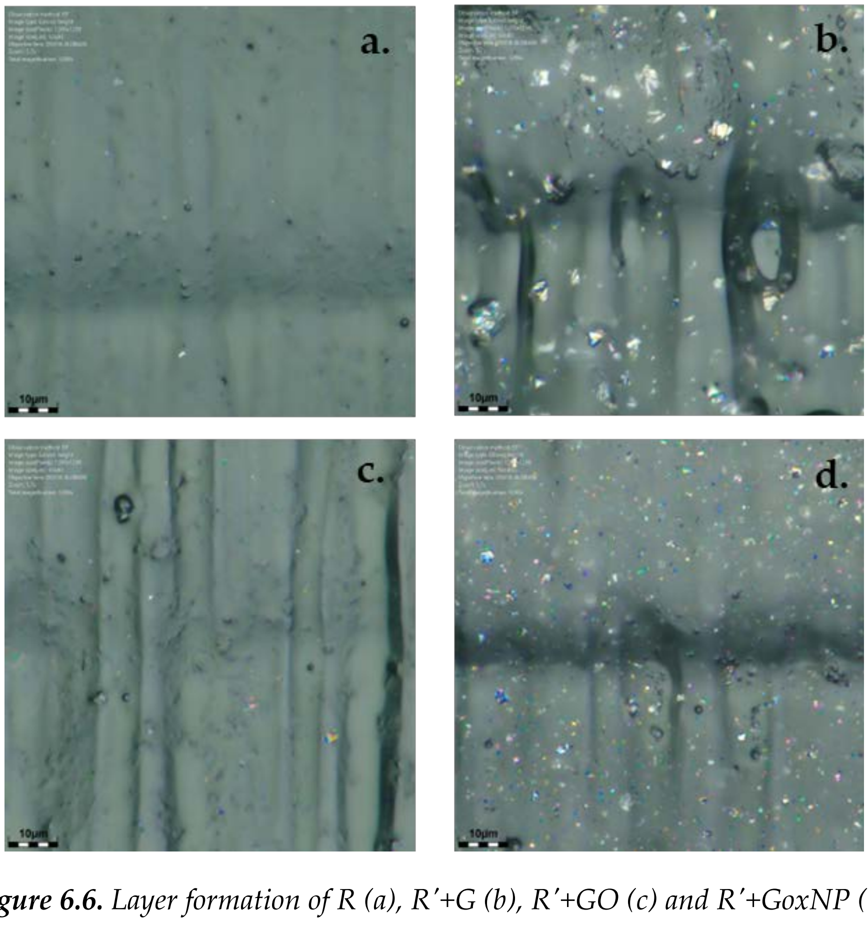

Figure 6.6. *Layer formation of R (a), R′+G (b), R′+GO (c) and R′+GoxNP (d).*

The effect of the different GBN on the interface could explain the differences found in mechanical properties. The GO produced the slightest effect on printing quality, only some marks can be seen due to the presence of the nanofiller. In the case of G, the surface was not smooth and showed imperfections, but the adhesion between the layers seemed to be adequate. Finally, the addition of GoxNP produced a decrease in the adhesion between layers seen as a clear discontinuity in the interface between the layers, which could be responsible for the observed decrease in mechanical properties of printed structures. The effect of GoxNP on layers could be due to the higher size of this GBN and the lower exfoliation degree compared to G and GO.

6.2.2.4. Optimization of postcuring process

Until this point, it was concluded that, in some cases, polymerization degree affected mechanical properties and, to remove this factor a postcuring process was carried out. Different combinations of the factors to optimize, i.e. temperature (T), time (t) and IPA cleaning time (C), were analyzed. The response for each configuration is shown in Table 6.8.

Table 6.8. *Response for each configuration.*

Configuration	*Tensile Strength (MPa)*
1	68.32 ± 0.44
T	72.31 ± 1.94
t	70.24 ± 0.64
C	67.41 ± 0.51
tC	69.27 ± 0.27
TC	71.58 ± 1.47
Tt	73.58 ± 0.67
TtC	72.71 ± 0.19

From these data, the effect of each parameter could be estimated, as well as the interactions between them. The values obtained from the tensile strength were the following (Table 6.9):

Table 6.9. *Effect of the three studied parameters and their interactions.*

	T	*t*	*C*
T	0.65	2.11	0.07
t	2.11	0.61	2.22
C	0.07	2.22	-2.50

Focusing on the effect of each parameter, it could be concluded that the cleaning time in the FormWash was the most affected. Besides, it presented a negative value (-2.50), which meant that the higher the cleaning time, the lower the strength. Time and temperature inside FormCure had a similar effect. The higher, the better, but their effect were not very important. The negative effect of C was, in part, counteracted by an increase in t. Probably, it was because the solvent inside the resin was desorbed inside the FormCure.

It could be seen that the combination of factors in FormCure that offered the higher response was 80 °C for 90 minutes. However, the most affecting factor was C. To optimize it, tests at lower cleaning times were carried out, trying to maximize the response. The results of these tests are shown in Table 6.10.

Table 6.10. *Optimization of time in FormWash.*

Time in FormWash (min)	*Tensile Strength (MPa)*
1	81.81 ± 1.40
2	81.61 ± 2.53
3	81.99 ± 1.93
4	80.14 ± 0.54
5	73.58 ± 0.67
10	72.71 ± 0.19

The trend indicated by the coefficient of Yates algorithm was supported by the results for different times in FormWash. The higher the cleaning time, the lower the tensile strength. This could be explained by the effect of the solvent inside the polymer network. It was placed in the free volume and produced the swelling of the resin with the consequent reduction in mechanical properties [22]. In samples with C < 3 minutes, the surface residual tack was found, therefore, these values for C were discarded.

The parameters that will be used from now on for the post printing processing of acrylic resin are shown in Table 6.11.

Table 6.11. *Post printing parameters of acrylic resin.*

Temperature in FormCure (T)	80 °C
Time in FormCure (t)	90 minutes
Time in FormWash (C)	3 minutes

It was proved that postcuring process was vital to achieving good mechanical properties. Unexpectedly, cleaning in IPA was the factor that most affected mechanical properties.

Unpolymerized resin was soluble in IPA, whilst polymerized resin was not soluble. Therefore, this solvent was adequate to clean the samples. However, the inclusion of IPA molecules inside the polymerized network could weaken the material, reducing its mechanical properties. The temperature and time obtained in this study were the same when compared to Bayarsaikhan et al study [29]. Besides, they found that post-curing process did not only affect mechanical properties, but also biological performance. These parameters were used with all the resin mixtures.

6.2.2.5. Effect of post-curing on samples obtained by different polymerization sources

Post-curing was done for all the studied samples, and the final tensile strengths are compared in Figure 6.7.

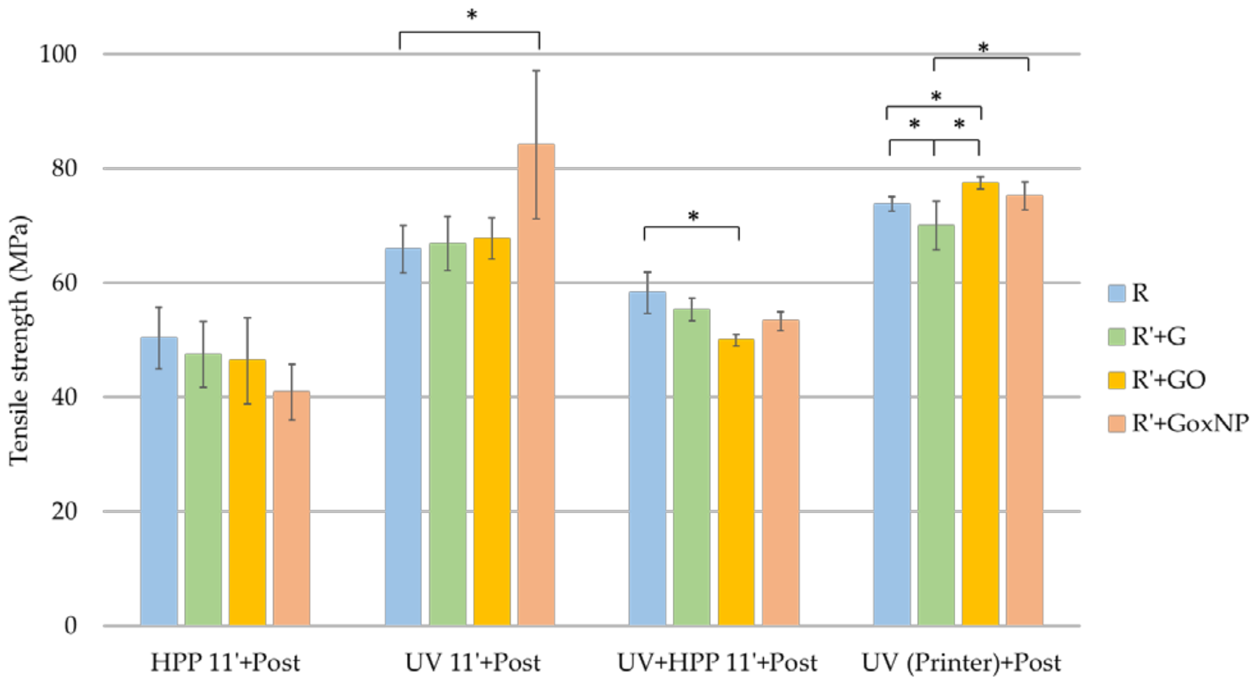

Figure 6.7. *Tensile strength of postcured samples obtained by molding and SLA.*
** means differences with p-value < 0.05*

When post-curing was carried out, in every case an increase in tensile strength was found compared to the same sample without post-curing. It is interesting to highlight the case of R'+GoxNP. In most non-post-cured samples, R'+GoxNP showed the lowest tensile strength, but this trend was not found when post-curing was applied. Differences between the nanocomposites seemed to be reduced when post-curing was applied, maybe because polymerization degree of all of them was similar after post-curing.

To demonstrate if differences were due to polymerization degree, it was calculated by FTIR and results are shown in Table 6.12.

Table 6.12. *Polymerization degree of post-cured samples obtained by FTIR.*

	R	*R′+G*	*R′+GO*	*R′+GoxNP*
HPP 11′ + Post	100	100	100	72.2
UV11′ + Post	35.8	38.5	31.5	19.2
UV (Printer) + Post	51.6	48.6	50.4	51.4
UV + HPP 11′ + Post	100	100	100	100

Unexpectedly, not in all cases, 100% of polymerization degree was achieved. Samples that were not subjected to heat (UV11′ and UV (Printer)) achieved the lowest polymerization degree probably because of a lack of photoinitiator or because its diffusion is not enough to reach the residual monomer [8]. The remaining C=C bonds must have remained unreacted after the action of the photoinitiator because they were trapped in the cross-linked polymer network.

As previously found in non-post-cured samples, polymerization degree did not correspond with mechanical performance, and it was observed that samples obtained by UV showed better mechanical performance with a lower polymerization degree. It could be because UV produced structures with a higher degree of crosslinking than heat.

To summarize the finding until this point, it could be concluded that:

- G produced improvements in mechanical properties when polymerization was carried out only by heat. When UV was present, its mechanical properties reduced.
- GO showed similar mechanical properties to R in every case, except for printed samples. The only reason why this decrease could happen was because of the slight reduction in polymerization degree or the presence of internal stresses during the printing process, which will be analyzed in the next section.
- GoxNP inhibited thermal polymerization in both, thermally- and UV-triggered. Only in the case of UV polymerization some improvements in mechanical properties were found. In the case of printed samples, the mechanical properties fell drastically because of an effect on adhesion between layers.
- When post-curing was carried out, differences were reduced, but R′+GoxNP UV 11′ + Post and R′+GO UV (printer) + Post showed significantly higher tensile strength than R.

6.3. Effect of post-treatments on mechanical properties

In this section, different post-treatments for the acrylic resin with and without GBN were studied. In this case, all samples were obtained by SLA printing.

6.3.1. Experimental methodology

Different post-treatments of printed samples were analyzed in this section. Post-curing and annealing were carried out as explained in Section 3.2.2.5. The nomenclature is shown in Table 6.13.

Table 6.13. *Conditions and nomenclature of samples with different post-treatments.*

	Cleaning	*Post-curing*	*Annealing*
As-printed	3 min IPA	No	No
Post		Yes	No
Ann		No	Yes
Post + Ann		Yes	Yes

Samples were analyzed from a chemical (FTIR and DSC), mechanical (tensile tests and DMTA) and visual (SEM micrographs) point of view.

6.3.2. Results

6.3.2.1. Polymerization and crosslinking degree

In Table 6.14 the T_g values of each resin with the different post-treatments are shown.

Table 6.14. *T_g(°C) of R, R′+G, R′+GO and R′+GoxNP samples obtained by DSC.*

	R	*R′+G*	*R′+GO*	*R′+GoxNP*
As-printed	109 ± 3	104 ± 6	103 ± 4	104 ± 1
Post	117 ± 3	110 ± 4	110 ± 2	111 ± 2
Ann	111 ± 2	108 ± 4	105 ± 2	115 ± 3
Post + Ann	121 ± 1	116 ± 2	112 ± 4	117 ± 4

When T_g was analyzed, it was found that during the printing process, whilst R′+GBN showed lower T_g than R, when samples were postcured, T_g increased in every case because the application of UV together with heat increased the crosslinking degree of samples. In the case of annealing, its effect was different depending on the sample: R and R′+GO showed similar T_g than as-printed samples, whilst R′+G and R′+GoxNP showed an increase in this parameter. Finally, compared with the other post-treatments, post-curing+annealing produced the most crosslinked network with the higher T_g. However, it is important to note, that in all cases, the T_g of the resin with the GBN was lower than R.

To know if the different post-treatments increased the carbon-carbon double bond conversion, polymerization degree was calculated for every sample and the results are shown in Table 6.15.

Table 6.15. *Polymerization degree obtained by FTIR.*

	R	*R'+G*	*R'+GO*	*R'+GoxNP*
As-printed	48.6	46.0	46.3	42.1
Post	51.6	48.6	50.4	51.4
Ann	48.5	48.6	48.3	51.3
Post + Ann	51.5	48.2	50.1	55.1

It was found that the addition of GBN, produced a reduction of polymerization degree during the printing process compared to R, which was especially remarkable in GoxNP. When post-treatments were carried out, it was found that all of them produced a minor increase in polymerization degree, being the extent of this increase different depending on the treatment and the sample. In the case of R and R'+GO, post-treatments with UV exposure were more efficient in terms of polymerization degree. R'+G showed a similar polymerization degree regardless of the kind of post-treatment applied. In R, R'+G and R'+GO samples, annealing after post-curing did not result in higher polymerization degree, therefore, the application of heat after post-curing did not produce the polymerization of the residual monomers. Conversely, post-treated R'+GoxNP samples showed in all cases a higher degree of polymerization than the printed samples, even in the case of annealing.

Mendes-Felipe et al [5] found that crosslinking degree of an acrylic photopolymer depended on the use of UV light in the postcuring process. When samples were postcured with UV light, a highly crosslinked material with better mechanical properties can be obtained. Besides, the homogeneity of the material was also affected by the postcuring process. In the case of thermally postcured samples, the network presented two differentiated parts with different crosslinking densities. When UV is used in the postcuring process, the material was more homogeneous.

6.3.2.2. Mechanical properties

The tensile strength of the nanocomposites subjected to the different post-treatments is shown in Figure 6.8.

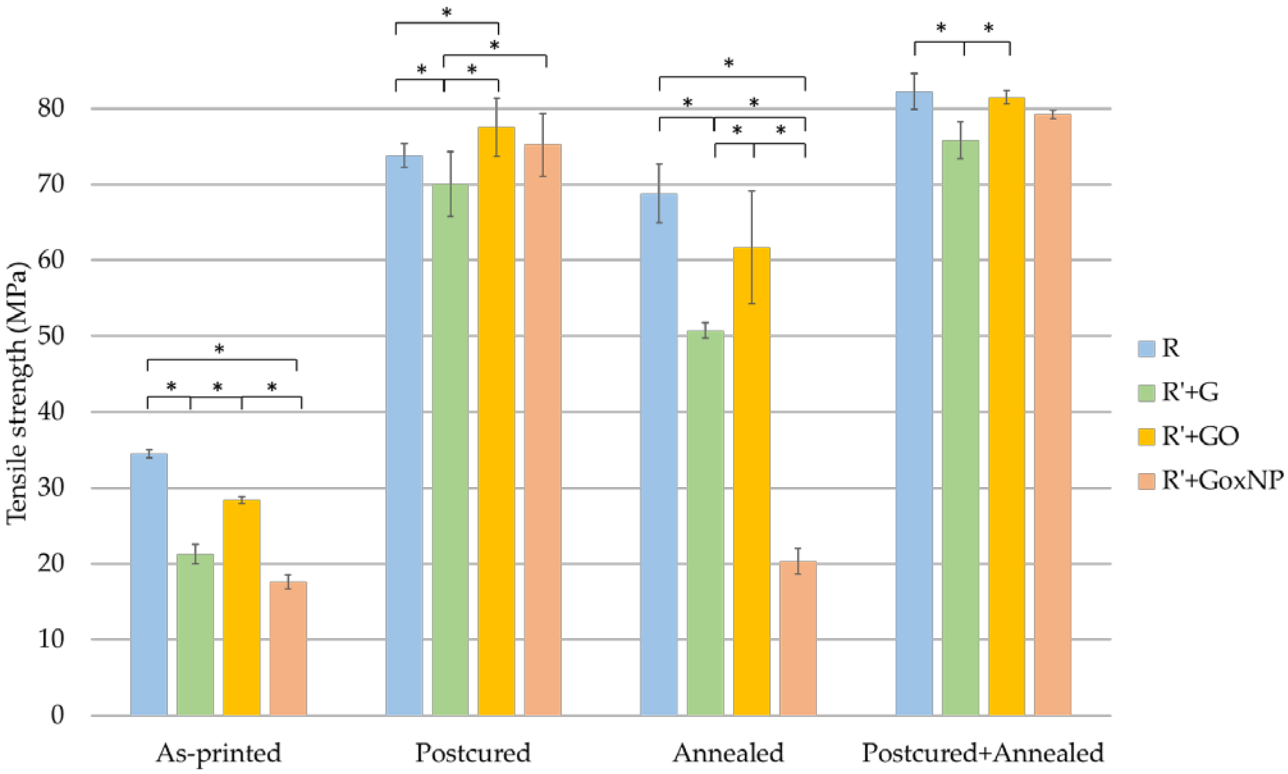

Figure 6.8. *Tensile strength of all the nanocomposites with the different post-treatments. * means differences with p-value < 0.05*

In the case of R’+G, taking R as a reference, it was found that for every post-treatment the addition of G resulted in a significant decrease in the tensile performance. Conversely, the addition of GO did not produce significant changes, except for post-cured samples, where an increase in tensile strength was found. Finally, and as previously found, GoxNP produced an important decrease in the mechanical performance when post-treatments were carried out without UV (Ann) and for as-printed samples.

Stress-strain curves of post-cured and post-cured+annealed samples are shown in Figure 6.9, together with the toughness calculated as the area under the stress-strain curve.

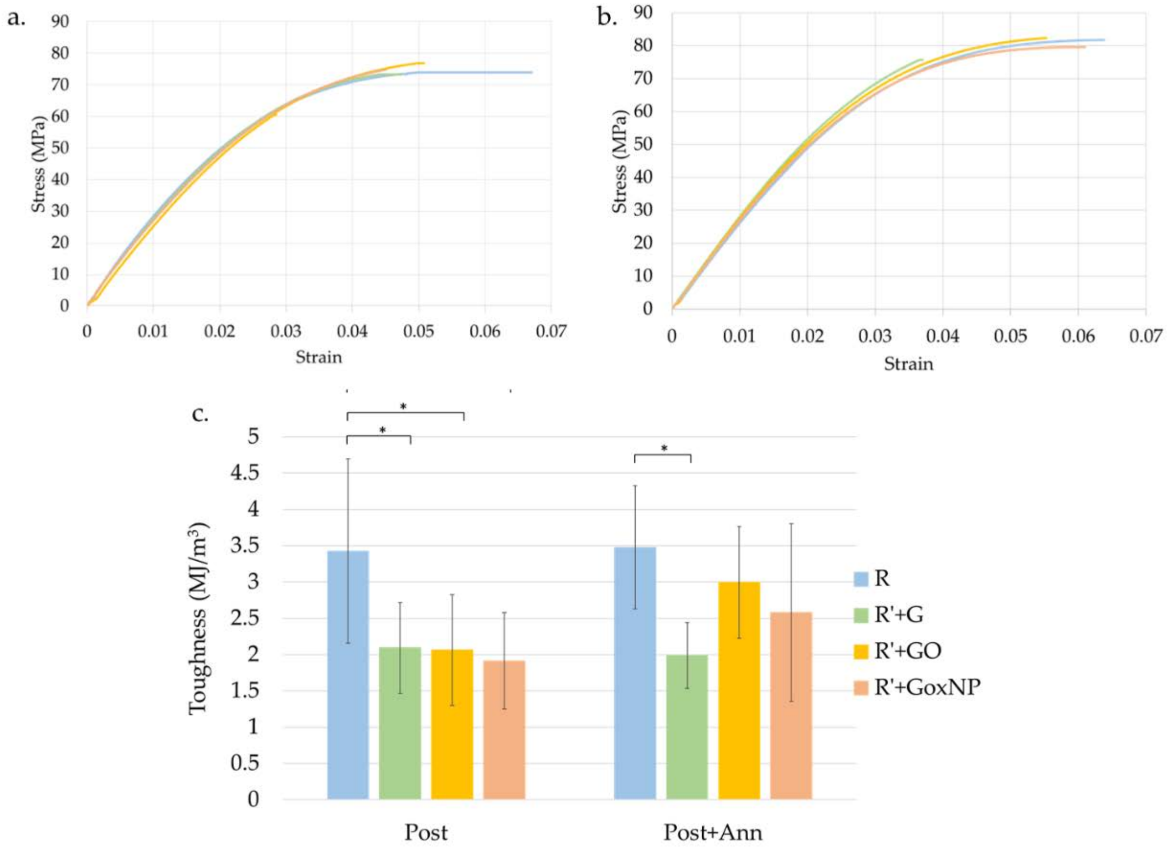

Figure 6.9. *Stress-strain curves of post-cured samples (a) and postcured + annealed samples (b). Toughness calculated as area under the curve (c).*
** means differences with p-value < 0.05*

It was found that the addition of GBN decreased the toughness of the post-cured resin. However, when annealing was applied to post-cured samples, behaviour under tensile forces changed, and the stress strain curves can be seen in Figure 6.9b. All samples, except R'+G, showed an increase in elongation at break when annealing was applied, and R'+GO and R'+GoxNP showed similar toughness than R. R'+G showed a relatively poor mechanical behaviour.

Tensile tests also give information about strength, stiffness and elasticity through tensile strength, Young's modulus and elongation at break, respectively. These parameters are shown in Table 6.16.

Table 6.16. *Young's modulus and elongation at break of samples with different post-treatments.*

		R	***R'+G***	***R'+GO***	***R'+GoxNP***
As-printed	***Tensile Strength (MPa)***	34.49 ± 0.52	21.27 ± 1.52	28.41 ± 3.87	17.65 ± 2.35
	Young's modulus (GPa)	1.29 ± 0.06	0.87 ± 0.34	1.06 ± 0.13	0.77 ± 0.12
	Elongation at break (%)	29.49 ± 8.56	28.66 ± 4.39	34.80 ± 3.87	20.20 ± 7.42
Post-cured	***Tensile Strength (MPa)***	73.79 ± 1.28	70.06 ± 4.23	77.55 ± 1.06	75.21 ± 2.39
	Young's modulus (GPa)	2.50 ± 0.13	2.72 ± 0.28	1.88 ± 0.39	3.68 ± 0.33
	Elongation at break (%)	6.68 ± 1.52	4.80 ± 1.11	5.25 ± 0.49	4.77 ± 0.31
Annealed	***Tensile Strength (MPa)***	68.78 ± 0.50	50.77 ± 3.86	61.74 ± 7.43	20.34 ± 0.91
	Young's modulus (GPa)	2.28 ± 0.07	2.19 ± 0.59	2.04 ± 0.15	1.12 ± 0.27
	Elongation at break (%)	6.54 ± 1.53	5.71 ± 1.14	5.54 ± 0.74	4.82 ± 1.54
Post-cured + Annealed	***Tensile Strength (MPa)***	82.22 ± 0.96	75.81 ± 4.13	81.49 ± 1.67	79.21 ± 0.57
	Young's modulus (GPa)	2.60 ± 0.11	2.74 ± 0.18	2.37 ± 0.21	2.34 ± 0.26
	Elongation at break (%)	6.30 ± 0.86	3.99 ± 0.72	5.56 ± 0.82	6.21 ± 0.94

In all cases, except post-curing+annealing, post-treatments led to an increase in the rigidity of samples and a decrease in elongation at break. It could be due to the higher polymerization and crosslinking degree which resulted in lower chain mobility. In the case of post-cured+annealed samples, elongation increased for R'+GO and R'+GoxNP, which could mean that internal stresses were released.

DMTA was carried out for the most interesting combinations of GBN and post-treatment, i.e., R'+G and R'+GO Post and Post+Ann. As a reference, R Post and R Post+Ann were tested. Tan δ (Figure 6.11) was obtained and analyzed from these tests.

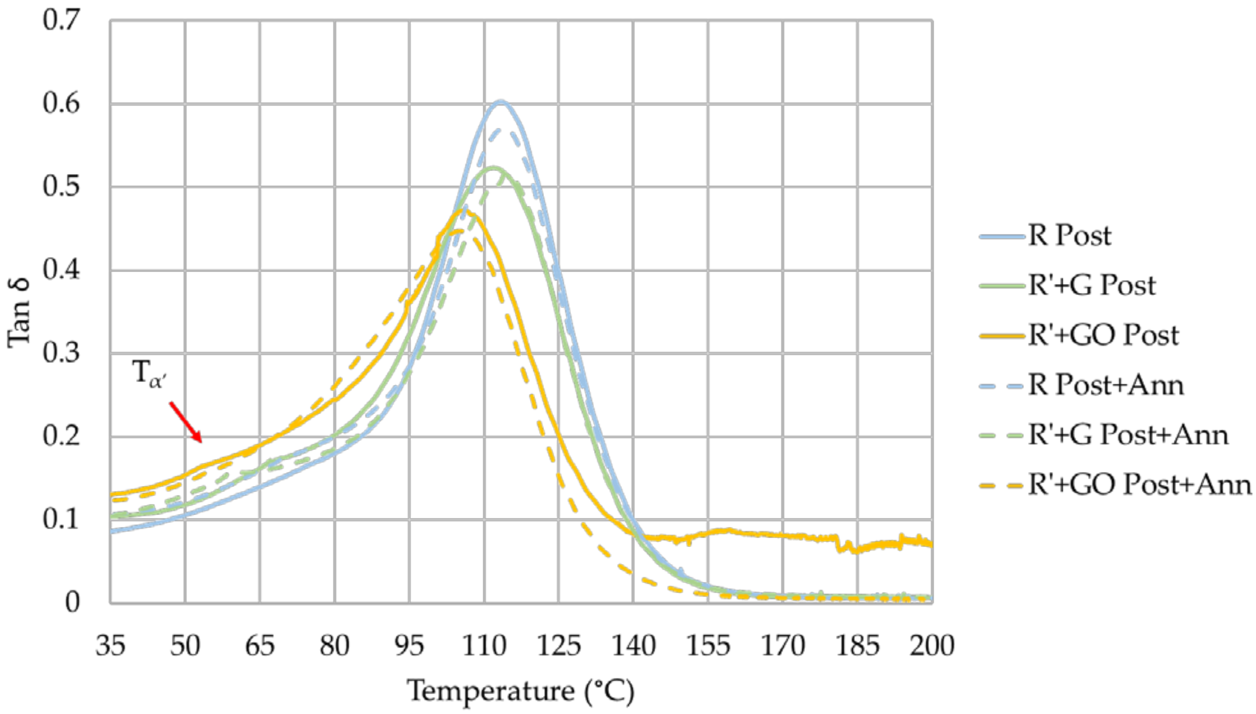

Figure 6.10. *Tan δ of post-cured and post-cured + annealed samples.*

The first zone of the curves corresponds to the glassy state of the polymer/nanocomposite and when temperature increased the rubbery state was reached. Curves showed that only one transition occurred during the heating. It suggested that all the samples analyzed were completely polymerized and only a physical transition could be observed, which corresponded to the glass transition [5]. The temperature of the peak on tan δ (T_α) corresponds to the glass transition temperature. It was found that DSC (Table 6.14) and DMTA (Table 6.17) detected similar temperatures and the minor differences could be due to the heating rate used to do the DSC scans. However, they also presented a small shoulder ($T_{\alpha'}$) before the glass transition, marked with a red arrow in Figure 6.11, which could be attributed to a sub-T_g [15]. To facilitate the analysis of the results, all the data explained in this paragraph are summarized in Table 6.17.

Table 6.17. *Summary of DMTA results.*

		***T_α* (°C)**	***$T_{\alpha'}$* (°C)**
R	***Post***	115	75
	Post+Ann	113	70
R′+G	***Post***	112	68
	Post+Ann	114	59
R′+GO	***Post***	106	53
	Post+Ann	105	53

G and GO produced a reduction in tan δ peak, especially GO. It suggested that GO interacted with the polymer chains, probably inhibiting the crosslinking. It could also be observed by the width of the peak, which is higher for R'+GO sample, regardless of the post-treatment, as can be seen in Figure 6.11. The high width also suggested that a less homogeneous network was formed [5]. The printing process and the post-treatments seemed to result in different networks, with different crosslinking degrees and linearity, which could be demonstrated in the presence of a sub-T_g, which probably corresponded to the glass transition of the polymer obtained during post-treatments.

R and R'+G showed similar temperatures for the final tan δ maximum. It suggested that the same final structure was obtained [16]. However, the addition of GO changed these values, especially for Post samples. It could be read as a different final structure, with a lower crosslinking degree. It was already found for the kinetics curves (Chapter 5), where a different polymerization rate was shown by R'+GO samples. Polymer structure was studied by calculating molecular weight between crosslinks (M_c), determined as explained in Section 3.2.7.3. using the density calculated for each sample with the procedure defined in Section 3.2.5.6. Results are shown in Table 6.18.

Table 6.18. *Density and molecular weight between crosslinks of post-cured and post-cured + annealed samples.*

		d (g/cm³)	***M_c (g/mol)***
R	***Post***	1.185	133.3
	Post+Ann	1.184	127.8
R'+G	***Post***	1.181	133.8
	Post+Ann	1.184	137.9
R'+GO	***Post***	1.182	145.8
	Post+Ann	1.181	128.5

It can be observed that R'+GO had a lesser crosslinked structure than R and R'+G, when the samples were only post-cured. Regarding the annealing, it was observed that R and R'+GO subjected to annealing after post-curing showed an increase in crosslinking degree (lower M_c), which was translated into an increase in tensile strength and Young's modulus (Table 6.16). However, this increase was not found for R'+G samples.

6.3.2.3. Fracture surface

To analyze the interaction between GBN and the matrix and the fracture produced by the different post-treatments, SEM images of the cryogenic fracture were taken. R'+G samples were analyzed for every post-treatment and R, R' and R'+GO were studied for the best post-treatments: post-curing and post-curing + annealing. Figure 6.11 shows the comparison of the R'+G surface with the four post-treatments.

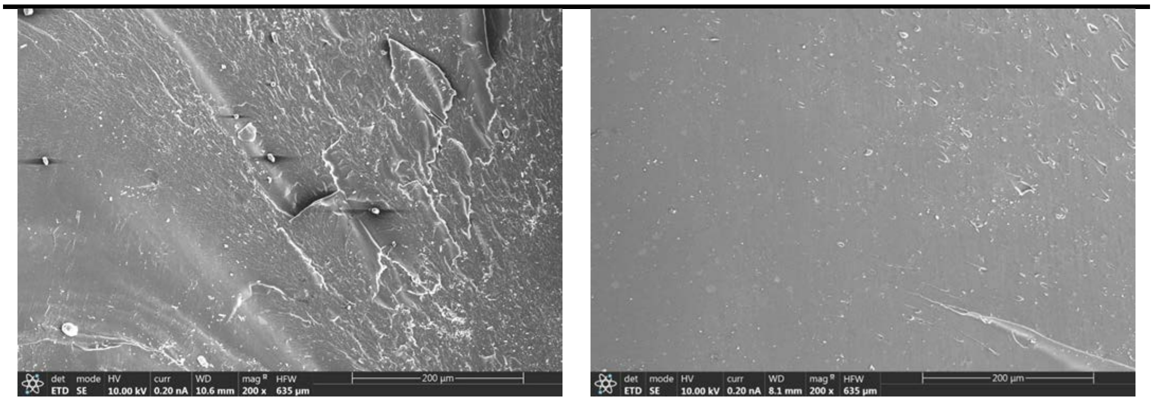

As-printed *Post*

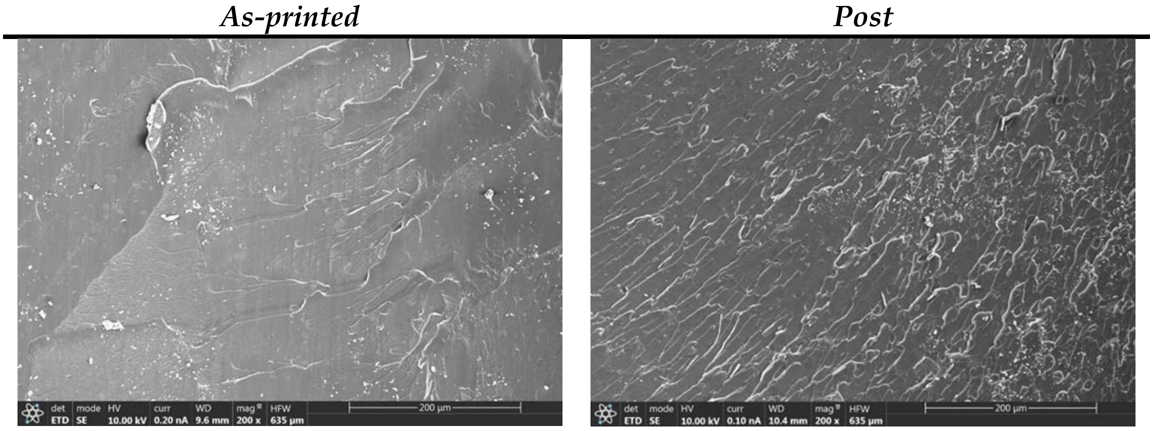

Ann *Post+Ann*

Figure 6.11. *SEM micrographs of fracture surface of R'+G with different post-treatments.*

In the as-printed micrograph, it can be seen how the fracture showed a ductile behaviour due to the low polymerization degree, which was also previously observed in the high elongation at break. Comparing the different post-treatments, it can be concluded that the behaviour changed with them. When Post was carried out, the fracture was more brittle than the as-printed fracture, showing a smoother surface. Ann did not change the kind of fracture and the surface was similar to the as-printed sample. Finally, when annealing was carried out after post-curing, an important change in the surface was found. Its roughness highly increased compared to both, as-printed and post samples. Therefore, this post-treatment resulted in a ductile fracture.

Figure 6.12 shows SEM micrographs of R, R'+G and R'+GO with two post-treatments, i.e. post-curing and post-curing + annealing.

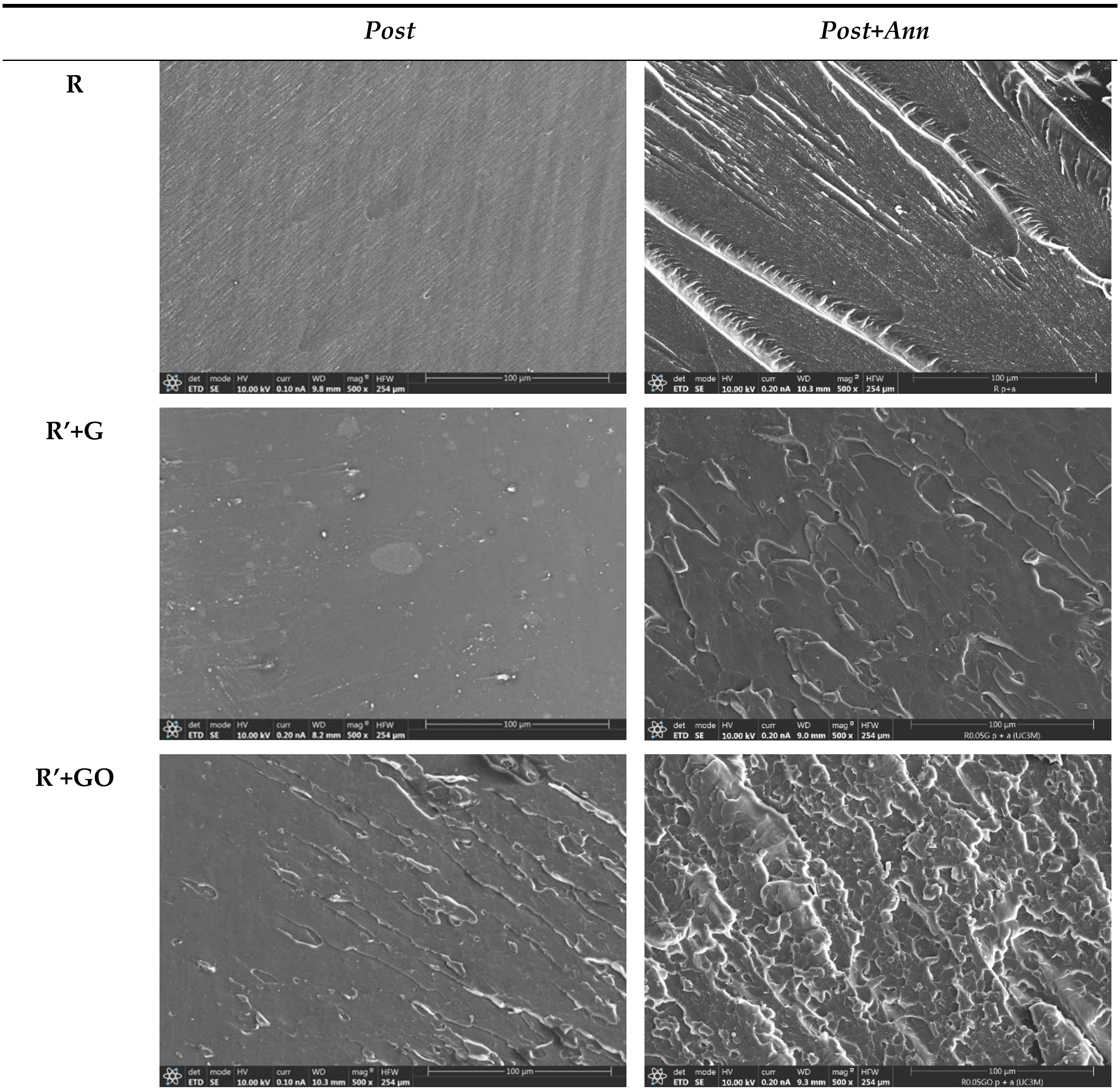

Figure 6.12. *SEM micrographs of fracture surfaces of post-cured and post-cured + annealed samples.*

The roughness of the surface provides information about the behaviour (i.e. brittle or ductile) and the crack deviation mechanism. The crack deviation is found as a change in the crack growth plane because micro-cracks encounter stiff GBN and by-pass them [13]. When post-curing was carried out, R and R'+G surfaces were smooth, without any undulation, which represented a brittle fracture. Therefore, the addition of G did not produce crack deviation, probably due to poor adhesion and interaction with the matrix. Post-cured R'+GO showed homogeneously distributed undulations, which indicated a reasonably uniform dispersion of GO and a ductile fracture. Post+Ann samples showed higher surface undulation as compared with post samples. Usually, this undulation indicates a higher resistance to fracture [14].

R'+GO showed ductile fracture surfaces, which should be reflected in an increase in toughness. However, this increase was not found, probably because GO affected polymer structure, producing a lesser crosslinked structure with lower toughness. Therefore, GO produced a double effect: on the one hand, it changed polymer structure, with faster polymerization and lower crosslinking degree and, on the other hand, it produced a toughening effect, which was only found on micrographs.

6.4. Discussion of the results

This study demonstrated that photocurable acrylic-based resin can be polymerized via heat or UV exposition. When only heat is involved in the process, it occurs by spontaneous self-initiated polymerization of the methacrylate monomers [17].

UV-triggered polymerization produced polymers with higher tensile strength and higher polymerization degree than thermally-triggered polymerization. The increase in tensile strength was 152%, 62%, 97%, and 897%, for R, R′+G, R′+GO and R′+GoxNP, respectively. The highest increase was found for R′+GoxNP samples because the presence of GoxNP greatly inhibited thermal polymerization, and the previous exposure to UV light slightly hindered this inhibition. However, the tensile strength of R′+GoxNP was significantly lower than the other materials for both thermally- and UV-triggered polymerized samples because its polymerization degree is much lower than the other materials. The addition of G and GO produced a slight increase in tensile strength for thermally-triggered polymerized samples, whilst UV-triggered polymerized samples showed similar tensile strength to R, but a slightly higher polymerization degree.

When polymerization was produced by UV exposition, the initialization of the reaction consists of the absorption of UV light by the photoinitiator, which decomposes and produces free radicals. The number of radicals formed is directly proportional to the number of absorbed photons [19]. GBN absorbed part of these photons and, for this reason, when polymerization occurred via UV, either in molding or printing, the polymerization degree was lower for R′+GBN (Table 6.7).

Feng et al [3] compared conventional manufacturing (direct casting) with additive manufacturing (SLA) of graphene-reinforced resin and found an increase in mechanical properties when SLA was used as manufacturing technology. It could be due to the defects and bubbles that inevitably appeared in casted samples, being the printed samples almost defect-free. The same trend was found for every sample, except R′+GoxNP, which showed a lower polymerization degree than the other samples because of the effect of GoxNP on layer formation.

When post-curing was applied, in all cases, differences between the samples studied were reduced. However, the polymerization degree was not in every case 100%, even after the post-curing, which could be explained because of steric hindrance. De Leon et al [20] found that when the polymeric 3D network is formed, monomers may find more difficulties when trying to diffuse across this network. Compared to R, improvements in tensile strength were found for R′+GoxNP UV11′ + Post samples and R′+GO UV (Printer) + Post samples.

It is well-known that a problem that acrylic resins present, specifically dental resins, is that the percentage of carbon-carbon double bonds that are converted into single bonds to obtain a polymer is low, which results in deficient mechanical properties [21]. Post-treatments slightly increased this conversion compared to the conversion obtained in as-printed samples. However, the degree of conversion was around 50% for all the samples.

SEM micrographs showed that the interaction with R was stronger for GO than G, which was also seen in the tensile strength of the samples. The effect of annealing after post-curing was higher for R than for the other mixtures in terms of tensile strength. Analyzing SEM images, it was found that R Post showed the layer ordering in the microstructure, which disappeared for the Post+ann samples. This absence of layer ordered microstructure suggested that the annealing minimize the anisotropy and released the internal stress concentration [22]. Besides, DMTA showed that R and R'+G had a similar structure after printing and post-treatment, and R'+GO had a different network structure because GO affected the polymerization reaction, which was also found in the kinetics study. In the case of R'+GoxNP, it needed a post-treatment with UV to achieve good mechanical performance.

The reinforcing effect of GBN via the mechanisms explained in Section 2.2.4. could be better found by subjecting the samples to cyclic loads or fracture tests, where the crack propagation is the main failure mechanism. However, this kind of tests are more complex and time consuming, and are not adequate for a first approach, therefore they should be considered for future works.

6.5. Conclusions of this chapter

In this chapter, the mechanical performance of acrylic resin and its nanocomposites was studied in depth, as a function of the polymerization source, manufacturing process and post-treatment applied. The main conclusions that can be extracted from this study are:

- Mechanical properties of acrylic resin with and without GBN were highly affected by the source that produced the polymerization, i.e. heat or UV. The differences found between the GBN could be explained by the differences in the polymerization kinetics found in Chapter 5.
- Mechanical performance was also affected by the manufacturing process (i.e. SLA or molding) because of the presence of defects and other factors, like adhesion between layers. Adhesion between layers was found to be inefficient for R'+GoxNP, being adequate for the other GBN.
- The interaction between GBN and resin produced different roughness on the fracture surfaces. It seemed that G had a weaker toughening effect than GO, which was well-dispersed inside the matrix and it had good interaction with the resin.
- Post-treatments produced an important increase in the mechanical performance of the printed structures because they produced an increase in polymerization degree and they released internal stresses.
- Therefore, the effect of each GBN on the different factors studied in this chapter is summarized in Figure 6.12.

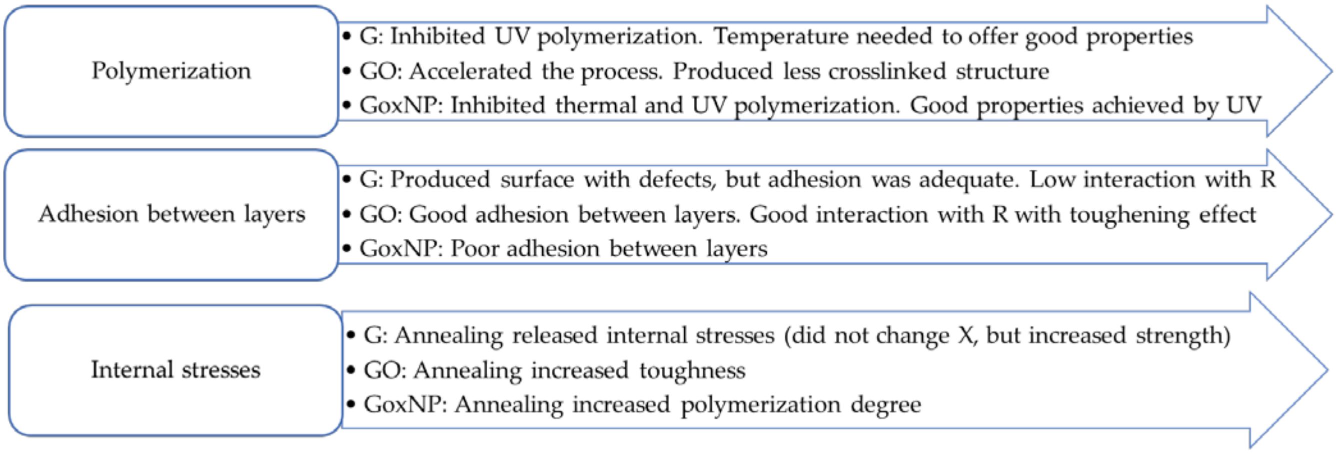

Polymerization
- G: Inhibited UV polymerization. Temperature needed to offer good properties
- GO: Accelerated the process. Produced less crosslinked structure
- GoxNP: Inhibited thermal and UV polymerization. Good properties achieved by UV

Adhesion between layers
- G: Produced surface with defects, but adhesion was adequate. Low interaction with R
- GO: Good adhesion between layers. Good interaction with R with toughening effect
- GoxNP: Poor adhesion between layers

Internal stresses
- G: Annealing released internal stresses (did not change X, but increased strength)
- GO: Annealing increased toughness
- GoxNP: Annealing increased polymerization degree

Figure 6.13. *Conclusions for each GBN.*

6.6. References

[1] M.M. Hanon, A. Ghaly, L. Zsidai, Z. Szakál, I. Szabó, L. Kátai, Investigations of the mechanical properties of dlp 3d printed graphene/resin composites, Acta Polytech. Hungarica. 18 (2021) 143–161. https://doi.org/10.12700/APH.18.8.2021.8.8.

[2] S.M. Lim, B.S. Shin, K. Kim, Characterization of products using additive manufacturing with graphene/photopolymer - Resin nano-fluid, J. Nanosci. Nanotechnol. 17 (2017) 5492–5495. https://doi.org/10.1166/jnn.2017.14159.

[3] Z. Feng, Y. Li, L. Hao, Y. Yang, T. Tang, D. Tang, W. Xiong, Graphene-Reinforced Biodegradable Resin Composites for Stereolithographic 3D Printing of Bone Structure Scaffolds, J. Nanomater. (2019) 1–13. https://doi.org/10.1155/2019/9710264.

[4] X. Feng, Z. Yang, S. Chmely, Q. Wang, S. Wang, Y. Xie, Lignin-coated cellulose nanocrystal filled methacrylate composites prepared via 3D stereolithography printing: Mechanical reinforcement and thermal stabilization, Carbohydr. Polym. 169 (2017) 272–281. https://doi.org/10.1016/j.carbpol.2017.04.001.

[5] C. Mendes-Felipe, D. Patrocinio, J.M. Laza, L. Ruiz-Rubio, J.L. Vilas-Vilela, Evaluation of postcuring process on the thermal and mechanical properties of the Clear02™ resin used in stereolithography, Polym. Test. 72 (2018) 115–121. https://doi.org/10.1016/j.polymertesting.2018.10.018.

[6] I.K. Cingesar, M.-P. Marković, D. Vrsaljko, Effect of post-processing conditions on polyacrylate materials used in stereolithography, Addit. Manuf. 55 (2022) 102813. https://doi.org/10.1016/j.addma.2022.102813.

[7] J.Z. Manapat, J.D. Mangadlao, B.D.B. Tiu, G.C. Tritchler, R.C. Advincula, High-Strength Stereolithographic 3D Printed Nanocomposites: Graphene Oxide Metastability, ACS Appl. Mater. Interfaces. 9 (2017) 10085–10093. https://doi.org/10.1021/acsami.6b16174.

[8] J. Bauer, A.G. Izard, Y. Zhang, T. Baldacchini, L. Valdevit, Thermal post-curing as an efficient strategy to eliminate process parameter sensitivity in the mechanical properties of two-photon polymerized materials, Opt. Express. 28 (2020) 20362. https://doi.org/10.1364/oe.395986.

[9] D. Karalekas, A. Aggelopoulos, Study of shrinkage strains in a stereolithography cured acrylic photopolymer resin, J. Mater. Process. Technol. 136 (2003) 146–150. https://doi.org/10.1016/S0924-0136(03)00028-1.

[10] J.Y.H. Fuh, L. Lu, C.C. Tan, Z.X. Shen, S. Chew, Curing characteristics of acrylic photopolymer used in stereolithography process, Rapid Prototyp. J. 5 (1999) 27–34. https://doi.org/10.1108/13552549910251855.

[11] A. Al Rashid, S.A. Khan, S. G. Al-Ghamdi, M. Koç, Additive manufacturing of polymer nanocomposites: Needs and challenges in materials, processes, and applications, J. Mater. Res. Technol. 14 (2021) 910–941. https://doi.org/10.1016/j.jmrt.2021.07.016.

[12] S.H. Ryu, J.H. Sin, A.M. Shanmugharaj, Study on the effect of hexamethylene diamine functionalized graphene oxide on the curing kinetics of epoxy nanocomposites, Eur. Polym. J. 52 (2014) 88–97. https://doi.org/10.1016/j.eurpolymj.2013.12.014.

[13] B. Ahmadi-Moghadam, M. Sharafimasooleh, S. Shadlou, F. Taheri, Effect of functionalization of graphene nanoplatelets on the mechanical response of graphene/epoxy composites, Mater. Des. 66 (2015) 142–149. https://doi.org/10.1016/j.matdes.2014.10.047.

[14] D.A. Hawkins, A. Haque, Fracture toughness of carbon-graphene/epoxy hybrid Nanocomposites, Procedia Eng. 90 (2014) 176–181. https://doi.org/10.1016/j.proeng.2014.11.833.

[15] A. Sharma, X. Pan, J.M. Bjuggren, D. Gedefaw, X. Xu, R. Kroon, E. Wang, J.A. Campbell, D.A. Lewis, M.R. Andersson, Probing the Relationship between Molecular Structures, Thermal Transitions, and Morphology in Polymer Semiconductors Using a Woven Glass-Mesh-Based DMTA Technique, Chem. Mater. 31 (2019) 6740–6749. https://doi.org/10.1021/acs.chemmater.9b01213.

[16] J.L. Vilas, J.M. Laza, M.T. Garay, M. Rodríguez, L.M. León, Unsaturated polyester resins cure: kinetic, rheologic, and mechanical dynamical analysis. II. The glass transition in the mechanical dynamical spectrum of polyester networks, J. Polym. Sci. Part B Polym. Phys. 39 (2001) 146–152. https://doi.org/10.1002/1099-0488(20010101)39:1<146::AID-POLB130>3.0.CO;2-A.

[17] S. Srinivasan, A.M. Rappe, M. Soroush, Theoretical Insights Into Thermal Self-Initiation Reactions of Acrylates, in: Comput. Quantum Chem., Elsevier Inc., 2019: pp. 99–134. https://doi.org/10.1016/b978-0-12-815983-5.00004-0.

[18] B. Sanay, B. Strehmel, V. Strehmel, Photoinitiated polymerization of methacrylates comprising phenyl moieties, J. Polym. Sci. 58 (2020) 3196–3208. https://doi.org/10.1002/pol.20200483.

[19] M.C. Rusu, C. Block, G. Van Assche, B. Van Mele, Influence of temperature and UV intensity on photo-polymerization reaction studied by photo-DSC, J. Therm. Anal. Calorim. 110 (2012) 287–294. https://doi.org/10.1007/s10973-012-2465-5.

[20] A.S. De León, S.I. Molina, Influence of the degree of cure in the bulk properties of graphite nanoplatelets nanocomposites printed via stereolithography, Polymers (Basel). 12 (2020) 1103. https://doi.org/10.3390/POLYM12051103.

[21] M.L. Berlanga Duarte, L.A. Reyna Medina, P. Torres Reyes, S.C. Esparza González, A.M. Herrera González, Dental restorative composites containing methacrylic spiroorthocarbonate monomers as antishrinking matrixes, J. Appl. Polym. Sci. 136 (2019) 47114. https://doi.org/10.1002/app.47114.

[22] G. V. Salmoria, C.H. Ahrens, M. Fredel, V. Soldi, A.T.N. Pires, Stereolithography somos 7110 resin: Mechanical behavior and fractography of parts post-cured by different methods, Polym. Test. 24 (2005) 157–162. https://doi.org/10.1016/j.polymertesting.2004.09.008.

CHAPTER 7

BIOLOGICAL PROPERTIES OF THE NANOCOMPOSITES

Table of Contents

In this chapter, the biological properties of the nanocomposites are explored. To have a first approach to the biological performance of the studied nanomaterials, *in vitro* cytotoxicity tests were carried out with MC3T3 cells.

7.1. Introduction

Acrylic polymers have been used for over 80 years to manufacture prostheses. However, these materials have a limitation in terms of biological performance: the residual monomer that remains after polymerization may influence the biological properties of the final medical device [1]. The main issue of residual monomer is that it can leach from the resin, together with other substances, like formaldehyde, which also show cytotoxicity [2].

The mechanism behind the cytotoxicity of methacrylates and dimethacrylates monomers is the reaction of highly active α,β-unsaturated carbon-carbon double bonds with the amino and thiol groups, leading to the inactivation and denaturation of proteins [3]. Results obtained in the study carried out by Chan et al [4] suggested that differences in toxicity of acrylates and methacrylates could be related to their electrophilic reactivity which corresponds to their ability to deplete glutathione (GSH) and protein thiols Figure 7.1.

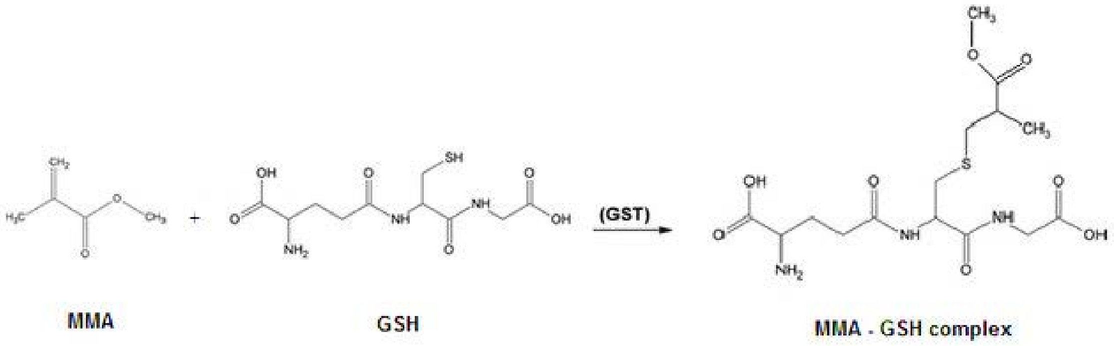

Figure 7.1. *Formation of MMA-GSH complex that leads to cytotoxicity [5].*

Besides, the cytotoxicity of resin monomers is also associated with excessive reactive oxygen species (ROS) production [6]. The presence of ROS can induce oxidative DNA damage and trigger various signal transduction pathways, which may potentially affect chemical cytotoxicity.

Different parameters were found to influence the cytotoxicity of acrylic resins:

- Polymer to monomer ratio: the higher this ratio, the lower the residual monomer and, therefore, the cytotoxicity [7].
- Polymerization method: Raszewski [1] explored different acrylic resins which differ in the polymerization method (hot-cured, polymerized under pressure and at lower temperatures). Their results revealed that there were differences in terms of cytotoxicity depending on the polymerization method.

It was found that there was a negative correlation between residual monomer and cell proliferation [8]. Therefore, it seems that by reducing the residual monomer amount, lower cytotoxicity may be achieved. Sheridan et al [9] found that the cytotoxicity effect was higher for the first 24 hours after polymerization. They hypothesized that the toxic substances released into the medium during the first day were either broken down over time or complexed with other chemicals in the medium that could alter their cytotoxic potential. Besides residual monomer, impurities could also appear and leached out over time. Unreacted fragments of photoinitiator due to its incomplete usage in the polymerization reaction or plasticizers can increase cytotoxicity due to processes like oxidative stress, enzymatic inhibition, and lipophilic reactions with cell membranes [10,11].

Several methods to reduce the cytotoxicity due to the leaching of some components of acrylic resins were proposed in the literature, e.g. soaking in warm water [8,9,12], ultrasonic cleaning [13,14], microwaving [12], autoclaving [15]. In the case of 3D printed acrylic resins, Oskui et al [16] explored different post-treatment to improve the biological performance of the acrylic resin. Compared to rinsing in IPA and water for different times, the exposure to UV light produced an important decrease in cytotoxicity.

The monomer of the acrylic resin used in this study is urethane dimethacrylate (UDMA) and methacrylate monomers. Compared with other acrylic monomers, UDMA is less toxic than Bisphenol A-Glycidyl Methacrylate (BisGMA), but more toxic than Triethylene Glycol Dimethacrylate (TEGDMA) and Hydroxyethyl Methacrylate (HEMA) [17]. Besides its cytotoxic effect, UDMA has been shown to decrease cell differentiation of some cells, e.g. mouse embryonic stem cells [18], and human pulp cells [19]. However, some studies [20] have found that UDMA enhanced HL-60 (human promyelocytic leukemia cells) differentiation. Therefore, the presence of residual monomer is not desirable in terms of cytotoxicity.

Another component that could show cytotoxicity is the photoinitiator. The photoinitiator used in this case is TPO. In literature, some studies found a cytotoxic character in TPO. Van Landuyt et al [21] found that TPO usage in an adhesive as a photoinitiator implied lower biocompatibility compared with other kinds of photoinitiators. Its cytotoxicity showed a dose-dependent behaviour. Zeng et al [22] also reported medium cytotoxicity of TPO, but their results did not indicate a dose dependent cytotoxicity.

The mechanism behind the possible cytotoxicity of TPO was explained by Popal et al [23]. They hypothesized that the molecular structure of TPO suggested an interaction, e.g., with amino acids residues of cellular proteins. This interaction could affect important protein functions, even at low concentrations of TPO. Besides, the non-polar character of the phenyl groups could increase the ability of TPO to cross thee cell membrane and interact with cellular metabolism.

Another possible mechanism of cytotoxicity of acrylic resin could be the effect of resin surface on the cell adhesion. Some acrylic resins were found to be biologically inert because of their relatively low wettability and the lack of biofunctional groups, that could cause a negative effect on cell adhesion and biocompatibility [24].

7.2. Direct and indirect viability

With the tests carried out in this section, direct and indirect cytotoxicity were analyzed. Cell viability on the sample surfaces was studied. Besides, it was determined if there was any toxic component that could be released to the media, resulting in a reduction of biocompatibility. Released components could be the residual monomer, the photoinitiator, the plasticiers or other additives.

7.2.1. Experimental methodology

In this section, R' was also analyzed together with the other composites to discern if the possible effect was due to the addition of GBN or the addition of MMA. Besides, MMA could be responsible for the cytotoxicity of samples and adding it could modify the cell response.

Samples used to carry out these tests were postcured and sterilized. The timeslots selected were 24, 48 and 72 hours. As explained in Section 3.2.8.2., possible released components and their effect on cytotoxicity were determined by elution tests.

7.2.2. Results

7.2.2.1. Direct viability

Calcein/PI staining images are shown in Figure 7.2. Live cells were stained in green, whilst dead cells could be observed in red. Images quality was sometimes low because of the autofluorescence that acrylic photocurable resins show [11].

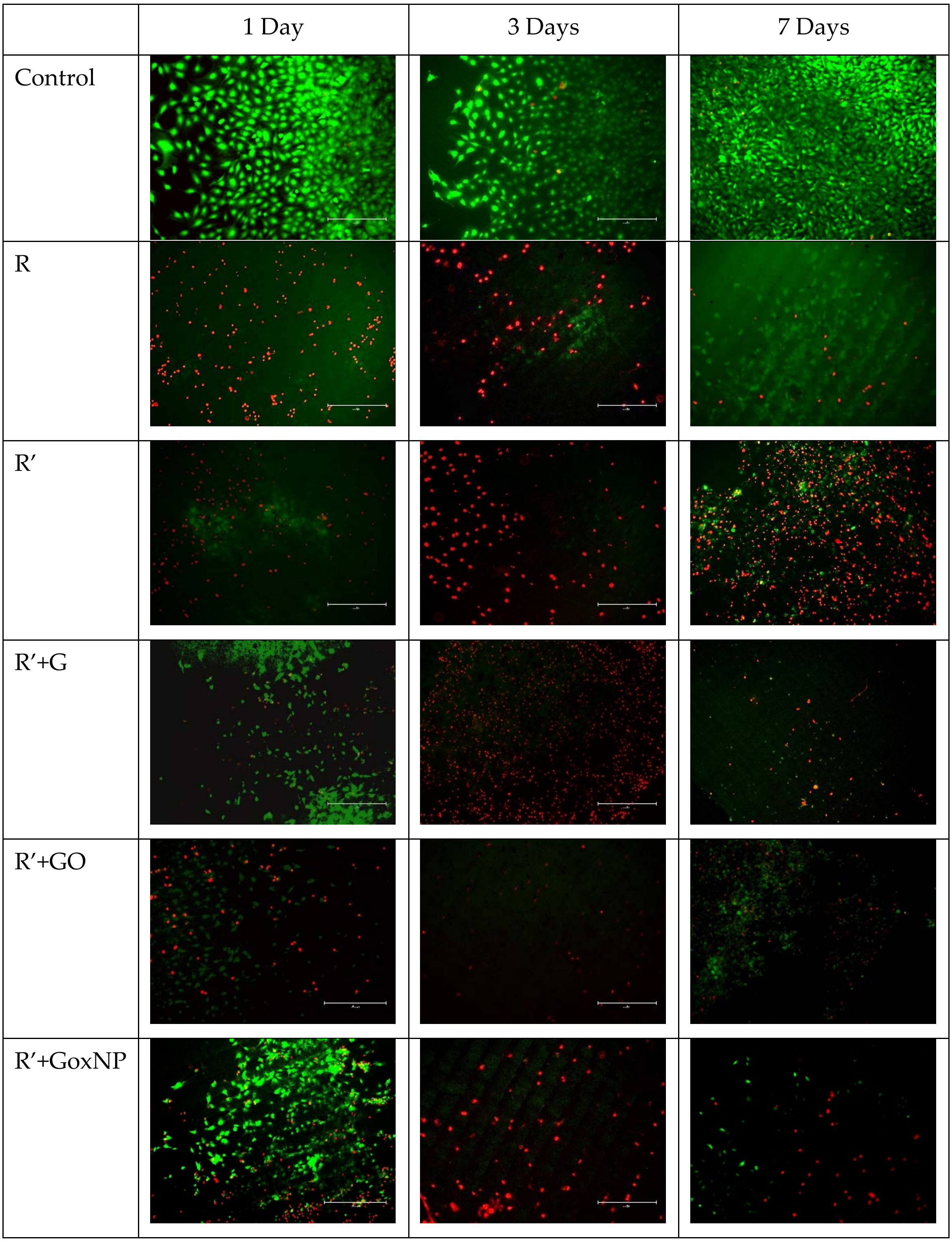

Figure 7.2. *Direct viability on unwashed acrylic samples. Live and dead cells were stained in green and red, respectively.*

Surfaces of acrylic resin showed cytotoxicity, even after 24 hours of cell contact. Surface viability seemed to increase after 24 h with the addition of GBN, specially GoxNP when staining images were analyzed. Cell viability seemed to increase with time for R, R′ and R′+GO samples. However, on R′+G and R’+GoxNP there were only a few cells after 7 days of culture time. The morphology of the cells showed that they were metabolically inactive in all cases, being all of them spherical in shape.

It is important to highlight again the high autofluorescence that the acrylic resin showed, which in some cases, resulted in not conclusive images. Therefore, these results must be completed with Alamar Blue tests. Metabolic activity was evaluated using Alamar Blue tests. The results of these tests for 1, 3 and 7 days of culture time are shown in Figure 7.2.

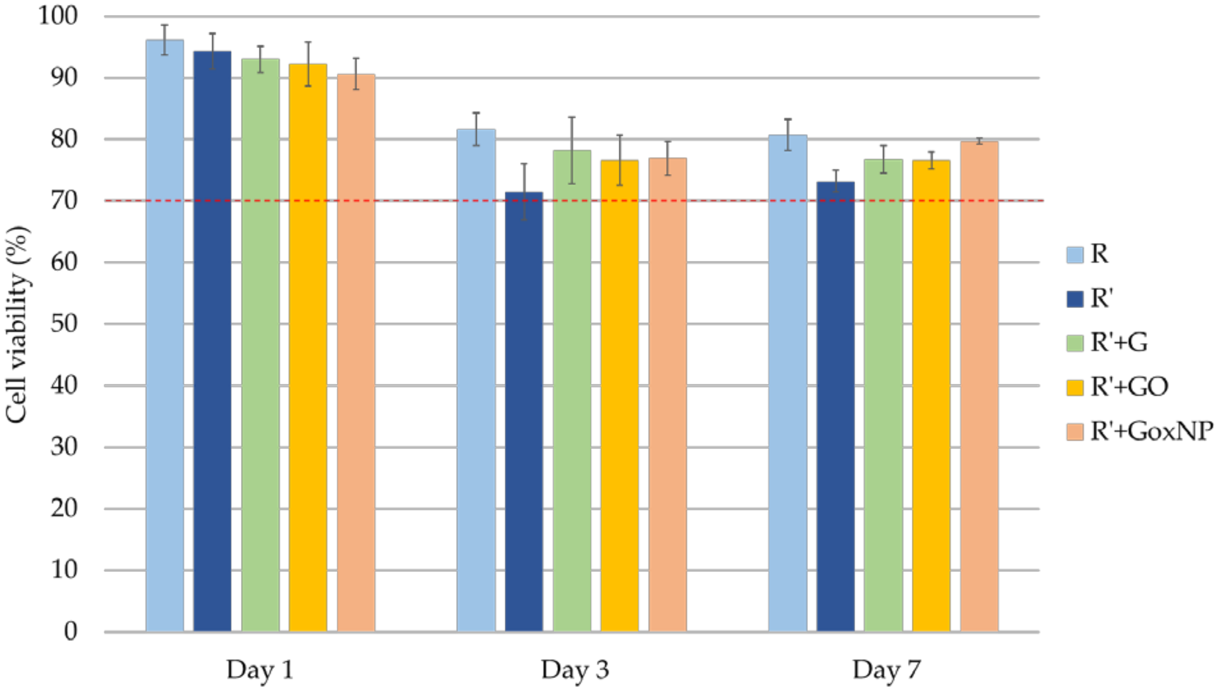

Figure 7.3. *Cell viability of acrylic resin and its nanocomposites determined by Alamar Blue.*

Alamar Blue tests suggested that the addition of MMA decreased slightly metabolic activity after all measured times, especially 3 and 7 days. The addition of all three types of GBN increased this metabolic activity, compared to R’. For long times (7 days) R showed more active cells than the other samples.

However, it was found that metabolic activity decreased with time. It could be due to two reasons: (i) cells started to differentiate and during this process they died, or (ii) surfaces showed cytotoxic behaviour. From Live/Dead staining it was possible to discern the reason for metabolic activity reduction. Cells were not confluent at any time, with levels of confluence lower than 50%. Therefore, differentiation could not start and the reduction of viability with time was due to surface cytotoxicity. Therefore, it seemed that all the studied samples presented some cytotoxic behavior and a deeper study was needed.

7.2.2.2. Elution tests

Analyzing the results obtained in the contact viability test, it was concluded that acrylic resin had some toxic components that led to a decrease in cell viability. To find out if these toxic components were released to the media or were attached to the polymer structure, the following test was carried out. In this case, cells were cultured with eluents collected after 24, 48 and 72 hours in contact with the resin to assess the cytotoxicity of sample extracts. Figure 7.4 shows the Live/Dead staining images of these tests.

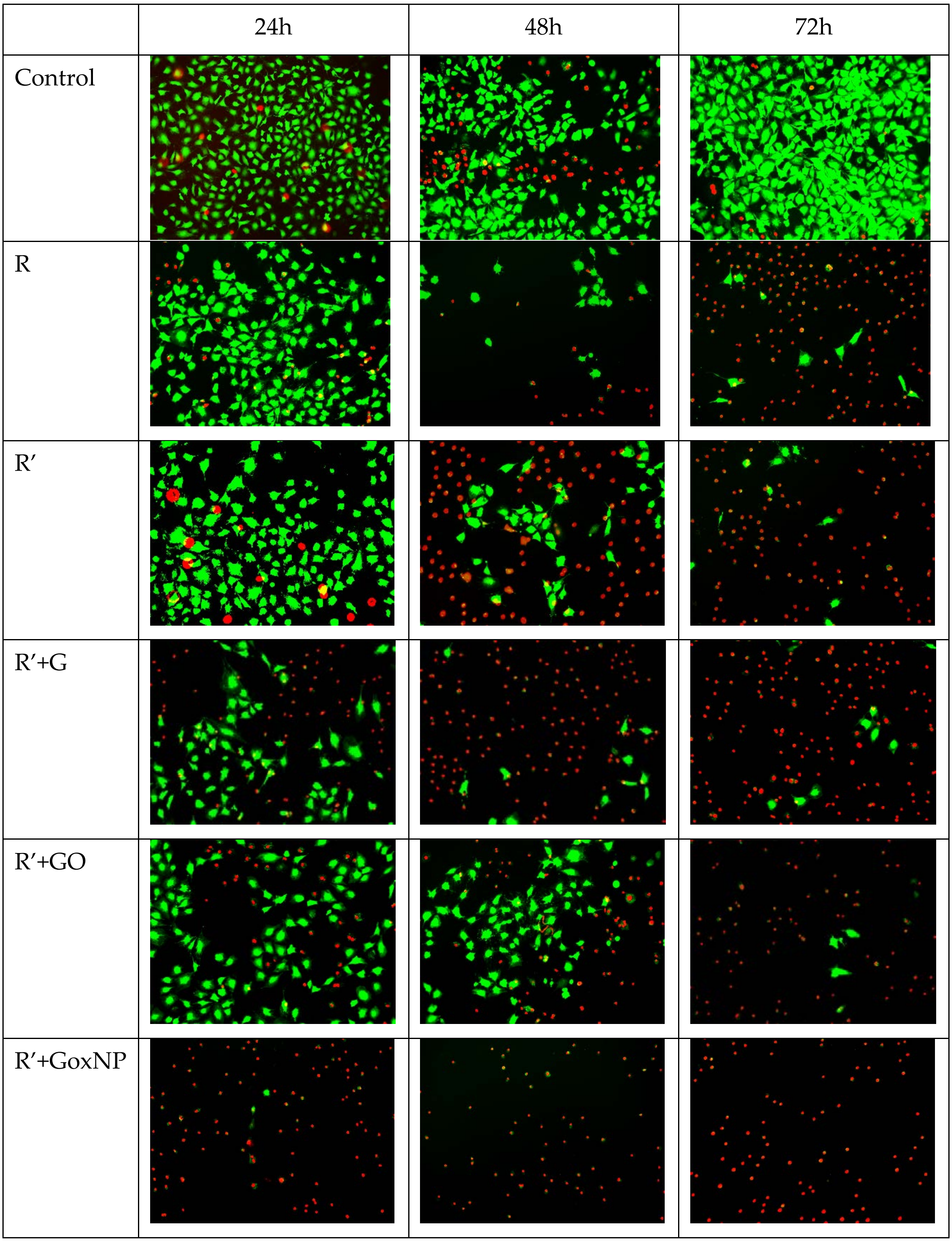

Figure 7.4. *Elution tests (24 h) with eluents collected after 24, 48 and 72 h in contact with R and its composites. Live and dead cells were stained in green and red, respectively.*

It was found that R showed high cytotoxicity after 48 hours of elution, similar to the cytotoxicity level at 72 hours. Therefore, it seems that there was still some residual monomer or any toxic component that was released to the medium after 48 hours. When MMA was added to R, the eluent had a similar cell performance.

The addition of GBN affected differently depending on the nanofiller. G showed higher cytotoxicity after 24 hours. After 48 hours it showed similar cytotoxicity to 72 hours. In the case of GO, it seems that it slightly reduced the elution of the toxic components, but it still showed high cytotoxicity after 72 hours. Finally, the most important difference with R' was found for R'+GoxNP samples. They showed high cytotoxicity after 24 hours of elution.

To determine which components were released from the samples and were responsible for the cytotoxic behaviour of the eluents, ^{1}H NMR spectra were obtained. To analyze them, it is important to know where the characteristic peaks of the possible components (MMA and TPO) appear.

MMA spectrum showed the most intense peaks at 6.10, 5.55, 3.75 and 1.95 ppm, corresponding to A, B, C and D hydrogens shown in Figure 7.3, respectively [25]. Acrylate monomers of the commercial resin were unknown, but A, B and D hydrogens appear for all the acrylate monomers. Therefore, monomers of the resin could also be detected from these peaks.

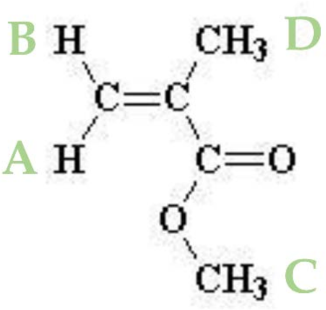

Figure 7.5. *MMA molecule.*

TPO (photoinitiator) could also be found in NMR spectrum of resin eluents. TPO characteristic peaks are at 7.99, 7.55, 7.50, 6.80, 2.25 and 2.03 ppm for A to F hydrogens shown in Figure 7.4, respectively [26].

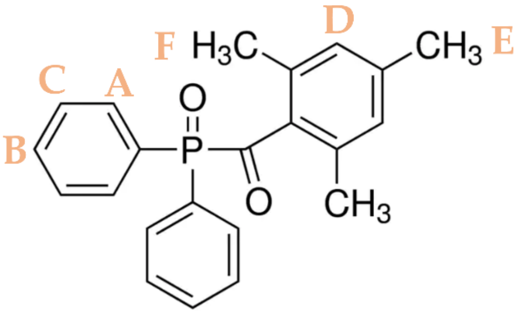

Figure 7.6. *TPO molecule.*

All spectra were referenced to the residual solvent peak, which in deuterated water (D2O) will be around 4.790 ppm. Figure 7.5 shows the spectra of unwashed samples.

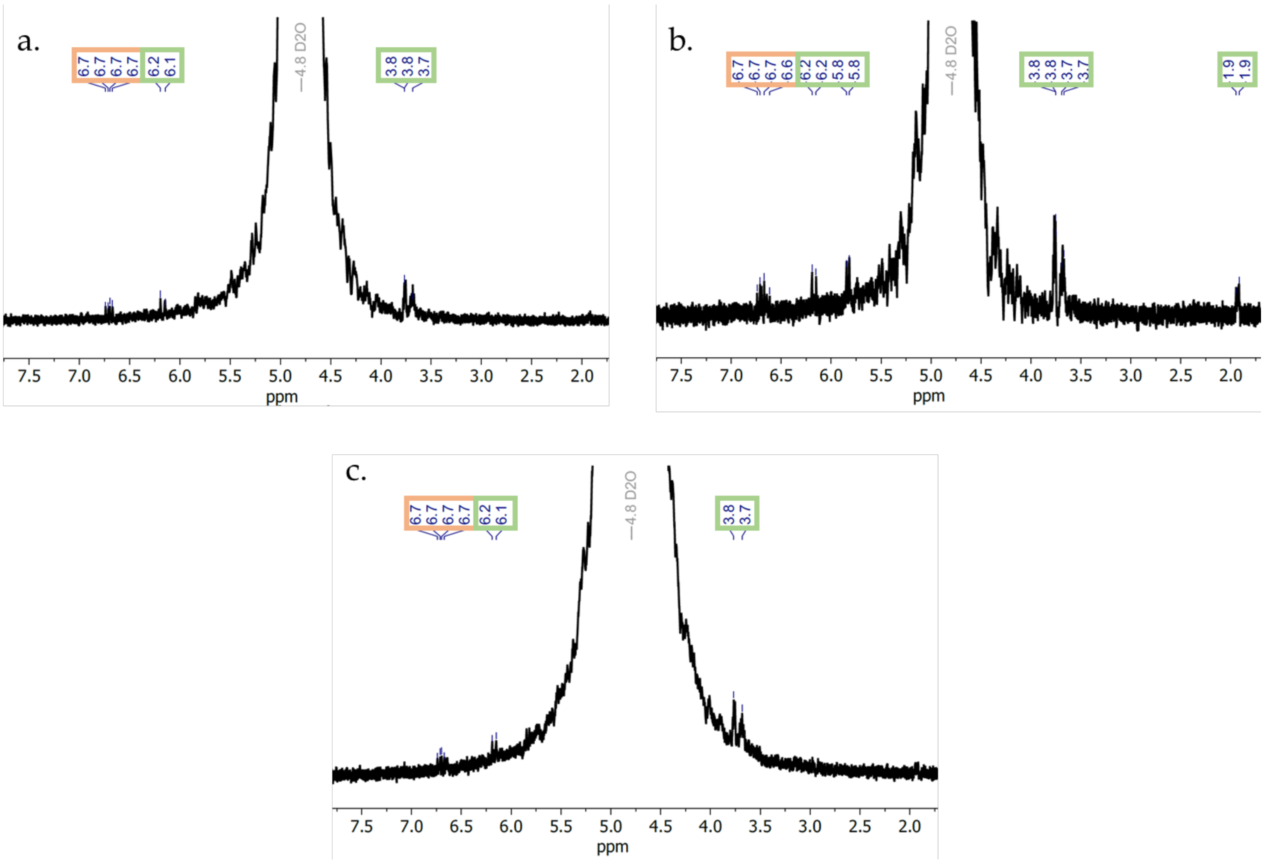

Figure 7.7. *NMR spectrum of unwashed R (a), R′ (b) and R′+G (c). Peaks boxed in green are due to MMA and in orange are due to TPO.*

They presented very small peaks around 6.7 ppm. This is in the region where aromatic protons fall and, based on the resin composition, the only place the aromatics would be coming from was the photoinitiator. Therefore, in all the samples some residual photoinitiator seemed to be found.

Besides, the peaks around 3.8-3.7 ppm were due to residual monomer in the sample, which could be responsible for the cytotoxicity. It was found that the R′ samples showed some extra peaks that did not appear in the other samples. These peaks could be associated with the acrylic monomer, and it suggested that the addition of MMA led to a higher amount of residual monomer in the printed resin. By DSC residual monomer should be found as an evaporation peak at low temperatures (around 110°C [27]). However, the intensity of the analyzed peaks was almost in the limit of detection of the equipment. Therefore, the amount of residual monomer and photoinitiator was very low and, for this reason, evaporation peak at DSC did not appear.

7.3. Viability of washed samples

7.3.1. Experimental methodology

These tests explored the possibility of removing the components that produced cytotoxicity found in the previous section by 1 or 2 washing cycles of 24 hours each. Besides, with the best washing procedure, elution was carried out for 7 days and Live/Dead staining tests were carried out for 1, 3 and 7 days of cell culture in a 48-well plate (culture plate).

Finally, direct viability was analyzed for the washed samples by Live/Dead staining and Alamar Blue after 1, 3 and 7 days.

7.3.2. Results

7.3.2.1. Washing optimization

Cell viability was analyzed after 1 day to determine if cell viability improved with the washing of the samples. Results of 1 and 2 washes are shown in Figure 7.8.

It seems that the washing procedure was successful in all the cases. Analyzing R, only with one wash, the cell viability increased, whilst R’ needed two washes to achieve the same level of cell viability as R. R’+G showed lower cell viability in the pristine sample, but after one wash it achieved the same level of biocompatibility than R. R’+GO was found to have the same cell performance than R’ with the washing procedure. Finally, R’+GoxNP, which showed the highest cytotoxicity without being washed, showed high cell viability after one wash and, even higher after two washes.

Therefore, the global conclusion that can be drawn after these tests is that acrylic resin had some toxic components that were released to the media, causing high cytotoxicity levels. Fortunately, these components could be removed after 2 cycles of 24 hours of washing with media, probably because the residual monomer/photoinitiator released reacted with the proteins in the medium, following the mechanism shown in Figure 7.1.

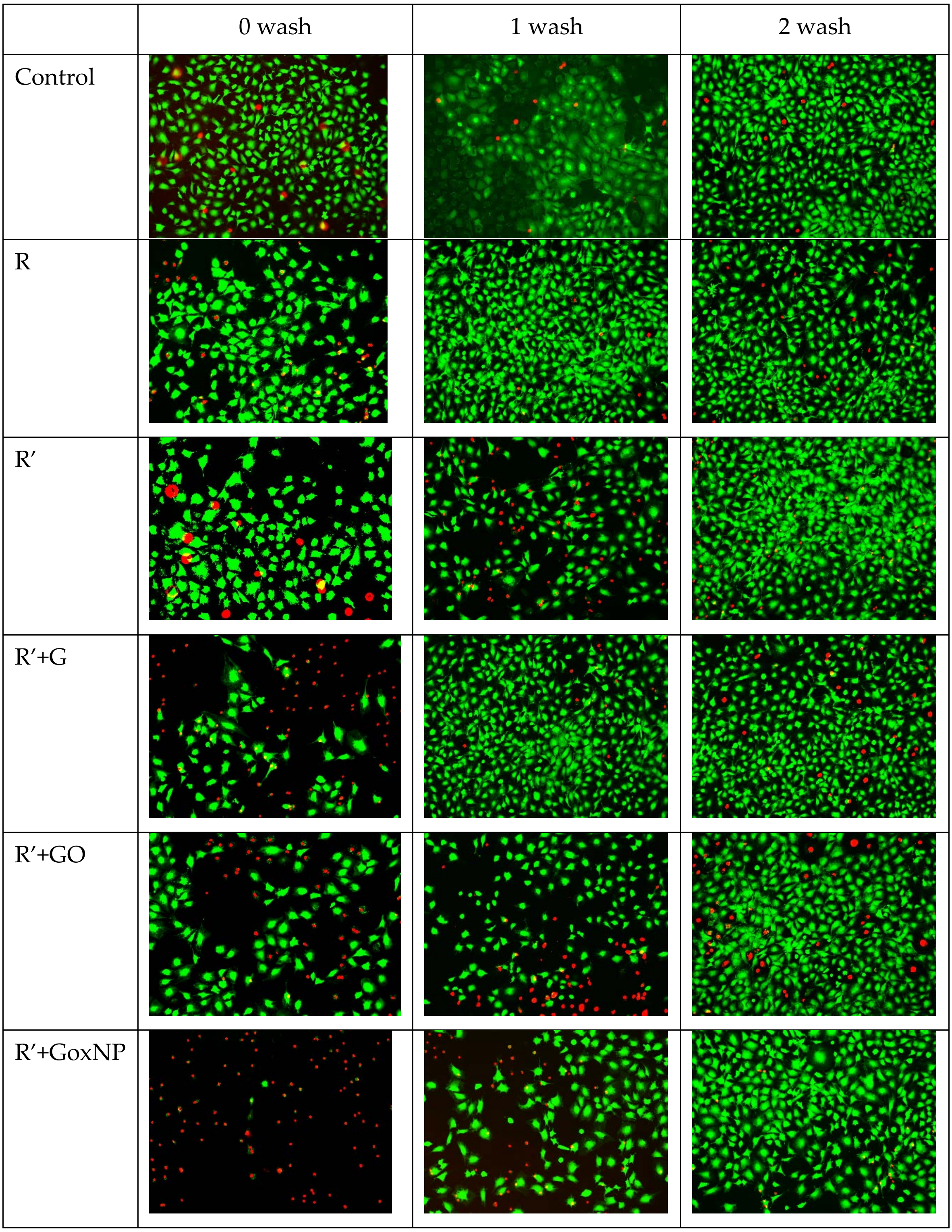

Figure 7.8. *Elution tests (24 h) with eluents collected after 24 h in contact with R and its composites after 0, 1 and 2 washes. Live and dead cells were stained in green and red, respectively.*

Considering these findings, and to assure the possibility of toxic components removal, one more test was carried out. Samples were washed twice with media, and eluents were collected after 7 days of incubation with the sample. They were used to culture cells for 1, 3 and 7 days, and Live/Dead staining tests were carried out (Figure 7.9).

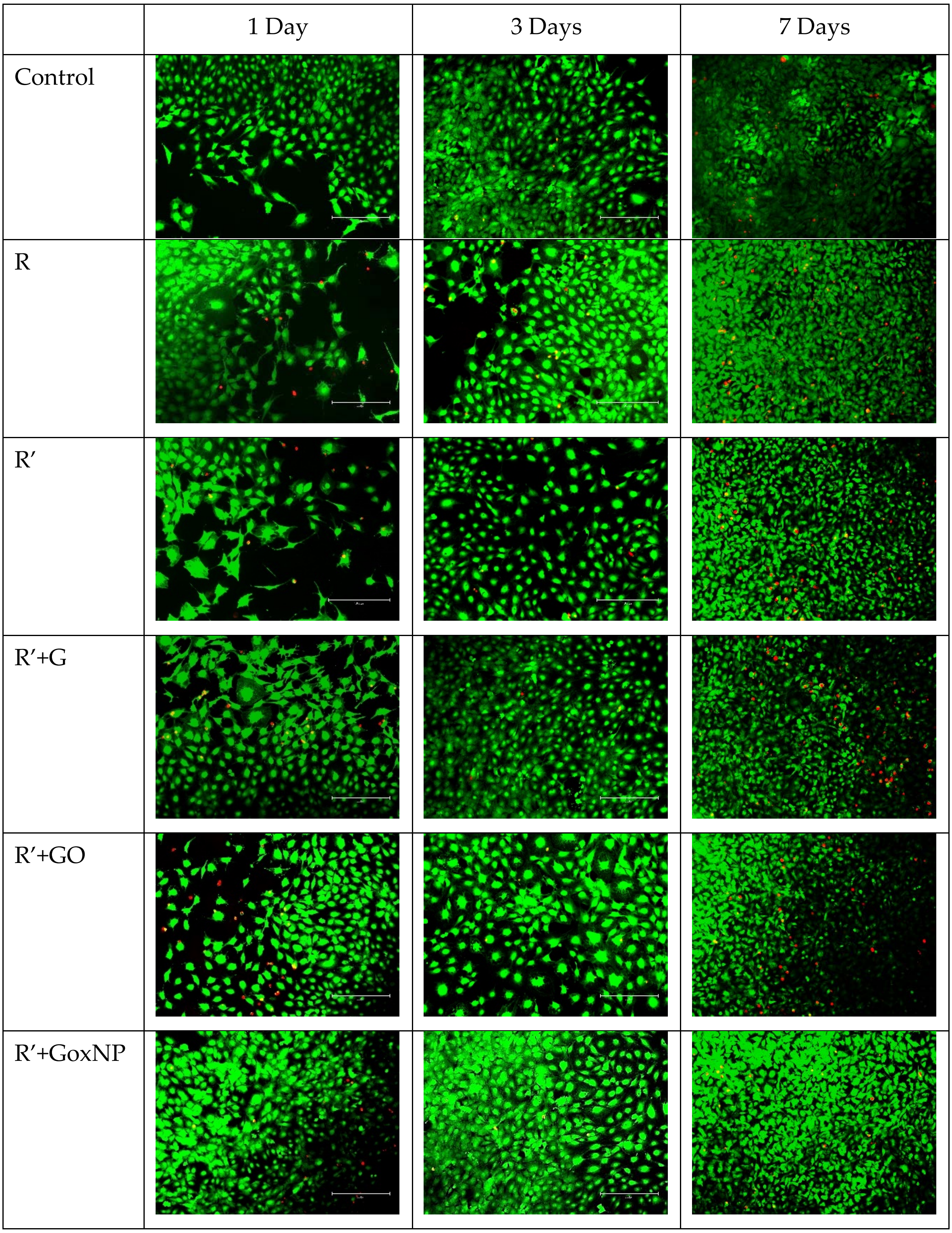

Figure 7.9. *Elution tests (1, 3 and 7 days) with eluents collected after 7 days in contact with double washed samples. Live and dead cells were stained in green and red, respectively.*

When samples were double-washed, eluents did not show cytotoxicity for culture times until 7 days at least.

7.3.2.2. *Direct viability of washed samples*

Therefore, direct viability was determined on doubled-washed samples by Live/Dead staining and Alamar Blue for 1, 3 and 7 days. The results are shown in Figure 7.10.

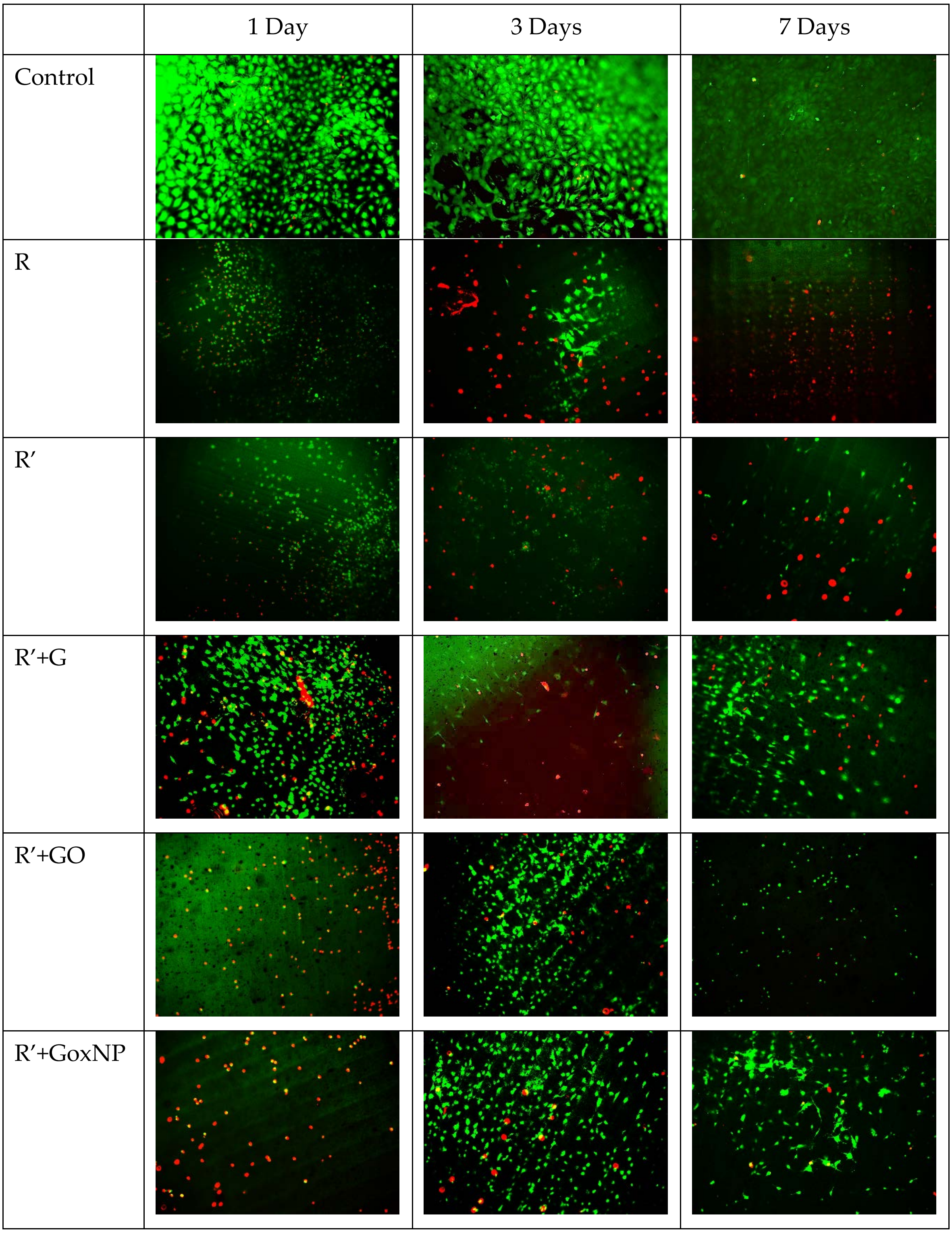

Figure 7.10. *Direct viability on washed acrylic samples. Live and dead cells were stained in green and red, respectively.*

From staining images, it can be concluded that G and GoxNP increased cell viability compared to R and R'. In the case of R'+GO, only some cells in spherical form, indicative of metabolically inactive or dead cells, were found. However, quantitative results were only obtained by Alamar Blue tests, which were more reliable because of the high autofluorescence of the resin. The results of Alamar Blue tests can be seen in Figure 7.6.

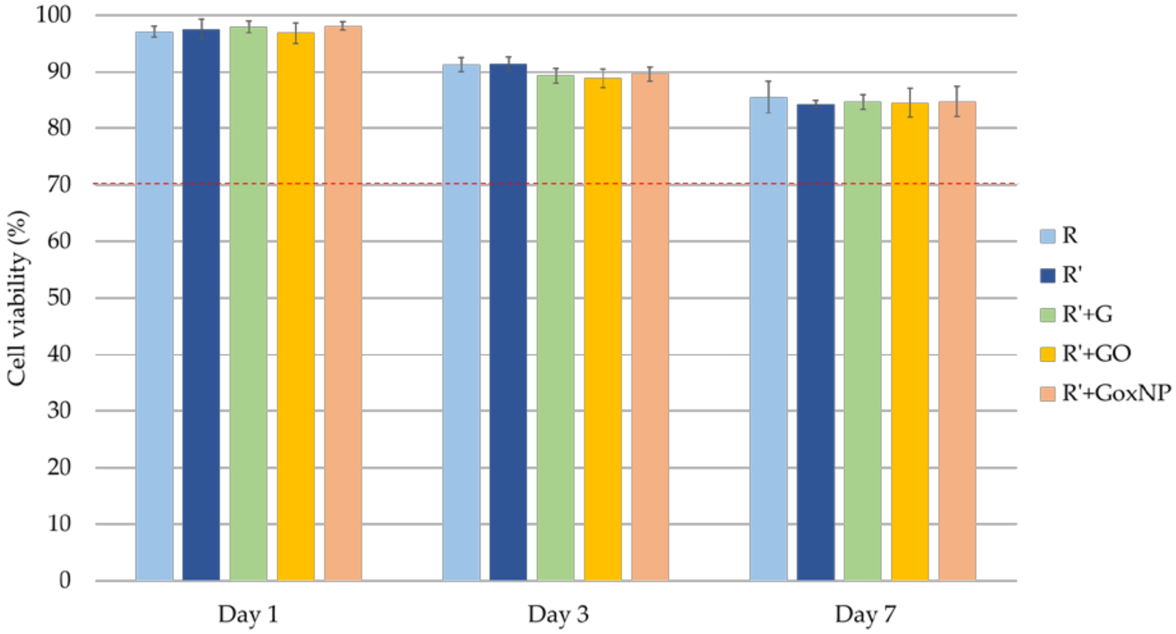

Figure 7.11. *Cell viability of double-washed samples determined by Alamar Blue.*

When samples were analyzed by the Alamar Blue test, it was found that the metabolic activity of all of them was similar in every time slot. It is important to keep in mind that, according to ISO 10993-5: 2009 [28], relative metabolic activities above 70% of the control indicate that specimens had no cytotoxic effects. In this case, all the studied samples achieved levels of cell viability higher than 80%. However, and as previously found on unwashed samples, metabolic activity decreased with time without having confluence of cells on the surface. Therefore, samples still showed some cytotoxicity and washing procedure should be optimized in future works.

To determine if the toxic components were completely removed after the washing, ^{1}H NMR spectra were recorded again. Figure 7. 7 shows the NMR spectra of double-washed samples.

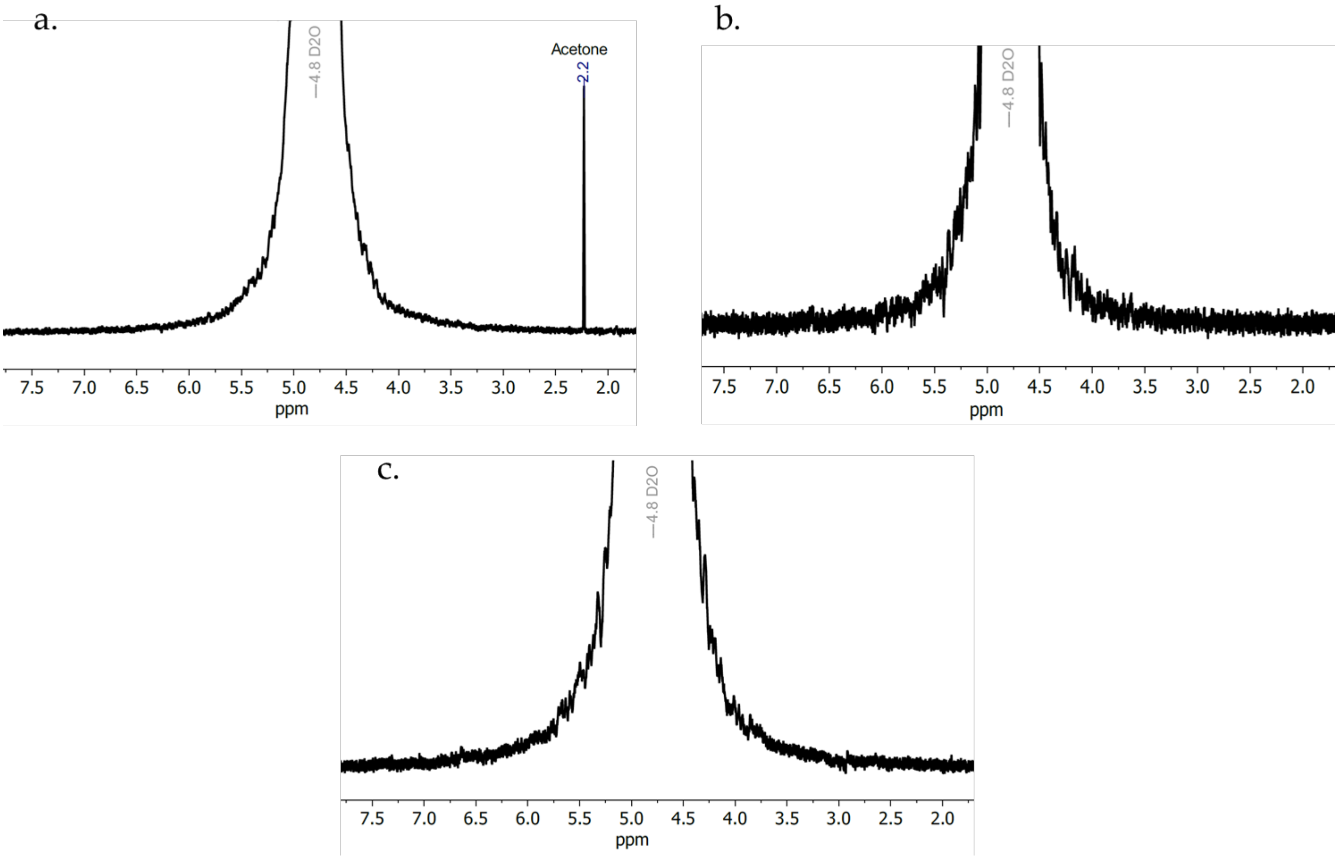

Figure 7. 12. *NMR spectrum of washed R (a), R′ (b) and R′+G (c).*

It was found that all the peaks found in unwashed samples disappeared when they were washed twice for 24 hours. Therefore, all the remaining monomer and photoinitiator were removed with the washing procedure. For this reason, cell viability increased for washed samples compared to the pristine samples. Even having achieved an important improvement on biocompatibility with washing, other cytotoxic mechanisms could still be present, which should be studied more in depth.

7.4. Discussion of the results

The surface of printed samples showed some cytotoxic behaviour due to the residual monomer and photoinitiator. It was found that the addition of MMA decreased metabolic activity, which could be due to the presence of a higher amount of residual monomer, as seen by NMR.

Analyzing indirect cytotoxicity tests of unwashed samples, it was found that the extracts of unwashed resin showed cytotoxic behaviour. It had already been observed by Xu et al [29], who studied acrylic resin cytotoxicity and the effect of rinsing time on this parameter. They concluded that the cytotoxic behaviour was due to the residual monomer, which could be removed by rinsing in ethanol.

R’+G and R’+GoxNP extracts showed higher cytotoxicity at short times (1 day) than the other studied materials. Two hypotheses can explain this phenomenon:

- The nanofiller was released to the media together with the monomer or the toxic component.
- The nanofiller was not properly adhered to the matrix, resulting in a higher free volume which favoured the release of toxic components.

By NMR, the reason could not be concluded because of the low loading of nanofillers and the small signal that appeared due to the reduced solubility of resin.

Different methods were explored to reduce the cytotoxicity of extracts by reducing the amount of residual monomer: rinsing in IPA [29], water [9] or autoclaving [15]. As it was found that washing with media was effective in terms of reduction of cytotoxicity of eluents, the washing procedure was carried out with media. After washing, collected eluents were analyzed and the toxic component had been removed or, at least, it was not released to the media, as was corroborated by NMR.

After washing, the surface of all the studied samples showed higher biocompatibility than those unwashed, reaching cell viability higher than 80% for culture times until 7 days. Washing was especially efficient in the case of R’, which equalled the cell viability of the other samples after washing. However, other mechanisms responsible for cytotoxicity could be present because cell viability still reduced with time. Therefore, an optimization of washing procedure should be carried out in future works.

7.5. Conclusions of this chapter

- Cell viability of acrylic resin and its nanocomposites was higher than 70% in all the cases, but it reduced with time when cells were not confluence, which meant that surfaces showed cytotoxic behaviour.

- The addition of MMA produced a slight decrease in the cell viability of unwashed samples.

- It was found that one of the responsible for the slight cytotoxicity were the residual photoinitiator and monomer.

- Eluents of washed samples showed no cytotoxicity, and their surfaces showed cell viability higher than 80% in all cases, but some cytotoxicity still remained which needs to be explored in future works.

- The addition of GBN did not produce an increase in the cytotoxicity of the resin, which is of high interest due to the controversial results found in the literature regarding the cytotoxicity of GBN. Besides, when GBN were properly incorporated and dispersed within the matrix they were not released to the medium and the indirect cytotoxicity was also adequate.

7.5. References

[1] Z. Raszewski, Influence of polymerization method on the cytotoxicity of three different denture base acrylic resins polymerized in different methods, Saudi J. Biol. Sci. 27 (2020) 2612–2616. https://doi.org/10.1016/j.sjbs.2020.05.039.

[2] M. Souto-Lopes, Á. Azevedo, A. Teixeira, D. Bastos-Aires, J. Lordelo, D. Pérez-Mongiovi, Cytotoxicity of acrylic based resin compounds in a human gingival fibroblast cell line, Rev. Port. Estomatol. Med. Dent. e Cir. Maxilofac. 54 (2013) 87–90. https://doi.org/10.1016/j.rpemd.2013.02.003.

[3] P. Li, A.L. Lambart, B. Stawarczyk, M. Reymus, S. Spintzyk, Postpolymerization of a 3D-printed denture base polymer: Impact of post-curing methods on surface characteristics, flexural strength, and cytotoxicity, J. Dent. 115 (2021) 103856. https://doi.org/10.1016/j.jdent.2021.103856.

[4] K. Chan, P.J. O'Brien, Structure-activity relationships for hepatocyte toxicity and electrophilic reactivity of α,β-unsaturated esters, acrylates and methacrylates, J. Appl. Toxicol. 28 (2008) 1004–1015. https://doi.org/10.1002/jat.1366.

[5] M. Awatef, A. Kassab, D. Hadyaoui, An In Vivo Investigation into Oxidative Stress of Methacrylate Monomers Used In Dentistry, Int. J. Sci. Res. Technol. 5 (2017) 46–55.

[6] M.C. Chang, L.D. Lin, C.P. Chan, H.H. Chang, L.I. Chen, H.J. Lin, H.W. Yeh, W.Y. Tseng, P.S. Lin, C.C. Lin, J.H. Jeng, The effect of BisGMA on cyclooxygenase-2 expression, PGE2 production and cytotoxicity via reactive oxygen species- and MEK/ERK-dependent and -independent pathways, Biomaterials. 30 (2009) 4070–4077. https://doi.org/10.1016/j.biomaterials.2009.04.034.

[7] J.H. Jorge, E.T. Giampaolo, A.L. Machado, C.E. Vergani, Cytotoxicity of denture base acrylic resins: A literature review, J. Prosthet. Dent. 90 (2003) 190–193. https://doi.org/10.1016/S0022-3913(03)00349-4.

[8] C. Bural, E. Aktaş, G. Deniz, Y. Ünlüçerçi, N. Kizilcan, G. Bayraktar, Effect of post-polymerization heat-treatments on degree of conversion, leaching residual MMA and in vitro cytotoxicity of autopolymerizing acrylic repair resin, Dent. Mater. 27 (2011) 1135–1143. https://doi.org/10.1016/j.dental.2011.08.007.

[9] P.J. Sheridan, S. Koka, N.O. Ewoldsen, C.A. Lefebvre, M.T. Lavin, Cytotoxicity of denture base resins, Int. J. Prosthodont. 10 (1997) 73–77. http://www.ncbi.nlm.nih.gov/pubmed/9484073.

[10] W.A. Green, Industrial Photoinitiators - A Technical Guide, CRC Press, 2010. https://doi.org/10.1201/9781439827468.

[11] H.B. Musgrove, M.A. Catterton, R.R. Pompano, Applied tutorial for the design and fabrication of biomicrofluidic devices by resin 3D printing, Anal. Chim. Acta. 1209 (2022) 339842. https://doi.org/10.1016/j.aca.2022.339842.

[12] V.M. Urban, A.L. Machado, R. V. Oliveira, C.E. Vergani, A.C. Pavarina, Q.B. Cass, Residual monomer of reline acrylic resins. Effect of water-bath and microwave post-polymerization treatments, Dent. Mater. 23 (2007) 363–368. https://doi.org/10.1016/j.dental.2006.01.021.

[13] T. Charasseangpaisarn, C. Wiwatwarrapan, N. Leklerssiriwong, Ultrasonic cleaning reduces the residual monomer in acrylic resins, J. Dent. Sci. 11 (2016) 443–448. https://doi.org/10.1016/j.jds.2016.07.003.

[14] T. Charasseangpaisarn, C. Wiwatwarrapan, The effect of various frequencies of ultrasonic cleaner in reducing residual monomer in acrylic resin, Ultrasonics. 63 (2015) 163–167. https://doi.org/10.1016/j.ultras.2015.07.005.

[15] S. Tangpothitham, P. Pongprueksa, M. Inokoshi, S. Mitrirattanakul, Effect of post-polymerization with autoclaving treatment on monomer elution and mechanical properties of 3D-printing acrylic resin for splint fabrication, J. Mech. Behav. Biomed. Mater. 126 (2022) 105015. https://doi.org/10.1016/j.jmbbm.2021.105015.

[16] S.M. Oskui, G. Diamante, C. Liao, W. Shi, J. Gan, D. Schlenk, W.H. Grover, Assessing and Reducing the Toxicity of 3D-Printed Parts, Environ. Sci. Technol. Lett. 3 (2016) 1–6. https://doi.org/10.1021/acs.estlett.5b00249.

[17] H.H. Chang, M.C. Chang, L.D. Lin, J.J. Lee, T.M. Wang, C.H. Huang, T.T. Yang, H.J. Lin, J.H. Jeng, The mechanisms of cytotoxicity of urethane dimethacrylate to Chinese hamster ovary cells, Biomaterials. 31 (2010) 6917–6925. https://doi.org/10.1016/j.biomaterials.2010.05.059.

[18] S. Schwengberg, H. Bohlen, N. Kleinsasser, K. Kehe, M. Seiss, U.I. Walther, R. Hickel, F.X. Reichl, In vitro embryotoxicity assessment with dental restorative materials, J. Dent. 33 (2005) 49–55. https://doi.org/10.1016/j.jdent.2004.08.001.

[19] I. About, J. Camps, T.A. Mitsiadis, M.J. Bottero, W. Butler, J.C. Franquin, Influence of resinous monomers on the differentiation in vitro of human pulp cells into odontoblasts, J. Biomed. Mater. Res. 63 (2002) 418–423. https://doi.org/10.1002/jbm.10253.

[20] G. Nocca, G.E. Martorana, P. De Sole, F. De Palma, C. Callà, P. Corsale, M. Antenucci, G. Gambarini, C. Chimenti, B. Giardina, A. Lupi, Effects of 1,4-butanediol dimethacrylate and urethane dimethacrylate on HL-60 cell metabolism, Eur. J. Oral Sci. 117 (2009) 175–181. https://doi.org/10.1111/j.1600-0722.2008.00606.x.

[21] K.L. Van Landuyt, S. Krifka, K.A. Hiller, C. Bolay, C. Waha, B. Van Meerbeek, G. Schmalz, H. Schweikl, Evaluation of cell responses toward adhesives with different photoinitiating systems, Dent. Mater. 31 (2015) 916–927. https://doi.org/10.1016/j.dental.2015.04.016.

[22] B. Zeng, Z. Cai, J. Lalevée, Q. Yang, H. Lai, P. Xiao, J. Liu, F. Xing, Cytotoxic and cytocompatible comparison among seven photoinitiators-triggered polymers in different tissue cells, Toxicol. Vitr. 72 (2021) 105103. https://doi.org/10.1016/j.tiv.2021.105103.

[23] M. Popal, J. Volk, G. Leyhausen, W. Geurtsen, Cytotoxic and genotoxic potential of the type I photoinitiators BAPO and TPO on human oral keratinocytes and V79 fibroblasts, Dent. Mater. 34 (2018) 1783–1796. https://doi.org/10.1016/j.dental.2018.09.015.

[24] A. Ronca, F. Maiullari, M. Milan, V. Pace, A. Gloria, R. Rizzi, R. De Santis, L. Ambrosio, Surface functionalization of acrylic based photocrosslinkable resin for 3D printing applications, Bioact. Mater. 2 (2017) 131–137. https://doi.org/10.1016/j.bioactmat.2017.04.002.

[25] Chemical Book. Methyl methacrylate(80-62-6) 1H NMR spectrum, (2017). https://www.chemicalbook.com/SpectrumEN_80-62-6_1HNMR.htm.

[26] NMRshiftDB, NMRshiftDB Proj. V. 1.4.15. (2002). http://nmrshiftdb.nmr.uni-koeln.de.

[27] N.W. Elshereksi, S.H. Mohamed, A. Arifin, Z.A.M. Ishak, Thermal characterisation of poly(Methyl Methacrylate) filled with barium titanate as denture base material, J. Phys. Sci. 25 (2014) 15–27.

[28] UNE-EN ISO 10993-5:2009, Evaluación biológica de productos sanitarios. Parte 5: Ensayos de citotoxicidad in vitro, (2009).

[29] Y. Xu, A.. Xapapadeas, B. Koos, J. Geis-Gastorfer, P. Li, S. Spintzyk, Effect of post-rinsing time on the mechanical strength and cytotoxicity of a 3D printed orthodontic splint material, Dental. 37 (2021) e314–e327.

CHAPTER 8

CONCLUSION AND FUTURE WORK

Table of Contents

8.1. Final conclusions

The main objective of the thesis was to obtained GBN-reinforced photocurable resins that allow for fabrication of 3D printedscaffolds using Vat Polymerization technologies. From the conclusions extracted from each part of this thesis, the most significant contribution can be summarized as follows:

1. It was found that dispersibility in photocurable resins was not adequate because of the high viscosity that they presented. **The dispersion was improved by the addition of MMA**, which, compared to the use of solvents, presented the advantage of not adversely affecting mechanical or biological properties and it did not need to be removed.
2. A study was carried out regarding the polymerization process and the effect that both, MMA and GBN had on it. It was concluded that **MMA catalyzed the polymerization process and, in the case of GBN, it mainly depended on the kind of GBN**. Due to its high absorbance, G and, to a lower extent, GoxNP inhibited the polymerization process, whilst GO catalyzed it thanks to their oxygenated groups. It is important to highlight that GO catalyzed polymerization reaction but, at the same time, produced a lesser crosslinked structure, that partially hindered the toughening effect found analyzing the fracture surface.
3. It was found that during the 3D printing process, polymerization was not complete and residual stresses appeared. Besides, the presence of GBN, specially GoxNP affected the adhesion between layers. **To control the final mechanical performance of printed nanocomposites, optimized post-treatments must be applied**.
4. **Washing have demonstrated to reduce cytotoxicity of acrylic resin. Besides, GBN addition have not increase cytotoxicity of the nanocomposites.** Cytotoxicity was probably because some toxic components were released to the medium, i.e. residual photoinitiator and monomer. A washing procedure was studied to improve the cell viability of acrylic-based resin, obtaining good results with an improve in cell viability and the removal of the toxic components that were released to the media. However, this procedure needed to be optimized in future works.

8.2. Future works

From the results obtained in this thesis, many aspects could be studied in the future, and they could give interesting results:

- In this work, it was demonstrated that GBN could be used to obtain printed structures by SLA and the effect that they have on polymerization, mechanical properties and cell response. However, the amount of GBN added was not explored and the first step to continue with this research would be optimizing the percentage of GBN added for each kind of GBN.
- The optimization of the loading must be done not only from a mechanical point of view, but also considering the biological performance. Therefore, it would be needed to carry out more exhaustive study e.g., cell differentiation. Besides, it would be important to optimize the washing procedure to achieve good biocompatibility.
- Fatigue and fracture test must be done to test the reinforcing effect of GBN and see the reinforcing mechanism. Besides, scaffolds are subjected to cyclic loads instead of static forces and it is important to assure that the used materials can cope with this kind of loads.
- GBN surface could be functionalized to improve the interaction with the resin, which could lead to an improvement in mechanical performance.
- To mitigate the negative effect that was found for some GBN different options could be explored: adding a higher level of photoinitiator to reduce the inhibition in polymerization, or including other nanoparticles e.g., silica or hydroxyapatite, to reduce the absorbance of the GBN-loaded resin.
- Form 2 printer used in this thesis did not allow to freely change of the printing parameters, but to achieve the best performance of the nanocomposites it would be necessary to optimize exposure time, layer thickness, etc.
- Besides, the final application of this resin is for bone scaffolds. Therefore, it would be interesting to study the mechanical and biological performance of porous structures.

In this thesis, commercial photoresins were investigated to understand the effect of GBN on their properties and it has established a proper basis to know how to proceed and understand the effect that nanoparticles could have in photocurable resins. However, having a commercial resin does not allow for the control the properties, like molecular weight or degradation rate. For this reason, future work relating to the synthesis of a photocurable degradable and biocompatible resin is proposed. More specifically, the synthesis of poly(propylene fumarate) (PPF) has been explored.

PPF is a biocompatible and biodegradable polymer that has been investigated in its use for biomedical applications (bone tissue engineering and drug delivery) since the late 1980s [1–3]. Yaszemski et al. [4] studied the degradation of PPF-based composite materials and found that the mechanical properties of these materials increased with degradation time, which made PPF very useful in the biomedical field.

Some studies [5–10] explored the use of PPF as a photocurable resin. To make PPF photocurable, a photoinitiator must be added and, to reduce the viscosity and make PPF printable, diethyl fumarate (DEF) is used.

8.2.1. First promising results

PPF has been synthesized following the protocol proposed by Kasper et al [11]. It consists of the synthesis of PPF by a two-step reaction of DEF and propylene glycol, obtaining a bis(hydroxypropyl) fumarate diester intermediate, following the scheme shown in Figure 1.

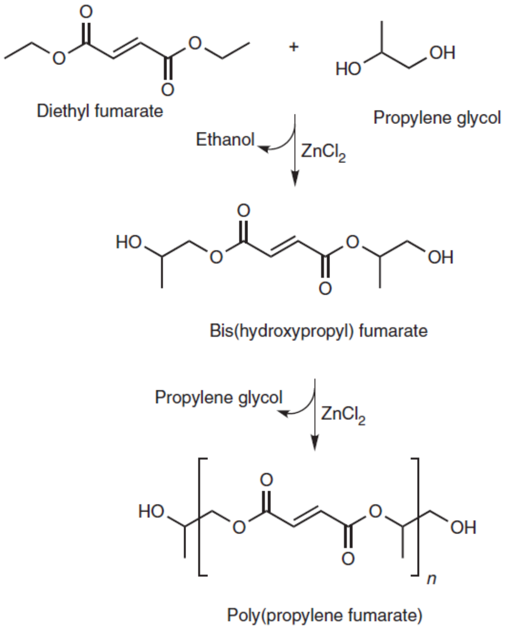

Figure 1. *Two-step synthesis of poly(propylene fumarate)* [11]

The first results show that it is possible to obtain PPF following this process, but some issues relating to the control of the parameters during the synthesis were found and it took a long time to obtain the polymer. When the reaction was successful, the product was characterized by RMN. Spectrum is shown in Figure 2 and it suggests that the synthesis was successful.

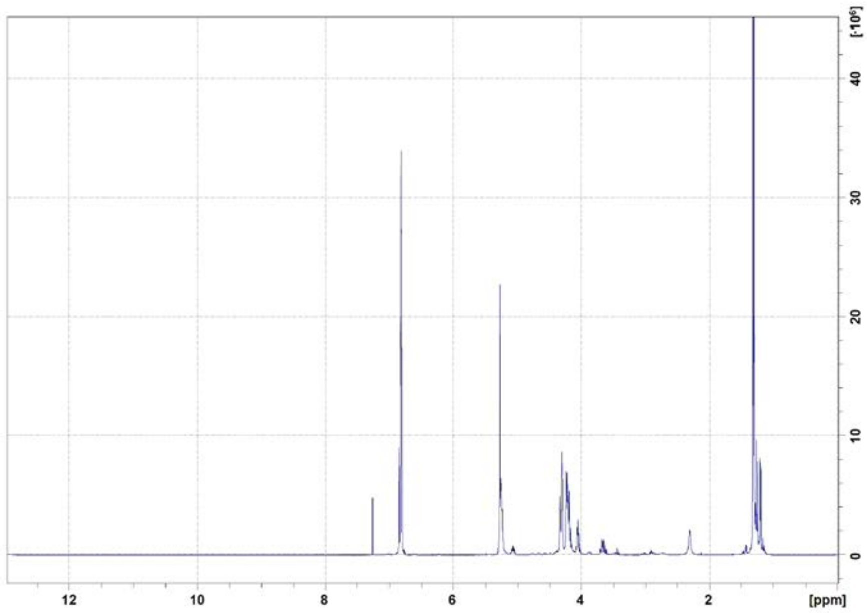

Figure 2. *RMN spectrum of synthesized PPF*

Besides, GPC was used to calculate the number average molecular weight (M_n) of the obtained PPF, obtaining a M_n of around 6,000 Da.

The next step is to make the obtained PPF photocurable. In literature, it can be found different proportions of DEF:BAPO:PPF. Therefore, the ratio has to be optimized. First attempts were carried out by measuring the viscosity of the resin.

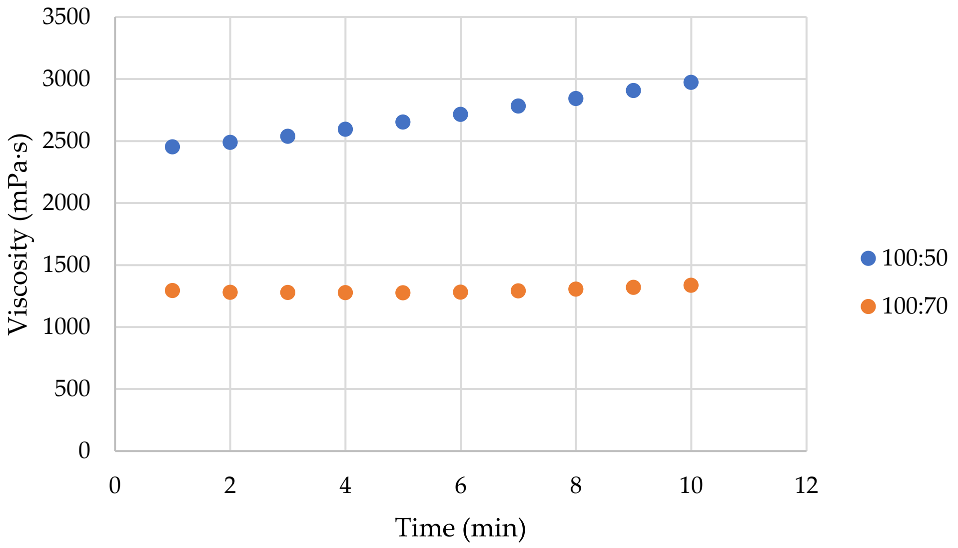

Figure 3. *Viscosity of PPF resin with different PPF:DEF ratio*

However, due to the issues found in the synthesis and the lack of time, this study was not finished and it needed more time to get conclusions. For this reason, the synthesis of PPF and its modification with GBN are presented as future works.

The results of this thesis established a good foundation to start the work with non-commercial resins synthesized in the lab. Therefore, the following steps using a synthesized resin would be:

- Study the polymerization process of PPF with different photoinitiators and different proportions of monomer.
- Set an adequate exposure time to achieve good printability.
- One advantage of producing the reins is that it is possible to study different procedures to add GBN: dispersion in the reactants before the reaction, dispersion in DEF added to reduce the viscosity after the reaction…
- Produce porous structures and study the cell response on them.

8.3. References

[1] J.E. Sanderson, Bone Replacement and Repair Putty Material From Unsaturated Polyester Resin And Vinyl Pyrrolidone, 1988.

[2] A.J. Domb, Poly(propylene glycol fumarate) compositions for biomedical applications, 1994.

[3] G.B. Kharas, M. Kamenetsky, J. Simantirakis, K.C. Beinlich, A.T. Rizzo, G.A. Caywood, K. Watson, Synthesis and characterization of fumarate-based polyesters for use in bioresorbable bone cement composites, J. Appl. Polym. Sci. 66 (1997) 1123–1137. https://doi.org/10.1002/(sici)1097-4628(19971107)66:6<1123::aid-app13>3.3.co;2-0.

[4] M.J. Yaszemski, R.G. Payne, W.C. Hayes, R. Langer, A.G. Mikos, In vitro degradation of a poly(propylene fumarate)-based composite material, Biomaterials. 17 (1996) 2127–2130. https://doi.org/10.1111/ocr.1999.2.2.49.

[5] M.N. Cooke, J.P. Fisher, D. Dean, C. Rimnac, A.G. Mikos, Use of Stereolithography to Manufacture Critical-Sized 3D Biodegradable Scaffolds for Bone Ingrowth, J. Biomed. Mater. Res. - Part B Appl. Biomater. 64B (2003) 65–69. https://doi.org/10.1002/jbm.b.10485.

[6] J.W. Lee, K.S. Kang, S.H. Lee, J.Y. Kim, B.K. Lee, D.W. Cho, Bone regeneration using a microstereolithography-produced customized poly(propylene fumarate)/diethyl fumarate photopolymer 3D scaffold incorporating BMP-2 loaded PLGA microspheres, Biomaterials. 32 (2011) 744–752. https://doi.org/10.1016/j.biomaterials.2010.09.035.

[7] G.N. Abdelrasoul, B. Farkas, I. Romano, A. Diaspro, S. Beke, Nanocomposite scaffold fabrication by incorporating gold nanoparticles into biodegradable polymer matrix: Synthesis, characterization, and photothermal effect, Mater. Sci. Eng. C. 56 (2015) 305–310. https://doi.org/10.1016/j.msec.2015.06.037.

[8] J.W. Choi, R. Wicker, S.H. Lee, K.H. Choi, C.S. Ha, I. Chung, Fabrication of 3D biocompatible/biodegradable micro-scaffolds using dynamic mask projection microstereolithography, J. Mater. Process. Technol. 209 (2009) 5494–5503. https://doi.org/10.1016/j.jmatprotec.2009.05.004.

[9] J.P. Fisher, D. Dean, A.G. Mikos, Photocrosslinking characteristics and mechanical properties of diethyl fumarate/poly(propylene fumarate) biomaterials, Biomaterials. 23 (2002) 4333–4343. https://doi.org/10.1016/S0142-9612(02)00178-3.

[10] X. Liu, M.N. George, S. Park, A.L. Miller II, B. Gaihre, L. Li, B.E. Waletzki, A. Terzic, M.J. Yaszemski, L. Lu, 3D-printed scaffolds with carbon nanotubes for bone tissue engineering: Fast and homogeneous one-step functionalization, Acta Biomater. 111 (2020) 129–140. https://doi.org/10.1016/j.actbio.2020.04.047.

[11] F.K. Kasper, K. Tanahashi, J.P. Fisher, A.G. Mikos, Synthesis of poly(propylene fumarate), Nat. Protoc. 4 (2009) 518–525. https://doi.org/10.1038/nprot.2009.24.

PUBLICATIONS AND CONTRIBUTIONS

JCR Publications

Directly related with the thesis

- S. López de Armentia, J.C. del Real-Romero, E. Paz, N. Dunne. Advances in biodegradable 3D printed scaffolds with carbon-based nanomaterials for bone regeneration. Materials. Vol. 13, nº. 22, pp. 5083-1 - 5083-49, Nov 2020 JCR: 3.623 Q1 (2020) - SJR: 0.682 Q2 (2020)

- S. López de Armentia, S. Fernández-Villamarín, Y. Ballesteros, J.C. del Real-Romero, N. Dunne, E. Paz. 3D printing of a graphene-modified photopolymer using stereolithography for biomedical applications: a study of the polymerization reaction. International Journal of Bioprinting. Vol. 8, nº. 1, pp. 503-182 - 503-197, Mar 2022. JCR JCR: 6.638 Q1 (2020) - SJR: 1.014 Q1 (2020)

- S. López de Armentia, J. Abenojar, Y. Ballesteros, J.C. del Real, N. Dunne, E. Paz. Polymerization Kinetics of Acrylic Photopolymer loaded with Graphene-Based Nanomaterials for Additive Manufacturing. Sent to Journal of Thermal Analysis and Calorimetry.

Non-related with the thesis

- S. López de Armentia, B. Enciso, G. Mokry, J. Abenojar, M.A. Martínez. Novel application of a thermoplastic composite with improved matrix-fiber interface. Journal of Materials Research and Technology. Vol. 8, nº. 6, pp. 5536 - 5547, Dec 2019. JCR: 5.289 Q1 (2019) - SJR: 0.898 Q1 (2019)

- J. Abenojar, S. López de Armentia, A.Q. Barbosa, M.A. Martínez, F. Velasco, L.F.M. Da Silva, J.C. del Real-Romero. Coating cork particles with iron oxide: effect on magnetic properties. Wood Science and Technology. Vol. 54, nº. 4, pp. 869 - 889, Jul 2020. JCR: 2.506 Q1 (2020); - SJR: 0.631 Q1 (2020)

- P. Gálvez, S. López de Armentia, J. Abenojar, M.A. Martínez. Effect of moisture and temperature on thermal and mechanical properties of structural polyurethane adhesive joints. Composite Structures. Vol. 247, pp. 112443-1 - 112443-13, Sept 2020. JCR: 5.407 Q1 (2020) - SJR: 1.630 Q1 (2020)

- J. Abenojar, M.A. Martínez, S. López de Armentia, E. Paz, J.C. del Real-Romero, F. Velasco. Mechanical properties and fire-resistance of composites with marble particles. Journal of Materials Research and Technology. Vol. 12, pp. 1403 - 1417, Jun 2021. JCR: 5.039 Q1 (2020) - SJR: 0.832 Q1 (2020)

- M.A. Martínez, S. López de Armentia, J. Abenojar. Influence of sample dimensions on single lap joints: effect of interactions between parameters. The Journal of Adhesion. Vol. 97, nº. 14, pp. 1358 - 1369, Oct 2021. JCR: 2.917 Q2 (2021); 2.917 Q2 (2020) - SJR: 0.738 Q1 (2021); 0.738 Q1 (2020)

- J. Abenojar, S. López de Armentia, M.A. Martínez, J.C. del Real-Romero. Development of a green epoxy adhesive for cork by adding lignin: thermal and bonding properties. Wood Science and Technology. Vol. 56, nº. 3, pp. 721 - 742, May 2022. JCR: 2.506 Q1 (2020) - SJR: 0.631 Q1 (2020)

Book Chapters

- J.C, del Real, E. Paz, S. López de Armentia, H. Handwerker, F. Debor. Chapter 29: Biomedical adhesives: qualification, specification, quality control, and risk mitigation in Advances in Structural Adhesive Bonding, 2nd Ed (Elsevier). Approved by editor

- S. Lopez de Armentia, J.C. del Real, N. Dunne, E. Paz. Chapter 41: 3D printed graphene for biomedical applications in 3D Printing: Fundamentals to Emerging Applications (CRC Press). Approved by editor

Conferences

- E. Paz, Y. Ballesteros, S. Lopez de Armentia, J.C. del Real. Graphene nanoplatelets as economical alternative in the reinforcement of PMMA bone cements. Poster presentation. 31st Annual Conference of the European Society for Biomaterials, 2021. Online

- S. Lopez de Armentia, S. Fernández-Villamarín, J.C. del Real, N, Dunne, E. Paz. Polymeric Scaffolds reinforced with Graphene-Based Nanomaterials obtained by SLA: Preliminary study of the effect of nanofillers on curing and printability. Poster presentation. 31st Annual Conference of the European Society for Biomaterials, 2021. Online

- E. Paz, S. Lopez de Armentia, M. Jiménez, J.C. del Real, N. Dunne. Effect of Graphene-Based Nanomaterials on Photocurable PLA Resin: Study of Curing Depth and Optimization of Exposure Time on LCD 3D Printing. Poster presentation. 31st Annual Conference of the European Society for Biomaterials, 2022. Bordeaux, France

- S. Lopez de Armentia, Y. Ballesteros, J.C. del Real, N, Dunne, E. Paz. Mechanical Properties of Thermal and UV Polymerized Graphene-Reinforced Acrylic Resin: Effect of Post-treatment on Samples Obtained by Stereolithography. Poster presentation. 31st Annual Conference of the European Society for Biomaterials, 2022. Bordeaux, France

APPENDIX

Table of Contents

1. *FTIR spectra*

FTIR spectra of R, R+G, R+GO and R+GoxNP obtained in Chapter 4 are shown in Figure 1, Figure 2, Figure 3 and Figure 4, respectively.

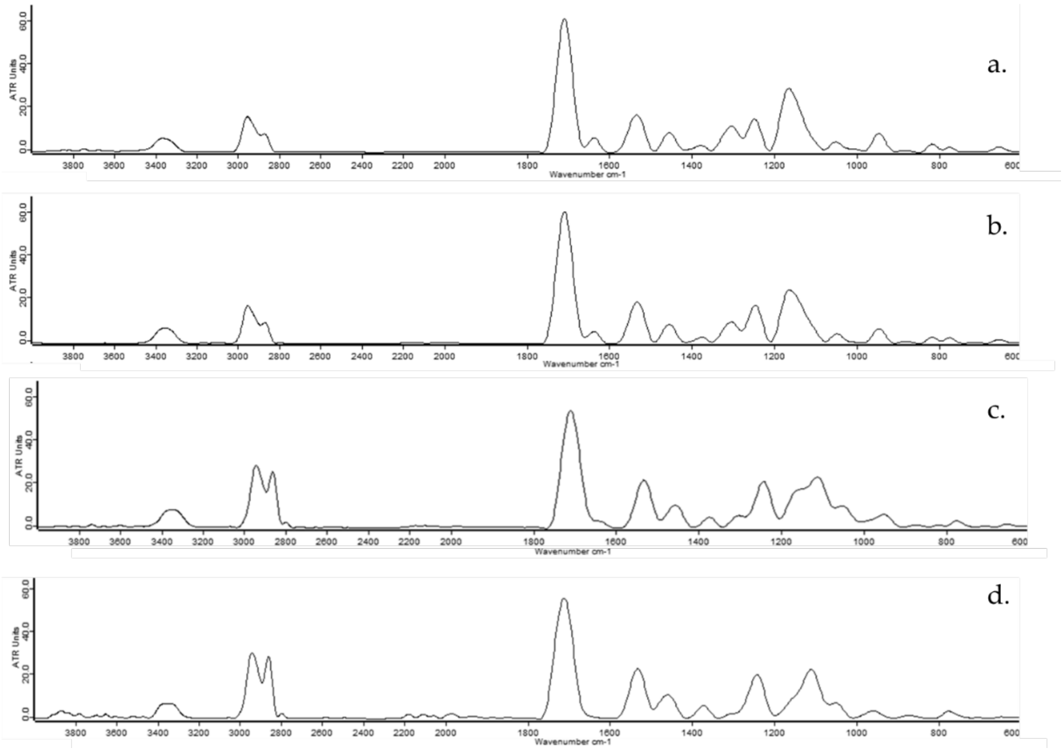

Figure 1. *FTIR spectra of R subjected to 0 (a), 5 (b), 15 (c) and 30 (d) min of UV light.*

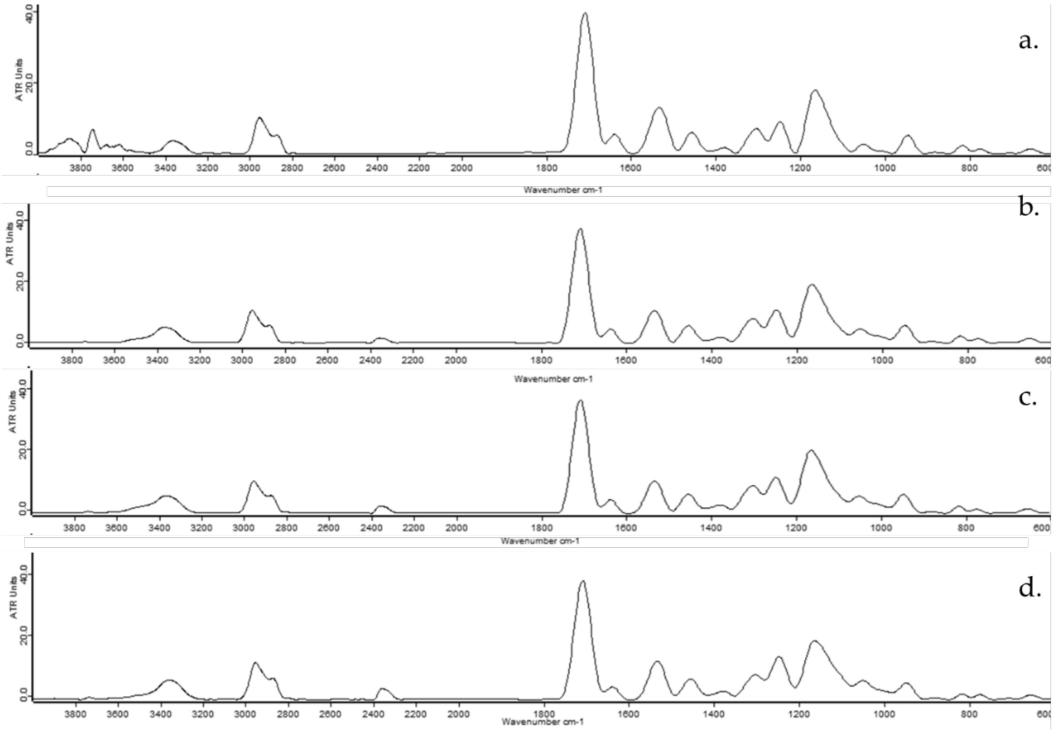

Figure 2. *FTIR spectra of R+G subjected to 0 (a), 5 (b), 15 (c) and 30 (d) min of UV light.*

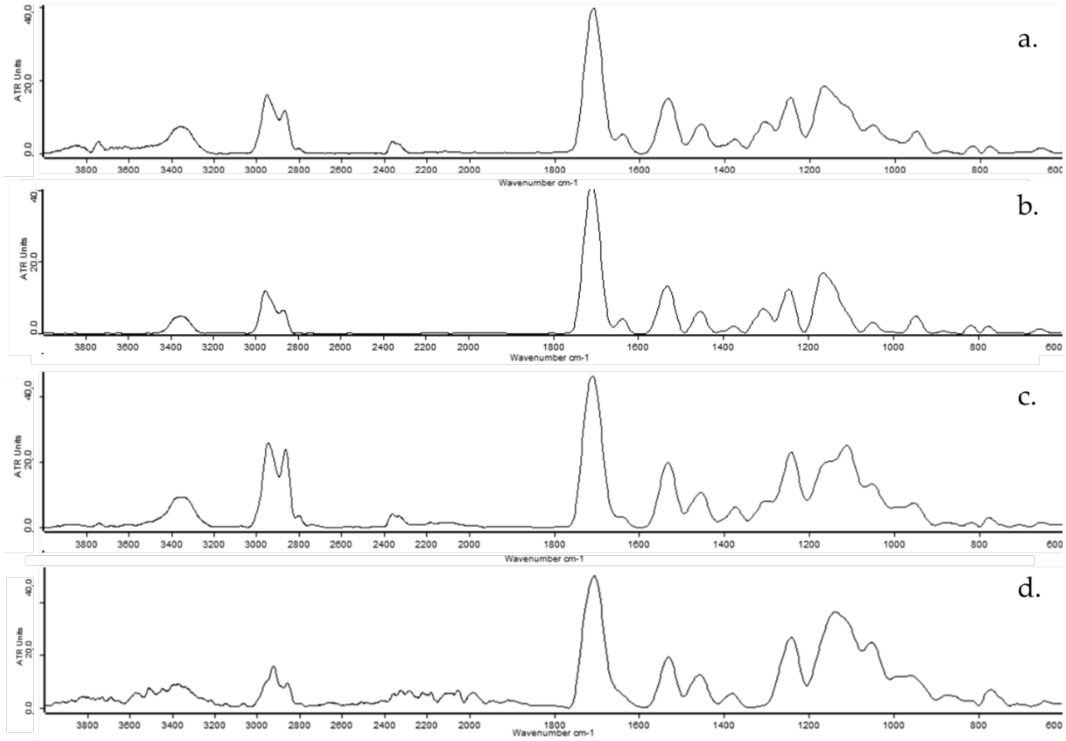

Figure 3. *FTIR spectra of R+GO subjected to 0 (a), 5 (b), 15 (c) and 30 (d) min of UV light.*

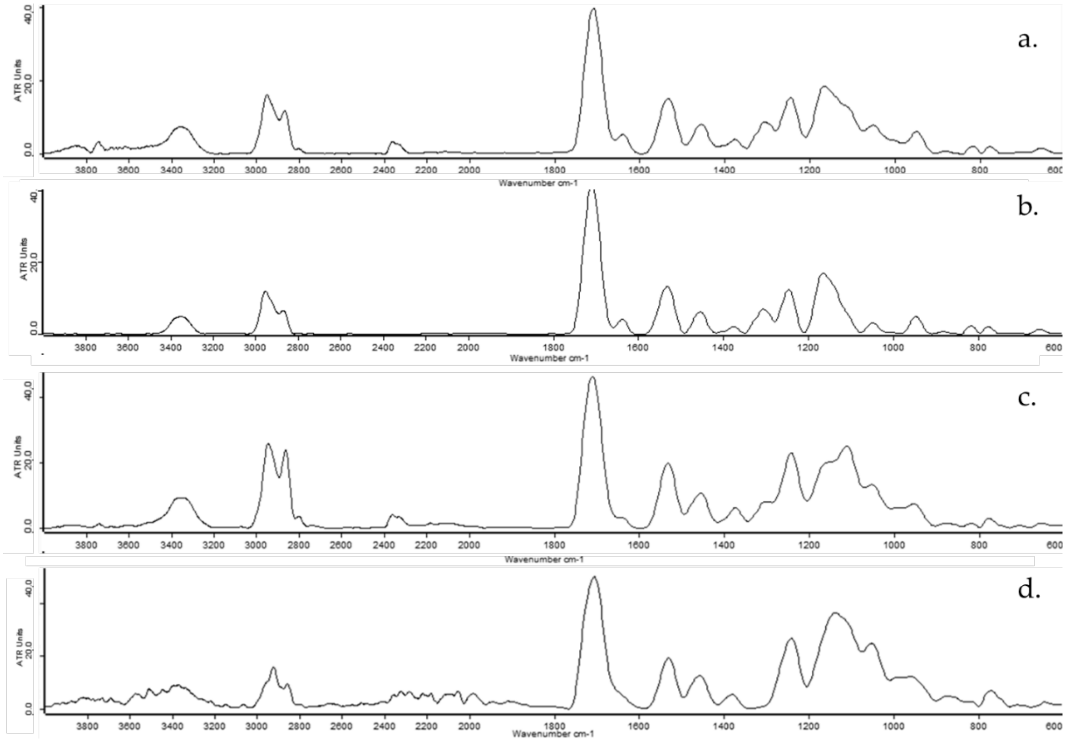

Figure 4. *FTIR spectra of R+GoxNP subjected to 0 (a), 5 (b), 15 (c) and 30 (d) min of UV light.*

2. *DSC thermograms*

DSC thermograms used in Chapter 5 to calculate activation energy from MFK are shown in Figure 1 and Figure 2. In both cases, different heating rates were used: 5°C/min (red), 10°C/min (green) and 20°C/min (blue).

In Figure 1, DSC thermograms corresponding to thermally-triggered polymerization can be seen.

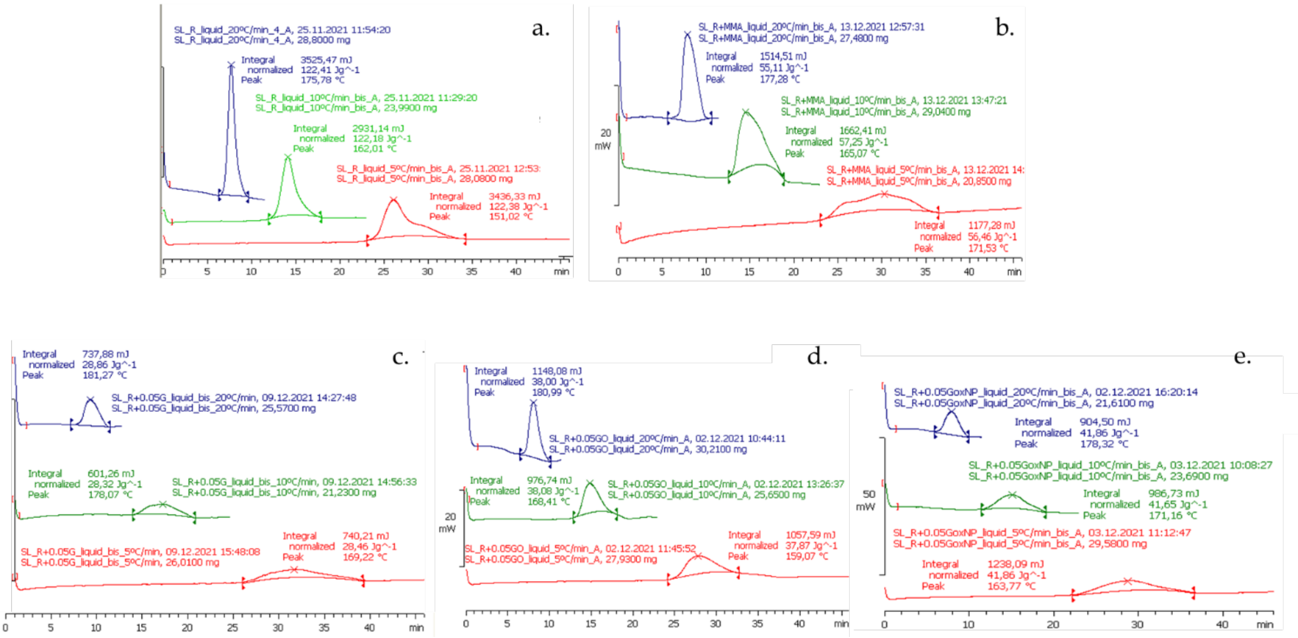

Figure 5. *DSC thermograms of thermally-triggered polymerization of R (a), R′ (b), R′+G (c), R′+GO (d) and R′+GoxNP (e).*

In Figure 2, DSC thermograms corresponding to UV-triggered polymerization can be seen.

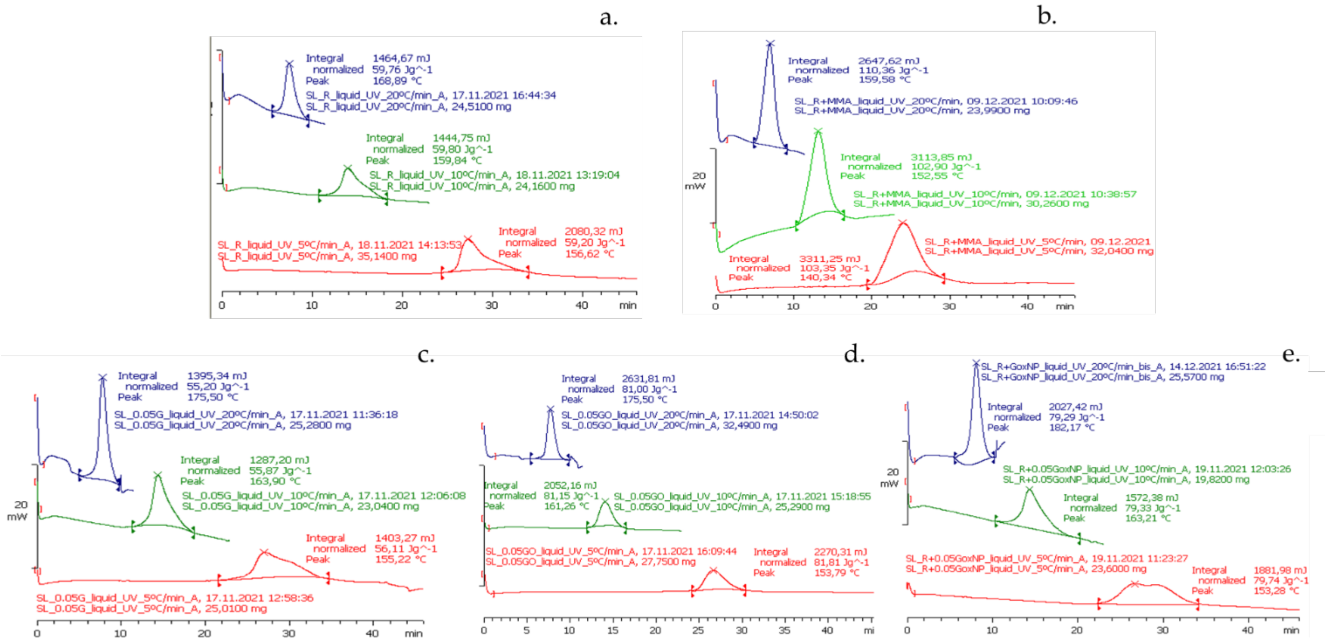

Figure 6. *DSC thermograms of UV-triggered polymerization of R (a), R′ (b), R′+G (c), R′+GO (d) and R′+GoxNP (e).*

3. *Technical Datasheet*

Technical DataSheet of acrylic resin and the three different GBN (G, GO and GoxNP) used in this work are shown in this Section.

MATERIAL DATA SHEET

Standard

Materials for High-Resolution Rapid Prototyping

High Resolution. For demanding applications, our carefully-engineered resins capture the finest features in your model.

Strength and Precision. Our resins create accurate and robust parts, ideal for rapid prototyping and product development.

Surface Finish. Perfectly smooth right out of the printer, parts printed on the Form 2 printer have the polish and finish of a final product.

CLEAR	WHITE	GREY	BLACK	COLOR
FLGPCL04	FLGPWH04	FLGPGR04	FLGPBL04	FLGPCB01

Prepared 04 . 19 . 2016
Rev 01 04 . 18 . 2017

Material Properties Data

The following material properties are comparable for all Formlabs Standard Resins.

	METRIC[1]		IMPERIAL[1]		METHOD
	Green[2]	Post-Cured[3]	Green[2]	Post-Cured[3]	
Tensile Properties					
Ultimate Tensile Strength	38 MPa	65 MPa	5510 psi	9380 psi	ASTM D 638-10
Tensile Modulus	1.6 GPa	2.8 GPa	234 ksi	402 ksi	ASTM D 638-10
Elongation at Failure	12 %	6.2 %	12 %	6.2 %	ASTM D 638-10
Flexural Properties					
Flexural Modulus	1.25 GPa	2.2 GPa	181 ksi	320 ksi	ASTM C 790-10
Impact Properties					
Notched IZOD	16 J/m	25 J/m	0.3 ft-lbf/in	0.46 ft-lbf/in	ASTM D 256-10
Temperature Properties					
Heat Deflection Temp. @ 264 psi	42.7 °C	58.4 °C	108.9 °F	137.1 °F	ASTM D 648-07
Heat Deflection Temp. @ 66 psi	49.7 °C	73.1 °C	121.5 °F	163.6 °F	ASTM D 648-07

[1] Material properties can vary with part geometry, print orientation, print settings, and temperature.

[2] Data was obtained from green parts, printed using Form 2, 100 µm, Clear settings, washed and air dried without post cure.

[3] Data was obtained from parts printed using Form 2, 100 µm, Clear settings, and post-cured with 1.25 mW/cm^2 of 405 nm LED light for 60 minutes at 60 °C.

Solvent Compatibility

Percent weight gain over 24 hours for a printed and post-cured 1 x 1 x 1 cm cube immersed in respective solvent:

Solvent	24 Hour Weight Gain (%)	Solvent	24 Hour Weight Gain (%)
Acetic Acid, 5 %	< 1	Hydrogen Peroxide (3 %)	< 1
Acetone	sample cracked	Isooctane	< 1
Isopropyl Alcohol	< 1	Mineral Oil, light	< 1
Bleach, ~5 % NaOCl	< 1	Mineral Oil, heavy	< 1
Butyl Acetate	< 1	Salt Water (3.5 % NaCl)	< 1
Diesel	< 1	Sodium hydroxide (0.025 %, pH = 10)	< 1
Diethyl glycol monomethyl ether	1.7	Water	< 1
Hydrolic Oil	< 1	Xylene	< 1
Skydrol 5	1	Strong Acid (HCl Conc)	distorted

HIGH RESOLUTION

For demanding applications, our carefully-engineered resins capture the finest features in your model.

STRENGTH AND PRECISION

Our resins create accurate and robust parts, ideal for our rapid prototyping and product development.

SURFACE FINISH

Perfectly smooth right out of the printer, parts printed on the Form 2 printer have the polish and finish of a final product.

CLEAR

Our Clear Resin polishes to near optical transparency, making it ideal for showcasing internal features.

WHITE

Our White Resin emphasizes fine details and has a matte finish with a warm, slightly ivory color.

GREY

Our Grey Resin has a smooth, matte finish and shows details beautifully without primer.

BLACK

Our Black Resin's opaque matte finish rivals the look of injection-molded plastics, capable of producing incredible looks-like prototypes.

COLOR KIT

Color Kit contains a Color Base cartridge and five Color Pigments. Use Color Kit to mix and print matte, opaque parts in a range of colors without the manual work of finishing and painting.

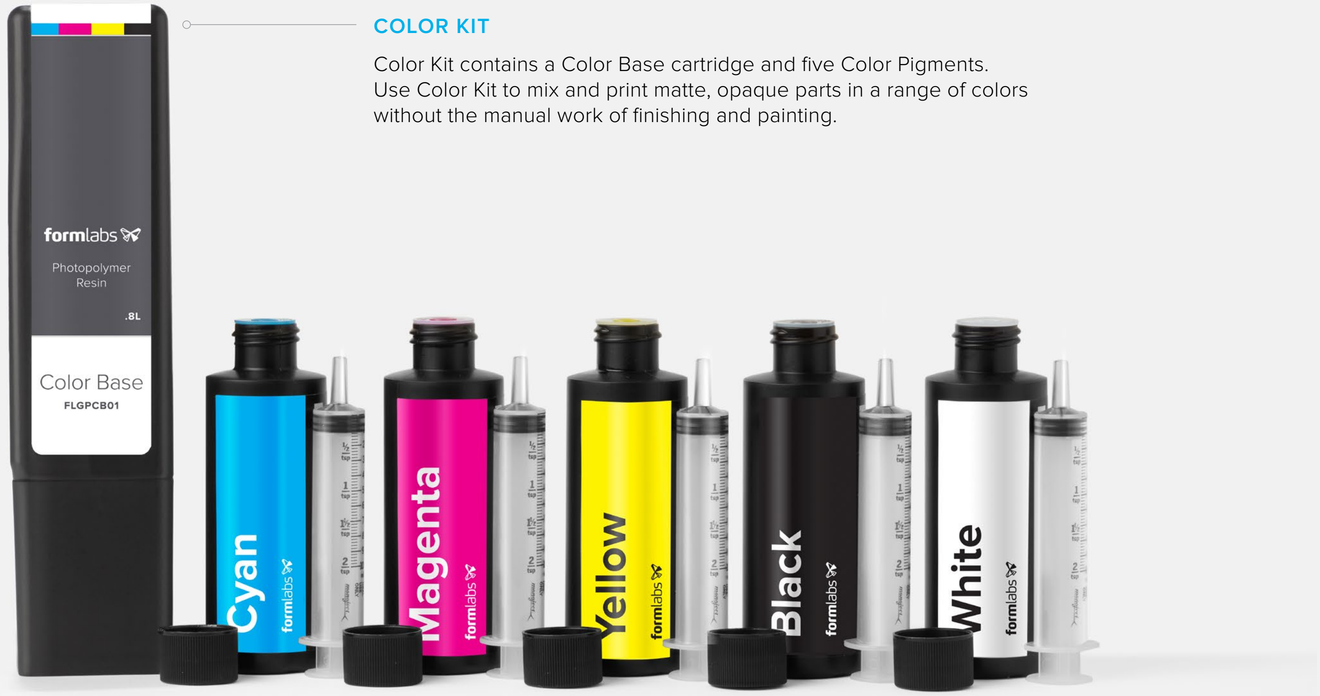

avanGRAPHENE (1-2 layers)

Product Description

This product consist on 1-2 layers of graphene

These products of graphene with lamellar structural morphology, are design for their use as fillers for conductive polymers as an alternative to carbon nanotubes and conductive blackcarbons and graphites due to its exceptional electrical conductivity.

This material is functionalized for their integration in most of the polymers such as PVC, TPU, polyamides, polypropylene or ABS and also for their incorporation in textiles

High conductivity can be obtained due to the easy to achieve percolation limit

avanGRAPHENE can be also use in resins and paints to obtain conductive resins, pains and composites allowing to obtain less than 10 Ohm/cm of surface and volumetric resistance

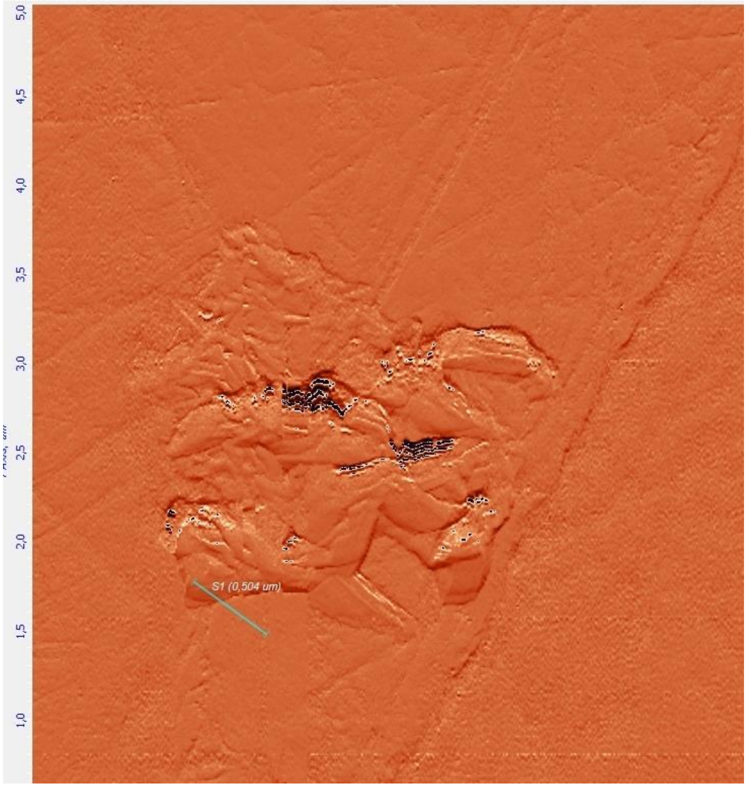

AFM picture of a single layer of graphene

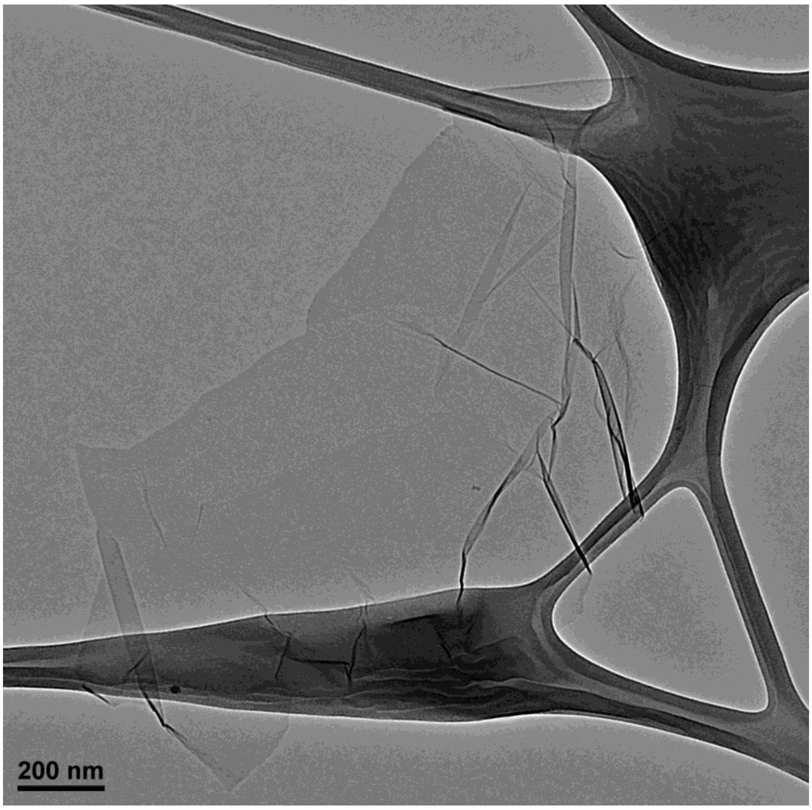

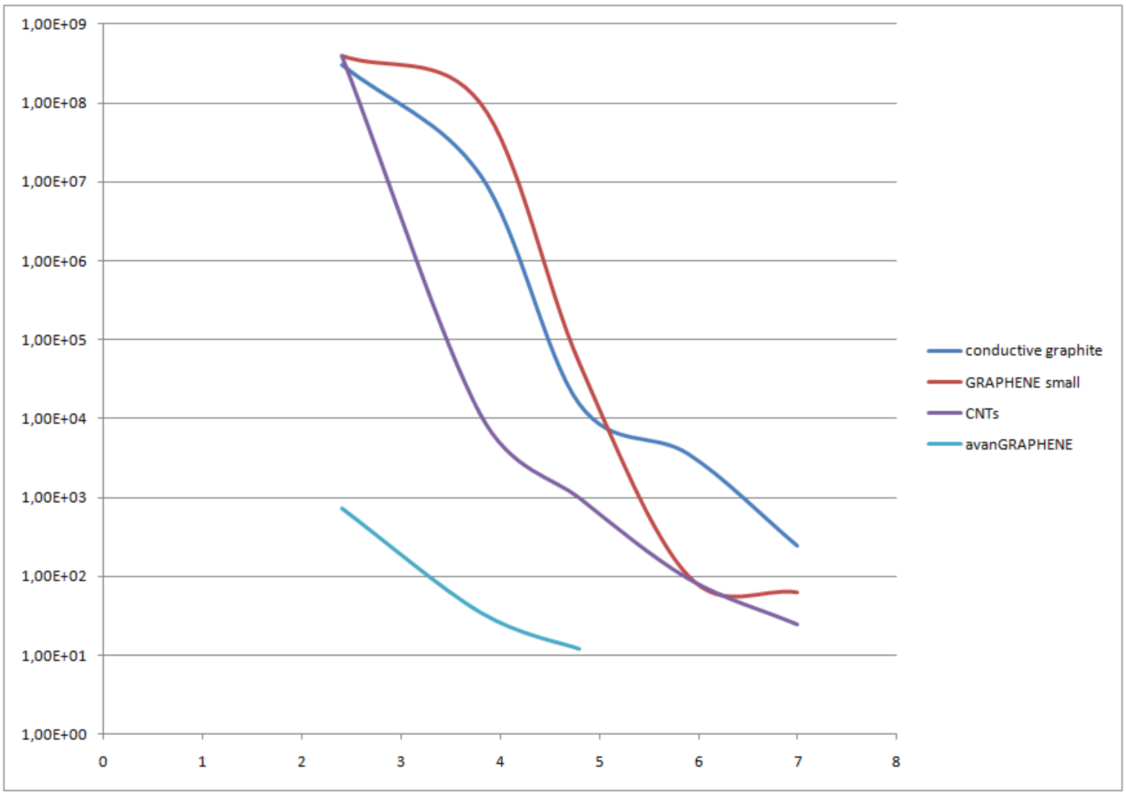

Percolation curve for a polymer composite

Graphene Oxide Characterization sheet

Reported data: FTIR Spectroscopy, Scanning Electron Microscopy, elemental analysis, %Mn by ICP-OES, X-ray diffraction (XRD), X-ray Photoelectron Spectroscopy (XPS), Zeta-potential and solid state 13C Nuclear Magnetic Resonance (NMR).

- FTIR Spectroscopy

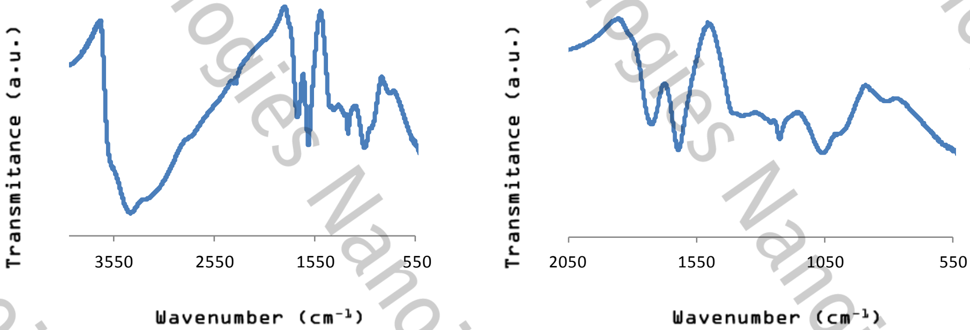

Left, full spectrum. Right, magnification between 2000 and 900 cm^{-1} wavenumbers.

Assignment (cm^{-1}) 1713 C=O (carbonyl/carboxy); 1611 C=C (aromatics); 1388 C-O (carboxy); 1217 C-O (epoxy); 1043 C-O (alkoxy).

- Scanning Electron Microscopy

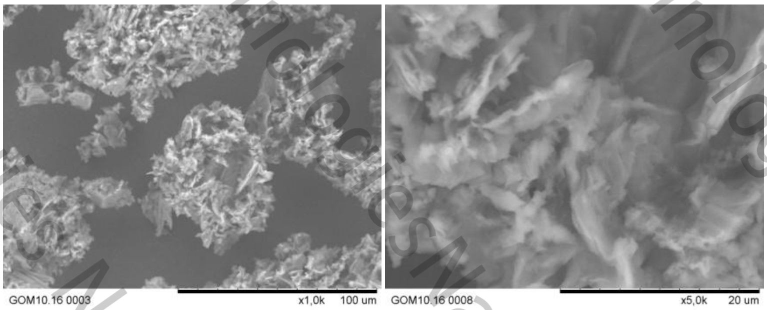

- Elemental analysis

	%C	%H	%N	%S	%O
GO	51.25	2.19	0.31	0.86	43.99

- %Mn by ICP-OES

The residual amount of Mn in graphene oxide measured by ICP-OES is 0.05%.

- XRD

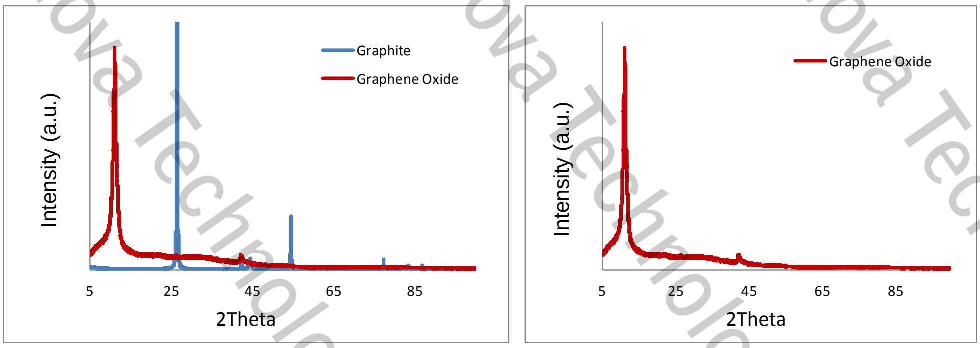

Left, XRD pattern for as-prepared graphene oxide bulk material. Right, comparison between XRD patterns of graphene oxide and graphite starting material evidencing that complete oxidation have occurred.

- TGA

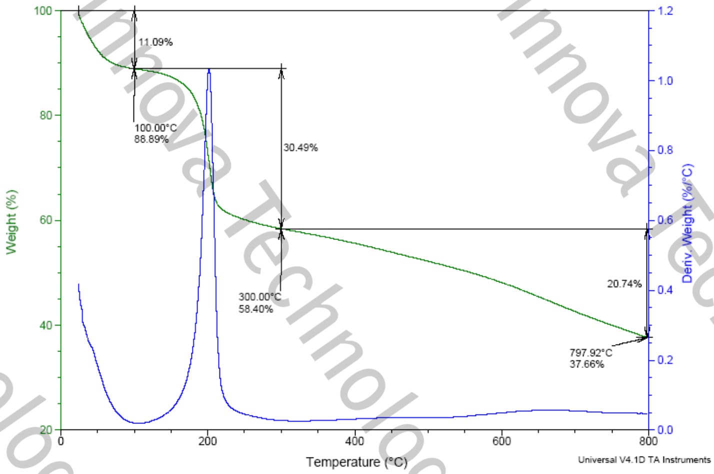

The first 11.9% mass loss (approx 100º C) it is due to water solvent molecules absorbed into the GO bulk material, the following 30.49% decrease at 300º C stands for GO decarboxylation process, further decomposition takes place up to 800ºC.

Experiment settings: temperature scanning rate: 1 ºC/min; temperature range 20-800 ºC; purging inert gas: N_2

- XPS

	C1s	**O1s**	**O/C atomic ratio**
GO	284.8 (38) 286.6 (54) 288.3 (8)	530.9 (21) 532.5 (79)	0.655

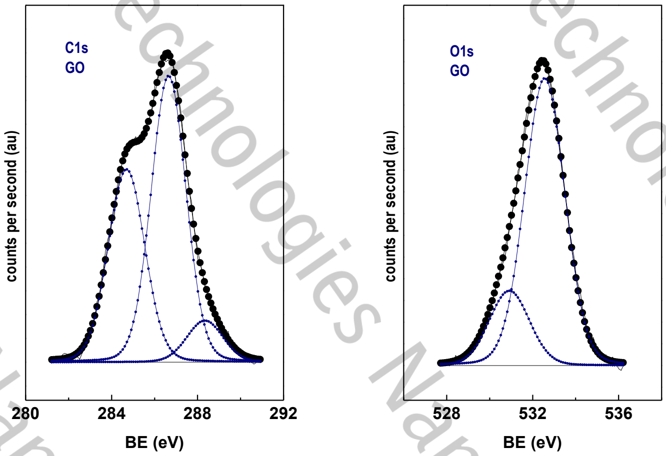

Binding energies (eV) and deconvoluted peaks (%) for C1s, O1s core levels.

Assignment (eV): 284.8 C-C 530.9 C=O
286.6 C-O 532.5 C-O
288.3 C=O

- AFM

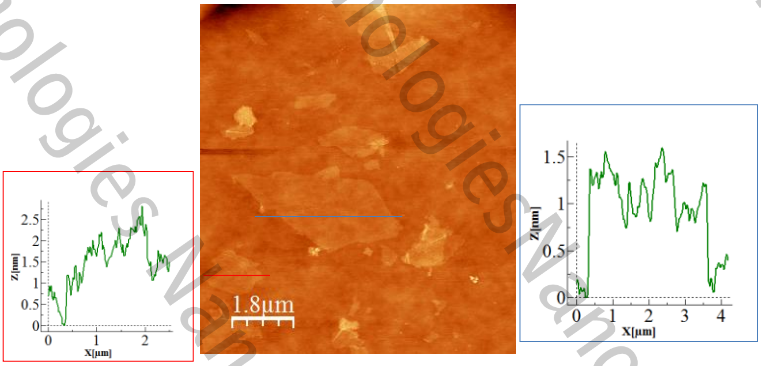

AFM topographic image and magnification of GO deposited onto a silicon wafer. The high profile of the observed GO flakes correlates accordingly calculated values (0.7-1.2 nm).

- Zeta-potential

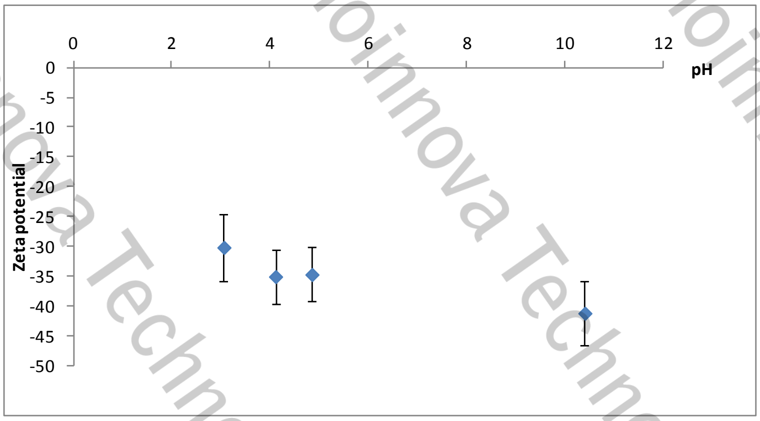

Zeta-potential versus pH curve.

- Solid state 13C NMR

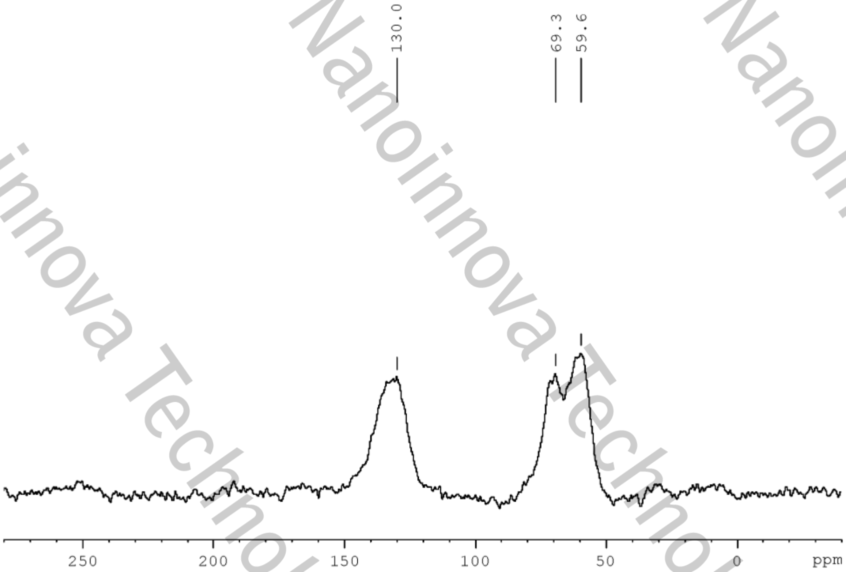

graphenit ® is a trade mark registered by Nanoinnova Technologies SL VAT= ESB85984367 Calle Faraday 7, 28049 Madrid (SPAIN)

graphenit®

Graphite Nano Platelets

powder

Industrial scale & affordable
Chemically Modified Graphene

GRAPHENIT-OX

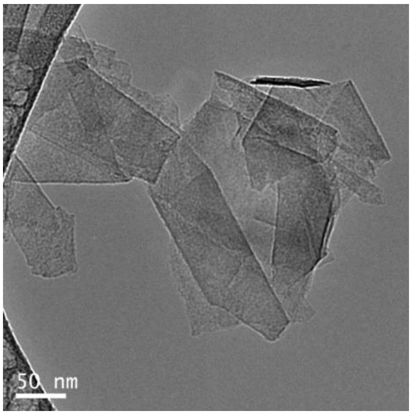

graphenit® is a series of chemically modified graphite nano-platelets for industrial applications. Chemical modification on the parent surface material yields different interactions with its surrounding matrix: polar/non polar solvent; thermostable, elastomer or thermosetting polymer, ceramic, etc. The ultimate goal is to achieve a good dispersion in the target matrix.

Graphene (single carbon 2D layer) is an extraordinary material at nanoscale dimension but difficult to manage in industrial processes. graphenit® brings a portfolio of derivatives not only in powder form but also in paste and masterbatch facilitating the full exploitation of its properties.

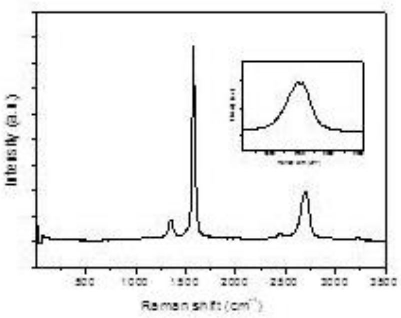

graphenit-OX is a low dimensional carbon nano platelet shape with a lateral dimension of about 2-3 micron with less than 5 layers thick. It is slightly oxidized (content of oxygen around 2%) yielding to a superior dispersion behavior in different solvent/matrix. It has been used with success as anti-corrosion additive in powder coating formulation among other properties.
Reproducibility between production batches is guaranteed by our internal quality control sample analysis.

REFERENCE	DESCRIPTION
graphenit-OX	Gaphene nanoplatelets slightly oxidized (2%). Highly dispersion properties in polar solvents. High chemical stability. BET surface area of 101 m2/g and bulk density of 0.2 g/mL. Less than 5 layers thick.

Graphite nano platelets have been claimed as mechanical reinforcement, electrical conductivity, thermal conductivity, anti-corrosion, lubricant, flame retardant, etc.